

Advanced in the chemistry of Molten Salt fuels with emphasis on Fission Products and Corrosion Products

Dumaire, T.

DOI

[10.4233/uuid:0752d005-7de4-4758-818f-08b30215f4d8](https://doi.org/10.4233/uuid:0752d005-7de4-4758-818f-08b30215f4d8)

Publication date

2024

Document Version

Final published version

Citation (APA)

Dumaire, T. (2024). *Advanced in the chemistry of Molten Salt fuels with emphasis on Fission Products and Corrosion Products*. [Dissertation (TU Delft), Delft University of Technology].
<https://doi.org/10.4233/uuid:0752d005-7de4-4758-818f-08b30215f4d8>

Important note

To cite this publication, please use the final published version (if applicable).
Please check the document version above.

Copyright

Other than for strictly personal use, it is not permitted to download, forward or distribute the text or part of it, without the consent of the author(s) and/or copyright holder(s), unless the work is under an open content license such as Creative Commons.

Takedown policy

Please contact us and provide details if you believe this document breaches copyrights.
We will remove access to the work immediately and investigate your claim.

**ADVANCES IN THE CHEMISTRY OF MOLTEN SALT
FUELS WITH EMPHASIS ON FISSION PRODUCTS AND
CORROSION PRODUCTS**

**ADVANCES IN THE CHEMISTRY OF MOLTEN SALT
FUELS WITH EMPHASIS ON FISSION PRODUCTS AND
CORROSION PRODUCTS**

Dissertation

for the purpose of obtaining the degree of doctor
at Delft University of Technology
by the authority of the Rector Magnificus, prof. dr. ir. T.H.J.J. van der Hagen,
chair of the Board for Doctorates
to be defended publicly on
Friday 6, September 2024 at 12:30 o'clock

by

Thomas DUMAIRE

Master of Science in Chemical Engineering
Sorbonne University, France
born in Melun, France

This dissertation has been approved by the promotor.

Composition of the doctoral committee:

Rector Magnificus,	chairperson
Prof. dr. R.J.M. Konings,	Delft University of Technology, <i>promotor</i>
Dr. ir. M. Rohde,	Delft University of Technology, <i>promotor</i>
Dr. A. L. Smith,	Delft University of Technology, <i>copromotor</i>

Independent members:

Prof. dr. M.J. Santofimia Navarro,	Delft University of Technology
Prof. dr. M. Rivenet,	Centrale Lille, France
Dr. C. Guéneau,	Paris-Saclay University, France
Dr. R.P. Hania,	Nuclear Research and Consultancy Group, the Netherlands
Prof. dr. ir. J.-L. Kloosterman,	Delft University of Technology, reserve member



This project has received funding from the Euratom research and training program 2014-2018 under grant agreement N° 847527



Keywords: Molten Salt Reactor, thermodynamics, CALPHAD, fission products, corrosion products

Printed by: Gildeprint - Enschede

Cover by: Pierre Dumaire

Copyright © 2024 by T. Dumaire

ISBN 978-94-6366-923-8

An electronic copy of this dissertation is available at <https://repository.tudelft.nl/>.

Tomorrow belongs to those who can hear it coming.

David Bowie

CONTENTS

Summary	xi
Samenvatting	xv
1. Introduction	1
1.1. Nuclear energy: solution to the environmental challenge	2
1.2. Molten Salt Reactor	2
1.2.1. General concept of the MSR	2
1.2.2. Historical background	4
1.2.3. Molten Salt Fast Reactor design	5
1.3. Fuels for Molten Salt Reactors	6
1.3.1. LiF-ThF ₄ -UF ₄	6
1.3.2. Other fuel options	7
1.4. Challenge with Molten Salt Reactors	8
1.4.1. Fission products	8
1.4.2. Corrosion products	9
1.5. Thermodynamic tool	10
1.6. Objectives of this work	11
1.7. Content of this dissertation	11
2. Influence of FP on some properties of molten fluoride salt fuels	23
2.1. Introduction	23
2.2. Methodology	24
2.3. Experimental	25
2.3.1. Sample preparation	25
2.3.2. X-ray Diffraction	26
2.3.3. Differential Scanning Calorimetry	26
2.3.4. Knudsen Effusion Mass Spectrometry	27
2.4. Results & Discussions	29
2.4.1. Impact on the melting properties of the fuels	29
2.4.2. Vaporization of fuel materials	31
2.4.3. Mass spectrometry analysis of Fission products	35
2.5. Conclusion	45
3. Thermodynamic assessment of the LiF-BaF₂-ZrF₄ system	51
3.1. Introduction	51
3.2. Experimental methods	53
3.2.1. Sample preparation	53
3.2.2. X-ray Diffraction	53

3.2.3. Differential Scanning Calorimetry	53
3.3. Thermodynamic modeling	54
3.3.1. Gibbs energies of pure compounds	54
3.3.2. Selected thermodynamic data	54
3.3.3. Solid solution modeling	55
3.3.4. Liquid solutions modeling for binary systems	57
3.3.5. Liquid solution for the ternary system	59
3.3.6. Gas phase	59
3.4. Results and discussions	59
3.4.1. LiF-BaF ₂	59
3.4.2. LiF-ZrF ₄	62
3.4.3. BaF ₂ -ZrF ₄	64
3.4.4. Ternary LiF-BaF ₂ -ZrF ₄	67
3.5. Conclusions	74
4. Management of gaseous Fission Products and metallic particles	81
4.1. Introduction	82
4.1.1. Literature review	82
4.1.2. Micro-sized particles investigations	83
4.1.3. Objectives of this work	83
4.2. Nanoparticles observation in a bubbly flow	84
4.2.1. Laser Induced Fluorescence	84
4.2.2. Setup and materials	86
4.2.3. Bubbling characteristics	88
4.3. Particles collection techniques	93
4.3.1. Effect of the Hallimond tube on the extraction efficiency	93
4.3.2. Research on alternative systems	94
4.3.3. Liquid filtration	95
4.3.4. Liquid filtration experiments	98
4.4. Results	103
4.4.1. Extraction of nanoparticles	103
4.4.2. Evolution of the particle extraction	104
4.4.3. Conclusion	106
5. Thermodynamic assessment of the FLiNaK-CrF₃ and CrF₂-CrF₃	109
5.1. Literature review	110
5.1.1. Structural data	110
5.1.2. Thermodynamic data	111
5.1.3. Phase diagram data	112
5.2. Thermodynamic modeling	113
5.2.1. Gibbs energies of pure compounds	113
5.2.2. Solid solutions	113
5.2.3. Liquid solution	115
5.3. Results and discussion	117
5.3.1. CrF ₂ -CrF ₃	117
5.3.2. AF-CrF ₃ (A = Li, Na, K)	119

5.3.3. Excess properties	124
5.4. Conclusion	125
6. CrF₂ corrosion product in the molten LiF-ThF₄ salt system	131
6.1. Introduction	131
6.2. Experimental	133
6.2.1. Sample preparation	133
6.2.2. X-ray Diffraction	135
6.2.3. Calorimetry measurements	135
6.2.4. Low-temperature heat capacity of CrF ₂	136
6.2.5. Magnetization measurements on CrF ₂	136
6.3. Thermodynamic modeling	137
6.3.1. Liquid solution	137
6.4. Results & discussions	140
6.4.1. CrF ₂ synthesis and product characterization	140
6.4.2. CrF ₂ low-temperature heat capacity	141
6.4.3. Binary systems	143
6.4.4. Ternary system LiF-CrF ₂ -ThF ₄	147
6.5. Conclusion	152
7. A promising fuel for fast neutron spectrum Molten Salt Reactor	161
7.1. Introduction	161
7.2. Thermodynamic modeling	163
7.2.1. Gibbs energies of pure compounds	163
7.2.2. Solid solution	164
7.2.3. Liquid solutions	165
7.2.4. Liquid solution for the ternary system	166
7.3. Results	167
7.3.1. NaCl-PuCl ₃ system	167
7.3.2. ThCl ₄ -PuCl ₃ system	170
7.3.3. NaCl-ThCl ₄ system	171
7.3.4. Ternary assessment	173
7.4. Discussion	176
7.5. Conclusion	181
8. Conclusion	189
8.1. Summary of the results	189
8.2. Main outcomes	191
8.3. Outlooks and suggestions	191
A. Appendices: CrF₂ in the molten LiF-ThF₄ salt system	195
A.1. Low temperature heat capacity of CrF ₂	195
A.2. Magnetization measurements of CrF ₂	196
A.3. Ternary equilibria	197
List of Publications	203

SUMMARY

The Molten Salt Reactor (MSR) is probably the most promising design of the 4th generation for the future of nuclear energy. The liquid nature of the fuel and the implementation of innovative safety measures could, in time, open up access to energy from atomic fission to the whole world. The adaptability of the concept makes it possible to consider different slow or fast neutron spectrum options, different fuel options depending on available resources, and different sizes and power outputs, from a few MWth to 3,000 MWth. This work aims to answer some of the many questions that need to be addressed to assess the safety of MSRs. One of the main objectives is to use a thermodynamic approach to describe the effect of the fission and corrosion products on the fuel salt behavior, and the other is to study methods for controlling and eliminating interfering fission product elements in the reactor core.

The introduction defines the objective of this thesis, detailing the historical background to the development of the Molten Salt Reactor from the 1950s to the present day. An overview of the different fuels considered is given, followed by a discussion of the challenges posed by chemical equilibrium of the solution. Finally, the focus is on the thermodynamic modeling method and its development in the context of nuclear research. This introduction finally presents the structure of this thesis, which is followed hereafter.

In the second chapter of this thesis, the impact of fission products on the thermodynamic properties of the fuel and its vaporization behavior is studied. A mixture representing simulated irradiated fuel composition during reactor operation with a LiF–ThF₄–UF₄ fuel, reference fuel of the Molten Salt Fast Reactor concept (MSFR), was determined and experimentally analyzed. The thermodynamic behavior of the fuel in presence of a large excess of fission products was investigated by calorimetry measurements. Then Knudsen effusion mass spectrometry measurements of the simulated fuel were performed. This study provides new insight on the relative retention of the main fission products in the LiF–ThF₄–UF₄ molten fuel, and its stability in extreme operating conditions.

To extend the safety assessment, the effect of two major fission products, barium and zirconium, were explored. In the third chapter, the thermodynamic properties of ZrF₄ and BaF₂ in molten LiF are studied. New experimental data were collected in the LiF–BaF₂ and LiF–ZrF₄ systems by Differential Scanning Calorimetry (DSC) on different compositions of mixture of pure end-members. These data were used to establish the phase diagrams of the binary systems LiF–BaF₂, LiF–ZrF₄, BaF₂–ZrF₄ and finally the ternary system LiF–BaF₂–ZrF₄. Thermodynamic models were moreover developed using the Modified Quasichemical Model in the Quadruplet (MQMQ) approximation, that is well adapted to ionic solutions with strong short range ordering and used in the framework of the JRC Molten Salt Database. Computations using the aforementioned models results confirmed the stability of a large number of intermediate compounds in the LiF–BaF₂–ZrF₄ system at the minimum operating temperature of 873 K. In particular, Ba₂ZrF₈ and Ba₃ZrF₁₀

were found to be stable above 1173 K (above the maximum operating temperature), indicating the potential formation of solid compounds of fission products in the liquid solution. These observations constitute valuable insights for the risk assessment of the MSR, especially to anticipate the release of fission products in case of an accident.

To conclude on the fission products safety assessment, the fourth chapter of this thesis focuses on the removal of metallic particles by helium bubbling. The implementation of a gaseous in-core bubbling flow was investigated in the framework of the MSFR. The helium bubbling flow should entrain the gaseous fission products (such as Kr and Xe), noble and semi-noble solid particles in suspension in the liquid core and concentrate them in a recovering system. The objective is to remove these potentially poisonous elements from the reactor without interfering with the flow dynamics of the reactor. In this work, an experimental setup was implemented to observe the dynamics of the removal of nanoparticles by bubbling using Laser Induced Fluorescence measurements. The removal efficiency of different sizes of nanoparticles (250nm, 530nm, 890nm) was measured for different flow rates (5, 10 and 15 standard cubic centimeter (sccm)). The results allowed to empirically evaluate the efficiency of the recovery of nanoparticles by gaseous bubbling as function of the size and the flow rate and can be used as a support for numerical simulations aiming to refine the strategy for the safety measures.

The next part of this thesis focused on an essential aspect of the perenity of the MSR, i.e. corrosion issues of the structural materials in contact with the molten salt. Corrosion is one of the most critical concerns for the long term use of the MSR because it can induce structural degradation of the reactor core alloy at the same time as dissolution of corrosion products inside the nuclear fuel salt matrix. The understanding of the effect of those corrosion products on the fuel salt behavior is thus of prime importance. Chromium is the main corrosion product encountered in all the experimental evaluations of the corrosion processes for Ni-based alloys considered for the containment of fluoride based salt. In the fifth chapter, the focus is on the phase equilibria of trivalent CrF_3 in the so-called FLiNaK salt (LiF-NaF-KF). The thermodynamic assessments of the binary systems LiF-CrF_3 , NaF-CrF_3 and KF-CrF_3 were performed using the MQMQ approximation based on literature data. In this work, the phase diagram of the $\text{CrF}_2\text{-CrF}_3$ system was also calculated, indicating a high instability of trivalent CrF_3 in molten salt conditions.

To extend this work, the sixth chapter of this thesis is focused on divalent CrF_2 , the most stable form of the chromium in lithium based molten salts. Two routes of synthesis of pure CrF_2 were investigated, and a high purity of the products was confirmed by DSC measurements and X-ray Diffraction. From pure CrF_2 , LiF and ThF_4 synthesized by gaseous fluorination, experimental phase diagram data of the LiF-CrF_2 , $\text{CrF}_2\text{-ThF}_4$ and $\text{LiF-CrF}_2\text{-ThF}_4$ systems were collected for different selected compositions. The two binary systems showed to be simple eutectic phase diagrams, without any intermediate compound formed. The results were confirmed by X-ray analysis. In the case of the ternary system, the only identified intermediate compounds were those formed in the system LiF-ThF_4 . The data collected were the basis of the first modeling of the LiF-CrF_2 , $\text{CrF}_2\text{-ThF}_4$ and $\text{LiF-CrF}_2\text{-ThF}_4$ systems using the modified quasichemical model. This work demonstrated the solubility of CrF_2 in the LiF-ThF_4 molten salt system, preventing the formation of solid compound in the solution.

Fluoride salts have been investigated most extensively in most Molten Salt Reactor projects to this date. However, using chloride salts as an alternative carrier salt, and in particular NaCl, is today a widely explored option worldwide, particularly for the development of fast neutron spectrum reactors. In the last and seventh chapter, a first exploration is made of the thermodynamic behavior of the chloride alternative for thorium-based MSR fuel, NaCl–ThCl₄–PuCl₃. Based on literature data, models of the binary phase diagrams NaCl–PuCl₃ and ThCl₄–PuCl₃ and the NaCl–ThCl₄–PuCl₃ ternary system were developed for the first time using the MQCM method. The ternary system exhibits two eutectics at relatively low temperatures, 597 K and 598 K, and the liquid field shows a wide composition range with a liquid transition below the minimum safe operating temperature proposed for MSR (873 K). The NaCl–ThCl₄–PuCl₃ demonstrates very promising thermodynamic properties and can be considered an interesting fuel option for the fast neutron spectrum MSR.

Ultimately, this research contributes to the overall understanding of essential aspects for the safety demonstration and the feasibility of MSRs. Understanding the thermodynamic behavior and more generally the impact of fission products were analyzed relatively exhaustively in this work. The in-core helium bubbling strategy was experimentally assessed with innovative measurement methods. The thermodynamic properties of the main corrosion product, chromium, were exhaustively determined in molten LiF–ThF₄ salt for the first time. Throughout this work, the thermodynamic tool of quasichemical modeling in the quadruplet approximation has demonstrated its potential, enabling to describe complex ionic molten salt solutions, including fuel, fission products and corrosion products elements, to assess essential aspects related to the safety assessment of MSRs.

SAMENVATTING

De gesmolten-zoutreactor (MSR) is waarschijnlijk het meest veelbelovende ontwerp van de 4de generatie voor de toekomst van kernenergie. De vloeibare toestand van de brandstof en de implementatie van innovatieve veiligheidsmaatregelen zouden op termijn de hele wereld toegang kunnen geven tot energie uit kernsplijting. De flexibiliteit van het concept maakt verschillende opties met een spectrum van langzame of snelle neutronen mogelijk, kan verschillende brandstoffen benutten afhankelijk van de beschikbare bronnen, en kan worden ontworpen met verschillende vermogens, van een paar MWth tot 3000 MWth. Het werk beschreven in dit proefschrift heeft als doel om enkele van de vele vragen te beantwoorden die beantwoord moeten worden om de veiligheid van MSR's te beoordelen. Een van de belangrijkste doelstellingen is het gebruik van een thermodynamische benadering om het effect van de splijtings- en corrosieproducten op het gedrag van het brandstofzout te beschrijven, en wordt gecombineerd met het bestuderen van methoden om storende splijtingsproducten in de reactorkern te beheersen en te verwijderen.

Het inleidende hoofdstuk beschrijft het doel van dit proefschrift en de historische achtergrond van de ontwikkeling van de gesmolten-zoutreactor vanaf de jaren vijftig tot nu. Er wordt een overzicht gegeven van de verschillende brandstoffen die in aanmerking kwamen, gevolgd door een bespreking van de uitdaging van het chemisch evenwicht van de oplossing. Tot slot ligt de nadruk op de thermodynamische modelleermethode en de ontwikkeling ervan in de context van nucleair onderzoek. De inleiding introduceert ten slotte de structuur van dit proefschrift, die hierna wordt gevolgd.

In het tweede hoofdstuk van dit proefschrift wordt de invloed van splijtingsproducten op de thermodynamische eigenschappen van de brandstof en het verdampingsgedrag bestudeerd. Een mengsel is geproduceerd dat een samenstelling van bestraalde $\text{LiF-ThF}_4\text{-UF}_4$ reactorbrandstof simuleert, de referentiebrandstof van het concept van de Molten Salt Fast Reactor (MSFR), en experimenteel geanalyseerd. Het thermodynamische gedrag van de brandstof in aanwezigheid van een grote overmaat aan splijtingsproducten is onderzocht met behulp van calorimetrische metingen. Vervolgens zijn Knudsen effusie massaspectrometriemetingen van de gesimuleerde brandstof uitgevoerd. Dit onderzoek geeft een nieuw inzicht in de oplosbaarheid van de belangrijkste splijtingsproducten in de gesmolten $\text{LiF-ThF}_4\text{-UF}_4$ brandstof en de stabiliteit ervan onder extreme bedrijfsomstandigheden.

Om de veiligheidsbeoordeling te verbreden, is vervolgens het effect van twee belangrijke splijtingsproducten, barium en zirkonium, onderzocht. In dit derde hoofdstuk worden de thermodynamische eigenschappen van ZrF_4 en BaF_2 in gesmolten LiF bestudeerd. Er zijn nieuwe experimentele gegevens verzameld in de systemen LiF-BaF_2 en LiF-ZrF_4 met behulp van Differential Scanning Calorimetrie (DSC) aan verschillende samenstellingen van mengsels van zuivere eindleden. Deze gegevens zijn gebruikt om

de fase-diagrammen van de binaire systemen $\text{LiF}-\text{BaF}_2$, $\text{LiF}-\text{ZrF}_4$, $\text{BaF}_2-\text{ZrF}_4$ te bepalen en uiteindelijk het ternaire systeem $\text{LiF}-\text{BaF}_2-\text{ZrF}_4$. Bovendien zijn thermodynamische modellen ontwikkeld met behulp van het MQMQ benadering, dat goed geschikt is voor ionogene oplossingen met een sterke ordening op korte afstand en gebruikt wordt in het kader van de JRC Molten Salt Database. Berekeningen met de bovengenoemde modellen bevestigen de stabiliteit van een groot deel van de tussenliggende verbindingen in het $\text{LiF}-\text{BaF}_2-\text{ZrF}_4$ systeem bij de minimale bedrijfstemperatuur van 873 K. Vooral Ba_2ZrF_8 en $\text{Ba}_3\text{ZrF}_{10}$ bleken stabiel te zijn boven 1173 K (boven de maximale werkingstemperatuur), wat wijst op de mogelijke vorming van vaste verbindingen van splijtingsproducten in de vloeibare oplossing. Deze waarnemingen vormen waardevolle inzichten voor de risicobeoordeling van de MSR, vooral om te anticiperen op het vrijkomen van splijtingsproducten in het geval van een ongeval.

Ter afsluiting van de veiligheidsbeoordeling van splijtingsproducten richt het vierde hoofdstuk van dit proefschrift zich op de afscheiding van metaaldeeltjes door helium borrelen. De relatieve retentie van een gasvormige borrelstroom in de kern is onderzocht in het kader van de MSFR. De helium borrelstroom moet zowel gasvormige splijtingsproducten (zoals Kr en Xe) als vaste deeltjes van de edele en semi-nobele metalen in suspensie in de vloeibare kern meevoeren en concentreren in een recuperatiesysteem. Het doel is om deze potentieel storende elementen uit de reactor te verwijderen zonder de stromingsdynamica van de reactor te verstoren. In dit werk is een experimentele opstelling geïmplementeerd om de dynamica van de verwijdering van nanodeeltjes door borrelen met helium te volgen met behulp van lasergeïnduceerde fluorescentiemetingen. De verwijderingsefficiëntie van nanodeeltjes van verschillende grootte (250nm, 530nm, 890nm) is gemeten voor verschillende stroomsnelheden (5, 10 en 15 standaard kubieke centimeter (sccm)). De resultaten maaken het mogelijk om de efficiëntie van de afscheiding van nanodeeltjes door gasbellen empirisch te evalueren als functie van de grootte en het debiet en kunnen worden gebruikt ter ondersteuning van numerieke simulaties om de veiligheidsstrategie te verfijnen.

Het volgende deel van dit proefschrift richt zich op een essentieel aspect van de duurzaamheid van de MSR, namelijk corrosieproblemen van de constructiematerialen die in contact komen met het gesmolten zout. Corrosie is een van de meest kritieke punten voor het gebruik van de MSR op lange termijn, omdat de degradatie van de legering van de reactorkern kan veroorzaken en tegelijkertijd corrosieproducten kan oplossen in de matrix van het splijststofzout. Het begrijpen van het effect van die corrosieproducten op het gedrag van het splijststofzout is dus van essentieel belang. Chroom is het belangrijkste corrosieproduct dat is aangetroffen in alle experimentele evaluaties van corrosie van Ni-gebaseerde legeringen die voor de insluiting van fluoride zouten worden overwogen. In het vijfde hoofdstuk lag de nadruk op de fase-evenwichten van driewaardig CrF_3 in het FLiNaK-zout ($\text{LiF}-\text{NaF}-\text{KF}$). De thermodynamische evaluatie van de binaire systemen $\text{LiF}-\text{CrF}_3$, $\text{NaF}-\text{CrF}_3$ en $\text{KF}-\text{CrF}_3$ zijn uitgevoerd met behulp van het Modified Quasichemical Model in de Quadruplet (MQMQ) benadering op basis van literatuurgegevens. In dit werk is ook het fase-diagram van het systeem driewaardig chroom $\text{CrF}_2-\text{CrF}_3$ geëvalueerd, wat wijst op een hoge instabiliteit van driewaardig chroom CrF_3 in gesmolten zout.

Om dit werk uit te breiden is het zesde hoofdstuk van dit proefschrift gericht op twee-

waardig chroom CrF_2 , de meest stabiele vorm van chroom in lithiumhoudende gesmolten zouten. Twee syntheseroutes van zuiver CrF_2 zijn onderzocht en een hoge zuiverheid van de producten is bevestigd door DSC-metingen en röntgendiffractie. Met zuiver CrF_2 , LiF en ThF_4 gesynthetiseerd door gasfluorgenering, zijn de experimentele fase-diagramgegevens van de $\text{LiF}-\text{CrF}_2$, $\text{CrF}_2-\text{ThF}_4$ en $\text{LiF}-\text{CrF}_2-\text{ThF}_4$ systemen verzameld voor verschillende geselecteerde samenstellingen. De twee binaire systemen blijken eenvoudige eutectische fase-diagrammen te zijn, zonder enige tussenverbinding. De resultaten zijn bevestigd door röntgenanalyse. In het geval van het ternaire systeem zijn enkel intermediaire verbindingen die worden gevormd in het $\text{LiF}-\text{ThF}_4$ systeem geïdentificeerd. De verkregen gegevens vormen de basis voor de eerste modellering van de systemen $\text{LiF}-\text{CrF}_2$, $\text{CrF}_2-\text{ThF}_4$ en $\text{LiF}-\text{CrF}_2-\text{ThF}_4$ met behulp van het gewijzigde quasichemische model. Dit werk toont dat CrF_2 oplosbaar is in het $\text{LiF}-\text{ThF}_4$ gesmolten zoutsysteem, waardoor de vorming van vaste verbindingen in de oplossing wordt voorkomen.

Fluoridezouten zijn tot nu toe het meest uitgebreid onderzocht in de meeste projecten voor gesmolten-zoutreactoren. Het gebruik van chloridezouten als alternatief draagerzout, en in het bijzonder NaCl , is tegenwoordig echter wereldwijd een veel onderzochte optie, vooral voor de ontwikkeling van reactoren met een snel neutronenspectrum. In het laatste en zevende hoofdstuk is een eerste verkenning gemaakt van het thermodynamische gedrag van het chloride-alternatief voor MSR-splijtstof op basis van thorium, namelijk $\text{NaCl}-\text{ThCl}_4-\text{PuCl}_3$. Op basis van literatuurgegevens zijn de eerste modellen ontwikkeld van de binaire fase-diagrammen $\text{NaCl}-\text{PuCl}_3$ en $\text{ThCl}_4-\text{PuCl}_3$ en het ternaire systeem $\text{NaCl}-\text{ThCl}_4-\text{PuCl}_3$ met behulp van de MQCM-methode. Het ternaire systeem vertoont twee eutectische gebieden bij relatief lage temperaturen, 597 K en 598 K, en het vloeistofveld vertoont een breed samenstellingsbereik met een vloeistofovergang onder de minimale veilige bedrijfstemperatuur die is voorgesteld voor MSR (873 K). Het $\text{NaCl}-\text{ThCl}_4-\text{PuCl}_3$ heeft veelbelovende thermodynamische eigenschappen en kan worden beschouwd als een interessante brandstofoptie voor MSR met een snel neutronenspectrum.

Samenvattend draagt dit onderzoek bij tot het brede inzicht in essentiële aspecten van de veiligheid en de haalbaarheid van MSR's. Het thermodynamische gedrag en meer in het algemeen de impact van splijtingsproducten zijn in dit werk vrij uitvoerig geanalyseerd. De helium borrelstrategie in de kern is experimenteel beoordeeld met innovatieve meetmethoden. De thermodynamische eigenschappen van het belangrijkste corrosieproduct, chroom, zijn voor het eerst uitgebreid bepaald in gesmolten $\text{LiF}-\text{ThF}_4$ -zout. In dit werk heeft thermodynamische modelering met behulp van het quasichemische benadering zijn potentieel bewezen, waardoor complexe ionogene gesmolten zoutoplossingen kunnen worden beschreven, inclusief splijtstof, splijtingsproducten en elementen van corrosieproducten, om essentiële aspecten met betrekking tot de veiligheid van MSR's te beoordelen.

1

INTRODUCTION

HUMANITY faces a vital survival challenge in this century. Global population is growing inexorably and should reach 10.4 billion people at the horizon 2100 according to the projection of the United Nations [1]. Providing equal access to new technologies and modern conveniences for all, while preserving a sustainable environment, is the main challenge.

Since the Kyoto protocol ratification in 1997, most countries seem aware of the necessity to limit global warming [2]. According to the Paris agreement of 2015, the objective of an increase below 1.5 °C compared to the pre-industrial area, should be fulfilled thanks to the development of more ecological ways to produce energy [3].

Currently, fossil fuels (coal, natural gas, oil) represent 67% of the power generation mix worldwide according to an evaluation by the World Energy Council in 2014 [4]. To reach the minimum objective of reduction of CO₂ emissions, this proportion should decrease to 19% by 2060. Given the urgent need for reduced carbon emissions, nuclear power stands as an essential element of the future energy mix. Unlike its carbon-intensive counterparts, nuclear power generates electricity without the direct release of greenhouse gases during operation. This inherent quality positions nuclear energy as a powerful instrument in mitigating the adverse effects of climate change, and larger investments in this source of energy were recommended by the Intergovernmental Panel on Climate Change [5].

1.1. NUCLEAR ENERGY: SOLUTION TO THE ENVIRONMENTAL CHALLENGE

The World Energy Council suggests to increase to 17% the proportion of nuclear energy in the global energy mix, estimated at 11% nowadays [4]. But the global investments in the nuclear industry have slightly decreased since the beginning of the century [6].

Multiple factors can substantiate the declining of the nuclear power generation over the years. It is firstly due to the cost of construction of light water reactors [7]. The example of the EPR (European Pressurized Reactor), with an extra cost of 16 billion euros for the construction of the reactor in Flamanville (France), shows the limits of oversized reactors to comply with safety regulations [8]. The second reason is related to the ecological concern linked to the difficulty of managing radioactive waste (including fission products and actinides such as Pu, Am, Np) coming from the fission reaction [9–11]. Lastly, there are more political reasons, such as a poor image of a high-risk industry, particularly following the Chernobyl and Fukushima Daiichi accidents [12], and a concern about the proliferation [13, 14].

To fulfill the issues mentioned above, the Generation IV forum, an International cooperation for the development of the fourth generation of nuclear reactors, proposed to focus research and development on six reactor designs. The objective was to determine the most promising designs for the horizon 2030 [15], based on the following selection criteria:

- **Sustainability:** management and reduction of waste, especially long-lived components.
- **Economics:** reduction in implementation costs to achieve a financial risk equivalent to that of other energy sources.
- **Safety and Reliability:** minimizing the risk of reactor core damage and promoting on-site emergency response.
- **Proliferation Resistance and Physical Protection:** restricting opportunities for the proliferation of weapons-grade materials and developing counter measures against terrorist attacks.

One of the six selected concepts is the Molten Salt Reactor (MSR), which is the focus of this thesis and will be presented below.

1.2. MOLTEN SALT REACTOR

1.2.1. GENERAL CONCEPT OF THE MSR

Molten salt reactors (MSRs) can be defined as a type of advanced nuclear reactor design that use liquid salts as both the fuel and the coolant (Figure 1.1). In the core of the reactor, where the nuclear reaction takes place, the salt is the carrier of fertile and fissile materials. The salt comes out of the reactor primary circuit at a

maximum operating temperature, and the heat is extracted via heat exchangers in a secondary circuit. This second circuit is filled with molten salt, which acts as a coolant and allows to transfer heat at a higher temperature than the water-cooled reactor. The heat exchanger then transfers heat to a tertiary circuit. A water circuit transforms the heat in a steam turbine, which drives the rotation of an electricity generator. Heat can also be used directly for industrial purposes.

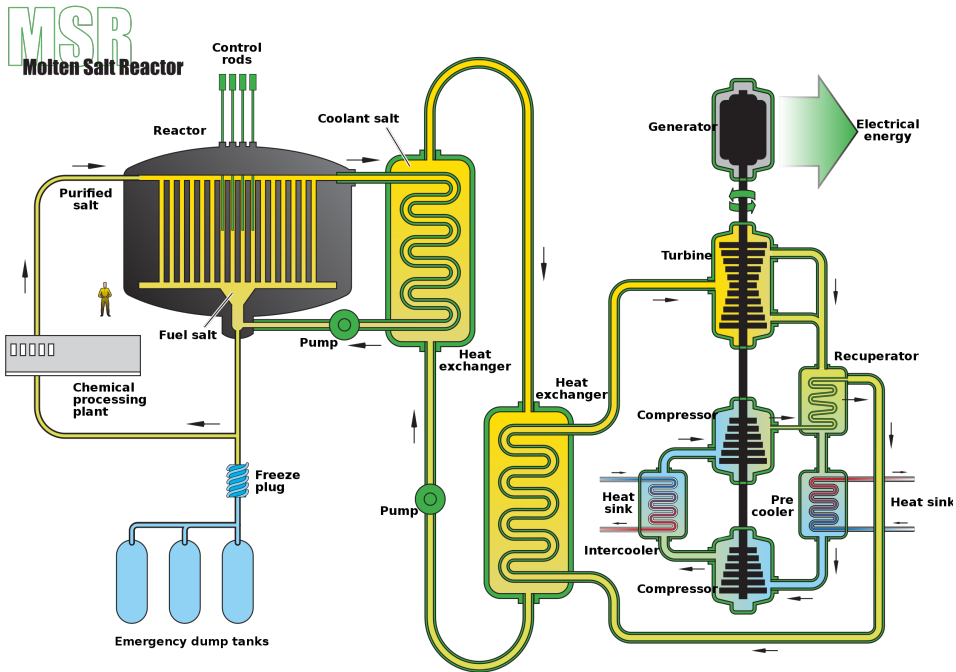
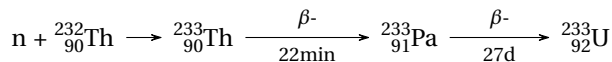


Figure 1.1.: Sketch of the Molten Salt Reactor concept issued by the Generation IV forum in 2002 [16].

In the first MSR conceptual scheme, a reprocessing unit was envisaged, in which part of the primary salt is continuously cleaned by eliminating fission products and separating fissile and fertile products, which are returned to the reactor core. Protactinium, a decay product of Th-232, for instance, is isolated for three months in the reprocessing unit until most of it has decayed into uranium before being sent back to the reactor core according to the transmutation chain presented below:



An Emergency Draining System (EDS) was also designed, which allows to stop the reaction almost immediately in case of uncontrollable fission, in a non-critical

configuration and keeping the fuel salt in safe conditions. A freeze plug guaranteed this safety measure even in case of power outage [17].

MSRs offer several advantages compared to traditional solid fueled, water-cooled nuclear reactors [18–20]:

- **Inherent Safety:** MSRs have built-in safety features. If the reactor overheats or experiences a loss of coolant, the fuel salt expands which will have the effect of naturally slowing down the nuclear reactions, preventing a thermal runaway. The passive safety mechanisms, such as the freeze plug, reduce the risk of catastrophic accidents [21].
- **Improved Environmental Impact:** MSRs can be a solution to efficiently consume fissile materials to produce energy and transmute some of the long-lived transuranium elements into shorter-lived isotopes [18]. The waste produced is easier to manage and store due to its reduced volume [22].
- **High Fuel Efficiency and Flexibility:** MSRs can use a wide variety of nuclear fuels, and can be designed as breeder reactors. They can achieve high fuel utilization rates, extracting more energy from the same amount of fuel compared to light water reactors [23, 24].
- **Proliferation Resistance:** Some MSR designs can be configured to reduce the risk of nuclear weapons proliferation by minimizing the availability of weapons-grade materials [25–27].
- **High Operating Temperatures:** MSRs operate at much higher temperatures than traditional reactors, which makes them suitable for various applications, including hydrogen production and high-temperature industrial processes [18].
- **Longer Fuel Cycles:** MSRs can potentially operate for longer periods without refueling due to their efficient fuel utilization and continuous reprocessing, reducing downtime and maintenance costs [28, 29].

The Molten Salt Reactor concept may look like an innovative solution, but it's actually the fruit of a story that began at the dawn of the nuclear age.

1.2.2. HISTORICAL BACKGROUND

The first concept of Molten Salt Reactor was developed after the World War II by the Oak Ridge National Laboratory (ORNL), besides other military projects. The first scheme was an attempt of nuclear-powered aircraft, which led to the Aircraft Reactor Experiment (ARE) [30]. Fueled with a $\text{NaF-ZrF}_4\text{-UF}_4$ mixture, the reactor reached criticality for 221 hours, at a maximum temperature of 1133 K. A 453 K gradient of temperature was measured between the inlet and the outlet. This reactor reached an energy production of 96 MWhr. Although the initial objective of becoming a power generator for an aircraft was not achieved, this experiment did enable the operating conditions of the reactor to be determined.

Experiments for a first civilian development to demonstrate the feasibility of the molten salt concept were initiated by the ORNL in the 1960s-1970s [31]. The Molten Salt Reactor Experiment (MSRE), conducted between 1964 and 1969, was based on a small reactor prototype (1.37 m in diameter, 1.62 m height), moderated by graphite. The vessel was composed of Hastelloy-N and the cover gas was helium. The reactor was connected to a chemical reprocessing plant, ensuring the purity of the fuel. The primary fuel was ${}^7\text{LiF}\text{-BeF}_2\text{-ZrF}_4\text{-UF}_4$ (65.0-29.1-5.0-0.9 mol%), the coolant in the secondary loop was ${}^7\text{LiF}\text{-BeF}_2$ and the reactor operated at 923 K. The first series of experiments were performed with ${}^{235}\text{U}$ enriched at 33%. The reactor was operated for 15 months and was critical 80% of the time, generating 8 MWhr. The uranium was later substituted with ${}^{233}\text{U}$ for the first time as fissile material, and operated for 2500 hours with the same efficiency, thereby proving the effectiveness of this isotope as fuel.

The successor to the MSRE was the MSBR (Molten Salt Breeder Reactor) program, still managed by the Oak Ridge National Laboratory [32–35]. This was a comprehensive research program, with the aim of scaling up the MSR concept to a 1000 MW reactor. Different parameters were studied in detail: design, fuel chemistry, materials development and fuel processing. This work aimed at the large scale use of thorium-based fuel for the first time with the $\text{LiF}\text{-BeF}_2\text{-ThF}_4\text{-UF}_4$ salt mixture [36]. It was also the first study using forced convection loops to study materials degradation and corrosion [37]. Although this program yielded very promising results, the parallel expansion of already more mature light water reactor designs, combined with abundant uranium resources and the competitiveness of the Sodium-cooled Fast Reactor (SFR) concept in terms of breeding gain, meant that most molten salt projects were discontinued in the 1970s.

The Generation IV International Forum (GIF), in 2002, brought back the Molten Salt Reactor into focus [15]. Many concepts are currently being developed worldwide, for example the Molten Chloride Fast Reactor by Terrapower [38], the TMSR-LF1 thorium-powered molten-salt reactor in China [39] or the Compact Molten Salt Reactor by Seaborg Technologies [40]. In the framework of the EURATOM treaty [41], the SAMOFAR project (Safety Assessment of the Molten Salt Fast Reactor - MSFR) [42], and its follow-up the SAMOSAFER project (Severe Accident Modeling and Safety Assessment for Fluid-fuel Energy Reactors) [43, 44], investigated key safety aspects of the Molten Salt Fast Reactor system. The present thesis was conducted in the framework of the SAMOSAFER project.

1.2.3. MOLTEN SALT FAST REACTOR DESIGN

The SAMOSAFER project, has adopted the Molten Salt Fast Reactor (MSFR) design, as its reference, i.e. a fast neutron spectrum breeder reactor [45–47]. In this concept, there is no graphite moderator in the reactor core and the fertile material (thorium) is contained in a blanket lining the reactor's wall (Figure 1.2).

With a 3 cubic meters volume and an operating temperature between 873 K and 1073 K, the targeted power of the MSFR is 300 MWth. The breeder concept allows to drastically reduce the volume of salt reprocessed daily (from 4000 liters per day in

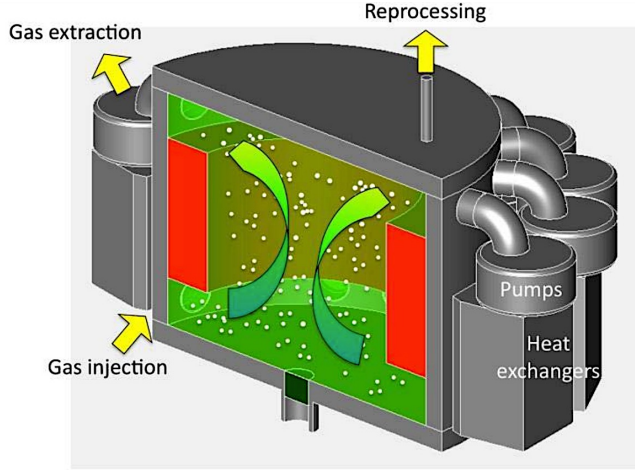


Figure 1.2.: Scheme of the Molten Salt Fast Reactor concept by Merle *et al.* [47]. The green arrows show the molten salt flow, in red is the thorium blanket, and the white bubbles represent helium gas injection.

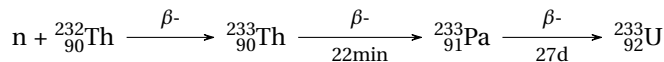
the MSBR design to 40 liters) [46]. This contributes to safety by reducing the amount of radioactive material to be processed in the chemical unit. The MSFR also allows the use of a wide variety of fuels and is open to fluoride and chloride options [24, 48].

1.3. FUELS FOR MOLTEN SALT REACTORS

1.3.1. LiF-ThF₄-UF₄

The fuel mixture LiF-ThF₄-UF₄ is a reference for many research activities related to MSR. This specific fuel mixture is generally associated with the Molten Salt Breeder Reactor or the Molten Salt Fast Reactor [24]. In this fuel:

- **LiF (lithium fluoride):** LiF serves as the solvent or matrix for the other components in the fuel mixture. It has good heat transfer properties and is chemically stable at high temperatures. Lithium also plays a role as it does not inhibit neutron scattering [49, 50].
- **ThF₄ (thorium tetrafluoride):** Thorium (²³²Th) is a fertile material, meaning it can capture neutrons and be converted into fissile uranium-233 (²³³U) following the transmutation reaction:



Thorium is three to four times more abundant than uranium on Earth [51]. However, the ore formations are more complex to exploit. It is generally a by-product of rare earth purification processes, and its utilization in the fuel cycle thus also contributes to resource efficiency [52]. In addition, thorium has shown very interesting properties for lowering the melting temperature of fuel mixtures [53].

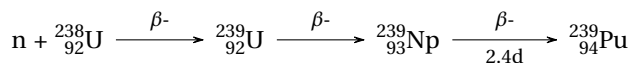
- **UF₄ (uranium tetrafluoride):** Uranium (²³³U or ²³⁵U) is a fissile material, meaning it can sustain a nuclear chain reaction. The use of ²³³U instead of ²³⁵U has the advantage of producing less long-lived radioactive waste [54].

LiF–ThF₄–UF₄ fuel is of particular interest in the development of Molten Salt Reactors due to its potential to efficiently breed fissile material (²³³U) from fertile thorium (²³²Th). This breeding process can help extend fuel cycles, reduce nuclear waste, and utilize thorium in combination with fissile material.

1.3.2. OTHER FUEL OPTIONS

During the Molten Salt Reactor project by the ORNL, mainly fluoride-based salts were used and the final focus was on LiF-based fuels [32]. As mentioned already, promising results were obtained with the so-called FLiBe (LiF–BeF₂) salt, as support for the uranium fluoride and as coolant. In the next steps, ZrF₄ and ThF₄ were introduced, forming LiF–BeF₂–ZrF₄–UF₄ and LiF–BeF₂–ThF₄–UF₄ fuel mixtures [32, 55]. One of the most explored fluoride salt options nowadays is the so-called FUNaK (NaF–KF–UF₄), notably by Seaborg Technologies and Terrestrial Energy [40, 56]. The introduction of UF₃ in the fuel mix is also considered in order to control the redox potential and mitigate corrosion of the structural materials in contact with the salt, following the recommendation of the ORNL [31].

The flexibility of the MSR concept allows to consider other halide salts as well notably chloride mixtures. The use of ²³⁸U isotope as fertile material is also investigated and is a way to use the existing stockpiles from natural and depleted uranium coming from the enrichment process in LWRs [57]. The transmutation chain can be described as:



The introduction of separated plutonium in the fuel mixture is also considered because of the large resources coming from military and civilian stockpiles [58]. There is a vast amount of this fissile material worldwide coming from the LWRs spent fuels and dismantlement of warheads, introduced by the USA and Russia under the START and New START treaties [59]. Furthermore, plutonium shows better neutron economy properties than uranium, particularly for the fast neutron spectrum designs [60]. The use of other long-lived transuranic elements (such as Np, Am or Cm) is also seen as a potential option for the recycling of actinide materials in fuel, and represents a good opportunity to transmute those elements, thereby reducing the burden for future generations.

While fluoride salts were the reference for many years, chloride salts have seen a increased interest in the last twenty years. Already introduced during the British MSR Programme [61], chloride salts such as PuCl_3 and UCl_3 have been explored. The main carrier salt studied is sodium chloride (NaCl). Available in abundance, NaCl , which is nothing other than table salt, represents a less scarce resource than lithium and can be easily mined or even extracted from sea water. The most explored options are based on the binary system $\text{NaCl}-\text{PuCl}_3$ and per extension the ternary system $\text{NaCl}-\text{MgCl}_2-\text{PuCl}_3$ [38, 62].

1.4. CHALLENGE WITH MOLTEN SALT REACTORS

1.4.1. FISSION PRODUCTS

When a heavy atomic nucleus, like ^{233}U or ^{239}Pu , undergoes fission, it splits into two lighter nuclei, releasing energy, two to three neutrons, and several fission products. In light water reactors, these products were exhaustively identified and quantified [63]. In the case of the Molten Salt Reactor, once again the most comprehensive study of the fission products production and speciation, was provided by the Oak Ridge National Laboratory by Compere *et al.* during the study of the chemical composition of the MSRE [64].

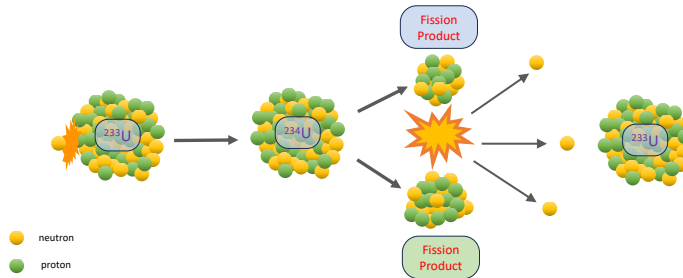


Figure 1.3.: Schematic example of a ^{233}U fission reaction producing two random isotopes.

According to the observations of the ORNL in the MSR project, the reprocessing process had almost no impact on the removal of the fission products, but they were retained in the graphite moderator [55]. The fission product elements showed overall a good solubility in the fuel, and did not interact with initial compounds. They formed the most stable fluoride forms, following their preferential valence. The gaseous fission products, Kr and Xe, were found almost insoluble. In the MSRE, a helium bubbly flow removed most of the latter, that were collected by the filtration system [64].

In the case of the MSFR concept, the absence of a solid moderator in the reactor core means that a fresh look at the generation of the fission products needs to be taken. The behavior of cesium and iodine, which are important for the assessment

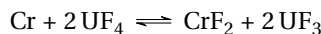
of the source term, was already thermodynamically assessed in LiF–ThF₄ by Capelli *et al.* [65]. CsF and CsI are the most likely stable chemical compounds to form. The solubility of CsF in the molten salt was found generally good. However, CsI showed a very limited solubility in the fuel mixture and was found to vaporize easily out of the fuel. The stability, speciation and phase equilibria of many other fission products need to be explored to realize the safety assessment of the MSFR.

One of the key features of the MSFR technology, which is studied in this thesis, is in-line extraction of fission products by helium bubbling: as helium bubbles are passed through the salt, they remove gaseous fission products which are strong neutron poisons, and suspended metallic particles from the fuel (Figure 1.2). Metallic particles formed during fission were found to remain neutral and form particles of a multi-element (Pd, Rh, Ru, Tc, Mo) alloy. Only a fraction of the molybdenum could form MoF₄. These elements were preferentially attached to the cold part of the reactor or the graphite moderator in the MSRE [64]. In the MSFR, these colloidal particles must be taken into account, considering the absence of graphite to adhere to the wall. An empirical observation of the coalescence of the noble and semi-noble metallic nanoparticles in molten FLiNaK salt, by Capelli, has shown that the average size of the aggregates is around 400 nm [66]. The solution being explored to solve this problem is a flow of bubbling helium directly into the core, which binds and carries the particles to a collection device.

1.4.2. CORROSION PRODUCTS

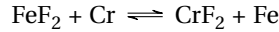
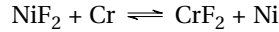
Corrosion is the most critical structural problem encountered in most nuclear reactors. It could lead to uptake of corrosion products in the coolant, affecting the neutron economy and coolant chemistry. Notably reaction with corroded metals, modification of the structure of the vessel or tubing and in the worst case, formation of cracks in the core resulting in accidental release of radioactive materials. In the Molten Salt Reactor Experiment [31], the corrosion issue was obviously central.

The ORNL carried out an extensive study of the degradation of the vessel materials subjected to various lithium-based molten salts [67]. Several alloys were tested and the best performance was found with Hastelloy-N (68 Ni-17 Mo-7 Cr-5 Fe-0.5 Mn), showing a higher resistance to structural depletion and mass transfer [37, 68]. For nine years, exposure of Hastelloy-N convection loops were performed with LiF–BeF₂–ZrF₄–UF₄–ThF₄ (approximately 70-23-5-1-1 mol%) fuel salt at operating temperature between 833 K and 973 K. The study of the alloy samples dispatched at different positions in the loops showed the presence of mechanical stress at the interface. Interstitial voids at the surface of the material were created, almost exclusively, by the depletion of chromium from the alloy. These observations were moreover supported by the analysis of the salt composition, which confirmed the significant increase of the chromium amount (from 100 ppm to 1800 ppm after 9 years) along the process [37]. The chromium depletion seemed mainly driven by the reaction [69]:



The impurities in the mixture LiF–BeF₂–UF₄ were moreover found to play a major

role in the corrosion process. The other corroded elements from the alloy, Ni and Fe, participate to the chromium oxidation according to the two reactions:



Impurities such as hydrogen, originating from external contamination of water or residues from fluoride synthesis, create acidic conditions and promote reactions like for instance:



It was also proven that the oxide films on the metal surface would participate as well:



In the MSRE, it was demonstrated that the corrosion products in the fuel were controlled by the adhesion on the graphite moderator, notably with the formation of carbides such as Cr_7C_3 [70].

1.5. THERMODYNAMIC TOOL

For the safety assessment of the MSFR, the understanding and modeling of the fission products and corrosion products is of paramount importance, and thermodynamic assessment of the equilibrium chemical state is a powerful tool to reach this objective. Thermodynamic modeling plays a crucial role in nuclear reactor development for several reasons. Firstly, its predictive capability helps engineers and scientists to understand and predict fuel behavior under various conditions [71]. Nuclear reactors involve complex interactions between various materials, fluids and energy transfer processes. Thermodynamic models enable researchers to predict equilibrium states and study how changes in parameters such as temperature, pressure and composition affect reactor performance [72]. These models also play an essential role in the study of fuel cycles, heat transfer mechanisms and overall energy conversion efficiency. This information is invaluable for optimizing reactor design to improve efficiency and safety.

Additionally, thermodynamic modeling helps to identify and mitigate potential problems and risks associated with nuclear reactors. For example, it can help predict and analyze fuel behavior under transient conditions, such as start-up, shutdown or accidents [73]. Understanding how the system reacts to these events enables the development of effective safety measures and protocols.

In this context, CALPHAD appears to be a powerful tool, seamlessly integrating thermodynamic principles and experimental data to predict and understand the complex interaction of phases under varying conditions of temperature, pressure and composition. CALPHAD stands for "CALculation of PHase Diagrams", and was coined in the late 1960s by Larry Kaufman [74, 75]. The first CALPHAD conference recognized the need for a more comprehensive and systematic approach

to thermodynamic modeling. The CALPHAD method aims to combine the strengths of computational techniques with experimental data to predict phase diagrams and other thermodynamic properties.

This led to the emergence of different databases, grouping the thermodynamic data of the different materials of interest for the development of the next generation of nuclear reactors (such as fuel or vessel materials). One can cite, in the framework of the Molten Salt Reactor, the American MSTDB-TC [76, 77], the international TAF-ID [78], or, finally the JRCMSD database, developed by the Joint Research Centre of the European Commission, in collaboration with many institutions [79–81]. The thermodynamic data and models presented in this thesis, are integrated in this latter database.

1.6. OBJECTIVES OF THIS WORK

This research project aims to answer questions that are essential for ensuring the safety of molten salt reactors (MSRs). Using a dual approach, the main objective is to use a thermodynamic framework to describe the complex effects of fission and corrosion products on the behavior of fuel salt within the reactor system. By investigating the thermodynamic interactions governing these components, we also aim to improve our understanding of their dynamics and implications.

Simultaneously, our secondary goal is to understand the disruptive elements formed in the fuel solution, notably gases and metallic fission products particles, and to explore innovative methods designed to eliminate them within the reactor core, as they could potentially compromise the optimal operation of the reactor core.

The primary objective of this research is to make a significant contribution to improving the safety and efficiency of Molten Salt Reactors. Through in-depth examination of these critical aspects, the aim is to contribute to advances that not only deepen our understanding of MSR dynamics, but also pave the way for practical solutions guaranteeing safe and reliable operation of these advanced reactor systems.

The purpose of this thesis can be divided into three main axis:

- A description of the fission product behavior in molten salt.
- A study of the behavior of the main corrosion product, chromium, in molten salt.
- A research of alternative fuel for Molten Salt Reactor.

The content of the dissertation is summarized in the graphical representation below (Figure 1.4) and is defined in further detail in the next section (Section 1.7).

1.7. CONTENT OF THIS DISSERTATION

As part of the general safety assessment of the Molten Salt Reactor, and more specifically of the Molten Salt Fast Reactor, this thesis will focus on the following aspects:

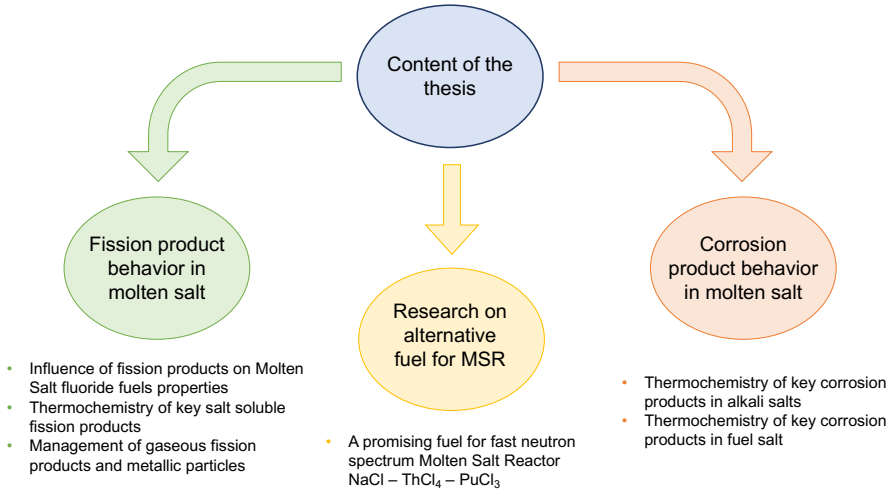


Figure 1.4.: Schematic representation of the content of this thesis.

1. Influence of fission products on molten fluoride salt fuels properties (Chapter 2)
2. Thermochemistry of key salt soluble fission products: Thermodynamic assessment of the LiF–ZrF₄–BaF₂ system (Chapter 3)
3. Management of gaseous fission products and metallic particles: Extraction by helium bubbling technique (Chapter 4)
4. Thermochemistry of key corrosion products in alkali salts: Thermodynamic assessment of the AF–CrF₃ (A = Li, Na, K) and CrF₂–CrF₃ systems. (Chapter 5)
5. Thermochemistry of key corrosion products in fuel salt: Thermodynamic properties of CrF₂ and behavior in the molten LiF–ThF₄ system (Chapter 6)
6. A promising fuel for fast neutron spectrum Molten Salt Reactor NaCl–ThCl₄–PuCl₃ (Chapter 7)

In the first chapter, the influence of fission products on fuel properties of the LiF–ThF₄–UF₄ system is studied. A representative mixture of the main fission products was determined for the operating MSFR running with LiF–ThF₄ and LiF–ThF₄–UF₄ salts, i.e. the most promising options in the literature. The impact of the fission products on the melting behavior and vapor pressure of the fuel salts were studied by calorimetric measurements and Knudsen Effusion Mass Spectrometry. The second chapter covers the thermodynamic assessment of two key fission products, namely BaF₂ and ZrF₄, in equilibrium with lithium fluoride. Phase diagrams of the three binary systems and of the ternary system LiF–BaF₂–ZrF₄

were established based on experimental data and literature. In the third chapter, the helium bubbling method for the removal of gaseous and metal particles is studied. An experimental setup for the collection of noble and semi-noble metallic particles by helium bubbling was designed, and experimental evaluation of the recovery of nanoparticles by this method is presented. The fourth chapter is focused on the thermochemistry of key chromium corrosion products in alkali salt, with the thermodynamic assessment of CrF_3 in FLiNaK. The binary phase diagrams of AF- CrF_3 (A = Li, Na, K) systems were modeled using the modified Quasichemical Model in the Quadruplet Approximation based on literature data. To assess the stability of chromium in fluoride salts, the CrF_2 - CrF_3 system was modeled as well. The last corrosion studies of this work, are detailed in the fifth chapter. A synthesis method and the melting temperature of CrF_2 were newly determined. Thanks to these results, the thermodynamic properties of CrF_2 in the LiF-ThF₄ mixture were measured for the first time, leading to the thermodynamic assessments of LiF- CrF_2 , CrF_2 -ThF₄ and LiF- CrF_2 -ThF₄ systems. In the sixth and last chapter, a potential promising chloride fuel for fast neutron spectrum Molten Salt Reactor is presented. On the basis of an in-depth study of literature data, thermodynamic assessment of the NaCl-ThCl₄-PuCl₃ system is performed and thereby confirming the high potential of the chloride fuel options in Molten Salt Reactor framework. This manuscript ends with a conclusion, including the highlights of this thesis, perspectives and suggestions for further research.

REFERENCES

- [1] United Nations, Department of Economic and Social Affairs, Population Division. *World Population Prospects 2022: Summary of Results*. UN DESA/POP/2022/TR/NO. 3. 2022.
- [2] United Nations, Framework Convention on Climate Change. *Kyoto protocol to the United Nations Framework on Climate Change*. FCCC/CP/1997/L.7/Add.1. Dec. 10, 1997.
- [3] United Nations, Framework Convention of Climate Change. *Conference of the Parties: Adoption of the Paris Agreement*. Dec. 11, 2023.
- [4] H.-W. Schiffer, T. Kober, and E. Panos. “World Energy Council’s Global Energy Scenarios to 2060”. In: *Zeitschrift für Energiewirtschaft* 42.2 (2018), pp. 91–102. DOI: 10.1007/s12398-018-0225-3.
- [5] J. Rogelj, D. Shindell, K. Jiang, S. Fifita, P. Forster, V. Ginzburg, C. Handa, H. Kheshgi, S. Kobayashi, E. Kriegler, L. Mundaca, R. Séférian, and M. V. Vilarino. “2018: Mitigation Pathways Compatible with 1.5 °C in the Context of Sustainable Development.” In: *Global Warming of 1.5 °C. An IPCC Special Report on the impacts of global warming of 1.5 °C above pre-industrial levels and related global greenhouse gas emission pathways, in the context of strengthening the global response to the threat of climate change, sustainable development, and efforts to eradicate poverty*. Ed. by V. Masson-Delmotte, P. Zhai, H.-O. Pörtner, D. Roberts, J. Skea, P. Shukla, A. Pirani, W. Moufouma-Okia, C. Péan, R. Pidcock, S. Connors, J. B. R. Matthews, Y. Chen, X. Zhou, M. I. Gomis, E. Lonnoy, T. Maycock, M. Tignor, and T. Waterfield. Intergovernmental Panel on Climate Change, 2018, pp. 93–174.
- [6] H. Ritchie and P. Rosado. “Energy Mix”. In: *Our World in Data* (2020). <https://ourworldindata.org/energy-mix>.
- [7] M. Berthélemy and L. E. Rangel. “Nuclear reactors’ construction costs: The role of lead-time, standardization and technological progress”. In: *Energy Policy* 82 (July 2015), pp. 118–130. DOI: 10.1016/j.enpol.2015.03.015.
- [8] EDF. *Point d’actualité sur l’EPR de Flamanville*. URL: <https://www.edf.fr/sites/groupe/files/epresspack/2337/c41a2d7e09b78e04cf2f0b06a68a4e1e.pdf>. Jan. 12, 2022.
- [9] M. Greenberg. *Nuclear waste management, nuclear power, and energy choices: Public preferences, perceptions, and trust*. Vol. 2. Springer Science & Business Media, 2012.

- [10] A. Brunnengraber and C. Gorg. “Nuclear Waste in the Anthropocene: Uncertainties and Unforeseeable Timescales in the Disposal of Nuclear Waste”. In: *GAIA - Ecological Perspectives for Science and Society* 26.2 (Jan. 2017), pp. 96–99. DOI: 10.14512/gaia.26.2.8.
- [11] M. Alwaeli and V. Mannheim. “Investigation into the Current State of Nuclear Energy and Nuclear Waste Management - A State-of-the-Art Review”. In: *Energies* 15.12 (June 2022), p. 4275. DOI: 10.3390/en15124275.
- [12] S. Tateno and H. M. Yokoyama. “Public anxiety, trust, and the role of mediators in communicating risk of exposure to low dose radiation after the Fukushima Daiichi Nuclear Plant explosion”. In: *Journal of Science Communication* 12.2 (2013), A03.
- [13] P. R. Lavoy. “Nuclear Myths and the Causes of Nuclear Proliferation”. In: *Security Studies* 2.3-4 (June 1993), pp. 192–212. DOI: 10.1080/09636419309347524.
- [14] E. Gartzke and M. Kroenig. “A Strategic Approach to Nuclear Proliferation”. In: *Journal of Conflict Resolution* 53.2 (Jan. 2009), pp. 151–160. DOI: 10.1177/0022002708330039.
- [15] J. E. Kelly. “Generation IV International Forum: A decade of progress through international cooperation”. In: *Progress in Nuclear Energy* 77 (2014), pp. 240–246. DOI: 10.1016/j.pnucene.2014.02.010.
- [16] U.S. DOE Nuclear Energy Research Advisory Committee and the Generation IV International Forum. *A Technology Roadmap for Generation IV Nuclear Energy Systems*. GIF-002-00. Dec. 2002. URL: https://www.gen-4.org/gif/jcms/c_40481/technology-roadmap.
- [17] M. Tiberger, D. Shafer, D. Lathouwers, M. Rohde, and J.-L. Kloosterman. “Preliminary investigation on the melting behavior of a freeze-valve for the Molten Salt Fast Reactor”. In: *Annals of Nuclear Energy* 132 (Oct. 2019), pp. 544–554. ISSN: 0306-4549. DOI: 10.1016/j.anucene.2019.06.039.
- [18] J. Serp, M. Allibert, O. Beneš, S. Delpech, O. Feynberg, V. Ghetta, D. Heuer, D. Holcomb, V. Ignatiev, J.-L. Kloosterman, L. Luzzi, E. Merle-Lucotte, J. Uhlř, R. Yoshioka, and D. Zhimin. “The molten salt reactor (MSR) in generation IV: Overview and perspectives”. In: *Progress in Nuclear Energy* 77 (Nov. 2014), pp. 308–319. ISSN: 0149-1970. DOI: 10.1016/j.pnucene.2014.02.014.
- [19] O. Beneš and R. J. M. Konings. “Molten Salt Reactor Fuel and Coolant”. In: *Comprehensive Nuclear Materials*. Ed. by R. J. M. Konings and R. E. Stoller. Amsterdam: Elsevier, 2020, pp. 609–644. DOI: 10.1016/b978-0-12-803581-8.11790-4.
- [20] R. Roper, M. Harkema, P. Sabharwall, C. Riddle, B. Chisholm, B. Day, and P. Marotta. “Molten salt for advanced energy applications: A review”. In: *Annals of Nuclear Energy* 169 (May 2022), p. 108924. ISSN: 0306-4549. DOI: 10.1016/j.anucene.2021.108924.

- [21] B. M. Elsheikh. “Safety assessment of molten salt reactors in comparison with light water reactors”. In: *Journal of Radiation Research and Applied Sciences* 6.2 (Oct. 2013), pp. 63–70. ISSN: 1687-8507. DOI: 10.1016/j.jrras.2013.10.008.
- [22] B. J. Riley, J. McFarlane, G. D. DelCul, J. D. Vienna, C. I. Contescu, and C. W. Forsberg. “Molten salt reactor waste and effluent management strategies: A review”. In: *Nuclear Engineering and Design* 345 (Apr. 2019), pp. 94–109. ISSN: 0029-5493. DOI: 10.1016/j.nucengdes.2019.02.002.
- [23] L. Ponomarev, M. Seregin, A. Parshin, S. MelNikov, A. Mikhailichenko, L. Zagorets, R. Manuilov, and A. Rzhetskii. “Fuel salt for the molten-salt reactor”. In: *Atomic energy* 115.1 (2013), pp. 5–10.
- [24] O. Beneš and P. Souček. “Molten salt reactor fuels”. In: *Advances in Nuclear Fuel Chemistry*. Amsterdam: Elsevier, 2020, pp. 249–271. DOI: 10.1016/b978-0-08-102571-0.00007-0.
- [25] U. Gat and J. R. Engel. “Non-proliferation attributes of molten salt reactors”. In: *Nuclear Engineering and Design* 201.2–3 (2000), pp. 327–334. ISSN: 0029-5493. DOI: 10.1016/s0029-5493(00)00276-4.
- [26] M. Allibert, E. Merle, S. Delpech, D. Gerardin, D. Heuer, A. Laureau, and S. Moreau. “Preliminary proliferation study of the molten salt fast reactor”. In: *EPJ Nuclear Sciences & Technologies* 6 (2020), p. 5.
- [27] J. Emblemståg. “Safe, clean, proliferation resistant and cost-effective Thorium-based Molten Salt Reactors for sustainable development”. In: *International Journal of Sustainable Energy* 41.6 (June 2021), pp. 514–537. ISSN: 1478-646X. DOI: 10.1080/14786451.2021.1928130.
- [28] A. Rykhlevskii, B. R. Betzler, J. W. Bae, and K. Huff. “Fuel Cycle Performance of Fast Spectrum Molten Salt Reactor Designs”. In: (Feb. 2019). DOI: 10.31224/osf.io/zkvn9.
- [29] V. V. Ignatiev, M. V. Kormilitsyn, L. A. Kormilitsyna, Y. M. Semchenkov, Y. S. Fedorov, O. S. Feinberg, O. V. Kryukov, and A. V. Khaperskaya. “Molten-salt reactor for nuclear fuel cycle closure on all actinides”. In: *Atomic Energy* 125 (2019), pp. 279–283. DOI: 10.1007/s10512-019-00481-w.
- [30] E. S. Bettis, W. B. Cottrell, E. R. Mann, J. L. Meem, and G. D. Whitman. “The Aircraft Reactor Experiment—Operation”. In: *Nuclear Science and Engineering* 2.6 (1957), pp. 841–853. DOI: 10.13182/nse57-a35497.
- [31] P. N. Haubenreich and J. R. Engel. “Experience with the Molten-Salt Reactor Experiment”. In: *Nuclear Applications and Technology* 8.2 (1970), pp. 118–136. DOI: 10.13182/nt8-2-118.
- [32] M. W. Rosenthal, P. R. Kasten, and R. B. Briggs. “Molten-Salt Reactors - History, Status, and Potential”. In: *Nuclear Applications and Technology* 8.2 (Feb. 1970), pp. 107–117. DOI: 10.13182/nt70-a28619.
- [33] L. McNeese. *Molten-salt reactor program. Semiannual progress report for period ending February 29, 1976*. Tech. rep. Oak Ridge National Laboratory, Aug. 1976. DOI: 10.2172/7239598.

- [34] J. Engel, H. Bauman, J. Dearing, W. Grimes, and H. J. McCoy. *Development status and potential program for development of proliferation-resistant molten-salt reactors*. Tech. rep. Oak Ridge National Lab., 1979. DOI: 10.2172/6368411.
- [35] J. Engel, H. Bauman, J. Dearing, W. Grimes, H. McCoy, and W. Rhoades. *Conceptual design characteristics of a denatured molten-salt reactor with once-through fueling*. Tech. rep. 1980. DOI: 10.2172/5352526.
- [36] L. McNeese, L. Ferris, and E. Nicholson. *MOLTEN-SALT BREEDER REACTOR FUEL PROCESSING*. Tech. rep. Oak Ridge National Laboratory, 1972. DOI: 10.2172/4628558.
- [37] J. W. Koger. *Evaluation of Hastelloy N alloys after nine years exposure to both a molten fluoride salt and air at temperatures from 700 to 560°C*. ORNL-TM-4189. Dec. 1972. DOI: 10.2172/4468052.
- [38] J. Latkowski. *TerraPower's Molten Chloride Fast Reactor (MCFR)*. 2021. URL: <https://www.nationalacademies.org/event/02-22-2021/docs/DB0D308269688B2BD7B1AF60BAA143D48890C2DE80BB>.
- [39] X. Yu and H. Xu. "Update on SINAP TMSR research". In: *MSR Workshop, ORNL*. 2016. URL: <https://msrworkshop.ornl.gov/wp-content/uploads/2018/04/MSR2016-day1-15-Hongjie-Xu-Update-on-SINAP-TMSR-Research.pdf>.
- [40] M. Pater, E. B. Klinkby, and D. Cooper. *Molten salt revisited: the CMSR*. 2022. URL: <https://www.neimagazine.com/features/featuremolten-salt-revisited-the-cmsr-9423379/>.
- [41] European Union. "CONSOLIDATED VERSION OF THE TREATY ESTABLISHING THE EUROPEAN ATOMIC ENERGY COMMUNITY". In: *Official Journal of the European Union* C 327 (01 Oct. 26, 2012).
- [42] J.-L. Kloosterman and SAMOFAR consortium. "Safety assessment of the Molten Salt Fast Reactor (SAMOFAR)". In: *Molten Salt Reactors and Thorium Energy*. Elsevier, 2017, pp. 565–570. DOI: 10.1016/b978-0-08-101126-3.00020-8.
- [43] SAMOSAFER consortium. *Severe Accident Modeling and Safety Assessment for Fluid-fuel Energy Reactors*. DOI: 10.3030/847527.
- [44] J.-L. Kloosterman. *SAMOSAFER: Bringing Nuclear Safety To The Next Level*. 2019. URL: https://www.janleenkloosterman.nl/samosafer_20191001.php.
- [45] C. Renault, M. Hron, R. J. M. Konings, and D. E. Holcomb. "The Molten Salt Reactor (MSR) in Generation IV: Overview and Perspectives". In: *GIF Symposium - Paris, France*. Sept. 9, 2009, pp. 191–200. URL: https://www.gen-4.org/gif/jcms/c_43528/2009-gif-symposium-proceedings.
- [46] S. Delpech, E. Merle-Lucotte, T. Auger, X. Doligez, D. Heuer, and G. Picard. "MSFR: Material issues and the Effect of Chemistry Control". In: *GIF Symposium - Paris, France*. Sept. 9, 2009, pp. 201–208. URL: https://www.gen-4.org/gif/jcms/c_43528/2009-gif-symposium-proceedings.

- [47] E. Merle-Lucotte, M. Allibert, M. Brovchenko, D. Heuer, V. Ghetta, A. Laureau, and P. Rubiolo. "Introduction to the Physics of Thorium Molten Salt Fast Reactor (MSFR) Concepts". In: *Thorium Energy for the World*. Springer International Publishing, 2016, pp. 223–231. ISBN: 9783319265421. DOI: 10.1007/978-3-319-26542-1_34.
- [48] E. Capelli and R. J. M. Konings. "Halides of the Actinides and Fission Products Relevant for Molten Salt Reactors". In: *Konings, Rudy JM and Stoller Roger E (eds.) Comprehensive Nuclear Materials 2nd edition*. Vol. 7. Elsevier, 2020, pp. 256–283. DOI: 10.1016/b978-0-12-803581-8.11794-1.
- [49] L. Mei, X. Cai, D. Jiang, J. Chen, W. Guo, and W. Xiong. "Investigation of thermal neutron scattering data for BeF₂ and LiF crystals". In: *Journal of Nuclear Science and Technology* 50.4 (Apr. 2013), pp. 419–424. DOI: 10.1080/00223131.2013.773169.
- [50] T. Mollik, M. M. Hossain, S. Hasan, M. A. R. . Sarkar, and M. A. Zulquarnain. "Conceptual Study and Analysis of Neutron Diffusion and Moderation in Nuclear Reactor". In: *International Conference on Mechanical, Industrial and Materials Engineering 2015 (ICMIME2015)*. Dec. 13, 2015.
- [51] U.S. Geological Survey. *Minerals Yearbook, volume I, Metals and Minerals*. U.S. Geological Survey, 2021. DOI: 10.3133/mybvI.
- [52] Z. Zhu, Y. Pranolo, and C. Y. Cheng. "Separation of uranium and thorium from rare earths for rare earth production – A review". In: *Minerals Engineering* 77 (June 2015), pp. 185–196. ISSN: 0892-6875. DOI: 10.1016/j.mineng.2015.03.012.
- [53] J. A. Ocadiz-Flores, E. Carré, J.-C. Griveau, E. Colineau, E. Capelli, P. Souček, O. Beneš, R. J. M. Konings, and A. L. Smith. "Thermodynamic assessment of the KF-ThF₄, LiF-KF-ThF₄ and NaF-KF-ThF₄ systems". In: *The Journal of Chemical Thermodynamics* 145 (2020), p. 106069. ISSN: 0021-9614. DOI: 10.1016/j.jct.2020.106069.
- [54] W. Zhu, Z. Wang, X. Zhu, N. Shu, and T. Fan. "A new evaluation of fission product yields for the neutron induced fission of U-233 and Th-232". In: *Fusion Engineering and Design* 125 (2017), pp. 608–614. ISSN: 0920-3796. DOI: 10.1016/j.fusengdes.2017.05.026.
- [55] W. R. Grimes. "Molten-Salt Reactor Chemistry". In: *Nuclear Applications and Technology* 8 (Feb. 1970), pp. 137–155.
- [56] J. Choe, M. Ivanova, D. LeBlanc, S. Mohaptra, and R. Robinson. "Fuel cycle flexibility of terrestrial energy's integral molten salt reactor (IMSR)". In: *38th Annual Conference of the Canadian Nuclear Society and 42nd Annual CNS/CNA Student Conference*. 2018, pp. 3–6.
- [57] D. Heuer, E. Merle-Lucotte, M. Allibert, M. Brovchenko, V. Ghetta, and P. Rubiolo. "Towards the thorium fuel cycle with molten salt fast reactors". In: *Annals of Nuclear Energy* 64 (2014), pp. 421–429. DOI: 10.1016/j.anucene.2013.08.002.

- [58] E. Capelli, O. Beneš, and R. J. M. Konings. “Thermodynamic assessment of the LiF–ThF₄–PuF₃–UF₄ system”. en. In: *Journal of Nuclear Materials* 462 (2015), pp. 43–53. ISSN: 0022-3115. DOI: 10.1016/j.jnucmat.2015.03.042.
- [59] International Panel on Fissile Materials (IPFM). *Global Fissile Material Report 2015: Nuclear Weapon and Fissile Material Stockpiles and Production*. 8. International Panel on Fissile Materials (IPFM), 2015.
- [60] J. Krepel, B. Hombourger, and E. Losa. “Fuel cycle sustainability of Molten Salt Reactor concepts in comparison with other selected reactors”. In: PHYTRA4. Marrakech, Marocco, 2018.
- [61] The Weinsberg Foundation. *The UKs forgotten Molten Salt Reactor Programme*. Nov. 2023. URL: <https://www.the-weinberg-foundation.org/the-uks-forgotten-molten-salt-reactor-programme/>.
- [62] O. Beneš and R. J. M. Konings. “Thermodynamic evaluation of the NaCl–MgCl₂–UCl₃–PuCl₃ system”. In: *Journal of Nuclear Materials* 375.2 (2008), pp. 202–208. DOI: 10.1016/j.jnucmat.2008.01.007.
- [63] M. B. Chadwick, M. Herman, P. Obložinský, M. E. Dunn, Y. Danon, A. C. Kahler, D. L. Smith, B. Pritychenko, G. Arbanas, R. Arcilla, R. Brewer, D. A. Brown, R. Capote, A. D. Carlson, Y. S. Cho, H. Derrien, K. Guber, G. M. Hale, S. Hoblit, S. Holloway, T. D. Johnson, T. Kawano, B. C. Kiedrowski, H. Kim, S. Kunieda, N. M. Larson, L. Leal, J. P. Lestone, R. C. Little, E. A. McCutchan, R. E. MacFarlane, M. MacInnes, C. M. Mattoon, R. D. McKnight, S. F. Mughabghab, G. P. A. Nobre, G. Palmiotti, A. Palumbo, M. T. Pigni, V. G. Pronyaev, R. O. Sayer, A. A. Sonzogni, N. C. Summers, P. Talou, I. J. Thompson, A. Trkov, R. L. Vogt, S. C. van der Marck, A. Wallner, M. C. White, D. Wiarda, and P. G. Young. “ENDF/B-VII.1 Nuclear Data for Science and Technology: Cross Sections, Covariances, Fission Product Yields and Decay Data”. In: *Nuclear Data Sheets* 112.12 (2011), pp. 2887–2996. DOI: 10.1016/j.nds.2011.11.002.
- [64] E. L. Compere, E. G. Bohlmann, S. S. Kirslis, F. F. Blankenship, and W. R. Grimes. *Fission product behavior in the Molten Salt Reactor Experiment*. ORNL-4865. ORNL-4865. Oak Ridge National Laboratory, 1975. DOI: 10.2172/4077644.
- [65] E. Capelli, O. Beneš, and R. J. M. Konings. “Thermodynamics of soluble fission products cesium and iodine in the Molten Salt Reactor”. In: *Journal of Nuclear Materials* 501 (Apr. 2018), pp. 238–252. DOI: 10.1016/j.jnucmat.2018.01.024.
- [66] E. Capelli. *Molten Salt Chemistry - Final project Report*. Tech. rep. TU Delft, 2019.
- [67] E. DeVan. *Corrosion behavior of reactor materials in fluoride salt mixtures*. Tech. rep. Oak Ridge National Laboratory, Oak Ridge, TN, 1962.
- [68] H. E. McCoy, R. L. Beatty, W. H. Cook, R. E. Gehlbach, C. R. Kennedy, J. W. Koger, A. P. Litman, C. E. Sessions, and J. R. Weir. “New Developments in Materials for Molten-Salt Reactors”. In: *Nuclear Applications and Technology* 8.2 (1970), pp. 156–169. DOI: 10.13182/nt70-a28622.

- [69] J. W. Koger. "Chromium Depletion and Void Formation in Fe-Ni-Cr Alloys During Molten Salt Corrosion and Related Processes". In: *Advances in corrosion science and technology*. Vol. 4. Springer, 1974, pp. 245–318.
- [70] K. Sridharan and T. R. Allen. "Corrosion in Molten Salts". In: *Molten Salts Chemistry*. Elsevier, 2013, pp. 241–267. DOI: 10.1016/b978-0-12-398538-5.00012-3.
- [71] O. Beneš and R. J. M. Konings. "Thermodynamic properties and phase diagrams of fluoride salts for nuclear applications". In: *Journal of Fluorine Chemistry* 130.1 (Jan. 2009), pp. 22–29. DOI: 10.1016/j.jfluchem.2008.07.014.
- [72] T. B. Lindemer, T. M. Besmann, and C. E. Johnson. "Thermodynamic review and calculations - alkali-metal oxide systems with nuclear fuels, fission products, and structural materials". In: *Journal of Nuclear Materials* 100.1–3 (Sept. 1981), pp. 178–226. ISSN: 0022-3115. DOI: 10.1016/0022-3115(81)90533-x.
- [73] C. Guéneau, N. Dupin, B. Sundman, C. Martial, J.-C. Dumas, S. Gossé, S. Chatain, F. D. Bruycker, D. Manara, and R. J. M. Konings. "Thermodynamic modelling of advanced oxide and carbide nuclear fuels: Description of the U–Pu–O–C systems". In: *Journal of Nuclear Materials* 419.1–3 (Dec. 2011), pp. 145–167. ISSN: 0022-3115. DOI: 10.1016/j.jnucmat.2011.07.033.
- [74] L. Kaufman and H. Bernstein. "Computer calculation of phase diagrams. With special reference to refractory metals". In: *Refractory Materials. A Series of Monographs*. Ed. by A. P. Inc. Vol. 4. New York, 1970, p. 344.
- [75] P. Spencer. "A brief history of CALPHAD". In: *Calphad* 32.1 (Mar. 2008), pp. 1–8. ISSN: 0364-5916. DOI: 10.1016/j.calphad.2007.10.001.
- [76] J. C. Ard, J. A. Yingling, K. E. Johnson, J. Schorne-Pinto, M. Aziziha, C. M. Dixon, M. S. Christian, J. W. McMurray, and T. M. Besmann. "Development of the Molten Salt Thermal Properties Database-Thermochemical (MSTDB-TC), example applications, and LiCl-RbCl and UF₃UF₄ system assessments". In: *Journal of Nuclear Materials* 563 (May 2022), p. 153631. ISSN: 0022-3115. DOI: 10.1016/j.jnucmat.2022.153631.
- [77] J. C. Ard, J. Schorne-Pinto, M. Aziziha, J. A. Yingling, A. M. Mofrad, K. E. Johnson, C. M. Dixon, and T. M. Besmann. "Thermodynamic assessments or reassessments of 30 pseudo-binary and ternary salt systems". In: *The Journal of Chemical Thermodynamics* 177 (Feb. 2023), p. 106931. ISSN: 0021-9614. DOI: 10.1016/j.jct.2022.106931.
- [78] C. Guéneau, N. Dupin, L. Kjellqvist, E. Geiger, M. Kurata, S. Gossé, E. Corcoran, A. Quaini, R. Hania, A. Smith, M. Piro, T. Besmann, P. Turchi, J. Dumas, M. Welland, T. Ogata, B. Lee, J. Kennedy, C. Adkins, M. Bankhead, and D. Costa. "TAF-ID: An international thermodynamic database for nuclear fuels applications". In: *Calphad* 72 (Mar. 2021), p. 102212. ISSN: 0364-5916. DOI: 10.1016/j.calphad.2020.102212.
- [79] O. Beneš and R. J. M. Konings. "Molten Salt Reactor Fuel and Coolant". In: (2012), pp. 359–389. DOI: 10.1016/b978-0-08-056033-5.00062-8.

- [80] O. Beneš and R. J. M. Konings. “Thermodynamic Calculations of Molten-Salt Reactor Fuel Systems”. In: *Molten Salts Chemistry - From Lab to Applications*. Ed. by H. G. Frederic Lantelme. Elsevier, 2013, pp. 49–78. DOI: 10.1016/b978-0-12-398538-5.00004-4.
- [81] Joint Research Centre - European Commission. *Joint Research Centre Molten Salt Database - JRCMSD*. Ed. by E. S. Hub. https://joint-research-centre.ec.europa.eu/joint-research-centre-molten-salt-database-jrcmsd_en. Accessed: 2024-02-05.

2

INFLUENCE OF FISSION PRODUCTS ON SOME PROPERTIES OF MOLTEN FLUORIDE SALT FUELS

Understanding the behavior of fission products is essential for optimizing Molten Salt Reactor performance, ensuring safety, and managing environmental impact. Fission products in fission MSR reactors pose particular problems due to the specific properties of molten salts. In this work, the composition of irradiated fuel salt of the MSFR concept was simulated. The evolution of the thermodynamic properties of two representative fuel salt mixtures, in presence of fission products, was studied by comparative calorimetry measurements. The vaporization behavior was also assessed using Knudsen Effusion Mass Spectroscopy. The impact of the fission products on the studied fuel salt properties was investigated overall and for the different species. This work provides new insights on the retention of the fission products species in molten salt fuels and their impact on the general thermochemistry of the fuel.

2.1. INTRODUCTION

THE study of fission product behavior in molten salt reactors (MSRs) is a critical aspect of the reactor engineering with profound implications for reactor safety, efficiency, and environmental impact [1, 2]. Understanding fission product behavior in MSRs is crucial already at the reactor design stage and during reactor operation. Insights into fission product behavior also contribute to the development of effective strategies for waste management and to the minimization of the environmental impact in an accidental scenario.

The thermodynamic properties of the fresh fuels have been explored in a number of studies, and the behavior of some of the fission products has been deduced from online and post-irradiation analyses during the operation of the Molten Salt Reactor Experiment [3, 4]. However, there is still limited knowledge of the properties of multi-component systems representative of irradiated fuel salt.

In this work, a first experimental approach is undertaken to assess the impact of some key fission products on the evolution of the thermodynamic properties of the fuel, more specifically melting and vaporization behavior of selected fluoride-based fuels:

- LiF–ThF₄ (76.0–24.0 mol%): the eutectic composition determined by Capelli *et al.* [5].
- LiF–ThF₄–UF₄ (77.5–19.5–3.0 mol%): the optimal composition determined for the Molten Salt Fast Reactor for a fuel with fissile uranium-233 [6–8].

The choice was made to consider an extreme case scenario, without any reprocessing, and consequently with maximum accumulation of fission products in the reactor core. The calculations from the SAMOSAFER project were used to define the simulated fuel composition corresponding to a 5 years irradiation cycle [8]. The experimental results on melting temperatures were obtained by Differential Scanning Calorimetry and were compared with the data of the fresh fuel prior to the addition of fission products. The vaporization properties of the mixtures were studied by Knudsen Effusion Mass Spectrometry and the results compared to fresh fuel already explored in literature [9, 10].

2.2. METHODOLOGY

The fission products found in molten salt fuel do not differ greatly from those found in fuel from "conventional" reactors, although the chemical forms differ. The relative yields are similar, and the quantification of the uranium 235 fission products compiled by the Evaluate Nuclear Data File (ENDF) is reliable for the MSR evaluation [11]. To determine the fission products accumulated in the Molten Salt Reactor fuel, the LiF–ThF₄–UF₄ mixture was selected as reference. The fission yields were simulated by Hombourger *et al.* in the SAMOSAFER project for different operating conditions with the EQLOD tool [8, 12]. In the latter work, a 5 years cycle without reprocessing was selected, equivalent to a total concentration of fission products reaching 6.85 mol%. The results are listed in Table 2.1.

In this work, a mixture of inactive salts of selected fission products was made, with a concentration of 7.0 mol% in the two selected fuel salts. This concentration was chosen as representative for the extreme case of accumulation of fission products in the solution. The noble metals and noble gases were omitted in this mixture considering their low impact on the thermodynamic properties, i.e., their chemical inertness. Noble and semi-noble metals are considered insoluble and not affected by the fluoroacidity of the fuel according the criteria applied in the simulation [12], in agreement with the experimental observation of the MSRE [3, 4]. To simplify the mixture of fission products, compounds with similar chemical properties were grouped under a representative class [13]. The lanthanides fluorides were grouped under the neodymium trifluoride with the exception of the cerium tri-fluoride, considered as standalone because of its particular properties (different crystalline structure compared to other lanthanides fluorides) [14]. Barium difluoride was

Table 2.1.: Main fission products in ${}^7\text{LiF}-{}^{232}\text{ThF}_4-{}^{233}\text{UF}_4$ fuel salt after 5 years operation of the MSFR reactor, corresponding to a burn-up of 1.376%FIMA, without reprocessing, calculated with the EQL0D method [12].

Nuclide	Z	Mol%	Main expected chemical state	Nuclide	Z	Mol%	Main expected chemical state
Zr	40	1.107	ZrF ₄	Kr	36	0.208	Noble gas
Xe	54	0.726	Noble gas	Pr	59	0.203	PrF ₃
Mo	42	0.656	Metal	Rb	37	0.189	RbF
Nd	60	0.598	NdF ₃	Tc	43	0.140	Metal
Cs	55	0.594	CsF & CsI	Te	52	0.103	Metal
Ce	58	0.469	CeF ₃	Sm	62	0.084	SmF ₃
Sr	38	0.405	SrF ₂	I	53	0.065	CsI
Ru	44	0.259	Metal	Rh	45	0.047	Metal
Ba	56	0.253	BaF ₂	Pd	46	0.046	Metal
Y	39	0.211	YF ₃				
La	57	0.209	LaF ₃	SUM		6.573	

grouped with strontium difluoride. In this work, it was assumed that all the iodine would bond with cesium in the form of CsI, while the remainder of the cesium produced would form CsF.

Table 2.2.: Composition of the mixture of the main soluble fission products prepared in this work. Melting temperatures of each individual constituents are also indicated. Neodymium is used as surrogate for lanthanum, praseodymium and samarium; strontium is used as surrogate for barium.

End-members	Conc.(mol%)	Melting temperature in literature	Melting temperature measured in this work
ZrF ₄	25.2	(1183 ± 1) K, [15]	(1131 ± 5) K**
NdF ₃ (La,Pr,Sm)	24.9	1647 K*, [16]	above device limitation***
SrF ₂ (Ba)	15.0	(1736 ± 5) K, [17, 18]	above device limitation***
CsF	12.1	(976 ± 5), [19] K	(979.1 ± 5) K
CeF ₃	10.7	(1710 ± 5) K, [17, 19, 20]	above device limitation***
YF ₃	4.8	(1421 ± 1) K, [17, 21]	above device limitation***
RbF	4.3	(1068 ± 5) K, [19]	(1068 ± 5) K
CsI	3.0	(900 ± 5), [19] K	(896.8 ± 5) K

* No uncertainty given. ** The discrepancy with literature is considered to be caused by the sublimation of ZrF₄. *** The device temperature limitation is 1523 K.

2.3. EXPERIMENTAL

2.3.1. SAMPLE PREPARATION

Thorium tetrafluoride (ThF₄) and uranium tetrafluoride (UF₄) were synthesized by high-temperature HF gas fluorination of the pure actinide oxides, according to the method developed at the Joint Research Centre of Karlsruhe by Souček *et al.* [22].

The other inactive end-members were obtained from commercial suppliers (Alfa Aesar, Sigma Aesar and Thermo Scientific) (Table 2.3). These powders were dried at 573 K under argon atmosphere to remove traces of moisture. The purity of all the end-members was checked by measurements of the melting temperatures by Differential Scanning Calorimetry (DSC) and X-ray Diffraction (XRD) analyses.

The powders of the different end members were intimately mixed, respecting the composition established in Table 2.2. The same absolute content and ratio of fission products was tested for the two selected fuel salt mixtures, neglecting slight differences in the fission yields of the different actinides (^{233}U , ^{235}U , ^{239}Pu) [11].

Table 2.3.: Purity and providers of the chemicals used in this work.

Compound	Provider	Purity
LiF powder	Alfa Aesar	99.999% (metal basis)
NaF powder	Alfa Aesar	99.99% (metal basis)
KF powder	Alfa Aesar	99.99% (metal basis)
ZrF ₄ powder	Sigma Aldrich	99.9% (metal basis)
NdF ₃ powder	Alfa Aesar	99.9% (metal basis)
SrF ₂ powder	Alfa Aesar	99.99% (metal basis)
CsF powder	Alfa Aesar	99.99% (metal basis)
CeF ₃ powder	Alfa Aesar	99.9% (REO)
YF ₃ powder	Sigma Aldrich	99.5%
RbF powder	Alfa Aesar	99.975% (metal basis)
CsI powder	Thermo Scientific	99.999% (metal basis)

2.3.2. X-RAY DIFFRACTION

The purity of the pure compounds used in this work as starting materials, were controlled using X-ray Diffraction (XRD) at room temperature ($T = 293 \pm 2$ K), using a Bruker D8 X-ray diffractometer mounted in a Bragg-Brentano configuration with a curved Ge monochromator (1, 1, 1) and a ceramic copper tube (40 kV, 40 mA) and equipped with a LinxEye position-sensitive detector. Samples were placed on a sample holder and measured in a glovebox under inert atmosphere. X-ray data were collected by step scanning in the range $10^\circ < 2\theta < 120^\circ$ in a Bragg-Brentano configuration. The purities of each powder were analyzed by Rietveld refinement method using the FullProf suite software [23, 24].

2.3.3. DIFFERENTIAL SCANNING CALORIMETRY

3D heat flux measurements were conducted with a Setaram Multi detector HTC module of the 96 line calorimeter. Every measurement consisted of at least four consecutive heating cycles with 10 K min^{-1} heating and cooling rates. The solidus and eutectic transition temperatures were extracted from the onset of the line integral of the corresponding endothermic peak in the heat flow curves, while the

liquidus transition temperatures were taken from the maximum of the corresponding peak according to the NIST recommendation [25]. A correction was applied to the collected temperature data according to the calibration determined for pure metals (Pb, In, Sn, Al, Ag, Au), correcting for the effect of the heating rate and apparatus geometry. The uncertainties on the measurements are estimated at 5 K for the solidus and eutectic transitions, and at 10 K for the liquidus transitions.

For the DSC measurements, the samples were inserted inside a pure nickel liner. The liners were hermetically closed in stainless steel crucibles designed according to the concept developed at the Joint Research Centre of Karlsruhe [26], ensuring the stability of the sample composition and limiting the vapor releases during heating.

2.3.4. KNUDSEN EFFUSION MASS SPECTROMETRY

The setup for the experiment involved a Knudsen effusion cell in which a solid or liquid sample is heated, leading to sublimation/vaporization of the sample. The gas phase in equilibrium with the sample was ionized by a cross-beam electron bombardment ion source, as illustrated in Figure 2.1. The ionized species were further analyzed with a quadrupole QMG422 mass spectrometer from Pfeiffer Vacuum GmbH. Specifically designed for the study of radioactive materials, the entire apparatus is housed within a glove box shielded with 5 cm lead [27, 28].

The mass spectrometer is capable of monitoring species within a mass range of 1 to 512 amu (atomic mass unit). Positioned at 90° to the filter axis are the Second Electron Multiplier (SEM), connected to an electrometer, and the axial Faraday cup. The Knudsen cell is placed within a high-temperature furnace featuring tungsten-coil heating elements and is surrounded by seven cylindrical thermal shields (three in tungsten, four in tantalum). The entire system is housed in an ultrahigh vacuum chamber with pressures ranging from 10^{-7} to 10^{-8} mbar. The measurements were conducted at an ionization energy of 32 eV [29].

The experiments were conducted with a tungsten effusion cell capable of sustaining temperatures up to 2700 K. The temperature was systematically raised at a gradual rate (10 K min^{-1}), and the mass spectrometer was employed to analyze the species evaporating from the sample.

According to the Hertz-Knudsen equation (2.1), the vapor pressure of species i , P_i , is related to the intensity of the molecular beam, I_i^+ , to the actual temperature, T , and to a calibration factor specific to species i , K_i :

$$P_i = I_i^+ \cdot T / K_i \quad (2.1)$$

The temperature, represented by T , underwent calibration through the measurement of the melting points of standard materials (Zn, Cu, Fe, Pt, Al_2O_3), identified as small plateaus on the vapor pressure curve. The calibration factor for a given species i , denoted as K_i , is further linked to an instrumental factor, K_g , which remains independent of the detected species. It is also influenced by the species' ionization cross-section, σ_i , isotopic weight, f_i , and the efficiency of the second electron multiplier, γ_i , as expressed by the following equation:

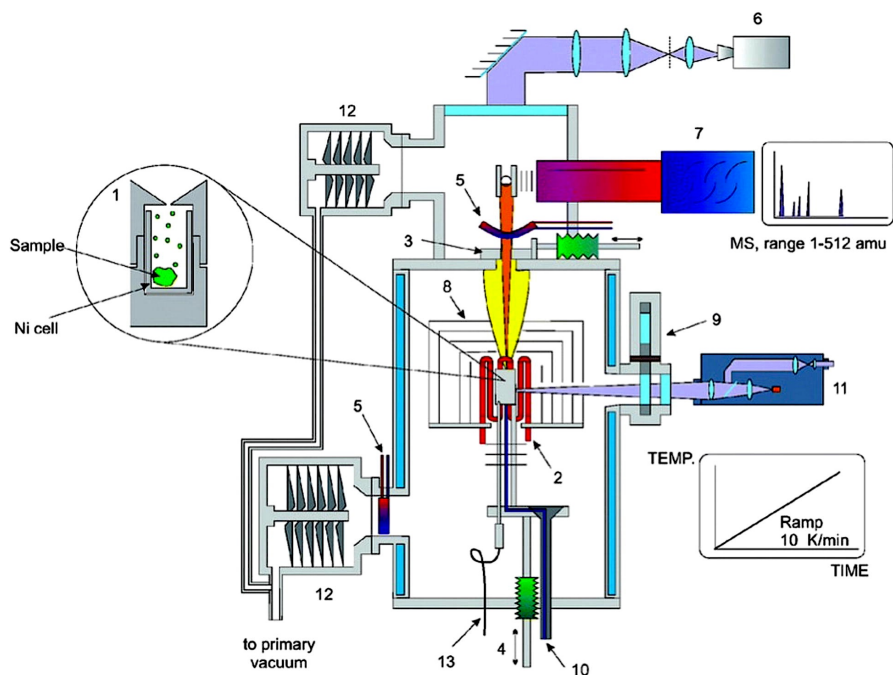


Figure 2.1.: The KEMS experimental setup used in this study, (1) Knudsen cell with sample, in W cell, (2) Tungsten heating coil, (3) Molecular beam chopper, (4) Cell lift facilities for fast heating or cooling, (5) Liquid nitrogen trap to reduce background signal, (6) Camera to align the cell holder and chopper diaphragm, (7) Quadrupole mass spectrometer, (8) Thermal shield, (9) Revolving protection windows, (10) Inlet gas capillary, (11) Linear pyrometer, (12) Turbo molecular pump, (13) Removable W/Re thermocouple [29].

$$K_i = K_g \cdot \sigma_i \cdot \gamma_i \cdot f_i \quad (2.2)$$

The calculation assumes a linear variation of the ionization cross-section at low energies, σ_i , with respect to $(E_i - AP_i)$, where E_i and AP_i represent the electron beam energy and appearance potential of species, i respectively, as described by Drowart *et al.* [30, 31]. This linear relationship holds up to the ionization cross-section at the maximum of the ionization efficiency curve, denoted as σ_{mi} :

$$\sigma_i = \sigma_{mi} \cdot (E_i - AP_i) / (E_{mi} - AP_i) \quad (2.3)$$

The estimation of the instrumental factor K_g involves vaporizing a known quantity of silver alongside the sample, which vaporizes in the same temperature range as our studied material and maintains relative inertness in the system. This characteristic makes it an ideal reference material for calibration, with complete vaporization occurring at approximately 1500 K. The experimental determination of the calibration factor for silver, denoted as K_{Ag} , becomes possible by examining the ion intensities, I_{Ag^+} , for the silver isotopes ^{107}Ag and ^{109}Ag :

$$K_{Ag} = I_{Ag^+} \cdot T_{Ag} / P_{Ag} \quad (2.4)$$

Knowing K_{Ag} , the partial pressure of species i is deduced by combining equations (2.1), (2.2), (2.3), (2.4):

$$P_i = \frac{I_i^+ \cdot T}{K_{Ag}} \cdot \Gamma_i \cdot \frac{f_{Ag}}{f_i} \cdot \left(\frac{M_i}{M_{Ag}} \right)^{1/2} \quad (2.5)$$

$$\Gamma_i = \frac{\sigma_{mAg}(E_i - AP_{Ag})}{\sigma_{mi}(E_i - AP_i)} \quad (2.6)$$

where, T represents the actual temperature, I_i^+ is the intensity of the molecular beam corresponding to species i , K_{Ag} is the calibration factor determined for silver, E_i represents the electron beam energy, AP_i (and AP_{Ag}) denotes the appearance potential, σ_{mi} (and σ_{Ag}) is the ionization cross-section at the maximum of the ionization efficiency curve, f_i (and f_{Ag}) represents the isotopic weight, and M_i (and M_{Ag}) signifies the molar mass of species i (and silver, respectively).

2.4. RESULTS & DISCUSSIONS

2.4.1. IMPACT ON THE MELTING PROPERTIES OF THE FUELS

THE LiF-ThF₄ SYSTEM

The composition of the LiF-ThF₄ salt mixture was selected as the eutectic determined by Capelli *et al.* (LiF-ThF₄, 76.0-24.0) at (832 ± 5) K [5]. In this study, a temperature of (839 ± 5) K was measured for the same eutectic composition, thus slightly higher than in the previous work but similar to the measurement of Beneš *et al.* at (839.1 ± 5) K [32]. These two studies used the same set-up as in the present work [27, 28]. After addition of 7 mol% of the fission product mixture listed in Table 2.2, a single transition was observed by DSC at a lower temperature, i.e. (818 ± 5) K,

thus around 21 K lower than the initial eutectic transition, as highlighted in Figure 2.2. This decrease in the melting temperature of the simulated irradiated salt is related to the complex phase equilibria in a multi-component system. The fact that a single transition is still observed indicates a good solubility of the fission products in the molten salt mixture [3]. In the salt with multiple components, formation of intermediate compounds from complexation with certain fission products is taking place, which affects the phase equilibria and thus the melting temperature. As an example, in the thermodynamic evaluation of the behavior of CsI and CsF in the LiF–ThF₄ salt system, Capelli *et al.* included many intermediates with lithium and thorium [33]: CsTh₃F₁₃, Cs₂Th₃F₁₄, CsThF₅, LiCsF₂, CsTh₆F₂₅, CsTh₂F₉, Cs₂ThF₆ and Cs₃ThF₇. According to the study of Benes *et al.*, CsI has the largest impact on the thermodynamics of the LiF–ThF₄ salt system. A detailed study of the effect of its addition on the eutectic transition was performed by Benes *et al.*, and a decrease of approximately 5 K was observed for an addition of 1 mol% CsI. Exchange reactions were also identified, leading to the formation of LiI and ThI₄ compounds. In the mixture with 8 main fission products (Table 2.2), additional interactions are expected and the impact of the presence of fission products on the melting behavior of the LiF–ThF₄ eutectic composition is seen to be non negligible.

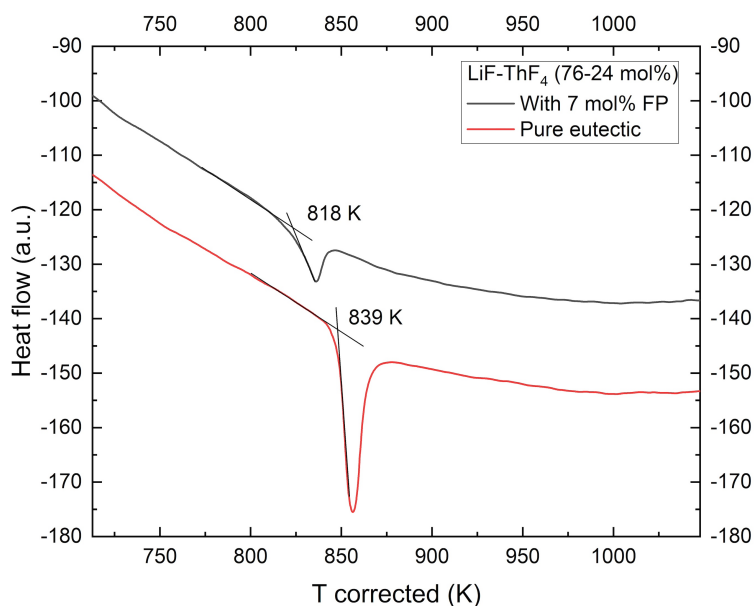


Figure 2.2.: Comparison of the differential scanning measurements of the eutectic transition in the mixture LiF–ThF₄ (76.0–24.0 mol%) pure and 93.0% LiF–ThF₄ (76.0–24.0 mol%) + 7.0 mol% selected fission products admixed measured in this work.

THE LiF-ThF₄-UF₄ SYSTEM

LiF-ThF₄-UF₄ (77.5-19.5-3.0 mol%) is the composition considered for the fresh fuel in the frame of the SAMOSAFER project [7]. Two comparative calorimetry measurements were made on this system, with and without the addition of fission products. Only the eutectic transitions were clearly identified in both DSC measurements (Figure 2.3). The eutectic temperature was measured in this work at (829 ± 5) K, in close agreement with the temperature published by Tosolin *et al.* of (828 ± 5) K [10], for a slightly different composition, namely LiF-ThF₄-UF₄ (77.5-20.0-2.5 mol%). With the addition of the fission products mixture, the eutectic was measured at (808 ± 5) K. A decrease of 21 K was thus observed, identical to the LiF-ThF₄ eutectic composition (Figure 2.3). The observed impact of the presence of soluble fission products appears again non negligible on the melting temperature of the fuel.

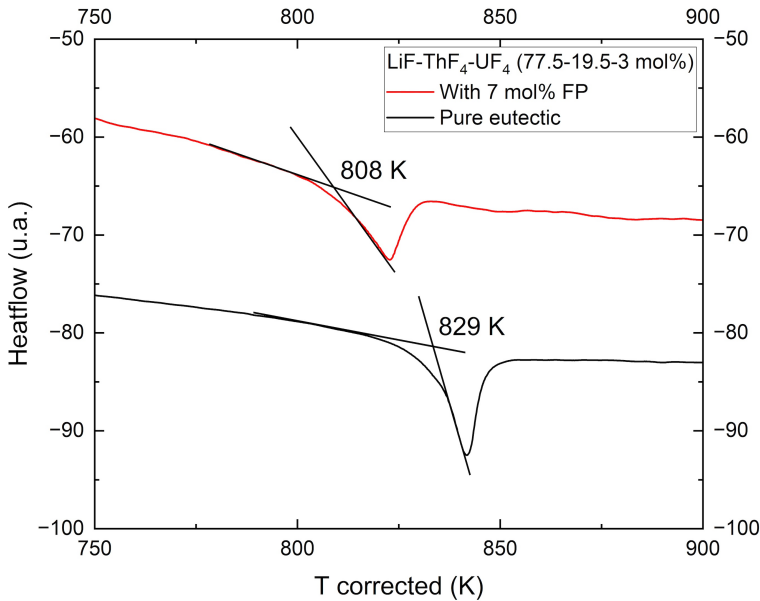


Figure 2.3.: Comparison of the differential scanning measurement of the eutectic transition in the mixture LiF-ThF₄-UF₄ (77.5-19.5-3.0 mol%) and 93.0% LiF-ThF₄-UF₄ (77.5-19.5-3.0 mol%) + 7.0 mol% FP mix measured in this work.

2.4.2. VAPORIZATION OF FUEL MATERIALS

KEMS analysis was performed on a 10.80 mg sample collected after the DSC measurement on the 93.0% LiF-ThF₄-UF₄ (77.5-19.5-3.0 mol%) + 7.0 mol% FP

mix system (Section 2.4.1), in the temperature ranged from 674 K to 1897 K, until complete vaporization of the sample. The mass spectrometry data showed the presence of the same ions as those observed by Tosolin *et al.* [10]: ${}^7\text{Li}^+$, ${}^{14}\text{Li}_2^+$, ${}^{26}\text{LiF}^+$, ${}^{33}\text{Li}_2\text{F}^+$, ${}^{251}\text{ThF}^+$, ${}^{270}\text{ThF}_2^+$, ${}^{289}\text{ThF}_3^+$, ${}^{238}\text{U}^+$, ${}^{251}\text{UF}^+$, ${}^{276}\text{UF}_2^+$, ${}^{295}\text{UF}_3^+$ and ${}^{314}\text{UF}_4^+$ (as shown in Figure 2.4). Because of the very large number of masses, only the intensities of the most predominant isotopes were recorded in this work, as is common practice in the literature (i.e. with intensity higher than $1 \cdot 10^{-10}$) [9, 27, 28]. The maximal release was observed at a temperature of 1357 K for thorium species and 1323 K for uranium species, respectively.

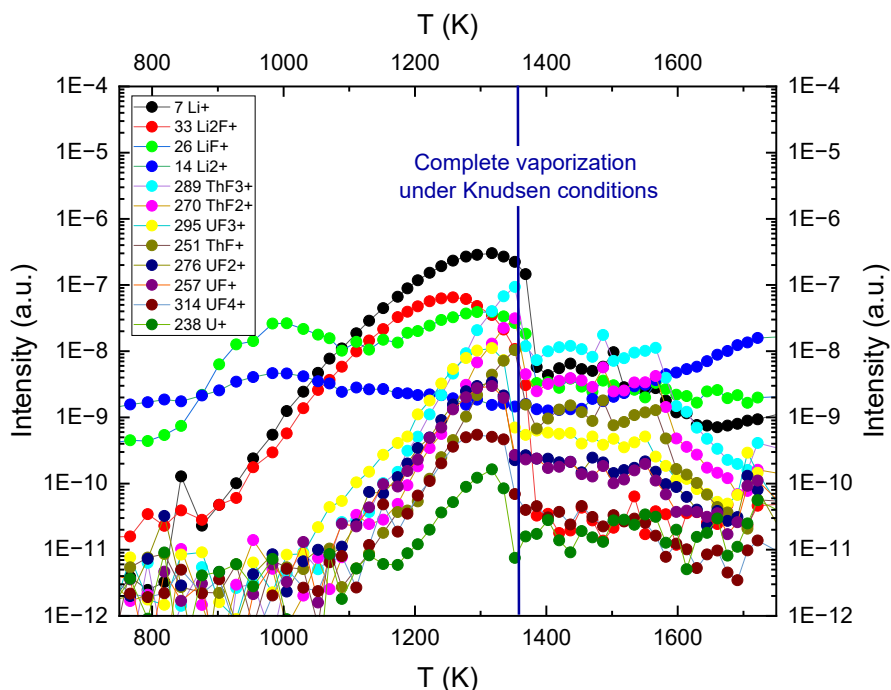


Figure 2.4.: Ion intensities of the fuel species versus temperature obtained for the 93.0% LiF–ThF₄–UF₄ (77.5–19.5–3.0 mol%) + 7.0 mol% selected fission products admixed system. The main species recorded are: ${}^7\text{Li}^+$, ${}^{14}\text{Li}_2^+$, ${}^{26}\text{LiF}^+$, ${}^{33}\text{Li}_2\text{F}^+$, ${}^{251}\text{ThF}^+$, ${}^{270}\text{ThF}_2^+$, ${}^{289}\text{ThF}_3^+$, ${}^{238}\text{U}^+$, ${}^{251}\text{UF}^+$, ${}^{276}\text{UF}_2^+$, ${}^{295}\text{UF}_3^+$ and ${}^{314}\text{UF}_4^+$. Only the intensities of the most predominant isotopes were measured in each case.

The vapor pressures of LiF, Li₂F₂, Li₃F₃, ThF₄ and UF₄ were calculated from the data collected for the different ionized species of lithium, thorium, and uranium. The linear variation of the logarithm of their vapor pressure versus the reciprocal

temperature is given by an equation of the type:

$$\ln P(\text{Pa}) = -\frac{a \pm \Delta a}{T(\text{K})} + (b \pm \Delta b) \quad (2.7)$$

where a and b are two independent parameters from the fitting and T is the temperature.

These results were compared with the data as measured by Tosolin *et al.* [10]. The partial vapour pressure of LiF monomer is higher than the dimer, itself higher than the trimer. The UF_4 partial pressure is found to be higher than ThF_4 , despite the large difference in molar proportions in the mixture. Similar observation was made in the work of Tosolin *et al.* [10]. Considering the confidence interval of the vapor pressure measurements by KEMS, estimated at 50%, the agreement between our measurements and the data on pure fuel salt mixture is very good [10], as seen in Figure 2.5. This shows the limited impact of the presence of fission products on the fuel vaporization behavior, even at high concentration.

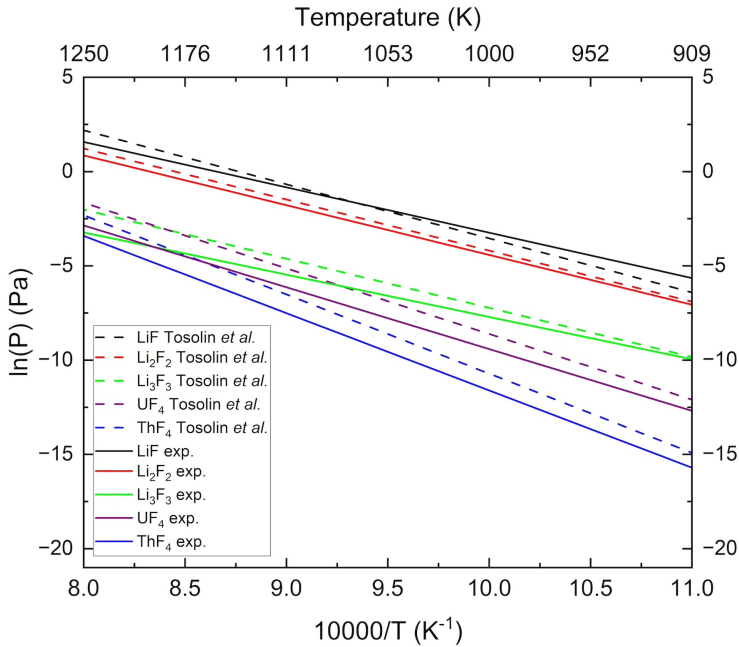


Figure 2.5.: Comparison of partial vapor pressures above the mixture $\text{LiF}-\text{ThF}_4-\text{UF}_4$ (77.5-19.5-3.0 mol%) + 7.0 mol% selected fission products admixed measured in this work, compared with data reported by Tosolin *et al.* on the $\text{LiF}-\text{ThF}_4-\text{UF}_4$ (77.5-20.0-2.5 mol%) system [10].

Table 2.4.: Formulas for partial vapor pressures fitting curves for the mixture 93.0% LiF–ThF₄–UF₄ (77.5-19.5-3.0 mol%) + 7.0 mol% FP mix based on the values measured in this work.

Species	Equation	Temperature range (K)
LiF(g)	$\ln P(Pa) = -\frac{(32754 \pm 324)}{T(K)} + (23.343 \pm 0.189)$	911 - 1323
Li ₂ F ₂ (g)	$\ln P(Pa) = -\frac{(26391 \pm 261)}{T(K)} + (21.973 \pm 0.200)$	1012 - 1211
Li ₃ F ₃ (g)	$\ln P(Pa) = -\frac{(22410 \pm 224)}{T(K)} + (14.706 \pm 0.162)$	1076 - 1211
ThF ₄ (g)	$\ln P(Pa) = -\frac{(40972 \pm 410)}{T(K)} + (29.368 \pm 0.200)$	1118 - 1229
UF ₄ (g)	$\ln P(Pa) = -\frac{(32754 \pm 328)}{T(K)} + (23.343 \pm 0.189)$	1059 - 1229

Uncertainties on the fitting curves were taken from Tosolin *et al.*: LiF(a: 9.9·10⁻³%, b: 8.1·10⁻³%), Li₂F₂(a: 9.9·10⁻³%, b: 9.1·10⁻³%), Li₃F₃(a: 0.010%, b: 0.011%), ThF₄(a: 0.010%, b: 6.8·10⁻³%), UF₄(a: 0.010%, b: 8.1·10⁻³%).

2.4.3. MASS SPECTROMETRY ANALYSIS OF FISSION PRODUCTS

The mass spectrometry measurements showed the appearance of the fission products at varying temperatures. As listed in Table 2.5, the first ions observed came from the cesium iodine species, that show a high volatility [32], followed by species from the ionization of CsF, and then different species from ZrF₄. The vaporization of rubidium species appeared at a maximum temperature of 1341 K. It is interesting to note that these four species vaporized below or at the same temperature as the fuel as shown in figure 2.4. The maximum vaporization of SrF₂, YF₃, CeF₃ and NdF₃ were observed in this order and above the complete fuel vaporization temperature under Knudsen conditions (1357 K). This point is an element of discussion in the detailed analysis for each species in the next sections.

Table 2.5.: Temperatures at which maximum intensity was recorded for the various species, indicating maximum release.

Initial species	Observed ions	Temperature of maximum ion intensity (K)
Fresh fuel compounds		
LiF	²⁶ LiF ⁺ (1 st peak)	1005
	³³ Li ₂ F ⁺	1258
	⁷ Li ⁺ , ²⁶ LiF ⁺ (2 nd peak)	1317
UF ₄	²³⁸ U ⁺ , ²⁵¹ UF ⁺ , ²⁷⁶ UF ₂ ⁺ , ²⁹⁵ UF ₃ ⁺ , ³¹⁴ UF ₄ ⁺	1323
ThF ₄	²⁵¹ ThF ⁺ , ²⁷⁰ ThF ₂ ⁺ , ²⁸⁹ ThF ₃ ⁺	1357
Fission products		
CsI	¹³³ Cs ⁺ (1 st peak), ¹³⁴ LiI ⁺	827
	¹²⁷ I ⁺	1572
CsF	¹³³ Cs ⁺ (2 nd peak), ¹⁵² CsF ⁺	1137
ZrF ₄	¹²⁸ ZrF ₂ ⁺ , ¹⁴⁷ ZrF ₃ ⁺	1159
	⁹³ Zr ⁺ , ¹⁰⁹ ZrF ⁺ *, ¹²⁸ ZrF ₂ ⁺ , ¹⁴⁷ ZrF ₃ ⁺	1323
RbF	¹⁰⁸ RbF ⁺	1341
SrF ₂	⁸⁸ Sr ⁺ , ¹⁰⁷ SrF ⁺ , ¹²⁶ SrF ₂ ⁺	1442
YF ₃	⁸⁹ Y ⁺ , ¹⁰⁸ YF ⁺ , ¹²⁷ YF ₂ ⁺ , ¹⁴⁶ YF ₃ ⁺	1572
CeF ₃	^{140,142} Ce ⁺ , ^{159,161} CeF ⁺ , ^{178,180} CeF ₂ ⁺ , ^{197,199} CeF ₃ ⁺	1580
NdF ₃	^{142,144,146} Nd ⁺ , ^{161,163,165} NdF ⁺ , ^{180,182,184} NdF ₂ ⁺ , ¹⁹⁹ NdF ₃ ⁺	1580

*¹⁰⁹ZrF⁺ is disturbed, overlapping with ¹⁰⁹Ag⁺ reference.

CESIUM AND IODINE SPECIES

From the mass spectra (Figure 2.6), ¹²⁷I⁺, ¹³³Cs⁺, ¹³⁴LiI⁺ and ¹⁵²CsF⁺ were intense enough to be observed. The mass spectrum of ¹³³Cs⁺ showed two maxima corresponding to fragmentation of cesium from CsI(g) and CsF(g), respectively. The first peak was correlated with the ionization of ¹²⁷I⁺, in the same range of temperature, the second peak being related to the signal of ¹²⁷YF⁺ (see Section 2.4.3). It is moreover interesting to observe, even at low intensity, the release corresponding to ¹³⁴LiI⁺, indicating the recombination of iodine in the fuel mixture. This combination of iodine was also observed by Beneš *et al.* in the study on the behavior of CsI and CsF in the reference molten LiF–ThF₄–UF₄ fuel [32], confirming

the low retention of CsI in the fuel matrix. On the contrary, the retention of CsF is higher, as the cesium coming from CsF(g) is released at higher temperature.

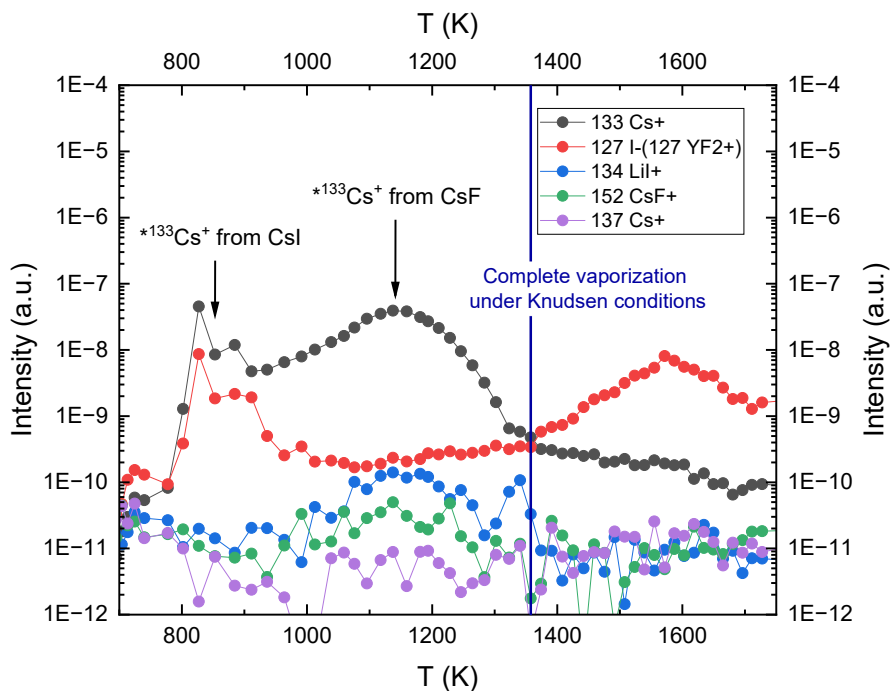


Figure 2.6.: Ion intensities of the cesium and iodine species versus temperature obtained for the 93.0% LiF–ThF₄–UF₄ (77.5–19.5–3.0 mol%) + 7.0 mol% selected fission products admixed. The main species recorded are: ¹²⁷I⁺, ¹³³Cs⁺, ¹³⁴LiI⁺, ¹³⁷Cs⁺ and ¹⁵²CsF⁺; the first peak of the mass spectra of ¹²⁷I⁺ is the signal of ¹²⁷YF₂⁺; the two peaks of ¹³³Cs⁺ are due to the presence of the two species CsI and CsF in the FP mixture. Only the intensities of the most predominant isotopes were measured in each case.

ZIRCONIUM SPECIES

The mass spectrometry measurement revealed the presence of the following species: ¹⁰⁹ZrF⁺, ¹²⁸ZrF₂⁺ and ¹⁴⁷ZrF₃⁺. Since ¹⁰⁹ZrF⁺ has the same mass as the reference material, ¹⁰⁹Ag⁺, the signals are overlapping. The ¹⁶⁶ZrF₄⁺ signal was not intense enough. ¹²⁸ZrF₂⁺ and ¹⁴⁷ZrF₃⁺ signals showed a maximum intensity around 1159 K, but also a peak around 1323 K. Complementary measurements would be required to understand this behavior. Zirconium shows moderate retention in the fuel salt matrix, given that the release is observed at relatively low temperatures.

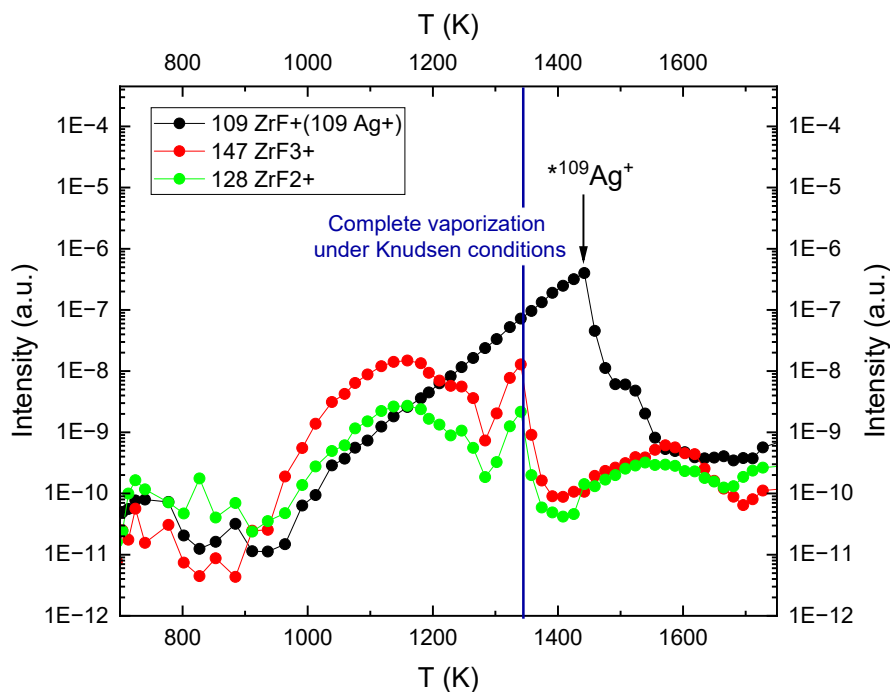


Figure 2.7.: Ion intensities of the zirconium species versus temperature obtained for the 93.0% LiF–ThF₄–UF₄ (77.5–19.5–3.0 mol%) + 7.0 mol% selected fission products admixed system. The main species recorded are: ⁹³Zr⁺, ¹⁰⁹ZrF⁺, ¹²⁸ZrF₂⁺ and ¹⁴⁷ZrF₃⁺; the ¹⁰⁹ZrF⁺ signal is considered to overlap with the reference signal ¹⁰⁹Ag⁺ more intense. Only the intensities of the most predominant isotopes were measured in each case.

RUBIDIUM SPECIES

Only the $^{104}\text{RbF}^+$ species was identified with a maximum intensity at a temperature of 1341 K. As shown in Figure 2.8, the $^{89}\text{Rb}^+$ ion is not intense enough to be detected. Rubidium species show a high retention in the molten reference fuel as they are released at a similar temperature.

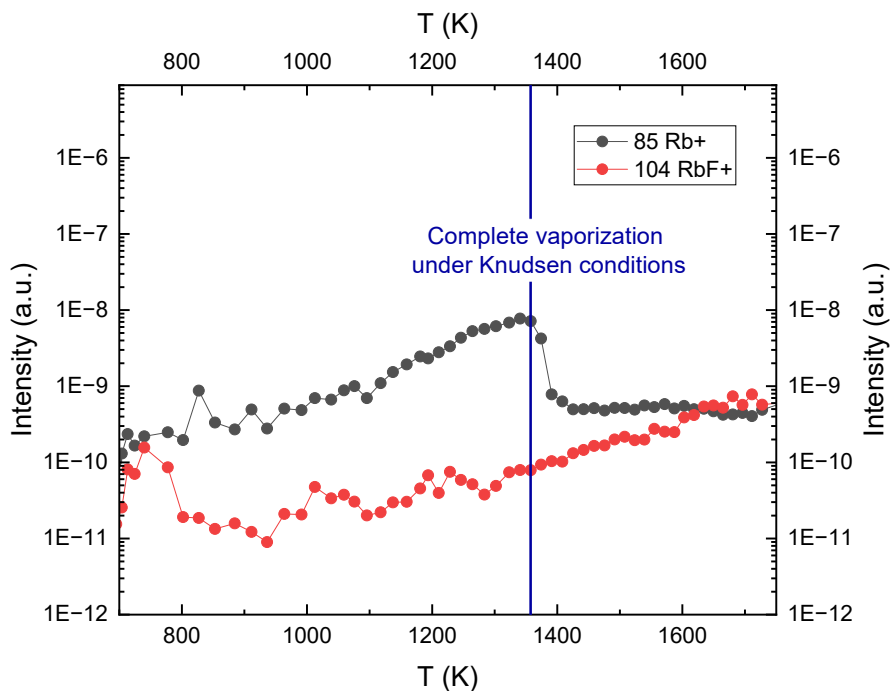


Figure 2.8.: Ion intensities of the rubidium species versus temperature obtained for the 93.0% $\text{LiF}-\text{ThF}_4-\text{UF}_4$ (77.5-19.5-3.0 mol%) + 7.0 mol% selected fission products admixed system. The main species recorded are: $^{89}\text{Rb}^+$, $^{108}\text{RbF}^+$. Only the intensities of the most predominant isotopes were measured in each case.

Based on the entire measured intensity for the rubidium species, the partial vapor pressure of the rubidium species was calculated in the fuel melt and compared to the literature data from Sense and Stone (Figure 2.9) [34]. For an equivalent range of temperature, the partial vapor pressure was calculated to be much lower (a factor 10^4). Considering the concentration of RbF in the melt (4.63 %), these results indicate a strong retention of the RbF species in the fuel matrix.

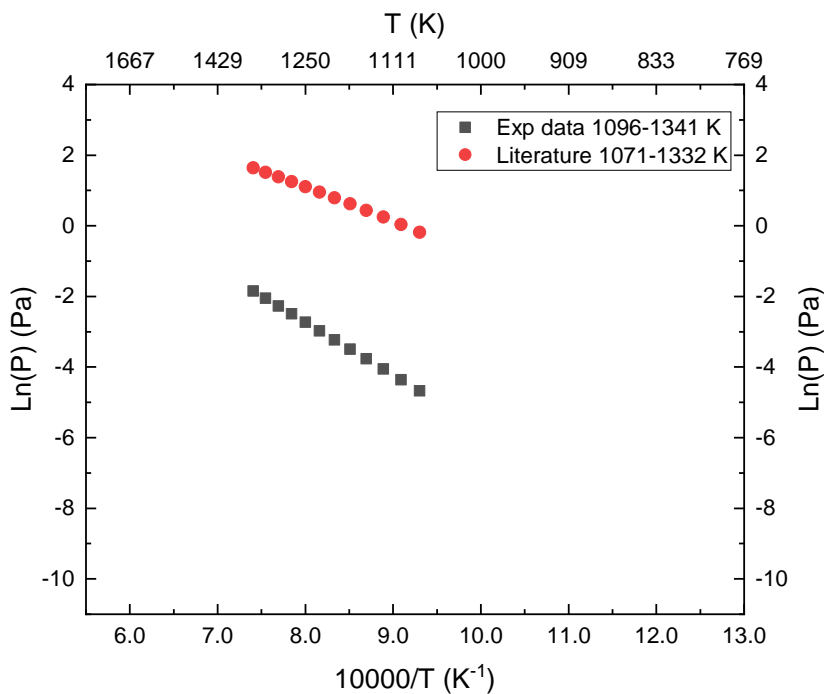


Figure 2.9.: Partial vapor pressure measured for the RbF species in the 93.0% LiF–ThF₄–UF₄ (77.5–19.5–3.0 mol%) + 7.0 mol% selected fission products admixed system compared to the literature data for the pure RbF [34].

STRONTIUM SPECIES

The species $^{88}\text{Sr}^+$, $^{107}\text{SrF}^+$, and at very low intensity $^{126}\text{SrF}_2^+$ were observed. In the case of mass 107, the first peak with a maximum intensity at a temperature of 1442 K, was identified as the vapor release of the $^{107}\text{Ag}^+$ isotope from the reference material (Figure 2.10). The $^{88}\text{Sr}^+$ and $^{107}\text{SrF}^+$ signals reached their maximum intensity around 1618 K. For $^{126}\text{SrF}_2^+$, the low intensity only allowed to observe a range of maximum release similar to the others. In the case of strontium, the release occurs at higher temperatures than the fuel salt melt itself. This indicates that strontium vaporize after the main matrix component, which may indicate that SrF_2 precipitates out of the fuel matrix upon heating.

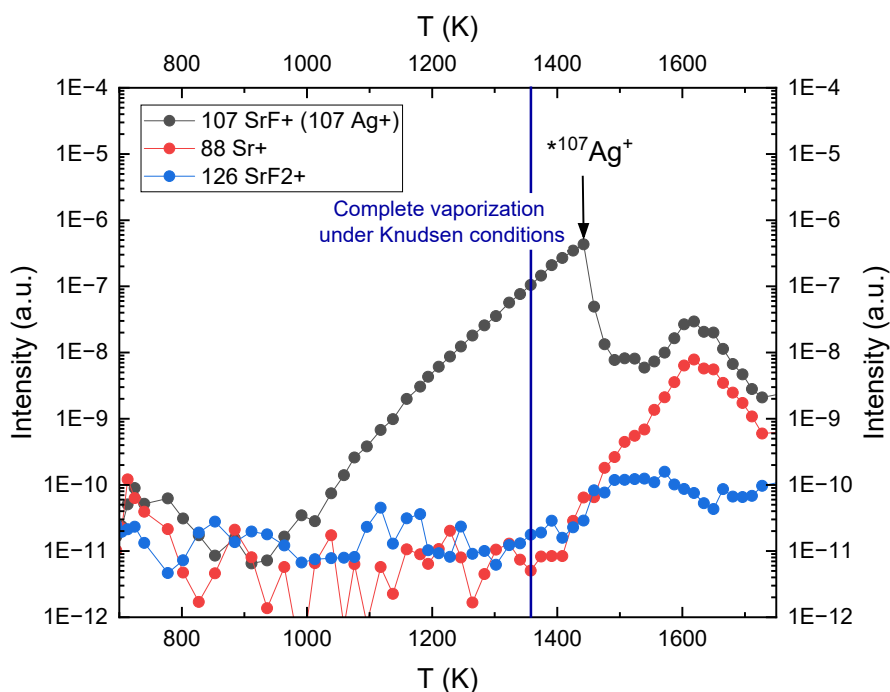


Figure 2.10.: Ion intensities of the strontium species versus temperature obtained for the 93.0% $\text{LiF}-\text{ThF}_4-\text{UF}_4$ (77.5-19.5-3.0 mol%) + 7.0 mol% selected fission products admixed system. The main species recorded are: $^{88}\text{Sr}^+$, $^{107}\text{SrF}^+$ and $^{126}\text{SrF}_2^+$; the first peak of the mass spectra of $^{107}\text{SrF}^+$ is the reference signal $^{107}\text{Ag}^+$. Only the intensities of the most predominant isotopes were measured in each case.

YTTRIUM SPECIES

Four ionized species with yttrium were detected during the mass spectrometry measurement: $^{89}\text{Y}^+$, $^{108}\text{YF}^+$, $^{127}\text{YF}_2^+$ and $^{146}\text{YF}_3^+$. The maximum intensity was measured at a temperature around 1572 K for all the species. Another peak was observed for the mass number 127, which is also the mass of the ion iodine $^{127}\text{I}^+$, identified at a lower temperature, as shown in Figure 2.11. As in the case of strontium above, the vaporization of YF_3 occurs after that of the main fuel matrix under Knudsen conditions, which may indicate precipitation of YF_3 out of the salt upon heating.

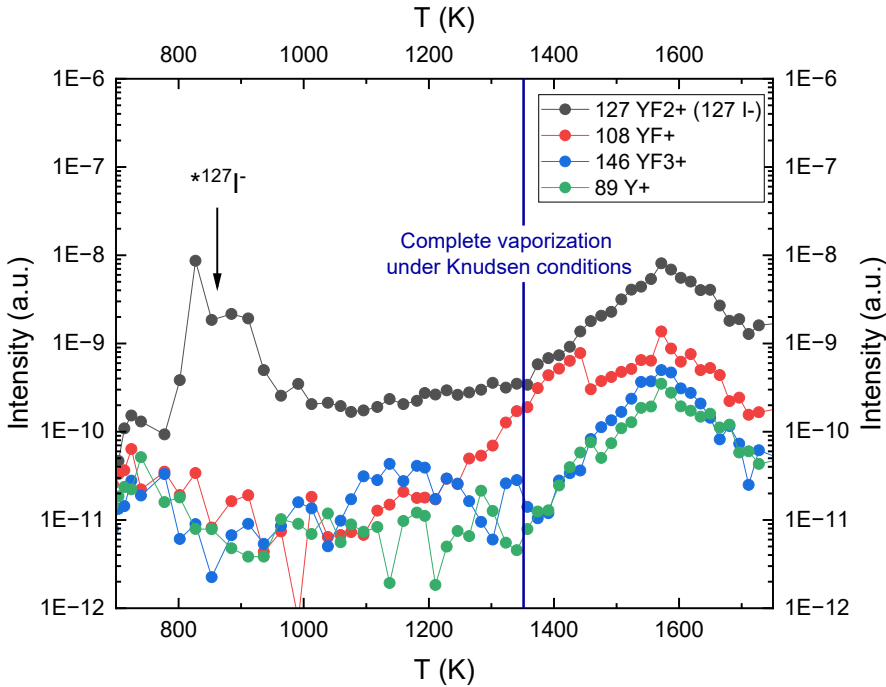


Figure 2.11.: Ion intensities of the yttrium species versus temperature obtained for the 93.0% $\text{LiF}-\text{ThF}_4-\text{UF}_4$ (77.5-19.5-3.0 mol%) + 7.0 mol% selected fission products admixed system. The main species recorded are: $^{89}\text{Y}^+$, $^{108}\text{YF}^+$, $^{127}\text{YF}_2^+$ and $^{146}\text{YF}_3^+$; the first peak of the mass spectra of $^{127}\text{YF}_2^+$ is the signal of $^{127}\text{I}^+$. Only the intensities of the most predominant isotopes were measured in each case.

LANTHANIDES SPECIES

2

Cerium has very similar ionization behavior to the neodymium 142 isotope. Because they have the same molecular weight, it is impossible to discern the two species from the mass spectrometry measurements for the 142 mass (Figure 2.12 and 2.13). During the measurement, different isotopes of cerium and neodymium were observed: $^{140}\text{Ce}^+$, $^{142}\text{Nd}^+$ (also $^{142}\text{Ce}^+$), $^{144}\text{Nd}^+$ and $^{146}\text{Nd}^+$. Likewise, the monovalent and divalent fluoride species of the previous isotopes were intense enough to be observed. The species recorded were: $^{159}\text{CeF}^+$, $^{161}\text{CeF}^+$, $^{161}\text{NdF}^+$, $^{162}\text{NdF}^+$, $^{163}\text{NdF}^+$, $^{164}\text{NdF}^+$, $^{165}\text{NdF}^+$, $^{178}\text{CeF}_2^+$, $^{180}\text{CeF}_2^+$, $^{180}\text{NdF}_2^+$, $^{180}\text{CeF}_2^+$, $^{181}\text{NdF}_2^+$, $^{182}\text{NdF}_2^+$, $^{183}\text{NdF}_2^+$, $^{184}\text{NdF}_2^+$. For mass 159, a first peak was observed with a maximum intensity at a temperature of 1080 K which might come from an impurity that was not identified. Only two trivalent species were identified, namely $^{197}\text{CeF}_3^+$ and with the lowest intensity, $^{199}\text{NdF}_3^+$ or $^{199}\text{CeF}_3^+$. Overall, a pretty clear maximum was observed around 1580 K for the entire range of the lanthanide compounds. It shows the vaporization of the neodymium and cerium species takes place at a higher temperature than the fuel matrix, confirming the high retention of the lanthanide fission products in the $\text{LiF}-\text{ThF}_4-\text{UF}_4$ molten salt, but also the probable precipitation out of the salt upon heating.

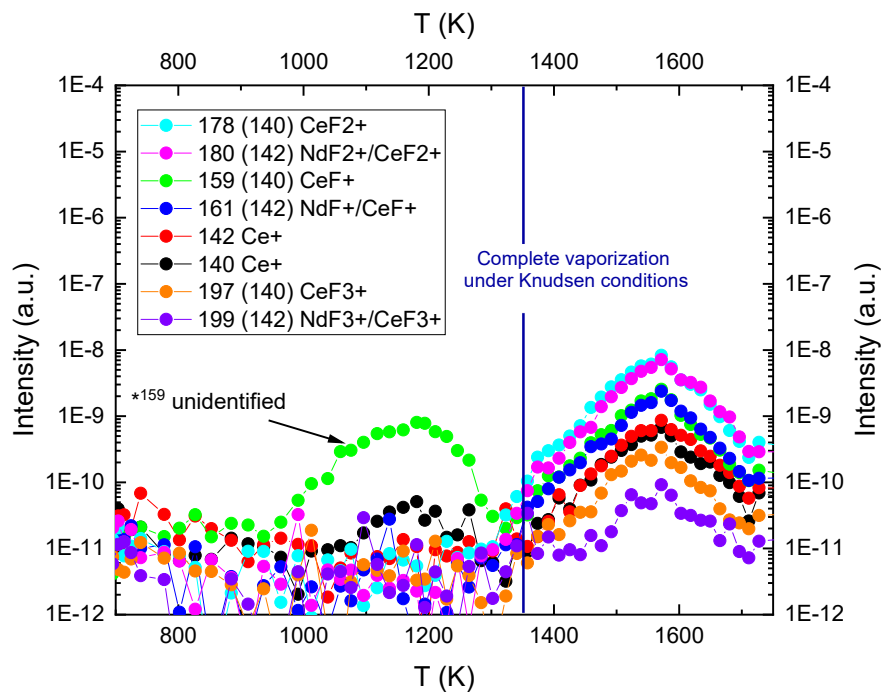


Figure 2.12.: Ion intensities of cerium species versus temperature obtained for the 93.0% $\text{LiF}-\text{ThF}_4-\text{UF}_4$ (77.5-19.5-3.0 mol%) + 7.0 mol% selected fission products admixed system. The main species recorded are: $^{140}\text{Ce}^+$, $^{142}\text{Ce}^+$, $^{159}\text{CeF}^+$, $^{161}\text{CeF}^+$, $^{178}\text{CeF}_2^+$, $^{180}\text{CeF}_2^+$, $^{197}\text{CeF}_3^+$ and $^{199}\text{CeF}_3^+$. The first peak of the mass spectra of $^{159}\text{CeF}^+$ is probably due to the presence of an impurity of atomic mass 159 that was not identified. Only the intensities of the most predominant isotopes were measured in each case.

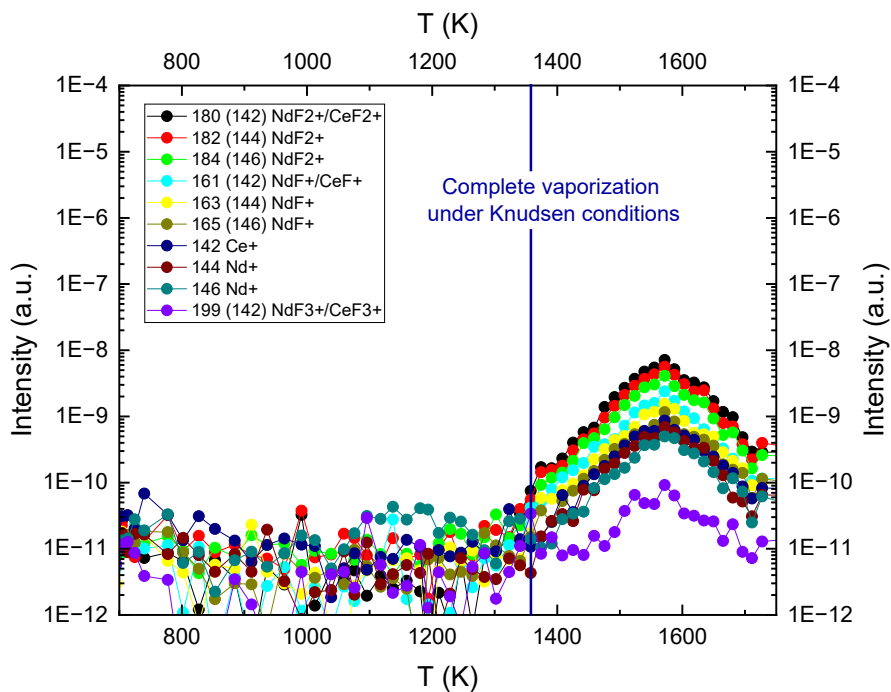


Figure 2.13.: Ion intensities of the neodymium (and cerium) species versus temperature obtained for the 93.0% LiF–ThF₄–UF₄ (77.5-19.5-3.0 mol%) + 7.0 mol% FP mix system. The main species recorded are: ¹⁴²Nd⁺ (¹⁴²Ce⁺), ¹⁴⁴Nd⁺, ¹⁴⁶Nd⁺, ¹⁶¹NdF⁺ (¹⁶¹CeF⁺), ¹⁶³NdF⁺, ¹⁶⁵NdF⁺, ¹⁸⁰NdF₂⁺ (¹⁸⁰CeF₂⁺), ¹⁸²NdF₂⁺, ¹⁸⁴NdF₂⁺ and ¹⁹⁹NdF₃⁺ (¹⁹⁹CeF₃⁺); the cerium and neodymium (142) species intensity are superposed. Only the intensities of the most predominant isotopes were considered in each case.

2.5. CONCLUSION

The experimental evaluation of fission product behavior in molten fuels such as LiF-ThF_4 and $\text{LiF-ThF}_4\text{-UF}_4$ showed insightful results for the Molten Salt Reactor (MSR) concept. Firstly, mass spectrometry measurements demonstrated the high retention of Rb and a very high retention of Sr, lanthanides (Nd, Ce), and Y in molten fluoride salts. Cesium, as noted by Beneš *et al.* [32], exhibited moderate retention as CsF , while CsI displayed low retention, leading to early vapor release and potential iodine recombination in the form of LiI . Zirconium showed comparable high volatility and limited retention in the fuel salt mixture. However, the present results did not allow to determine the exact speciation. Complementary measurements, especially of the dissociation patterns, would be required to gain more insight.

Secondly, from an engineering perspective, a crucial criterion is the limited overall impact on melting/solidification temperature and vapor pressure of the fuel. The addition of a significant amount of fission products decreased the measured melting temperature of the fuels by 21 K at eutectic compositions. The vapor pressure of fuel elements derived by KEMS on the same mixture remained almost unchanged compared to data measured in the literature on pure fuels.

These findings play an essential role for the safety assessment of the MSR, demonstrating the influence of fission product accumulation on the melting temperature and vapor pressure of the fuel. While limited variations in fuel vapor pressure are noticeable, some important fission products such as Cs, I and Zr, show rather moderate retention in the fuel matrix, under Knudsen conditions. The melting/solidification temperature of the simulated "irradiated" mixture decreases by about 21 K, which must be taken into account for the safety margin of the reactor operation.

ACKNOWLEDGMENTS

T. Dumaire acknowledges gratefully financial support from the Nuclear Research and Consultancy Group (NRG, Petten, Netherlands) and the SAMOSAFER project which has received funding from the Euratom research and training program 2014-2018 under grant agreement N°847527. The authors acknowledge P. Souček for the work on the synthesis of ThF_4 and UF_4 .

REFERENCES

- [1] T. Wiss, H. Matzke, V. V. Rondinella, T. Sonoda, W. Assmann, M. Toulemonde, and C. Trautmann. “Damage produced in magnesium aluminate spinel by high energy heavy ions including fission products of fission energy: microstructure modifications”. In: *Progress in Nuclear Energy* 38.3–4 (2001), pp. 281–286. ISSN: 0149-1970. DOI: 10.1016/s0149-1970(00)00118-9.
- [2] L. Yuanzhong and C. Jianzhu. “Fission product release and its environment impact for normal reactor operations and for relevant accidents”. In: *Nuclear Engineering and Design* 218.1–3 (Oct. 2002), pp. 81–90. ISSN: 0029-5493. DOI: 10.1016/s0029-5493(02)00200-5.
- [3] P. N. Haubenreich and J. R. Engel. “Experience with the Molten-Salt Reactor Experiment”. In: *Nuclear Applications and Technology* 8.2 (1970), pp. 118–136. DOI: 10.13182/nt8-2-118.
- [4] E. L. Compere, E. G. Bohlmann, S. S. Kirslis, F. F. Blankenship, and W. R. Grimes. *Fission product behavior in the Molten Salt Reactor Experiment. ORNL-4865*. ORNL-4865. Oak Ridge National Laboratory, 1975. DOI: 10.2172/4077644.
- [5] E. Capelli, O. Beneš, M. Beilmann, and R. J. M. Konings. “Thermodynamic investigation of the LiF–ThF₄ system”. en. In: *The Journal of Chemical Thermodynamics* 58 (2013), pp. 110–116. ISSN: 0021-9614. DOI: 10.1016/j.jct.2012.10.013.
- [6] E. Merle-Lucotte, M. Allibert, M. Brovchenko, D. Heuer, V. Ghetta, A. Laureau, and P. Rubiolo. “Introduction to the Physics of Thorium Molten Salt Fast Reactor (MSFR) Concepts”. In: *Thorium Energy for the World*. Springer International Publishing, 2016, pp. 223–231. ISBN: 9783319265421. DOI: 10.1007/978-3-319-26542-1_34.
- [7] SAMOSAFER consortium. *Severe Accident Modeling and Safety Assessment for Fluid-fuel Energy Reactors*. DOI: 10.3030/847527.
- [8] SAMOSAFER consortium. *SAMOSAFER project - WP 1 Safety requirements and Risk identification*. URL: <https://samosafer.eu/>.
- [9] E. Capelli, O. Beneš, J.-Y. Colle, and R. J. M. Konings. “Determination of the thermodynamic activities of LiF and ThF₄ in the Li_xTh_{1-x}F_{4-3x} liquid solution by Knudsen effusion mass spectrometry”. In: *Physical Chemistry Chemical Physics* 17.44 (2015), pp. 30110–30118. ISSN: 1463-9084. DOI: 10.1039/c5cp04777c.

- [10] A. Tosolin, O. Beneš, J.-Y. Colle, P. Souček, L. Luzzi, and R. Konings. “Vaporization behaviour of the Molten Salt Fast Reactor fuel: The LiF-ThF₄-UF₄ system”. In: *Journal of Nuclear Materials* 508 (Sept. 2018), pp. 319–328. ISSN: 0022-3115. DOI: 10.1016/j.jnucmat.2018.05.049.
- [11] M. B. Chadwick, M. Herman, P. Obložinský, M. E. Dunn, Y. Danon, A. C. Kahler, D. L. Smith, B. Pritychenko, G. Arbanas, R. Arcilla, R. Brewer, D. A. Brown, R. Capote, A. D. Carlson, Y. S. Cho, H. Derrien, K. Guber, G. M. Hale, S. Hoblit, S. Holloway, T. D. Johnson, T. Kawano, B. C. Kiedrowski, H. Kim, S. Kunieda, N. M. Larson, L. Leal, J. P. Lestone, R. C. Little, E. A. McCutchan, R. E. MacFarlane, M. MacInnes, C. M. Mattoon, R. D. McKnight, S. F. Mughabghab, G. P. A. Nobre, G. Palmiotti, A. Palumbo, M. T. Pigni, V. G. Pronyaev, R. O. Sayer, A. A. Sonzogni, N. C. Summers, P. Talou, I. J. Thompson, A. Trkov, R. L. Vogt, S. C. van der Marck, A. Wallner, M. C. White, D. Wiarda, and P. G. Young. “ENDF/B-VII.1 Nuclear Data for Science and Technology: Cross Sections, Covariances, Fission Product Yields and Decay Data”. In: *Nuclear Data Sheets* 112.12 (2011), pp. 2887–2996. DOI: 10.1016/j.nds.2011.11.002.
- [12] B. Hombourger, J. Křepel, and A. Pautz. “Breed-and-burn fuel cycle in molten salt reactors”. In: *EPJ Nuclear Sciences & Technologies* 5 (2019). Ed. by J. L. Kloosterman, E. Merle, and J. Ragusa, p. 15. DOI: 10.1051/epjn/2019026.
- [13] P. G. Lucuta, R. A. Verrall, H. Matzke, and B. J. Palmer. “Microstructural features of SIMFUEL — Simulated high-burnup UO₂-based nuclear fuel”. In: *Journal of Nuclear Materials* 178.1 (1991), pp. 48–60. ISSN: 0022-3115. DOI: 10.1016/0022-3115(91)90455-G.
- [14] S. Anderson, E. Auffray, T. Aziz, S. Baccaro, S. Banerjee, P. Bareyre, L. Barone, B. Borgia, D. Boutet, J. Burq, M. Chemarin, R. Chipaux, I. Dafinei, P. D’Atanasio, F. De Notaristefani, B. Dezillie, C. Dujardin, S. Dutta, J. Faure, J. Fay, D. Ferrère, O. Francescangeli, B. Fuchs, S. Ganguli, G. Gillespie, M. Goyot, S. Gupta, A. Gurtu, J. Heck, A. Hervé, H. Hillemanns, F. Holdener, B. Ille, L. Jönsson, J. Kierstead, W. Krenz, W. Kway, J. Le Goff, M. Lebeau, P. Lebrun, P. Lecoq, Y. Lemoigne, G. Loomis, K. Lubelsmeyer, N. Madjar, G. Majni, H. El Mamouni, S. Mangla, J. Mares, J. Martin, M. Mattioli, G. Mauger, K. Mazumdar, P. Mengucci, J. Merlo, B. Moine, N. Nikl, J. Pansart, C. Pedrini, J. Poinsignon, K. Polak, R. Raghavan, P. Rebourgeard, D. Rinaldi, J. Rosa, A. Rosowsky, P. Sahuc, V. Samsonov, S. Sarkar, V. Schegelski, D. Schmitz, M. Schneegans, D. Seliverstov, S. Stoll, K. Sudhakar, A. Svensson, S. Tonwar, V. Topa, J. Vialle, M. Vivargent, W. Wallraff, M. Weber, N. Winter, C. Woody, C. Wuest, and V. Yanovski. “Further results on cerium fluoride crystals”. In: *Nuclear Instruments and Methods in Physics Research Section A: Accelerators, Spectrometers, Detectors and Associated Equipment* 332.3 (Aug. 1993), pp. 373–394. ISSN: 0168-9002. DOI: 10.1016/0168-9002(93)90296-t.
- [15] R. E. Thoma, H. Insley, H. A. Friedman, and G. M. Hebert. “Condensed System LiF-NaF-ZrF₄ Phase Equilibria and Crystallographic Data.” In: *Journal of Chemical and Engineering Data* 10.3 (1965), pp. 219–230.

- [16] C. Liao, Z. Fu, L. Que, H. Tang, and X. Wang. “Experimental determination and thermodynamic optimization of the LiF-NdF₃ system”. In: *RSC Advances* 13.35 (2023), pp. 24174–24180. ISSN: 2046-2069. DOI: 10.1039/d3ra03003b.
- [17] B. Porter and E. A. Brown. “Melting Points of Inorganic Fluorides”. In: *Journal of the American Ceramic Society* 45.1 (1962), pp. 49–49. ISSN: 1551-2916. DOI: 10.1111/j.1151-2916.1962.tb11031.x.
- [18] B. Voronin and S. Volkov. “Ionic conductivity of fluorite type crystals CaF₂, SrF₂, BaF₂, and SrCl₂ at high temperatures”. In: *Journal of Physics and Chemistry of Solids* 62.7 (2001), pp. 1349–1358. ISSN: 0022-3697. DOI: 10.1016/s0022-3697(01)00036-1.
- [19] I. Barin. *Thermochemical Data of Pure Substances*. Ed. by Wiley. Wiley, 1995, p. 1368. ISBN: 9783527619825. DOI: 10.1002/9783527619825.ch12o.
- [20] A. F. Holleman and N. Wiberg. *Nebengruppenelemente, Lanthanoide, Actinoide, Transactinoide*. De Gruyter, 2017. ISBN: 9783110495904. DOI: 10.1515/9783110495904.
- [21] R. E. Thoma, C. F. Weaver, H. A. Friedman, H. Insley, L. A. Harris, and H. A. Yakel Jr. “Phase equilibria in the system LiF—YF₃”. In: *The Journal of Physical Chemistry* 65.7 (1961), pp. 1096–1099.
- [22] P. Souček, O. Beneš, B. Claux, E. Capelli, M. Ougier, V. Tyrpekl, J.-F. Vigier, and R. J. Konings. “Synthesis of UF₄ and ThF₄ by HF gas fluorination and re-determination of the UF₄ melting point”. In: *Journal of Fluorine Chemistry* 200 (2017), pp. 33–40. DOI: 10.1016/j.jfluchem.2017.05.011.
- [23] L. B. McCusker, R. B. V. Dreele, D. E. Cox, D. Louër, and P. Scardi. “Rietveld refinement guidelines”. In: *Journal of Applied Crystallography* 32.1 (1999), pp. 36–50. DOI: 10.1107/s0021889898009856.
- [24] J. Rodriguez-Carvajal. “Recent advances in magnetic structure determination by neutron powder diffraction”. In: *Physica B: Condensed Matter* 192.1-2 (1993), pp. 55–69.
- [25] W. J. Boettinger, U. R. Kattner, K.-W. Moon, and J. H. Perepezko. *NIST recommended practice guide: DTA and Heat-flux DSC Measurements of Alloy Melting and Freezing*. Ed. by N. I. of Standards and Technology. U.S. Government Printing Office, 2006. DOI: 10.6028/nbs.sp.960-15.
- [26] O. Beneš, R. J. M. Konings, S. Wurzer, M. Sierig, and A. Dockendorf. “A DSC study of the NaNO₃–KNO₃ system using an innovative encapsulation technique”. In: *Thermochimica Acta* 509.1-2 (2010), pp. 62–66. DOI: 10.1016/j.tca.2010.06.003.
- [27] J.-Y. Colle, D. Freis, O. Beneš, and R. J. M. Konings. “Knudsen Effusion Mass Spectrometry of Nuclear Materials: Applications and Developments”. In: *ECS Transactions* 46.1 (May 2013), pp. 23–38. ISSN: 1938-6737. DOI: 10.1149/04601.0023ecst.

- [28] D. Manara, A. Seibert, T. Gouder, O. Beneš, L. Martel, J.-Y. Colle, J.-C. Griveau, O. Walter, A. Cambriani, O. Dieste Blanco, D. Staicu, T. Wiss, and J.-F. Vigier. “Experimental methods”. In: *Advances in Nuclear Fuel Chemistry*. Elsevier, 2020, pp. 89–158. DOI: 10.1016/b978-0-08-102571-0.00003-3.
- [29] N. Vozárová, A. L. Smith, J.-Y. Colle, P. E. Raison, D. Bouëxière, R. J. M. Konings, and O. Beneš. “Thermodynamic determination and assessment of the CsF-ThF₄ system”. In: *The Journal of Chemical Thermodynamics* 114 (Nov. 2017), pp. 71–82. ISSN: 0021-9614. DOI: 10.1016/j.jct.2017.05.008.
- [30] J. Drowart and P. Goldfinger. “Investigation of Inorganic Systems at High Temperature by Mass Spectrometry”. In: *Angewandte Chemie International Edition in English* 6.7 (July 1967), pp. 581–596. ISSN: 0570-0833. DOI: 10.1002/anie.196705811.
- [31] J. Drowart, C. Chatillon, J. Hastie, and D. Bonnell. “High-temperature mass spectrometry: Instrumental techniques, ionization cross-sections, pressure measurements, and thermodynamic data (IUPAC Technical Report)”. In: *Pure and Applied Chemistry* 77.4 (Jan. 2005), pp. 683–737. ISSN: 0033-4545. DOI: 10.1351/pac200577040683.
- [32] O. Beneš, E. Capelli, N. Morelová, J.-Y. Colle, A. Tosolin, T. Wiss, B. Cremer, and R. J. M. Konings. “Cesium and iodine release from fluoride-based molten salt reactor fuel”. In: *Physical Chemistry Chemical Physics* 23.15 (2021), pp. 9512–9523. DOI: 10.1039/d0cp05794k.
- [33] E. Capelli, O. Beneš, and R. J. M. Konings. “Thermodynamics of soluble fission products cesium and iodine in the Molten Salt Reactor”. In: *Journal of Nuclear Materials* 501 (Apr. 2018), pp. 238–252. DOI: 10.1016/j.jnucmat.2018.01.024.
- [34] K. A. Sense and R. W. Stone. “Vapor Pressure and Molecular Composition of Vapors of the RbF-ZrF₄ and LiF-ZrF₄ Systems”. In: *The Journal of Physical Chemistry* 62.11 (1958), pp. 1411–1418.

3

THERMODYNAMIC ASSESSMENT OF THE LiF-BaF₂-ZrF₄ SYSTEM

Lithium-based fluoride salts are one of the leading options as fuel matrix in Molten Salt Reactors. The understanding of their thermodynamic behavior, e.g. chemical stability, activity, as well as heat transfer properties, in the reactor's environment is crucial for the safety assessment. In this work, the chemical equilibria of lithium fluoride with two important fission products dissolved in the salt matrix, namely barium fluoride and zirconium fluoride, are considered. The phase diagrams of the binary systems LiF-BaF₂, LiF-ZrF₄ and BaF₂-ZrF₄, as well as the ternary system LiF-BaF₂-ZrF₄ are assessed by the CALPHAD (CALculation of PHase Diagram) method using the quasichemical model in the quadruplet approximation for the liquid solution. These models are based on literature and new experimental data, and provide a good overview of the stability of intermediate compounds formed in the various systems and of the liquid solution.

3.1. INTRODUCTION

MOLTEN Salt Reactors (MSRs) offer a promising alternative to conventional nuclear power plants due to their potential for improved safety, fuel utilization, and waste management [1]. Lithium-based fluoride salts, for instance ⁷LiF-ThF₄-UF₄(-UF₃) [2], or the so-called FLiNaK (LiF-NaF-KF: 46.5-11.5-42 mol%) salt with dissolved AnF₄(-AnF₃) (An = actinide) [3], are leading candidates for use as a coolant and fuel carrier in MSRs, and have been characterized quite extensively already [4, 5]. The composition of the fuel salt changes continuously in the reactor core due to the fission process, introducing new species that can be dissolved, form metallic precipitates, or form gaseous species [6, 7]. By contrast with the base fuel salt, the knowledge on the thermodynamic properties and phase equilibria of the fission products in equilibrium with the fuel salt in the fuel salt is still limited, although information on irradiated fuel salt behavior is key for the design and optimization of MSRs.

Understanding the thermodynamics and phase behavior of the salt mixture in

general is crucial for the safe and efficient operation of the new generation of molten salt reactors. The phase diagram of the salt mixture can be used to predict the formation of different phases, such as solid precipitates or gas phases, which can have a significant impact on the performance of the reactor. The thermodynamic modeling of the complex irradiated salt system allows to identify potential issues, such as corrosion or clogging related to metallic precipitates formation, and is a perfect tool to develop strategies to minimize their impact. It can allow to anticipate equilibria in a complex fluid and to assess the risk of environmental impact in the event of accidental release.

As LiF is the main component of the fuel, it is essential to know how it interacts with the different compounds encountered in the reactor. Phase equilibria with actinides, such as ThF₄, UF₄ and PuF₃, composing the fresh fuels, have received particular attention in the literature [3, 8, 9]. Nowadays, the evolution of the fuel salt's composition and the possible change of its properties as a function of the burnup (residence time), with the addition of fission products [10], and corrosion products [11, 12], is an important milestone to assess the safety of the MSR technology.

Barium is a major fission product that is produced during the nuclear power generation process. It is a highly reactive element that can potentially form compounds with other chemical elements from the fuel salt leading to a complex fuel chemistry. Zirconium is also a main fission product which can significantly contribute to the source term in an accidental scenario with release to the environment. ZrF₄ is particularly volatile in the liquid state and can easily vaporize. Furthermore, when zirconium dissolves in the fluoride matrix [6, 13], it can also associate with other fission products, leading to the formation of multiple stable solid intermediate compounds, in association with for instance barium.

The most comprehensive experimental exploration of molten salt-fueled reactors in operation was carried out at the Oak Ridge National Laboratory, during the MSRE (Molten Salt Reactor Experiment). According to their measurements on various samples taken from a fully operating (up to 9000 hours) lithium-fueled reactor with ²³⁵U, fission yields for the isotope ¹⁴⁰Ba were 5.43% and 6.01% for ⁹⁵Zr, respectively [14]. Based on their empirical observations, BaF₂ and ZrF₄ stable were soluble and were not removed during fuel reprocessing. Their presence in the salt matrix did not appear to interfere with the fission reaction. However, the dissolution of barium and zirconium in the fuel salt will affect its properties, and the formation of barium and zirconium compounds could become problematic if this occurs during reactor operation. These radioisotopes could also contribute to the release of harmful radioactive material into the environment in an accidental scenario [15]. Knowing how these fission products behave in the reactor core is therefore crucial for the safety assessment.

In this work, the experimental phase diagram data on the binary system LiF-BaF₂ were updated to resolve discrepancies found in the literature. Then, phase diagrams of LiF-BaF₂, LiF-ZrF₄ and BaF₂-ZrF₄ were modeled using the quasichemical model in the quadruplet approximation for the liquid solution, based on collected and literature data. Finally the assessments of the binaries were used to extrapolate and

optimize the ternary system $\text{LiF}-\text{BaF}_2-\text{ZrF}_4$ based on mixing enthalpy data from the literature.

3.2. EXPERIMENTAL METHODS

3.2.1. SAMPLE PREPARATION

All experiments were performed in a glovebox with argon atmosphere, where O_2 and H_2O levels were maintained below 5 ppm. The starting materials were provided by Alfa Aesar: lithium (1+) fluoride LiF (99.99%), barium (2+) difluoride BaF_2 (99.998%) and zirconium (4+) tetrafluoride ZrF_4 (99.9%). The powders were preliminary dried for 8 hours at 500 K under argon atmosphere.

Table 3.1.: Purity and providers of the chemicals used in this work.

Compound	Provider	Purity
LiF powder	Alfa Aesar	99.99% (metal basis)
BaF_2 powder	Alfa Aesar	99.998% (metal basis)
ZrF_4 powder	Alfa Aesar	99.9% (metal basis)

LiBaF_3 was the only intermediate compound synthesized in this work. The synthesis was done by the solid state method from a stoichiometric mixture of LiF and BaF_2 powders. The pure end-members were thoroughly blended in an agate mortar, and placed in a hermetically closed stainless steel container inside a nickel liner, then heated in a ceramic tubular furnace under argon flow for 8 hours at 1093 K. The set heating and cooling rates were 5 K min^{-1} following the recommendation of Mishra *et al.* [16].

3.2.2. X-RAY DIFFRACTION

The purity of the pure salts (e.g. LiF , BaF_2 , ZrF_4) used as starting materials for the phase diagram measurements and synthesis of intermediate compounds, was checked using X-Ray Diffraction (XRD) at room temperature ($T = 293 \pm 2 \text{ K}$), using a PANalytical X'Pert PRO X-Ray diffractometer with a Cu anode (0.4 x 12 mm line focus, 45 kV, 40 mA). Samples were homogeneously distributed on a sample holder, closed under argon atmosphere with a Kapton[®] foil. X-ray data were collected by step scanning in the range $10^\circ < 2\theta < 120^\circ$ in a Bragg-Brentano configuration. The X-ray scattered intensities were measured with a Real Time Multi Strip (RTMS) detector (X'Celerator). The purities of each powder salt was analyzed by Rietveld refinement method using the FullProf suite software [17, 18], and no secondary phases were detected.

3.2.3. DIFFERENTIAL SCANNING CALORIMETRY

3D-heat flow measurements were conducted on the Setaram Multi Detector HTC module of the 96 line calorimeter. Every measurement consisted of at least four

consecutive heating cycles with 5 or 10 K min⁻¹ heating rates and cooling rates of the same order. The transition temperature data were collected from the heat flow signals obtained on the heating ramps. All transition temperatures were extracted from the onset of the corresponding endothermic heat flow signal, except for the liquidus transition temperature that was taken from the maximum of the corresponding peak according to the NIST recommendations [19]. A correction was applied on the collected temperature data using a calibration equation determined with pure metals (In, Pb, Al, Ag, Au), to correct for the effects of the heating rate and apparatus geometry. The uncertainties on the reported temperatures is estimated ± 5 K for pure compounds, and ± 10 K for mixtures. The data collected in this work for the LiF-BaF₂, LiF-ZrF₄ and LiF-BaF₂-ZrF₄ systems are listed in Table 3.6 and in the corresponding phase diagram figures.

For the DSC measurements, the samples were prepared from the end-member powders, intimately mixed at the desired molar composition and inserted inside a pure nickel liner. The liners were hermetically closed in a stainless steel encasing designed according to the concept developed at the Joint Research Centre - Karlsruhe [20], limiting the vapor releases during the heating.

3.3. THERMODYNAMIC MODELING

The thermodynamic models reported herein were developed using the FactSage software version 8.2 [21], and are based on the CALPHAD (CALculation of PHase Diagrams) method [22, 23]. The optimization of the different parameters of the Gibbs energy functions for all phases present in the systems was based on available phase diagram and mixing enthalpy data. These were collected from different experimental studies [24–30], and in this work, and were correlated with the computed phase diagrams.

3.3.1. GIBBS ENERGIES OF PURE COMPOUNDS

The Gibbs energy of pure compounds is expressed by:

$$G(T) = \Delta_f H_m^o(298.15) - S_m^o(298.15) \cdot T + \int_{298.15}^T C_{p,m}(T) dT - T \int_{298.15}^T \frac{C_{p,m}}{T} dT \quad (3.1)$$

where $\Delta_f H_m^o(298.15)$ is the standard enthalpy of formation, and $S_m^o(298.15)$ is the standard entropy of the pure compound at standard pressure and reference temperature 298.15 K. $C_{p,m}$ is the heat capacity expressed as a function of the temperature T.

3.3.2. SELECTED THERMODYNAMIC DATA

Thermodynamic data for lithium fluoride were taken from the Joint Research Centre Molten Salt Database (JRCMSD) which are from the NIST-JANAF recommendation [5, 31, 32]. The latter was also the source for BaF₂ thermodynamic functions [5, 33]. BaF₂ shows two phase transitions before melting. The transition between the α phase and the β phase at T = 1240 K is reported to be a second order

transition, while the transition from the β phase to the γ phase at $T = 1480$ K is of first order. The thermodynamic functions for ZrF_4 were taken from the SGTE database [34]. Several intermediate phases were reported in the literature for the binary LiF-BaF₂, LiF-ZrF₄, and BaF₂-ZrF₄ systems. The known and confirmed stoichiometries and crystal structures are listed in Table 3.2. For the intermediate compounds selected in this work for the modelling, the thermodynamic properties (enthalpy of formation, standard entropy and heat capacity) were not reported in existing literature. Therefore, the Neumann-Kopp rule was used to estimate the heat capacities [35]. Enthalpies of formation and standard entropies were first approximated from the stoichiometric sum of the pure end-member compounds, and then optimized during the modeling to fit the available phase diagram data. The optimized entropies were kept close to the additive approximation, since the entropies of formation of the intermediates compounds from the end-members (LiF, BaF₂ and ZrF₄) are expected to be relatively small.

The thermodynamic data of all compounds used and optimized in this work are listed in Table 3.3.

Table 3.2.: Reported intermediate compounds and crystal structures in the LiF-BaF₂-ZrF₄ system. Note that high pressure phases have not been included.

Compound	Crystal symmetry	Space group	Reference
LiBaF ₃	cubic	$Pm\bar{3}m$ (221)	[36]
Li ₂ ZrF ₆	trigonal	$P\bar{3}1m$ (162)	[37]
Li ₄ ZrF ₈	orthorhombic	$Pnma$ (62)	[38]
Li ₃ Zr ₄ F ₁₉	triclinic	$P\bar{1}$ (2)	[38]
Ba ₃ ZrF ₁₀	orthorhombic	$Cmcm$ (63)	[39]
Ba ₂ ZrF ₈	orthorhombic	$Pnma$ (62)	[40]
α -BaZrF ₆	monoclinic	$P2_1/c$ (14)	[41]
β -BaZrF ₆	orthorhombic	$Cmme$ (67)	[42]
α -BaZr ₂ F ₁₀	monoclinic	$P\bar{1}$ (2)	[43]
β -BaZr ₂ F ₁₀	monoclinic	$C2/c$ (15)	[44]

3.3.3. SOLID SOLUTION MODELING

A solid solution was observed in the BaF₂-ZrF₄ system between the compositions $X(ZrF_4) = 0.35$ and $X(ZrF_4) = 0.375$ (Figure 3.6). Defined as $Ba_{2+x}Zr_{1-x}F_{8+2x}$, this intermediate compound with homogeneity range was identified by Ratnikova *et al.* [46] and then by Grande *et al.* [29], as detailed below in section 3.4.3. The existence of this solid solution was finally experimentally confirmed by Babitsyna *et al.* using a water-quenching melt method [47, 48]. A one lattice polynomial model was used to describe the solid solution with Ba₂ZrF₈ and BaZrF₆ end-members. The Gibbs energy function $G(T)$ of the solid solution is described by the equation:

$$G(T) = (X_{Ba_2ZrF_8} \cdot G_{m,Ba_2ZrF_8}^o + X_{BaZrF_6} \cdot G_{m,BaZrF_6}^o) - T\Delta S^{ideal} + \Delta G_m^{xs} \quad (3.2)$$

Table 3.3.: Thermodynamic data for end-members and intermediate compound used in this work for the thermodynamic model. Standard enthalpy of formation $\Delta_f H_m^\circ$ (298.15 K), standard entropy S_m° (298.15 K) and heat capacity coefficient of pure compounds $C_{p,m}(T/K)/(J \cdot K^{-1} \cdot \text{mol}^{-1}) = a + b \cdot T + c \cdot T^2 + d \cdot T^{-2}$. Values optimized in this work in the thermodynamic modelling assessment are marked in bold.

Compound	$\Delta_f H_m^\circ$ (298.15 K) (kJ·mol ⁻¹)	S_m° (298.15 K) (J·K ⁻¹ ·mol ⁻¹)	$C_{p,m}(T/K)/(J \cdot K^{-1} \cdot \text{mol}^{-1}) = a + b \cdot T + c \cdot T^2 + d \cdot T^{-2}$	T(K)	Ref.			
LiF ^(cr)	-516.931	35.66	43.30898	0.016312168	5.0470398·10 ⁻⁷	-569123.6	298.15-2500	[33]
LiF ^(l)	-598.654	42.96	64.183	-	-	-	298.15-6000	[33]
LiF ^(g)	-340.946	200.08	35.397917	1.870664·10 ⁻³	-1.654306·10 ⁻⁷	-	298.15-6000	[33]
Li ₂ F ₂ ^(g)	-942.781	258.52	60.80524	5.13678·10 ⁻²	-3.433579·10 ⁻⁵	-882301	298.15-600	[33]
			82.55869	3.852765·10 ⁻⁴	-6.715069·10 ⁻⁸	-2142689	600-3100	[33]
			83.05533	2.587352·10 ⁻⁵	-2.112209·10 ⁻⁹	-2215248	3100-6000	[33]
			97.43992	8.075246·10 ⁻²	-5.345478·10 ⁻⁵	-1266154	298.15-600	[33]
Li ₃ F ₃ ^(g)	-1517.202	317.97	131.0814	1.723168·10 ⁻³	-4.214711·10 ⁻⁷	-3179819	600-2000	[33]
			132.9855	1.516407·10 ⁻⁵	-1.454542·10 ⁻⁹	-3852585	2000-6000	[33]
α -BaF ₂ ^(cr)	-1208.758	96.399	510.809	-0.7551455	0.0003813337	-42423270	700-1100	[33]
			30262.42	-36.20693	0.0122619	-6249891000	1100-1240	[33]
			444.9684	-0.236396	-	-	1240-1481	[33]
			107.6543	-	-	-	1481-1641	[33]
β -BaF ₂ ^(cr) ^a	-1182.7251	112.440	99.82606	-	-	-	1641-3500	[33]
γ -BaF ₂ ^(cr) ^b	-803.7464	301.186	57.28314	1.299299·10 ⁻³	-4.94381·10 ⁻⁷	-341665.4	298.15-1400	[33]
BaF ₂ ^(g)	-1911.300	104.6	58.20781	-2.102083·10 ⁻⁶	1.858868·10 ⁻¹⁰	-475260.6	1400-6000	[33]
ZrF ₄ ^(cr)	-1850.300	156.16	81.64412	0.08062462	-1.957282·10 ⁻⁵	-21580.19	298.15-1183	[34, 45]
ZrF ₄ ^(l)	-1669.506	322.77	150	-	-	-	1183-2000	[34, 45]
			93.77765	2.462543·10 ⁻²	-1.198783·10 ⁻⁵	-1112192	298.15-900	[34, 45]
			107.9627	5.26574·10 ⁻⁵	-5.370488·10 ⁻⁹	-2544208	900-6000	[34, 45]
LiBaF ₃ ^(cr)	-1829.689	132.1	127.73698	0.002998968	1.872487·10⁻⁵	-881770	298.15-6000	this work (model) ^c
Li ₂ ZrF ₆ ^(cr)	-3184.500	170.0	202.231	0.053124	1.01·10⁻⁶	-2738757	298.15-2500	this work (model) ^c
Li ₃ ZrF ₉ ^(cr)	-4419.800	241.3	288.8489	0.085749	2.02·10⁻⁶	-3877004	298.15-2500	this work (model) ^c
Li ₃ Zr ₄ F ₁₉ ^(cr)	-9558.500	515.0	592.3789	0.130937	1.51·10⁻⁶	-8109411	298.15-2500	this work (model) ^c
Li ₃ ZrF ₇ ^(cr)	-3755.050	270.0	245.53994	0.069436504	1.514111·10⁻⁶	-3307880.8	298.15-2500	this work (model) ^c
α -BaZrF ₆ ^(cr)	-3158.090	215.0	166.07212	0.06731142	-8.4795·10⁻⁷	-903350.19	298.15-817.15	this work (model) ^c
β -BaZrF ₆ ^(cr)	-3153.090	215.0	1166.07212	0.06731142	-8.4795·10⁻⁷	-903350.19	298.15-817.15	this work (model) ^c
Ba ₂ ZrF ₆ ^(cr)	-4396.567	311.5	250.50012	0.05399822	1.787692·10⁻⁵	-178120.19	298.15-6000	this work (model) ^c
Ba ₃ ZrF ₁₀ ^(cr)	-5635.500	392.5	334.92812	0.04068502	3.660179·10⁻⁵	-2666890.19	298.15-6000	this work (model) ^c
α -BaZr ₂ F ₁₀ ^(cr)	-5056.700	345.0	247.71624	0.14793604	2.042077·10⁻⁵	-924930.38	298.15-796.15	this work (model) ^c
β -BaZr ₂ F ₁₀ ^(cr)	-5053.700	345.0	247.71624	0.14793604	2.042077·10⁻⁵	-924930.38	796.15-6000	this work (model) ^c

^a $\alpha \leftrightarrow \beta$ second order transition at 1240 K, $\Delta H_T(T_{tr}) = 0 \text{ kJ} \cdot \text{mol}^{-1}$

^b $\beta \leftrightarrow \gamma$ first order transition at 1480 K, $\Delta H_T(T_{tr}) = 2.6736 \text{ kJ} \cdot \text{mol}^{-1}$

^c Heat capacity obtained using the Neumann-Kopp approximation [35].

with,

$$\Delta S^{ideal} = -R(X_{Ba_2ZrF_8} \ln X_{Ba_2ZrF_8} + X_{BaZrF_6} \ln X_{BaZrF_6}) \quad (3.3)$$

where $G_{m,Ba_2ZrF_8}^0$ and $G_{m,BaZrF_6}^0$ are the molar Gibbs energies of the pure end-members with Ba_2ZrF_8 and $BaZrF_6$ stoichiometries, respectively, $X_{Ba_2ZrF_8}$ and X_{BaZrF_6} the molar fractions of the end-members, R the universal gas constant and ΔG^{xs} is the excess Gibbs energy. The excess Gibbs energy is expressed by:

$$\Delta G_m^{xs} = \sum_{i,j} X_A^i \cdot X_B^j \cdot q^{i,j} \quad (3.4)$$

where A and B represent Ba_2ZrF_8 and $BaZrF_6$, respectively, and $q_{i,j}$ is an interaction coefficient which can depend on temperature T described by the equation:

$$q_{A,B}^{i,j} = \alpha + \beta T \quad (3.5)$$

The optimized excess energy parameters are given by the following equation:

$$G_{(Ba_2ZrF_8, BaZrF_6)}^{xs} = X_{Ba_2ZrF_8} \cdot X_{BaZrF_6} \cdot 2000 \text{ J mol}^{-1} \quad (3.6)$$

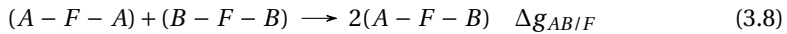
In addition, to allow the formation of a solid solution around the Ba_2ZrF_8 composition in the phase diagram that does not extend fully towards $BaZrF_6$, the Gibbs energy of the $BaZrF_6$ end-member of the solid solution had to be destabilized according to:

$$G_{BaZrF_6}(ss) = G_{BaZrF_6} + 4000 \text{ J mol}^{-1} \quad (3.7)$$

3.3.4. LIQUID SOLUTIONS MODELING FOR BINARY SYSTEMS

The liquid solutions were described by the modified quasichemical model in the quadruplet approximation [49, 50], where the quadruplet could be represented as two anions and two cations symmetrically disposed around an axis. Two atomic interactions are considered, the First Nearest Neighbor (FNN) interaction which describes the interaction cation - anion, and the Second Nearest Neighbor (SNN) interaction which describes the interactions between the two closest ions in the same sublattice. This model, which is particularly well-adapted to describe ionic liquids, allows to choose the composition of maximum short-range ordering in a binary system thanks to the variation of the ratio between the cation-cation coordination numbers $Z_{AB/FF}^A$ and $Z_{AB/FF}^B$. The short-range ordering is defined by the quadruplet approximation and includes the SNN interactions between each cation and each anion.

In a simple representation where A and B are two cations and F, the anion, the following reaction is obtained:



where $\Delta g_{AB/F}$ is the parameter of the Gibbs energy change associated with the SNN exchange reaction described as:

$$\Delta g_{AB/F} = \Delta g_{AB/F}^0 + \sum_{i \geq 1} g_{AB/F}^{i0} \chi_{AB/F}^i + \sum_{j \geq 1} g_{AB/F}^{0j} \chi_{BA/F}^j \quad (3.9)$$

where $\Delta g_{AB/FF}^0$ and $g_{AB/FF}^{ij}$ are possibly dependent on temperature, but independent of composition, and optimized to fit as best as possible the experimental data available on a given system. The dependence on composition is given by the term $\chi_{AB/FF}$ defined as:

$$\chi_{AB/FF} = \frac{X_{AA}}{X_{AA} + X_{AB} + X_{BB}} \quad (3.10)$$

where X_{AA} , X_{AB} and X_{BB} represent the different cation-cation pair fractions. To maintain electro-neutrality in the system, the anion-anion coordination should be determined. The following equation is applied after the selection of cation-cation coordination numbers:

$$\frac{q_A}{Z_{AB/FF}^A} + \frac{q_B}{Z_{AB/FF}^B} = 2 \cdot \frac{q_F}{Z_{AB/FF}^F} \quad (3.11)$$

with q_i representing the charges of the different ions and $Z_{AB/FF}^F$ is the anion-anion coordination number. These choices are based on the optimization of the systems in order to get the maximum short range ordering and highest excess Gibbs energy at a composition usually around the lowest eutectic in the phase diagram. The coordination numbers selected in this work are listed in Table 3.4.

Table 3.4.: Coordination numbers of the liquid solution used in this work.

A	B	$Z_{AB/FF}^A$	$Z_{AB/FF}^B$	$Z_{AB/FF}^F$
Li ⁺	Li ⁺	6	6	6
Ba ²⁺	Ba ²⁺	6	6	3
Zr ⁴⁺	Zr ⁴⁺	6	6	1.5
Li ⁺	Ba ²⁺	2	6	2.4
Li ⁺	Zr ⁴⁺	2	6	1.71
Ba ²⁺	Zr ⁴⁺	4	6	1.71

The optimized excess Gibbs energy of the liquid solutions obtained during the modeling of the binary systems determined in this work are given by the following equations:

$$\Delta g_{LiBa/FF} = -1900 + 2T - 1500\chi_{LiBa/FF} + (-6500 + 4.3T)\chi_{BaLi/FF} \quad \text{J mol}^{-1} \quad (3.12)$$

$$\begin{aligned} \Delta g_{LiZr/FF} = & -26000 + 3T + (-5500 + 2.2T)\chi_{LiZr/FF} \\ & + (-22000 - 4.9T)\chi_{ZrLi/FF} + (7000 + 23T)\chi_{ZrLi/FF}^2 \quad \text{J mol}^{-1} \end{aligned} \quad (3.13)$$

$$\Delta g_{BaZr/FF} = -30400 - (25000 + 15T)\chi_{ZrBa/FF} + 3000\chi_{BaZr/FF}^2 \quad \text{J mol}^{-1} \quad (3.14)$$

3.3.5. LIQUID SOLUTION FOR THE TERNARY SYSTEM

For the LiF–BaF₂–ZrF₄ system, the ternary diagram was modeled from the binary sub-systems LiF–BaF₂, LiF–ZrF₄ and BaF₂–ZrF₄ described above using the Kohler/Toop interpolation [51], where the latter is an asymmetric interpolation model of two groups of symmetry: the monovalent group of LiF considered as dissociated ionic liquid, and bivalent BaF₂ plus tetravalent ZrF₄ more likely to form molecular and oligomer species in the melt. Optimization of the ternary excess parameters was based on the only data available for the ternary system, from Hatem *et al.* [30, 52]. These authors measured the mixing enthalpy on different pseudobinary sections of the ternary system and were the base for the optimization (Section 3.4.4). More detail will be given in the next section. The ternary excess parameter optimized for the system LiF–BaF₂–ZrF₄ is given below:

$$\Delta g_{LiBa(Zr)/FF}^{011} = -90000 \text{ J mol}^{-1} \quad (3.15)$$

3.3.6. GAS PHASE

The gas phase is described by an ideal mixture of (LiF, Li₂F₂, Li₃F₃, BaF₂, and ZrF₄) gaseous species. The Gibbs energy is expressed by:

$$G^g = \sum_i y_i {}^0G_i^g + RT \sum_i y_i \ln y_i + RT \ln P/P^0 \quad (3.16)$$

where y_i is the fraction of the species i in the gas phase, ${}^0G_i^g$ the standard Gibbs energy of the gaseous species i , and P^0 the standard pressure. The functions for the gaseous species are listed in Table 3.3. To the best of our knowledge, only vapour pressure studies in the LiF–ZrF₄ binary system have been reported in the literature [53, 54]. Sense and Stone suggested the existence of the LiZr₂F₉ gaseous molecule above the LiF–ZrF₄ binary mixture. In the absence of structural and thermodynamic data for the latter species, it was not included in the present assessment. A comprehensive assessment of the vapour pressures in the LiF–BaF₂–ZrF₄ system is out of the scope of the present study, as it would require complementary experimental investigations.

3.4. RESULTS AND DISCUSSIONS

3.4.1. LiF–BaF₂

Phase diagram data were measured on this system by thermal analysis measurement techniques by Bergman and Banashek [24], Boukhalova [55], Taniuchi *et al.* [56], and Agulyanskii and Bessanova [25]. In the works of [24, 25, 55], the melting temperature of pure BaF₂ was measured at 1553 K, at odds with the temperature selected by the NIST-JANAF tables [33], (1641 ± 2) K (selected for the present assessment). The agreement between the four studies is generally good, as seen from Figure 3.2, although the data of Boukhalova [55] and Agulyanskii and Bessanova [25] show some discrepancy with results obtained in this work and in the other two studies, and are thus considered less reliable. The data reported by Taniuchi *et al.* [56] and Bergman

and Banashek [24] are consistent with respect to the eutectic transition temperature and composition. The experimental data measured in this work (Table 3.6), have enabled the determination of the peritectic decomposition temperature of LiBaF₃, and liquidus curve in greater detail at high BaF₂ concentrations (from $X_{\text{BaF}_2} = 0.6$ to 1), with a trend that is consistent with the selected reference value for the melting temperature of the BaF₂ end-member. Although the melting temperature of pure BaF₂ could not be measured with the equipment used in this work, it is in line with the measured trend of the liquidus temperatures at high BaF₂ concentrations.

The peritectic decomposition at the stoichiometric composition LiBaF₃ was measured on the synthesized sample (see Section 3.2.1). The XRD measurement conducted on the sample confirmed a cubic antiperovskite ($Pm\bar{3}m(221)$) crystal structure [36] (see Table 3.2), and the product's purity was found to be $(99.7 \pm 0.2)\%$ (with BaF₂ impurities) by Rietveld refinement (Figure 3.1) [17]. The experimental results are listed in Table 3.6 and the invariant equilibria in the phase diagram are listed in Table 3.5.

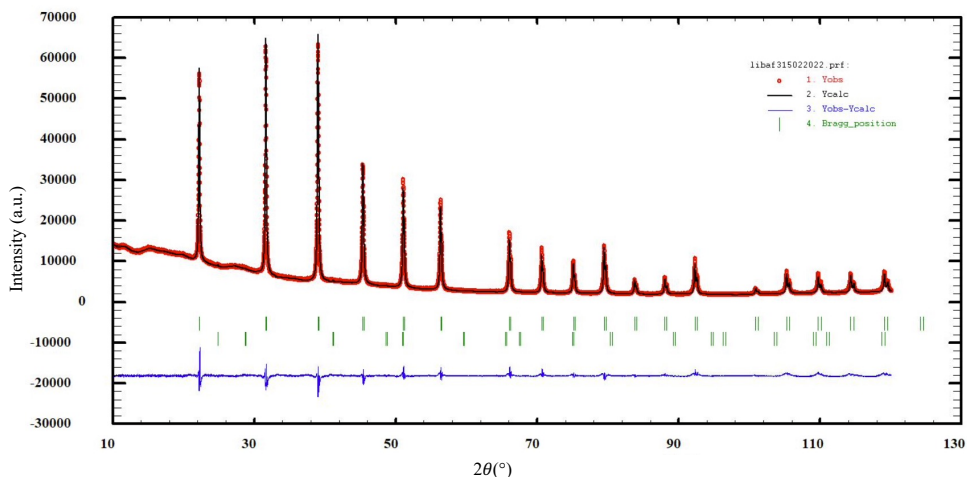


Figure 3.1.: Diffractogram of LiBaF₃ synthesized in this work Y_{obs} (red dots), measured at (293 ± 2) K, compared to the Rietveld refinement performed on the FullProf suite software. Represented by: Y_{calc} (black line) the calculated XRD pattern and $Y_{\text{obs}} - Y_{\text{calc}}$ (blue line) the differential calculation between observed and calculated data. The Bragg's reflection angular positions of LiBaF₃ ($(99.7 \pm 0.2)\%$) (top) and BaF₂ ($(0.3 \pm 0.2)\%$) (bottom) are shown by green marks.

Mixing enthalpy data were measured experimentally at $T = 1354$ K using twin micro-calorimetry by Hong and Kleppa [57]. From the calculation at the same temperature with the present model (Figure 3.3), the agreement is confirmed with the experimental data and particularly with the extrapolation proposed by Kleppa *et al.*

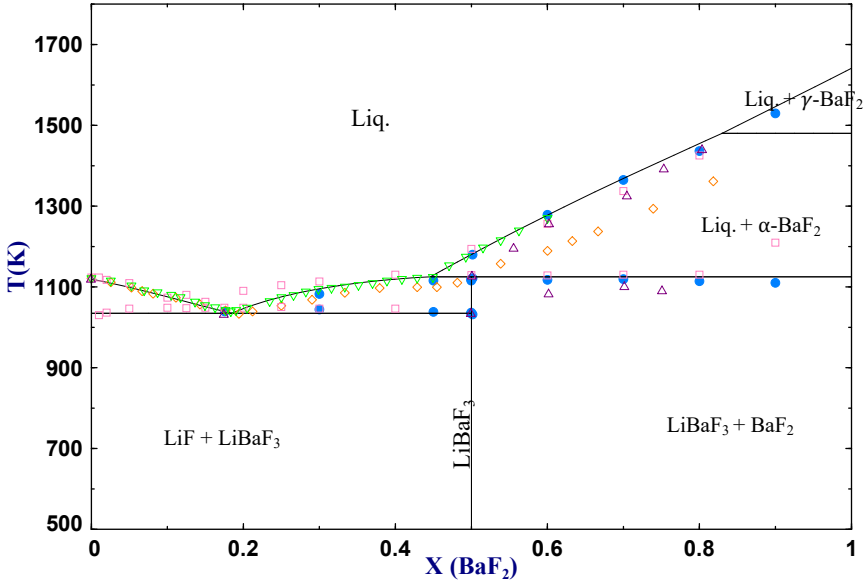


Figure 3.2.: Phase diagram of the LiF–BaF₂ system calculated in this work. (●) are the transitions measured experimentally in this work, (▽) represent the data from Bergman and Banashek [24], (◇) the data from Boukhalova [55], (△) the data from Taniuchi [56], and (□) the data from Agulanskii and Bessanova [25].

Table 3.5.: Invariant equilibria calculated in this work for the system LiF–BaF₂ compared to the experimental data measured and the references provided in the literature.

Invariant Reaction	Equilibrium	Calculated and literature data					
		<i>This study (model)</i>		Agulanskii <i>et al.</i> [25]		Taniuchi <i>et al.</i> [56]	
		X _{BaF₂}	T(K)	X _{BaF₂}	T(K)	X _{BaF₂}	T(K)
LiF + LiBaF ₃ =L	Eutectic	0.185	1034	0.175	1048	0.194	1033
LiBaF ₃ = L' + BaF ₂	Peritectic transition	0.5	1123	0.5	1129	0.5	1110

The model proposed here (Figure 3.2) reproduces well the new experimental data provided in this work. It is also conform to the invariant equilibria composition and temperature determined in the works of Bergman and Banashek [24], Boukhalova [55], Taniuchi *et al.* [56], and Agulyanskii and Bessanova [25], with the exception of the melting temperature of BaF₂ as explained above.

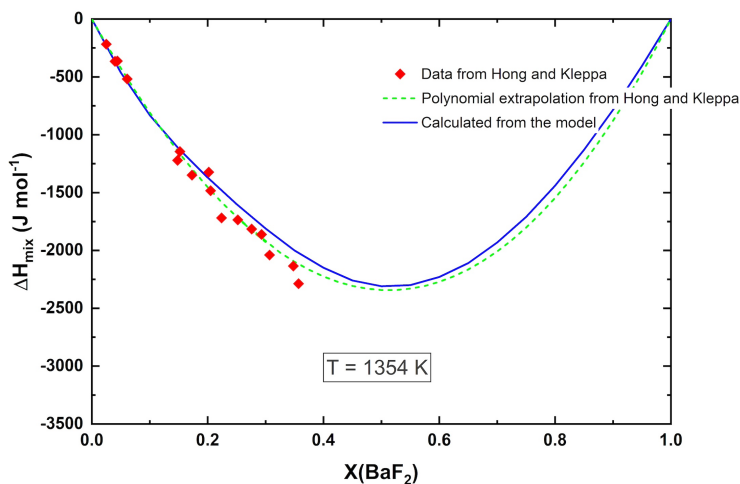


Figure 3.3.: Mixing enthalpy of the LiF–BaF₂ system calculated at 1354 K in this work, compared to the experimental data and polynomial fitting by Kleppa et Hong [57]. The calculation were performed with a constant pressure of 1 atm.

3.4.2. LiF–ZrF₄

A first set of phase diagram data were measured for the LiF–ZrF₄ system by Thoma *et al.* [27], who used different methods, namely quenching and differential scanning calorimetry. ZrF₄ is particularly volatile in solutions containing free F[−] anions [58, 59], so measurements at high ZrF₄ content are particularly difficult. The reported data were collected during cooling of the samples, allowing to confirm the exact composition on quenched samples. The experimental procedures are presented in further detail in ORNL reports and publications from the same authors [60–62], including details on the experimental accuracies. The quenching method was privileged by Thoma to obtain the experimental data on the liquidus transitions, while the differential calorimetry data on the cooling ramps were selected according to Thoma’s recommendations for the solidus and crystalline transitions. A second complete set of phase diagram data was provided by Korenev *et al.* [63], who used differential thermal analysis and X-ray diffraction. The reported liquidus equilibria are very similar to the previous work. The only significant difference is

Table 3.6.: DSC data collected in this work.

X_{LiF}	X_{BaF_2}	X_{ZrF_4}	T(K)	Equilibrium	Invariant reaction
-	1	-	1124	Congruent melting	$\text{LiF} = \text{L}$
0.824	0.176	-	1039	Eutectic	$\text{LiF} + \text{LiBaF}_3 = \text{L}$
0.700	0.300	-	1044	Eutectic	$\text{LiF} + \text{LiBaF}_3 = \text{L}$
0.700	0.300	-	1082	Liquidus	$\text{L}' + \text{LiBaF}_3 = \text{L}$
0.550	0.450	-	1038	Eutectic	$\text{LiF} + \text{LiBaF}_3 = \text{L}$
0.550	0.450	-	1115	Liquidus	$\text{L}' + \text{LiBaF}_3 = \text{L}$
0.500	0.500	-	1036	Eutectic	$\text{LiF} + \text{LiBaF}_3 = \text{L}$
0.500	0.500	-	1121	Peritectic	$\text{LiBaF}_3 = \text{L}' + \text{BaF}_2$
0.493	0.507	-	1119	Peritectic	$\text{LiBaF}_3 = \text{L}' + \text{BaF}_2$
0.493	0.507	-	1180	Liquidus	$\text{L}' + \text{BaF}_2 = \text{L}$
0.400	0.600	-	1117	Peritectic	$\text{LiBaF}_3 = \text{L}' + \text{BaF}_2$
0.400	0.600	-	1278	Liquidus	$\text{L}' + \text{BaF}_2 = \text{L}$
0.300	0.700	-	1119	Peritectic	$\text{LiBaF}_3 = \text{L}' + \text{BaF}_2$
0.300	0.700	-	1364	Liquidus	$\text{L}' + \text{BaF}_2 = \text{L}$
0.248	0.752	-	1114	Peritectic	$\text{LiBaF}_3 = \text{L}' + \text{BaF}_2$
0.248	0.752	-	1436	Liquidus	$\text{L}' + \text{BaF}_2 = \text{L}$
0.111	0.889	-	1110	Peritectic	$\text{LiBaF}_3 = \text{L}' + \text{BaF}_2$
0.111	0.889	-	1529	Liquidus	$\text{L}' + \text{BaF}_2 = \text{L}$
0.776	-	0.224	765	Peritectoid	$\text{Li}_2\text{ZrF}_6 + \text{Li}_4\text{ZrF}_8 = \text{Li}_3\text{ZrF}_7$
0.776	-	0.224	855	Eutectic	$\text{LiF} + \text{Li}_3\text{ZrF}_7 = \text{L}$
0.776	-	0.224	881	Liquidus	$\text{L}' + \text{Li}_3\text{ZrF}_7 = \text{L}$

Uncertainty for the temperature measurements are estimated at ± 5 K for pure compounds, and ± 10 K for mixtures.

that Korenev identified only one congruent melting for Li₃ZrF₇, while he suggested a peritectic decomposition for Li₂ZrF₆. On the ZrF₄-rich side, the authors also observed an $\alpha \rightarrow \beta$ -ZrF₄ polymorphic transition. In a study on the crystal structures of the intermediates Li₄ZrF₈ and Li₃Zr₄F₁₉, Dugat *et al.* moreover re-investigated the LiF-ZrF₄ phase diagram [38]. The authors collected experimental data for a few concentrations, but the invariant equilibria were not defined precisely. Considering more recent works on the crystal structure of ZrF₄ (it was showed that the β and γ phases are not stable above 673 K, and the γ -ZrF₄ was stabilized only for a high pressure of 28 GPa [64, 65]), it was decided not to include any phase transition in ZrF₄ for the thermodynamic models.

Table 3.7.: Invariant equilibria calculated in this work for the system LiF-ZrF₄ compared to the references provided in the literature.

Invariant Reaction	Equilibrium	Calculated and literature data					
		<i>This study (model)</i>		Thoma <i>et al.</i> [27]		Korenev <i>et al.</i> [63]	
		X _{ZrF₄}	T (K)	X _{ZrF₄}	T(K)	X _{ZrF₄}	T(K)
LiF + Li ₃ ZrF ₇ =L	Eutectic	0.194	899	0.21	871 ± 2	0.21	858 ± 5
Li ₃ ZrF ₇ =L	Congruent melting	0.250	886	0.25	935 ± 5	0.25	913 ± 5
Li ₂ ZrF ₆ + Li ₄ ZrF ₈ =Li ₃ ZrF ₇	Peritectoid	0.250	731	0.25	743 ± 3	0.25	747 ± 5
Li ₂ ZrF ₆ = L' + Li ₃ ZrF ₇	Peritectic	0.333	842	0.295	843 ± 2	0.33	843 ± 5
Li ₂ ZrF ₆ + Li ₃ Zr ₄ F ₁₉ =L	Eutectic	0.481	786	0.49	780 ± 3	0.50	775 ± 5
Li ₃ Zr ₄ F ₁₉ =ZrF ₄ + L'	Peritectic	0.571	791	0.571	793 ± 5	<i>not identified</i>	

The model shows overall a good agreement with the literature data and the invariant equilibria (Table 3.7). Only the liquidus temperatures around the congruently melting compound Li₃ZrF₇ are not reproduced as well as the rest of the data. It was not achievable to match the liquidus data in this region at the same time as the mixing enthalpy data and reported eutectic equilibria. We therefore attempted to re-measure the phase equilibria in this region. Our measurement at X_{ZrF₄} = 0.224 yielded a slightly lower liquidus temperature than reported by Thomas *et al.* [27], and in better agreement with the optimization (Figure 3.4). Obviously, the comprehensive re-examination of this composition range would be highly beneficial. The introduction of multiple coordination environments that could reflect better the local structure of the melt [9, 66], where oligomerization is expected [67], could help reproduce this region of the phase diagram with a higher accuracy. It is finally worth pointing out that the gas in equilibrium with solid ZrF₄ reaches 1 bar at T = 1175 K (i.e., below its melting temperature), which is related to the low boiling point and high volatility of ZrF₄.

Using the current assessment, the mixing enthalpy calculated from the model shows good agreement with the trend of the experimental data from Hatem *et al.* [68].

3.4.3. BaF₂-ZrF₄

In the literature, the phase diagram of the BaF₂-ZrF₄ system was studied by several groups. In 1989, Babitsyna *et al.* measured a first series of phase equilibria between X(ZrF₄)= 0.33 and X(ZrF₄)= 1 [47, 48]. The authors reported four intermediate

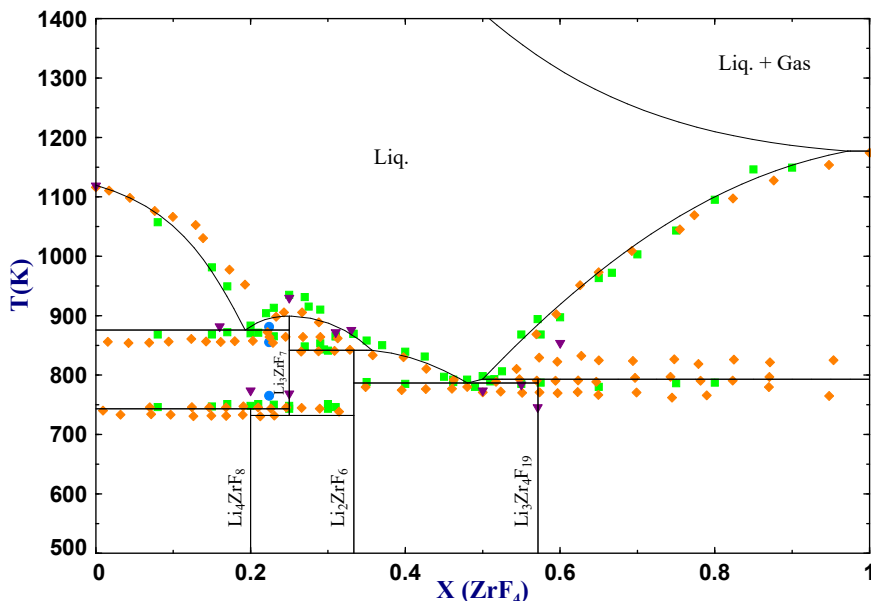


Figure 3.4.: Phase diagram of the LiF-ZrF_4 system calculated in this work. (●) are the transitions measured experimentally in this work, (■) represent the data from Thoma *et al.* [27], (◆) the data from Korenev *et al.* [63] and (▼) the data from Dugat *et al.* [38]. The calculation was performed for a constant pressure of 1 atm.

compounds, namely Ba_2ZrF_6 , $\text{Ba}_3\text{Zr}_2\text{F}_{14}$, BaZrF_6 and $\text{BaZr}_2\text{F}_{10}$. The latter compound was reported with a peritectic decomposition at $T = 850$ K [48]. Ba_2ZrF_8 was defined with a stable homogeneity range and a congruent melting at $T = 1285$ K.

In 1992, Grande *et al.* [29], reported new results by thermal analysis and compared their results to the work by Babitsyna *et al.* [48]. They observed that the transition data previously collected by Babitsyna *et al.* for pure ZrF_4 were not reliable: they found a melting temperature at (1183 ± 1) K, in agreement with literature recommended by the SGTE and NIST-JANAF databases [33, 34], in contrast with the previous work (1273 K). No phase transition was observed for pure BaF_2 [29]. A congruent melting was identified for $\text{BaZr}_2\text{F}_{10}$ at a temperature of (863 ± 2) K by thermal analysis. The latter transition was also reported around the same temperature by other authors [46–48], but defined as a crystalline transition. Congruent melting was found for Ba_2ZrF_8 at (1289 ± 1) K. Two phase transitions were also identified, at 796 K and 813 K, respectively. These results were moreover confirmed by X-ray Diffraction of the different polymorphs in quenched samples. A last work, by Ratnikova *et al.* in 1997 [46], shows a phase diagram without $\text{BaZr}_2\text{F}_{10}$, but with an homogeneity range for Ba_2ZrF_8 , melting congruently. The

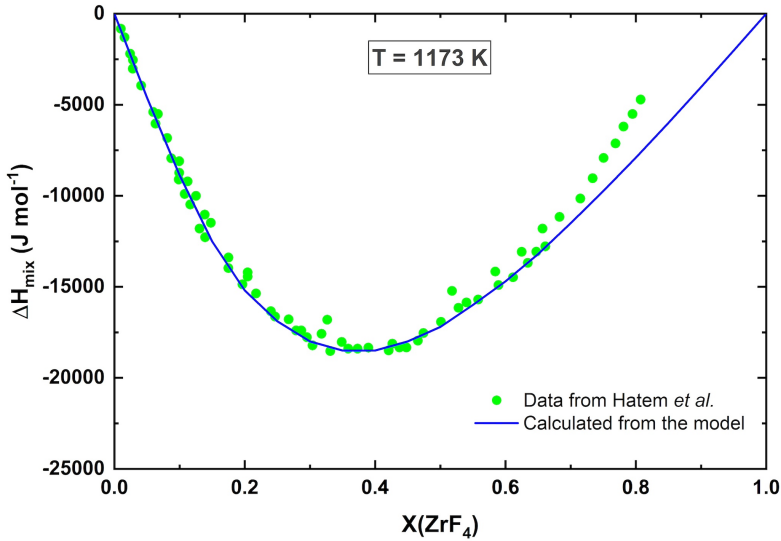


Figure 3.5.: Mixing enthalpy of the LiF–ZrF₄ system calculated at 1173 K in this work, compared with the experimental data from Hatem *et al.* [68].

phase equilibria at high temperature of the BaF₂–ZrF₄ system were also studied by Lin *et al.* [69], particularly at high concentration of ZrF₄, where previous work gave inconsistent data. The model proposed here (Figure 3.6), is in good agreement with data by Grande *et al.* [29], selected as reference for the optimization because the information in the paper allows for a detailed evaluation of experimental methods and interpretation. A comparison with the other datasets allows to consider this model as a satisfactory representation of the system BaF₂–ZrF₄ overall (Table 3.8).

Table 3.8.: Invariant equilibria calculated in this work for the system BaF₂–ZrF₄ compared to the references provided in the literature.

Invariant Reaction	Equilibrium	Calculated and literature data					
		<i>This study (model)</i>		Grande <i>et al.</i> [29]		Ratnikova <i>et al.</i> [46]	
		X _{ZrF₄}	T (K)	X _{ZrF₄}	T(K)	X _{ZrF₄} *	T(K)
Ba ₃ ZrF ₁₀ =BaF ₂ + L'	Peritectic	0.250	1294	0.250	1305	0.29	1285
Ba ₃ ZrF ₁₀ + Ba ₂ ZrF ₈ =L	Eutectic	0.321	1283	0.30	1270	0.31	1259
Ba ₂ ZrF ₈ =L	Congruent melting	0.333	1283	0.336	1289	0.333	1279
β-BaZrF ₆ =Ba ₂ ZrF ₈ + L'	Peritectic	0.500	838	0.500	858	0.500	833
β-BaZrF ₆ + BaZr ₂ F ₁₀ =L	Eutectic	0.597	832	0.62	822	<i>Only one eutectic identified:</i>	
BaZr ₂ F ₁₀ =L	Congruent melting	0.667	866	0.667	863		
BaZr ₂ F ₁₀ + ZrF ₄ = L	Eutectic	0.691	862	0.7	842	0.65	828

*Uncertainty on the composition reported to be: ± 0.02

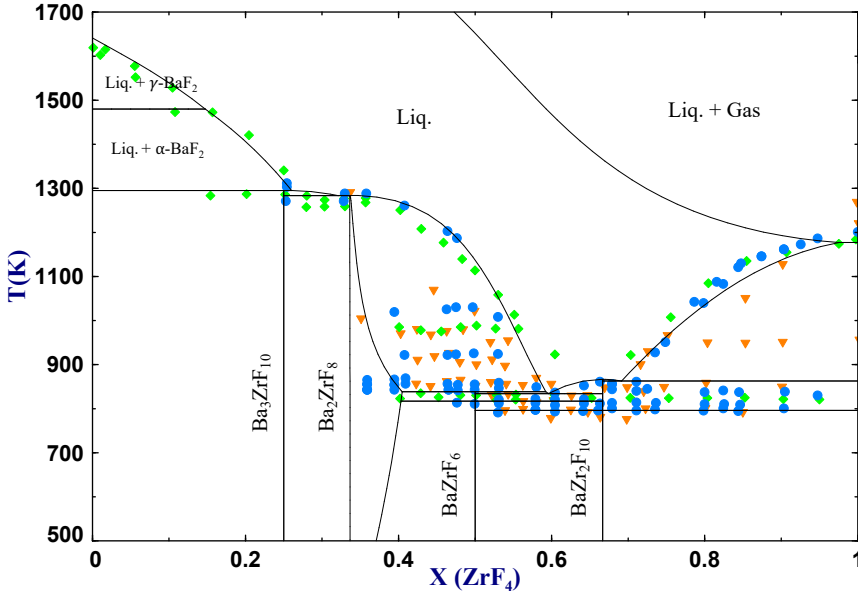


Figure 3.6.: Phase diagram of the $\text{BaF}_2\text{-ZrF}_4$ system calculated in this work. (●) are the data from Grande *et al.* [29], (◆) represent the data from Ratnikova *et al.* [46], and (▼) the data from Babitsyna *et al.* [47]. The calculation was performed for a constant pressure of 1 atm.

3.4.4. TERNARY $\text{LiF-BaF}_2\text{-ZrF}_4$

The optimization of the ternary phase diagram was based on the only set of experimental data determined by drop calorimetry and differential thermal analysis by Mahmoud [52], describing the mixing enthalpy along different pseudobinary sections (as defined in the Figure 3.7) of the phase diagram, shown in Figures 3.8 and 3.9. No mutual solid solubility is expected in the ternary system in between the intermediate compounds stable in the binary systems as the stoichiometries and crystal structures differ from one system to the other. Moreover, the large difference in ionic radius between the Li^+ and Ba^{2+} cations makes it unlikely for such solid solutions to form. A quaternary compound was reported, however, in the ternary system, with stoichiometry $\text{LiBaZr}_2\text{F}_{11}$, and tetragonal symmetry in space group $I4/m$ [70]. The latter was prepared with a hydrothermal synthesis route at 180°C in an hermetic Teflon jar. The information provided by Gao *et al.* [70] in their study does not allow to conclude if $\text{LiBaZr}_2\text{F}_{11}$ is a stable phase under standard pressure. We could also not find any thermodynamic data for the latter compound in the literature. The melting/decomposition temperature is not known. In the absence of sufficient information, the quaternary phase $\text{LiBaZr}_2\text{F}_{11}$ was thus not included in the present thermodynamic assessment.

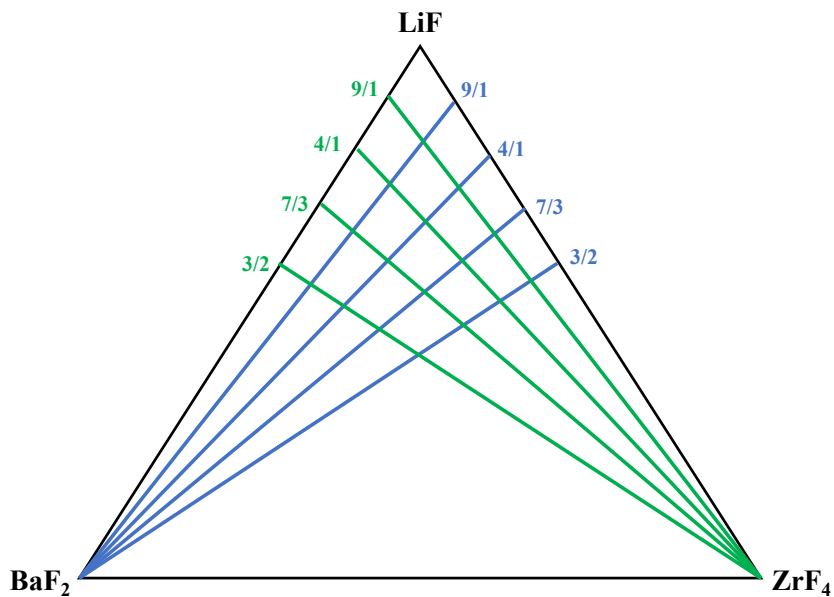


Figure 3.7.: Pseudobinary sections experimentally assessed in the ternary system LiF-BaF₂-ZrF₄ at 1173 K measured by Mahmoud [52] and calculated in this work.

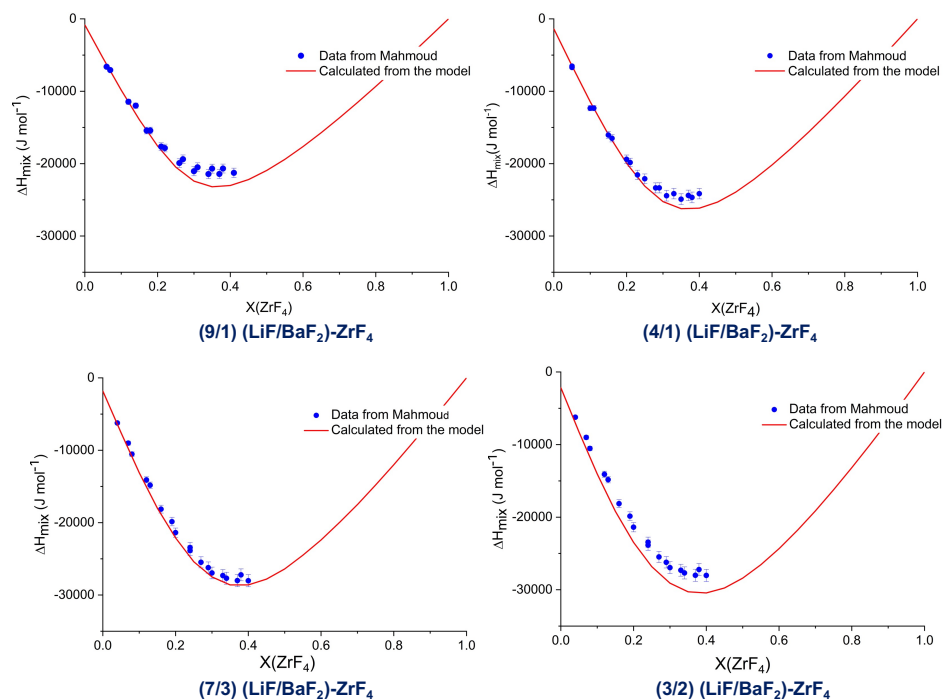


Figure 3.8.: Mixing enthalpy in the ternary system $\text{LiF}-\text{BaF}_2-\text{ZrF}_4$ for different pseudo-binary sections $(A/B)\text{LiF}/\text{BaF}_2-\text{ZrF}_4$ ($A/B = 9/1; 4/1; 7/3; 3/2$) at 1173 K measured by Mahmoud [52] and calculated in this work.

The ternary excess parameters of the liquid solution, obtained for a Kohler-Toop interpolation ($X_{\text{LiF}} = \text{asymmetric component}$) [71], allow a very good agreement in the different (LiF/BaF₂)-ZrF₄ sections (Figure 3.8). These data were first used for the optimization, considering their lower uncertainty ($\pm 3\%$), compared to the sections (LiF/ZrF₄)-BaF₂ ($\pm 6\%$) [52]. However, even for the latter case, the model remains also in very good agreement with these other data (Figure 3.9).

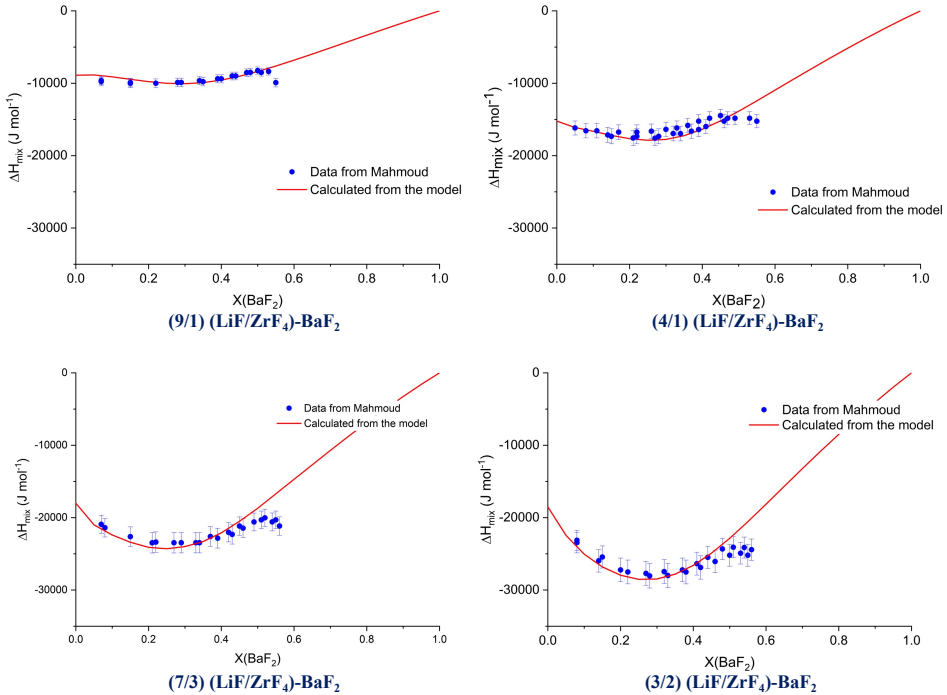


Figure 3.9.: Mixing enthalpy in the ternary system LiF-BaF₂-ZrF₄ for different pseudo-binary sections ((A/B)LiF/ZrF₄)-BaF₂ (A/B = 9/1; 4/1; 7/3; 3/2) at 1173 K measured by Mahmoud [52] and calculated in this work.

Although the ternary mixing enthalpy data do not cover the entire spectrum of composition in the ternary phase diagram, the good agreement obtained with the present model gives a good confidence in the description of the thermodynamic behavior of the LiF-BaF₂-ZrF₄ system (Figure 3.10). Fourteen ternary invariant equilibria are suggested with the present model. The lowest ternary eutectic was found at $T = 587$ K and $X_{\text{LiF}} = 0.38$, $X_{\text{BaF}_2} = 0.25$ and $X_{\text{ZrF}_4} = 0.37$. They are listed in Table 3.9.

Another element of comparison can be found in the thesis of Mahmoud (page 81) [52], that includes an isotherm of this ternary system at 1173 K. The same isothermal projection, calculated in Figure 3.11, is in good agreement with this work [52], with the presence of stable solid phases in equilibrium with the liquid at 1173 K at high

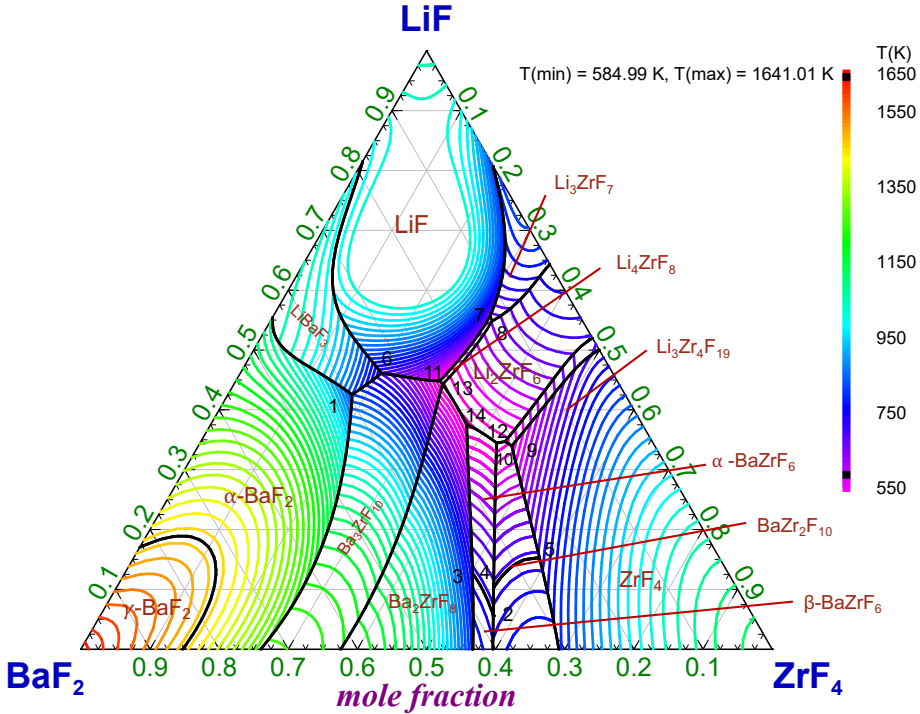


Figure 3.10.: Liquidus projection of the LiF–BaF₂–ZrF₄ system calculated in this work from 550 K to 1650 K with an increment of 15 K. Primary crystallization fields and invariant equilibria are detailed in the figure.

Table 3.9.: Invariant equilibria calculated in this work for the system LiF–BaF₂–ZrF₄.

N°	X _{LiF}	X _{BaF₂}	X _{ZrF₄}	Invariant equilibria	Transition	T(K)
1	0.425	0.395	0.180	Quasi-peritectic	$L + \alpha\text{-BaF}_2 = \text{Ba}_3\text{ZrF}_{10} + \text{LiBaF}_3$	890.3
2	0.071	0.374	0.555	Phase transition	$\alpha\text{-BaZrF}_6 = \beta\text{-BaZrF}_6$	817.15
3	0.051	0.378	0.571	Phase transition	$\alpha\text{-BaZrF}_6 = \beta\text{-BaZrF}_6$	817.15
4	0.148	0.263	0.589	Phase transition	$\alpha\text{-BaZr}_2\text{F}_{10} = \beta\text{-BaZr}_2\text{F}_{10}$	796.15
5	0.098	0.353	0.548	Phase transition	$\alpha\text{-BaZr}_2\text{F}_{10} = \beta\text{-BaZr}_2\text{F}_{10}$	796.15
6	0.461	0.335	0.204	Quasi-peritectic	$L + \text{Ba}_3\text{ZrF}_{10} = \text{LiBaF}_3 + \text{LiF}$	788.9
7	0.557	0.129	0.314	Peritectic	$L + \text{Li}_3\text{ZrF}_7 + \text{LiF} = \text{Li}_4\text{ZrF}_8$	743.0
8	0.548	0.131	0.321	Quasi-peritectic	$L + \text{Li}_3\text{ZrF}_7 = \text{Li}_2\text{ZrF}_6 + \text{Li}_4\text{ZrF}_8$	731.9
9	0.339	0.208	0.453	Quasi-peritectic	$L + \text{ZrF}_4 = \alpha\text{-BaZr}_2\text{F}_{10} + \text{Li}_3\text{Zr}_4\text{F}_{19}$	615.2
10	0.448	0.259	0.293	Quasi-peritectic	$L + \text{Ba}_3\text{ZrF}_{10} = \text{Ba}_2\text{ZrF}_8 + \text{LiF}$	602.9
11	0.346	0.214	0.440	Quasi-peritectic	$L + \text{Li}_2\text{ZrF}_6 = \alpha\text{-BaZr}_2\text{F}_{10} + \text{Li}_3\text{Zr}_4\text{F}_{19}$	599.8
12	0.449	0.256	0.295	Quasi-peritectic	$L + \text{Ba}_2\text{ZrF}_8 = \text{Li}_4\text{ZrF}_8 + \text{LiF}$	595.2
13	0.344	0.226	0.430	Quasi-peritectic	$L + \text{Li}_2\text{ZrF}_6 = \alpha\text{-BaZr}_2\text{F}_{10} + \alpha\text{-BaZrF}_6$	591.3
14	0.445	0.252	0.303	Quasi-peritectic	$L + \text{Ba}_2\text{ZrF}_8 = \text{Li}_4\text{ZrF}_8 + \text{Li}_2\text{ZrF}_6$	590.4
15	0.369	0.247	0.384	Eutectic	$\text{Ba}_2\text{ZrF}_8 + \alpha\text{-BaZrF}_6 + \text{Li}_2\text{ZrF}_6 = L$	589.1

BaF₂ and ZrF₄ contents. Overall, the agreement on the mixing enthalpies and on this isotherm give us good confidence in the accuracy of the ternary phase diagram presented here.

Based on the model, a calculation of the isothermal projection at 873 K, defined as the minimum operating temperature of the MSR [72], was carried out. As shown in Figure 3.12, some crystalline phases are stable in a large compositional area of the phase diagram at this temperature. Since the MSR fuel is not made exclusively of LiF, but of e.g. a LiF-UF₄-PuF₃/UF₃ mixture, the more complex equilibria in the fuel-BaF₂-ZrF₄ system should be considered to assess if precipitation of solid phases could occur under operating conditions. This work provides the basis for such calculations.

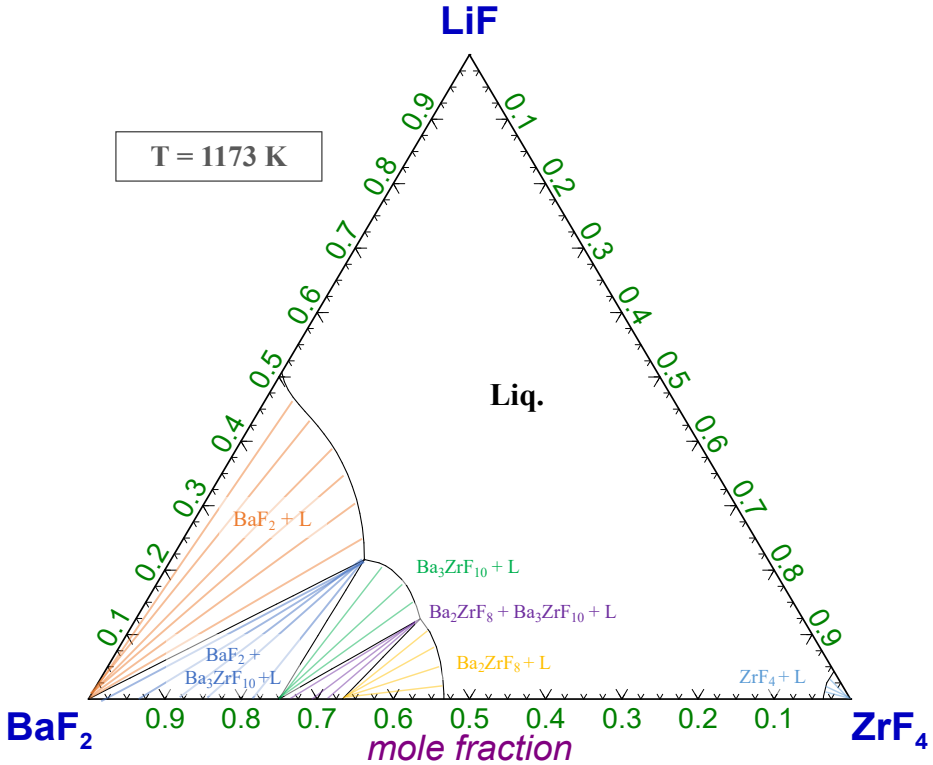


Figure 3.11.: Isothermal plot of the LiF-BaF₂-ZrF₄ system calculated in this work at 1173 K. The calculation were made excluding the gaseous phases. The different stable solid are indicated in the figure.

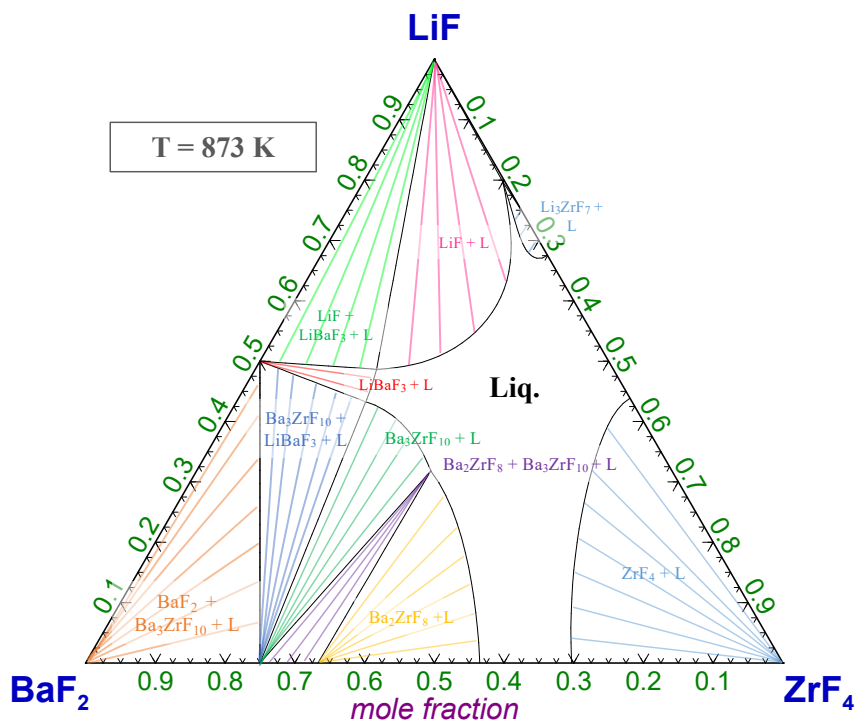


Figure 3.12.: Isothermal plot of the LiF–BaF₂–ZrF₄ system calculated in this work at 873 K. The calculation were made excluding the gaseous phases. The different stable solid phases are indicated in the figure.

3.5. CONCLUSIONS

Combining experimentally collected phase diagram data and literature sources on phase diagrams and mixing enthalpy data, thermodynamic models for the binary LiF-BaF₂, LiF-ZrF₄ and BaF₂-ZrF₄, and ternary LiF-BaF₂-ZrF₄ systems were developed for the first time using the modified quasichemical model in the quadruplet approximation for the liquid solution. A large fraction of the intermediates observed in the LiF-BaF₂-ZrF₄ system appear to stabilize at the minimum operating temperature of a MSR (873 K). Ba₂ZrF₈ and Ba₃ZrF₁₀ were found to be stable solid phases above 1173 K. The possible precipitation of solid phases of LiF, BaF₂ and ZrF₄ in the operating reactor must be taken into consideration for the risk assessment of the MSR. However, the current system only provides equilibria with LiF, which is present in large concentrations in the salt mixture. This forms a basis to study the more complex equilibria with the complete fuel system, e.g. LiF-ThF₄-UF₄/UF₃, that should be considered for a more accurate analysis. The volatility of ZrF₄ is in particular a factor to be taken into account for gaseous releases in an accidental scenario.

ACKNOWLEDGMENTS

T. Dumaire acknowledges gratefully financial support from the Nuclear Research and Consultancy Group (NRG, Petten, Netherlands) and the SAMOSAFER project which has received funding from the Euratom research and training program 2014-2018 under grant agreement N°847527. The authors acknowledge Jaén A. Ocádiz Flores for the helpful discussions.

REFERENCES

- [1] J. E. Kelly. “Generation IV International Forum: A decade of progress through international cooperation”. In: *Progress in Nuclear Energy* 77 (2014), pp. 240–246. DOI: 10.1016/j.pnucene.2014.02.010.
- [2] J. Serp, M. Allibert, O. Beneš, S. Delpech, O. Feynberg, V. Ghetta, D. Heuer, D. Holcomb, V. Ignatiev, J.-L. Kloosterman, L. Luzzi, E. Merle-Lucotte, J. Uhlíř, R. Yoshioka, and D. Zhimin. “The molten salt reactor (MSR) in generation IV: Overview and perspectives”. In: *Progress in Nuclear Energy* 77 (Nov. 2014), pp. 308–319. ISSN: 0149-1970. DOI: 10.1016/j.pnucene.2014.02.014.
- [3] O. Beneš and P. Souček. “Molten salt reactor fuels”. In: *Advances in Nuclear Fuel Chemistry*. Amsterdam: Elsevier, 2020, pp. 249–271. DOI: 10.1016/b978-0-08-102571-0.00007-0.
- [4] A. Tosolin, P. Souček, O. Beneš, J.-F. Vigier, L. Luzzi, and R. J. M. Konings. “Synthesis of plutonium trifluoride by hydro-fluorination and novel thermodynamic data for the PuF₃-LiF system”. In: *Journal of Nuclear Materials* 503 (2018), pp. 171–177. DOI: 10.1016/j.jnucmat.2018.02.037.
- [5] O. Beneš and R. J. M. Konings. “Molten Salt Reactor Fuel and Coolant”. In: (2012), pp. 359–389. DOI: 10.1016/b978-0-08-056033-5.00062-8.
- [6] R. J. Kedl. *Migration of a class of fission products (noble metals) in the Molten-Salt Reactor Experiment*. ORNL-TM-3884. 1972. DOI: 10.2172/4471292.
- [7] B. Hombourger, J. Křepel, and A. Pautz. “Breed-and-burn fuel cycle in molten salt reactors”. In: *EPJ Nuclear Sciences & Technologies* 5 (2019). Ed. by J. L. Kloosterman, E. Merle, and J. Ragusa, p. 15. DOI: 10.1051/epjn/2019026.
- [8] E. Capelli, O. Beneš, and R. J. M. Konings. “Thermodynamic assessment of the LiF–ThF₄–PuF₃–UF₄ system”. en. In: *Journal of Nuclear Materials* 462 (2015), pp. 43–53. ISSN: 0022-3115. DOI: 10.1016/j.jnucmat.2015.03.042.
- [9] J. A. Ocádiz Flores, A. E. Gheribi, J. Vlieland, K. Dardenne, J. Rothe, R. J. M. Konings, and A. L. Smith. “New insights and coupled modelling of the structural and thermodynamic properties of the LiF-UF₄ system”. In: *Journal of Molecular Liquids* 331 (2021), p. 115820. ISSN: 0167-7322. DOI: 10.1016/j.molliq.2021.115820.
- [10] E. Capelli, O. Beneš, and R. J. M. Konings. “Thermodynamics of soluble fission products cesium and iodine in the Molten Salt Reactor”. In: *Journal of Nuclear Materials* 501 (Apr. 2018), pp. 238–252. DOI: 10.1016/j.jnucmat.2018.01.024.

- [11] J. A. Ocadiz-Flores, E. Capelli, P. E. Raison, R. J. M. Konings, and A. L. Smith. “Thermodynamic assessment of the LiF-NiF₂, NaF-NiF₂ and KF-NiF₂ systems”. In: *The Journal of Chemical Thermodynamics* 121 (June 2018), pp. 17–26. DOI: 10.1016/j.jct.2018.01.023.
- [12] T. Dumaire, R. J. M. Konings, and A. L. Smith. “Thermodynamic Assessment of the AF-CrF₃ (A = Li, Na, K) and CrF₂-CrF₃ Systems”. In: *Thermo* 1 (2021), pp. 205–219. DOI: 10.3390/thermo1020014.
- [13] O. Beneš and R. J. M. Konings. “Molten Salt Reactor Fuel and Coolant”. In: *Comprehensive Nuclear Materials*. Ed. by R. J. M. Konings and R. E. Stoller. Amsterdam: Elsevier, 2020, pp. 609–644. DOI: 10.1016/b978-0-12-803581-8.11790-4.
- [14] E. L. Compere, E. G. Bohlmann, S. S. Kirslis, F. F. Blankenship, and W. R. Grimes. *Fission product behavior in the Molten Salt Reactor Experiment. ORNL-4865*. ORNL-4865. Oak Ridge National Laboratory, 1975. DOI: 10.2172/4077644.
- [15] World Health Organization and others. “Health risk assessment from the nuclear accident after the 2011 Great East Japan earthquake and tsunami, based on a preliminary dose estimation”. In: (2013).
- [16] A. K. Mishra, N. Garg, K. V. Shanavas, S. N. Achary, A. K. Tyagi, and S. M. Sharma. “High pressure structural stability of BaLiF₃”. In: *Journal of Applied Physics* 110.12 (Dec. 2011), p. 123505. DOI: <https://doi.org/10.1063/1.3670036>.
- [17] L. B. McCusker, R. B. V. Dreele, D. E. Cox, D. Louër, and P. Scardi. “Rietveld refinement guidelines”. In: *Journal of Applied Crystallography* 32.1 (1999), pp. 36–50. DOI: 10.1107/s0021889898009856.
- [18] J. Rodriguez-Carvajal. “Recent advances in magnetic structure determination by neutron powder diffraction”. In: *Physica B: Condensed Matter* 192.1-2 (1993), pp. 55–69.
- [19] W. J. Boettinger, U. R. Kattner, K.-W. Moon, and J. H. Perepezko. *NIST recommended practice guide: DTA and Heat-flux DSC Measurements of Alloy Melting and Freezing*. Ed. by N. I. of Standards and Technology. U.S. Government Printing Office, 2006. DOI: 10.6028/nbs.sp.960-15.
- [20] O. Beneš, R. J. M. Konings, S. Wurzer, M. Sierig, and A. Dockendorf. “A DSC study of the NaNO₃-KNO₃ system using an innovative encapsulation technique”. In: *Thermochimica Acta* 509.1-2 (2010), pp. 62–66. DOI: 10.1016/j.tca.2010.06.003.
- [21] C. W. Bale, E. Bélisle, P. Chartrand, S. A. Decterov, G. Eriksson, A. E. Gheribi, K. Hack, I.-H. Jung, Y.-B. Kang, J. Melançon, A. D. Pelton, S. Petersen, C. Robelin, J. Sangster, P. Spencer, and M.-A. van Ende. “FactSage thermochemical software and databases, 2010–2016”. In: *Calphad* 54 (2016), pp. 35–53.
- [22] U. R. Kattner, H. J. Seifert, and H. L. Lukas. “Editorial: Integrated computational materials engineering, CALPHAD”. In: *CALPHAD: Computer Coupling of Phase Diagrams and Thermochemistry* 34 (2010), pp. 385–386. ISSN: 0364-5916. DOI: 10.1016/j.calphad.2010.10.005.

- [23] Y. A. Chang, S. Chen, F. Zhang, X. Yan, F. Xie, R. Schmid-Fetzer, and W. A. Oates. "Phase diagram calculation: past, present and future". In: *Progress in Materials Science* 49.3-4 (2004), pp. 313–345. DOI: 10.1016/s0079-6425(03)00025-2.
- [24] A.G.Bergman and E.I.Banashek. "Ternary systems of Fluoride and Chloride Sodium and Barium". In: *Izvestija Sektora Fiziko-chimiceskogo Analiza (Trans. Knowledge of the Sector of Physical and Chemical Analysis)* 22 (1953), pp. 196–206.
- [25] A.I.Agulanskii and V.A.Bessonova. "Fusion in Salt Mixtures Containing Lithium, Barium and Lanthanum Fluorides". In: *Russian Journal of Inorganic Chemistry* 27.4 (1982), pp. 1029–1032.
- [26] K. C. Hong and O. J. Kleppa. "Enthalpies of mixing in some binary liquid alkali fluoride mixtures". In: *The Journal of Chemical Thermodynamics* 8 (1976), pp. 31–36. ISSN: 0021-9614. DOI: 10.1016/0021-9614(76)90147-6.
- [27] R. E. Thoma, H. Insley, H. A. Friedman, and G. M. Hebert. "Condensed System LiF-NaF-ZrF₄ Phase Equilibria and Crystallographic Data." In: *Journal of Chemical and Engineering Data* 10.3 (1965), pp. 219–230.
- [28] G. Hatem, M. Gaune-Escard, and M. Hoch. "Experimental thermodynamics and phase equilibria estimation in Zr-fluoride glasses". In: *Journal of Non-Crystalline Solids* 161 (1993), pp. 91–97.
- [29] T. Grande, S. Aasland, and S. Julsrud. "Phase equilibria in the glass-forming system ZrF₄-BaF₂". In: *Journal of Non-Crystalline Solids* 140 (1992), pp. 73–76. DOI: 10.1016/s0022-3093(05)80744-6.
- [30] G. Hatem, K. Mahmoud, and M. Gaune-Escard. "Les systemes ternaires fondus ZrF₄-BaF₂-MF: determination calorimétrique de l'enthalpie d'excès. Partie I. M = Na". In: *Thermochimica Acta* 1991 (1991), pp. 91–106. DOI: 10.1002/chin.199138016.
- [31] O. Beneš and R. J. M. Konings. "Thermodynamic Calculations of Molten-Salt Reactor Fuel Systems". In: *Molten Salts Chemistry - From Lab to Applications*. Ed. by H. G. Frederic Lantelme. Elsevier, 2013, pp. 49–78. DOI: 10.1016/b978-0-12-398538-5.00004-4.
- [32] Joint Research Centre - European Commission. *Joint Research Centre Molten Salt Database - JRCMSD*. Ed. by E. S. Hub. https://joint-research-centre.ec.europa.eu/joint-research-centre-molten-salt-database-jrcmsd_en. Accessed: 2024-02-05.
- [33] M. W. Chase Jr. and National Information Standards Organization (US). "NIST-JANAF Thermochemical Tables". In: *Journal of Physical and Chemical Reference Data*. Vol. 9. Washington DC: American Chemical Society, 1998.
- [34] I. Ansara, B. Sundman, and The Scientific Group Thermodata Europe (SGTE). *Computer Handling Determination of data*. Publishing house: Elsevier Science Pub. Co. Amsterdam, 1987, pp. 154–158.

- [35] J. Leitner, P. Voňka, D. Sedmidubský, and P. Svoboda. “Application of Neumann–Kopp rule for the estimation of heat capacity of mixed oxides”. In: *Thermochimica Acta* 497.1–2 (2010), pp. 7–13. ISSN: 0040-6031. DOI: 10.1016/j.tca.2009.08.002.
- [36] D. Wiedemann, E. M. Heppke, and A. Franz. “And Yet It Moves: A High-Temperature Neutron Diffraction Study of Ion Diffusion in the Inverse Perovskites BaLiX₃ (X = F, H, D)”. In: *European Journal of Inorganic Chemistry* 2019.48 (Dec. 2019), pp. 5085–5088. DOI: 10.1002/ejic.201901232.
- [37] G. D. Brunton. “Li₂ZrF₆”. In: *Acta Crystallogr. B* 29 (1973), pp. 2294–2296.
- [38] P. Dugat, M. E. Ghozzi, J. Metin, and D. Avignant. “Crystal Structures of Li₄ZrF₈ and Li₃Zr₄F₁₉ and Reinvestigation of the LiF–ZrF₄ Phase Diagram”. In: *J. Solid State Chem.* 120 (1995), pp. 187–196.
- [39] J. Laval and B. Frit. “Une nouvelle structure ordonnee derivee de la fluorine: Pb₃ZrF₁₀”. In: *Mater. Res. Bull.* 15 (1980), pp. 45–52.
- [40] A. L. Bail and J. P. Laval. “Synthesis and crystal structure of α -Ba₂ZrF₈ and Pb₂ZrF₈ determined ab initio from synchrotron and neutron powder diffraction data”. In: *Eur. J. Solid State Inorg. Chem.* 35 (1998), pp. 357–372.
- [41] J. P. Laval, R. Papiernik, and B. Frit. “BaZrF₆ α : Une structure a anion complexe [Zr₂F₁₂]⁴⁻”. In: *Acta Crystallogr. B* 34 (1978), pp. 1070–1074.
- [42] B. Mehlhorn and R. Hoppe. “Neue Hexafluorozirkonate(IV): BaZrF₆, PbZrF₆, EuZrF₆, SrZrF₆”. In: *Z. Anorg. Allg. Chem.* 425 (1976), pp. 180–188.
- [43] J. P. Laval. “The low-temperature barium fluoridozirconate variety α -BaZr₂F₁₀”. In: *Acta Crystallogr. C* 75 (2019), pp. 1482–1487.
- [44] J. P. Laval, B. Frit, and J. Lucas. “Crystal structure of the β -BaZr₂F₁₀ compound. Relations with the ReO₃-type and the fluorozirconate glasses”. In: *J. Solid State Chem.* 72 (1988), pp. 181–192.
- [45] C. W. Bale, P. Chartrand, S. Degterov, G. Eriksson, K. Hack, R. B. Mahfoud, J. Melançon, A. Pelton, and S. Petersen. “FactSage thermochemical software and databases”. In: *Calphad* 26.2 (2002), pp. 189–228.
- [46] I. D. Ratnikova, Y. M. Korenev, P. P. Fedorov, and B. P. Sobolev. “Phase Diagrams of BaF₂ - RF₄ systems (R = Zr, Hf)”. In: *Journal of Inorganic Chemistry* 42.2 (1997), pp. 246–251.
- [47] A. A. Babitsyna, T. A. Emelyanova, and A. N. Chernov. “Investigation of systems MF₂-ZrF₄ (M=Ba, Pb, Zn, Cd) (Russian)”. In: *Journal of Inorganic Chemistry* 34.12 (1989).
- [48] A. A. Babitsyna, T. A. Emelyanova, and E. G. Zhukov. “Phase relations in the PbF₂-BaF₂-ZrF₄ system”. In: *Inorganic materials* 42 (2006), pp. 1020–1022.
- [49] A. D. Pelton, S. Degterov, G. Eriksson, C. Robelin, and Y. Dessureault. “The modified quasichemical model I—binary solutions”. In: *Metallurgical and Materials Transactions B* 31.4 (Aug. 2000), pp. 651–659. ISSN: 1543-1916. DOI: 10.1007/s11663-000-0103-2.

- [50] O. Beneš, M. Beilmann, and R. J. M. Konings. “Thermodynamic assessment of the LiF–NaF–ThF₄–UF₄ system”. In: *Journal of Nuclear Materials* 405.2 (2010), pp. 186–198. DOI: 10.1016/j.jnucmat.2010.08.017.
- [51] A. D. Pelton and P. Chartrand. “The modified quasi-chemical model: Part II. Multicomponent solutions”. In: *Metallurgical and Materials Transactions A* 32.6 (June 2001), pp. 1355–1360. ISSN: 1543-1940. DOI: 10.1007/s11661-001-0226-3.
- [52] K. Mahmoud. “Mélanges fondus à base de fluorure de zirconium : Etude expérimentale à haute température et modélisation des fonctions thermodynamiques.” PhD thesis. Aix Marseille University, 1989.
- [53] K. A. Sense and R. W. Stone. “Vapor Pressure and Molecular Composition of Vapors of the RbF–ZrF₄ and LiF–ZrF₄ Systems”. In: *The Journal of Physical Chemistry* 62.11 (1958), pp. 1411–1418.
- [54] I. Nuta, C. Chatillon, H. Collas, L. Artaud, V. Guetta, and D. Heuer. “Vapor pressure measurements of LiF-ZrF₄ for Molten Salt Fast Reactor”. In: *Calphad* 51 (2015), p. 367.
- [55] M.A.Boukhalova. “Ternary systems of the Fluorides and Chlorides Sodium and Strontium”. In: *Izvestija Sektora Fiziko-chimiceskogo Analiza (Trans. Knowledge of the Sector of Physical and Chemical Analysis)* 26 (1955), pp. 138–146.
- [56] K. Taniuchi, T. Kanai, and A. Inoue. “Electrical Conductivities of Molten Salts of Some Binary Fluoride Systems Containing Lithium Fluoride”. In: *Journal of Japan Institute of Light Metals* 26.111 (1976).
- [57] K. C. Hong and O. J. Kleppa. “Thermochemistry of the liquid mixtures of the alkaline earth fluorides with alkali fluorides”. In: *The Journal of Physical Chemistry* 82.14 (1978), pp. 1596–1603.
- [58] R. J. M. Konings and D. L. Hildenbrand. “The vapor pressure, infrared spectrum, and thermodynamic properties of ZrF₄(g)”. In: *The Journal of Chemical Thermodynamics* 26.2 (1994), pp. 155–163. DOI: 10.1006/jcht.1994.1033.
- [59] Y. Luo, J. Dai, Q. Dou, H. Fu, and Q. Li. “Influence of free F⁻ anions on evaporation behavior of molten salts containing ZrF₄”. In: *Journal of Nuclear Materials* 561 (Apr. 2022), p. 153550. DOI: 10.1016/j.jnucmat.2022.153550.
- [60] C. J. Barton, H. A. Friedman, W. R. Grimes, H. Insley, R. E. Moore, and R. E. Thoma. “Phase Equilibria in the Alkali Fluoride-Uranium Tetrafluoride Fused Salt Systems: I, The Systems LiF-UF₄ and NaF-UF₄”. In: *Journal of the American Ceramic Society* 41.2 (Feb. 1958), pp. 63–69. DOI: 10.1111/j.1151-2916.1958.tb13520.x.
- [61] C. J. Barton, W. R. Grimes, H. Insley, R. E. Moore, and R. E. Thoma. “Phase Equilibria in the Systems NaF-ZrF₄, UF₄-ZrF₄ and NaF-ZrF₄-UF₄”. In: *The Journal of Physical Chemistry* 62.6 (1958), pp. 665–676.
- [62] H. A. Friedman, G. M. Hebert, and R. E. Thoma. *Thermal analysis and gradient quenching apparatus and techniques for the investigation of fused salt phase equilibria*. ORNL-3373. Oak Ridge National Laboratory, 1963.

- [63] Y. M. Korenev, A. V. Novoselova, K. K. Glinskii, and V. V. Shornikov. "A study of the LiF-ZrF₄ system". In: *Izvestiya Akademii Nauk SSSR, Neorganicheskie Materialy* 1.2 (0), pp. 201–203.
- [64] P. L. Brown, E. Curti, B. Grambow, and C. Ekberg. *Chemical thermodynamics of zirconium*. Ed. by F. J. Mompean, J. Perrone, and M. Illemassene. Vol. 8. Elsevier Amsterdam, 2005.
- [65] Junhua Xi and Yanwei Huang. "Pressure-Induced Phase Transitions of Hydrrous Zirconium Tetrafluoride". In: *Glass Physics and Chemistry* 45.2 (2019), pp. 133–137. ISSN: 1608-313X. DOI: 10.1134/S1087659619020123.
- [66] A. L. Smith, E. Capelli, R. J. M. Konings, and A. E. Gheribi. "A new approach for coupled modelling of the structural and thermo-physical properties of molten salts. Case of a polymeric liquid LiF-BeF₂". In: *Journal of Molecular Liquids* 299 (2020), p. 112165. ISSN: 0167-7322. DOI: 10.1016/j.molliq.2019.112165.
- [67] A. L. Smith. "Structure-property relationships in actinide containing molten salts – A review: Understanding and modelling the chemistry of nuclear fuel salts". In: *Journal of Molecular Liquids* 360 (2022), p. 119426.
- [68] G. Hatem, F. Tabaries, and M. Gaune-Escard. "Enthalpies de Formation des Mélanges Liquides ZrF₄-MF (M=Li, Na, K, Rb)". In: *Thermochimica Acta* 149 (1989), pp. 15–26.
- [69] I.-C. Lin, A. Navrotsky, J. Ballato, and R. E. Riman. "High-temperature calorimetric study of glass-forming fluorozirconates". In: *Journal of Non-Crystalline Solids* 215.2-3 (July 1997), pp. 113–124. DOI: [https://doi.org/10.1016/S0022-3093\(97\)00081-1](https://doi.org/10.1016/S0022-3093(97)00081-1).
- [70] Y. Gao, J. Guery, and C. Jacoboni. "ChemInform Abstract: Crystal Structure Determination of LiBaZr₂F₁₁." In: *ChemInform* 24.8 (1993). ISSN: 1522-2667. DOI: 10.1002/chin.199308012.
- [71] K. Wang and P. Chartrand. "The modified quasichemical model in the Distinguishable-Pair Approximation for multicomponent solutions". In: *arXiv preprint arXiv:2202.02588* (2022).
- [72] A. Mourogov and P. Bokov. "Potentialities of the fast spectrum molten salt reactor concept: REBUS-3700". In: *Energy Conversion and Management* 47.17 (2006), pp. 2761–2771. DOI: 10.1016/j.enconman.2006.02.013.

4

MANAGEMENT OF GASEOUS FISSION PRODUCTS AND METALLIC PARTICLES

To minimize the impact of gaseous and metallic fission products in the core of a Molten Salt Fast Reactor (MSFR), the most mature technique investigated is the in-core removal of these neutron poisoning elements by helium bubbling. The helium bubbling system has the advantage of potentially removing solid insoluble noble and semi-noble metallic particles, and represents a method to extract valuable materials (such as palladium, rhodium, molybdenum...). To build a reliable model for the extraction process in a MSFR, a preliminary experimental study was carried out on the extraction of simulant fluorescent nanoparticles in a bubbling column with a water based simulant fluid, mimicking the fluid dynamical properties of the molten salts. The concentration of the particles and the location of the bubbles were measured simultaneously in a simulant air bubbly flow with a Laser Induced Fluorescence (LIF) system, allowing an observation at nano-metric scale. The objective of this work was two-fold: (i) the collection of experimental result leading to better understanding of sub-micron particles behavior in molten salt flow, and (ii) to support simultaneous modeling efforts in OpenFOAM, employing a three-phase Eulerian model for the simulation of particles, bubbles, carrier fluid and their interaction.

4.1. INTRODUCTION

A MAJOR challenge for an efficient operation of the MSR on the long term, is the control and the extraction of insoluble particles, such as noble or semi-noble metals, and neutron poisoning gaseous fission products. The MSRE (ORNL) suggested the use of a flotation process to remove particles from the core, using an inert gas: helium [1, 2]. This idea is one of the leading concept investigated for the MSFR design and particularly in the SAMOSAFER project.

4.1.1. LITERATURE REVIEW

From the first experiment of the MSRE, it was observed than most of the metallic particles in suspension in the molten salt flow were accumulated on the different cold parts of the reactor, mainly on the graphite moderator bulk [3]. The removal of neutron poisonous gas (such as xenon and krypton) took place through an integrated pump ensuring flow in the circulation loop. A pressure relief space under the pump allowed gas to enter this chamber and to be removed from the operating loop. The concept of the helium bubbly flow injection in the operating reactor was conceptualized during a later stage of the project. However, the results observed were not substantially different than those of the primary experimental observations.

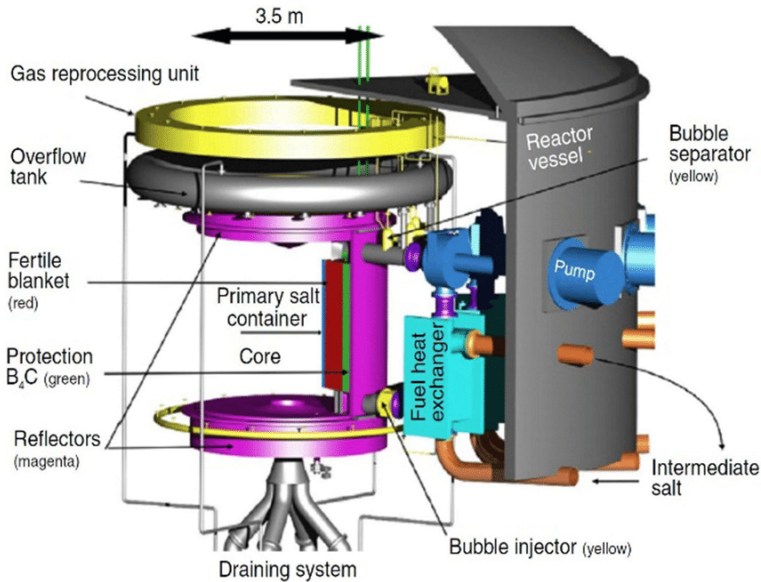


Figure 4.1.: Schematic representation of the reactor vessel of the concept of Molten Salt Fast Reactor [4]. The integrated helium bubbling system is shown in yellow including the bubble injector, bubble separator and the gas reprocessing unit.

In the framework of the development of the Molten Salt Fast Reactor, the design of which does not include a graphite moderator, the concept of in-core helium bubbling

to remove gaseous fission products as well as solid particles from the reactor has been reintroduced [5]. The European project SAMOFAR defined a preliminary design of breeder reactor with a central core surrounded by multiple circulation loops. To remove fission gas, noble and semi-noble metallic fission products, a continuous on-line bubbling flow was implemented to drive poisonous products out of the fuel, through an overflow tank (see Figure 4.1) [4]. The following European project, SAMOSAFER, including this thesis work, kept the same initial design.

4.1.2. MICRO-SIZED PARTICLES INVESTIGATIONS

Molten salts investigated as fuel and/or coolant, such as FLiBe, FLiNaK or LiF–ThF₄–UF₄ (77.5-19-3 mol%), operate in a range of temperature between 873 K and 1073 K. Consequently, the experimental work on liquid salt remains very complex in laboratory conditions. The development of different simulation tools is a necessary step to observe and analyze the flow behavior associated with a bubbly flow at high temperature.

The first feasibility study of the process, associating experimental work and simulation, was performed for different micro-sized particles by Capelli [6]. The molten salt fluid was simulated by a mixture of water and glycerol (41.6 wt%). This liquid presents a comparable dynamic viscosity at 293 K with that of the experimental dynamic viscosity of FLiNaK salt at 900 K. The major interests of this solution are its transparency, the neutral chemical activity, and an accurate knowledge of its kinematic viscosity. During Capelli's work, the removal of micro-sized metallic particles (from 0.1 μm to 149 μm) by a helium bubbly flow was studied, and first preliminary experimental observations for removal of nanoparticles of molybdenum (average size 50 nm) were made. The performance of the bubbling system was studied for sub-micron particles of molybdenum using a flotation column with a Hallimond tube [7]. A maximum extraction efficiency of approximately 45% was measured for 5 micron particles at a gas flow rate of 10 sccm (standard cubic centimeter), around 20% for the 1.5 microns particles, and 10% for the 0.1 microns particles at the same flow rate. At higher flow rate, a general increase in the efficiency of the removal of the particles was moreover observed.

Furthermore, in Capelli's work, a detailed evolution of the particles' size distribution in molten fluoride salt was experimentally determined. Molybdenum particles of 35 - 45 nm were mixed and diluted in a solution of FLiNaK for a duration of 72 hours at 973 K. Measurements by Scanning Electron Microscopy at room temperature after the experiment, indicated an average size of the particles around (418 \pm 50) nm. This study confirmed that coarsening of metallic particles was taking place in the salt at high temperatures, but remained limited and consequently the importance of the comprehension and quantification of the removal of nanoparticles by helium bubbling.

4.1.3. OBJECTIVES OF THIS WORK

This thesis chapter focuses on the particle removal, and building upon Capelli's work, with a particular interest for a range of smaller particles, expected in the core

of the reactor, namely nanoparticles.

The observation of nanoparticles comes with new challenges. The direct observation using a high resolution camera, is impossible due to a lack of resolution. In this work, Laser Induced Fluorescence (LIF) was used and a setup was developed. This technique allows to observe the flow and concentration of nanoparticles, selected for their property of fluorescence, directly in the liquid flow, thanks to the fluorescent emissions induced by laser illumination.

This chapter presents in further detail the design and the experimental method used to obtain data on the removal nanoparticles by helium bubbling in a molten salt flow. Here, the evolution of the concentration of nanoparticles in a bubbly flow recovery system is measured, with the objective to obtain the amount of particles effectively removed under those conditions. These data were moreover the foundation of the simulation work performed in OpenFOAM in collaboration with NRG within the SAMOSAFER project [8].

4.2. NANOPARTICLES OBSERVATION IN A BUBBLY FLOW

4.2.1. LASER INDUCED FLUORESCENCE

LIF is a spectroscopic method based on the spontaneous emission of light induced by the excitation of molecules by a laser. It can be described as a two-step process: absorption of a photon from a monochromatic laser, then followed by the emission of a fluorescent photon from the excited states of the absorbing center. Mainly used for studying flow and particle tracing, here the essential interest is to allow the observation of the concentration of nanoparticles, which are too small to be observed individually by a camera [9].

EXPERIMENTAL DEVICE

The system from LaVision[®] (as shown in Figure 4.2) is composed of a Nd:YAG pulse laser source with an emission wavelength of 532 nm, and an Imager MX 4MP CMOS high resolution camera (2048 x 2048 pixel, 180 frames per second), a filter for the camera with a bandwidth of 590nm-610nm which permits to select the particular emission of the Nile Red particles used in this work (as shown in the Figure 4.3). Calibration and measurement are performed by the software DaVis 8.4 (LaVision[®]).

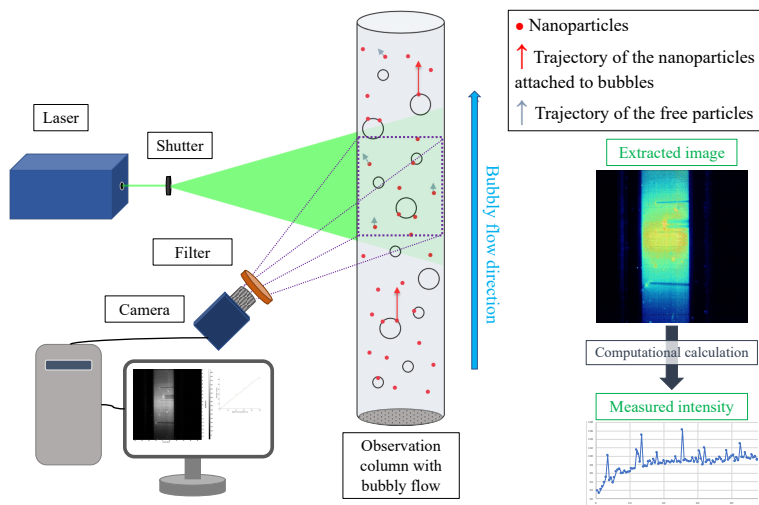


Figure 4.2.: Schematic representation of the LaVision[®] Laser Induced Fluorescence imaging setup mounted on the observation column designed in this work.

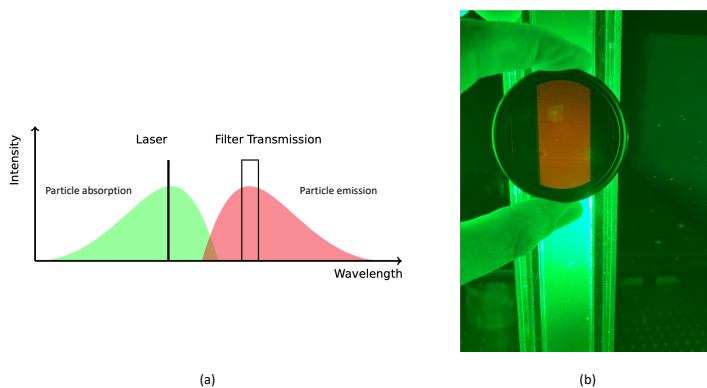


Figure 4.3.: (a) Graphical representation of the absorption/emission wavelengths of a particle under a monochromatic illumination with the associated filter from LaVision[®]. (b) Photography showing the selectivity of the BP 600 nm filter (LaVision[®]), on Nile Red nanoparticles (250 nm size average) in suspension in water under 532 nm illumination (green).

LIGHT INTENSITY MEASUREMENTS

The calibration of the particles' concentration is established before each measurement by incremental addition of equivalent volumes of the colloid homogeneous solution of nanoparticles (i.e., the exact same number of particles for each addition), in absence of bubbles. The amount of detected light, or measured intensity, is directly proportional to the actual concentration of particles in solution, as observed in Figure 4.4. The linear dependence of the form $I = A \cdot C$, where I is the relative measured intensity, A is a constant characterizing the slope, and C is the sample concentration. This first-order approximation between measured intensity and actual concentration allows to compute a calibration curve (Figure 4.4 (b)). From this calibration curve, a direct determination of the concentration is possible in follow-up experiments.

4

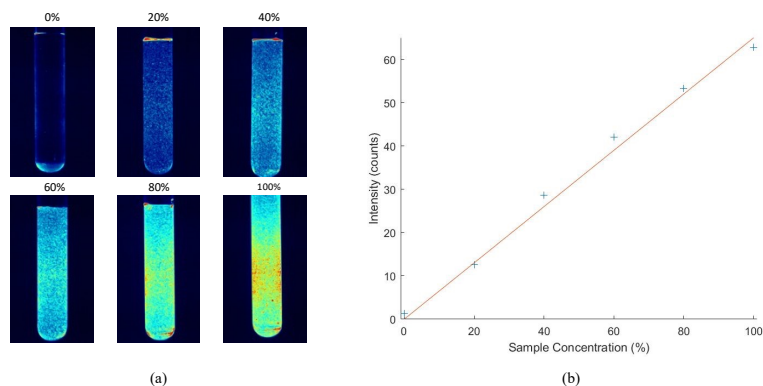


Figure 4.4.: (a) Example of calibration images with a volumetric gradient of nanoparticles ($0.87 \mu\text{m}$ size avg.) concentration in static vial, collected with DaVis software (a color treatment was applied on the images). (b) Calibration curve established with samples of known concentration.

4.2.2. SETUP AND MATERIALS

OBSERVATION COLUMN

The observation column was inspired by the initial setup designed by Capelli during her work at TU Delft [7]. The experimental measurements were carried out in a PMMA (poly(methyl) methacrylate) cylindrical central column (Dimensions: $H = 475 \text{ mm}$; $\varnothing = 25.7 \text{ mm}$), filled with a simulant liquid, surrounded by a squared external column, itself filled with deionized water (Figure 4.5). This specific shape allows to limit image distortion by refraction of the laser light [10, 11]. The bottom of the column is connected to a bubble sparger, producing bubbles coming from the gas introduced through a disk-shaped sintered metallic filter (SIKA-R3, $\varnothing = 26 \text{ mm}$,

height = 3 mm) with 3 μm pore size.

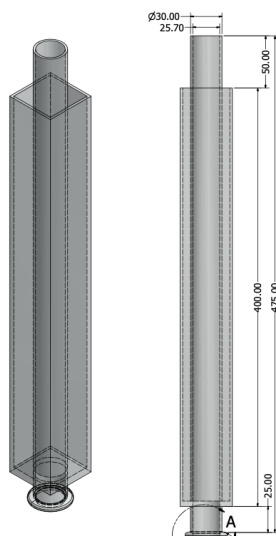


Figure 4.5.: Technical sketch of the in-house designed observation column in PMMA, with a central cylindrical column (connected to the bubble sparger in A), and the surrounding squared column, limiting the refraction of the laser light.

The gas used in this work is air, considering that the nature of the gas weakly impacts the bubbling conditions. The density of gas is so low compared to that of the liquid, that in most equations governing the flow dynamics in bubbly flow, it is negligible. The gas flow is controlled by a mass flow controller (Bronkhorst Series F-201CV, 0-500 sccm Air). Laminar flow was observed for a range of flow rates from 0 to 50 sccm (standard cubic centimeter per min), which was the experimental window used in this work.

SIMULANT MATERIALS

Because the water/glycerol solution induces a very high level of light disturbance during bubbling as well as a retention of bubbles at the interface, leading to a progressive accumulation during the process, the simulant liquid used in this work was demineralized water during the particles measurement. A solution of aqueous glycerol (41.6 wt%) was also used to explore the properties of bubbling in more viscous fluid.

SPHERO Fluorescent Nile Red particles (Spherotech) were selected for their fluorescent property. They are characterized by a specific emission wavelength of $(600 \pm 10 \text{ nm})$ under a monochromatic illumination of 532 nm (green laser). Four different calibrated sizes were used in this work: 0.25, 0.53, 0.87 and 2.11 μm average. The density of these particles is 1.05 g cm^{-3} . The second essential characteristic for

the particles selected in this work is the hydrophobicity, in order to reproduce this property of the metallic particles. As no colloidal fluorescent metallic nanoparticles were available from the different commercial suppliers, experiments on the attempts of gold and molybdenum nanoparticles with Rhodamine 6G were performed in this project [12]. Some tries have shown interesting fluorescent properties of the solution, but the observation scale of the setup did not allow a clear confirmation of the presence of fluorescent metallic nanoparticle with uniform sizes in the solution. Moreover, the surface properties of the particles seemed affected by the adsorption of rhodamine functions, leading to the coalescence of the particles in clusters.

4.2.3. BUBBLING CHARACTERISTICS

Considering that all the measurements are related to the intensity of the measured light, the impact of the bubbles on the measured signal has to be taken account. Indeed, the bubbles reflect the laser light on their surface which can significantly impact the accuracy of the concentration determination.

GAS HOLDUP EVOLUTION

In order to understand the gas holdup, the volume fraction occupied by the bubbles were empirically defined . The superficial gas velocity, describing qualitatively the flow velocity, was observed to be proportional to the gas flow rate. This means that the gas flow rate can be used as a measure of the bubble velocity. Both simulant fluids show reasonable agreement with literature according to the bubbly flow regime [13, 14]. 40 sccm was the maximum gas holdup result observable by the Matlab's bubbles identification and counting program used in this work. Moreover, the gas holdup reached 30% in the aqueous glycerol, and approximately 10% in the water for a gas flow rate of 40 sccm. The higher viscosity of the glycerol solution increased the bubble residence time, leading to a gas holdup three times as high as in water. The gas holdup in water increased as a function of the gas flow approximately in a linear fashion. Considering that the bubbles show a diameter with a small bandwidth, as seen in Figure 4.6, the number of bubbles increases linearly with the gas flow rate in water. From the results above, a corrective equation of the luminosity of the bubbles can be applied to the concentration measurements to correct for the impact of the bubbles (more detail can be found in the BSc report of Grooten [15]).

The mass flow controller (Bronkhorst EL-Flow Select) controls the flow rate from 10 to 500 sccm with 0.5% accuracy according to the supplier. For the measurements done in this work, measurements below 15 sccm are more representative of the process conditions; where the calculated void fraction was of approximately 1.5% in the column, which is comparable with the maximum void fraction for the MSFR reactor of 1.308% calculated thanks to multiphysics simulation of the helium bubbling [16]. The gas holdup measurements showed a standard deviation of 0.40% and 0.15% for 4 and 8 sccm, respectively. However, the general uncertainty on the flow rates was considered at 0.5% for all the 5 to 40 sccm range.

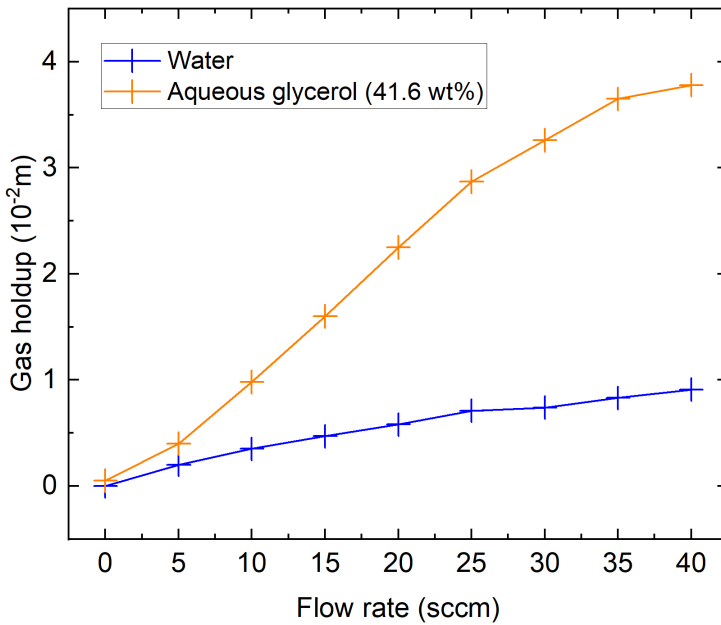


Figure 4.6.: Gas holdup evolution as a function of the flow rate in the observation column for the water and the aqueous glycerol solution (41.6 wt%).

SIZE DISTRIBUTION OF THE BUBBLES

The bubble diameter was investigated as well as their evolution as function of the gas flow rate. To visualize the bubbles, a standard imaging mode of the camera was operated [17]. The gas flow rates that were selected ranged from 5 to 40 sccm in steps of 5 sccm. For each selected gas flow rate, 60 images were collected and the average gas holdup and bubble diameter were calculated with the help of the bubble detection algorithm introduced as described in further detail by Lakerveld in his MSc thesis report [14].

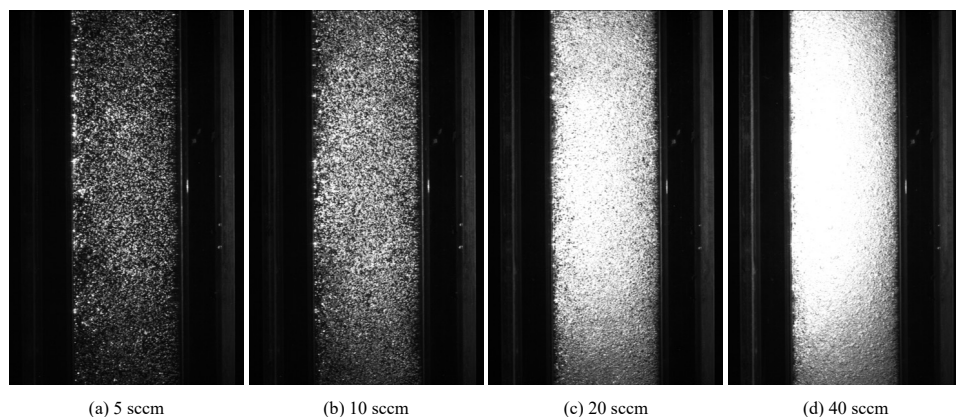


Figure 4.7.: Images of the bubbly flow with gas flow rates of (a) 5 sccm, (b) 10 sccm, (c) 20 sccm and (d) 40 sccm collected with DaVis software.

The algorithm first loads the images, and then searches for the bubbles as circles. The detected circles with a certain diameter and area were used to calculate an average diameter and gas holdup. The simulant fluids under consideration were an aqueous glycerol solution (41.6 wt%) and water. As detailed by in Lakerveld [14], the average bubble size was depicted for each fluid as function of the gas flow rate. An increase of the average bubble diameter was observed in aqueous glycerol solution with the increase in flow rate, i.e. from 0.63 mm at 5 sccm to 0.69 mm at 40 sccm. In contrast the bubble average diameter was almost constant in water: 0.71 mm.

IMPACT OF THE ILLUMINATION BUBBLES ON THE PARTICLE CONCENTRATION

Concentration measurements were realized for a range of gas flow rates in solutions from 0% to 100% particles relative concentration, controlled by the amount of particles added in the column (measured at 0 sccm). The water and the glycerol solutions were compared. The measurements in water showed a linear trend for the bubble correction curves, in agreement with the linear increase of the amount of bubbles in column and the intensity of the reflected light increasing linearly. Figure 4.8 shows the measurement points and fits for water, while Figure 4.9 shows those for 41.6 wt% glycerol. The "measured concentration" is the concentration measured while bubbling. The pre-determined concentrations are the concentrations that are

to be expected when measuring without reflection of fluorescent light by the bubbles for the solution at rest.

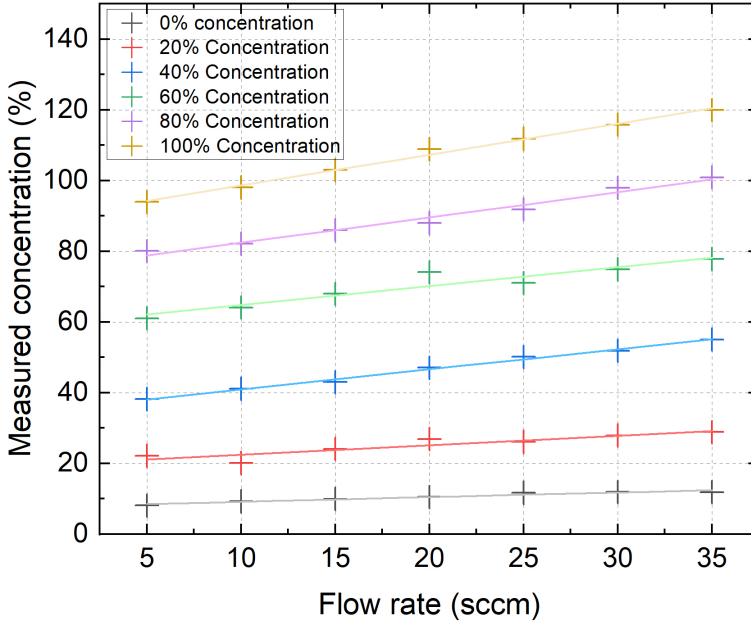


Figure 4.8.: Evolution of the impact of fluorescent light by bubbles on concentration measured by LIF as a function of the different flow rates, in water with 250 nm polystyrene nanoparticles.

Figure 4.8 shows that the relation between measured intensity and flow rate is linear in water up to 35 sccm. In Figure 4.9, it is also shown that this is not the case for 41.6 wt% glycerol up to 35 sccm. This was explained by the higher gas holdup in the more viscous 41.6 wt% glycerol. From 20 sccm on, it was impossible to discern any separate bubbles in the bubble column.

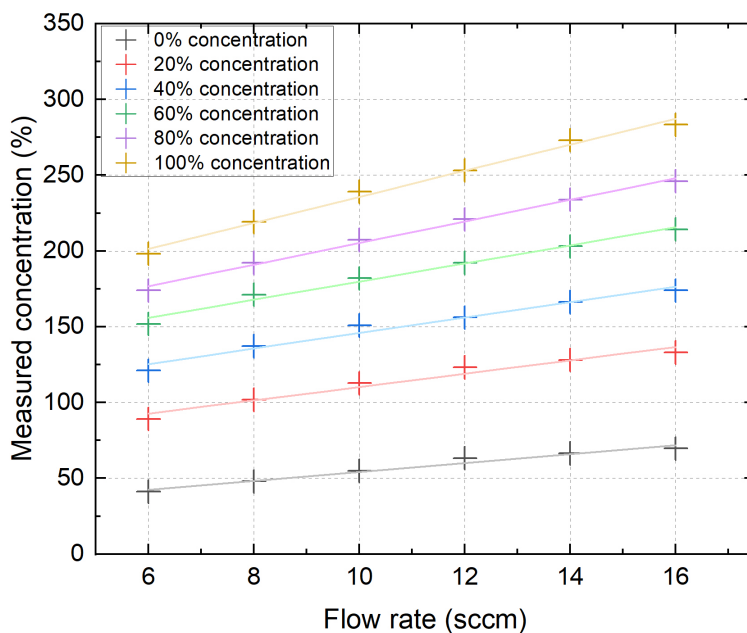


Figure 4.9.: Evolution of the impact of fluorescent light by bubbles on concentration measured by LIF as a function of the different flow rates, in solution glycerol/water (41.6 wt%) with 250 nm polystyrene nanoparticles.

4.3. PARTICLES COLLECTION TECHNIQUES

The method of collection of the particles is a Hallimond tube (Figure 4.10), which is a good laboratory scale mock-up of the conceptual design geometry investigated for the MSFR in-core helium bubbling extraction system, as proposed by Capelli [6].

4.3.1. EFFECT OF THE HALLIMOND TUBE ON THE EXTRACTION EFFICIENCY

The Hallimond tube is a glass tube with a curvature angle of 115° , and a conical inlet with a manual valve at its bottom part (See Figure 4.10). When the bubble/particle aggregates reach the top of the bubbling column, the bubbles will collapse and release attached particles in a dedicated reservoir. A valve closes the reservoir and allows the collection of the extracted particles from the solution. This design has demonstrated its performances for the collection of the micro-sized particles ($3\ \mu\text{m}$ to $149\ \mu\text{m}$) and is a good option to reduce re-circulation and the fraction of particles flowing back into the column [18].

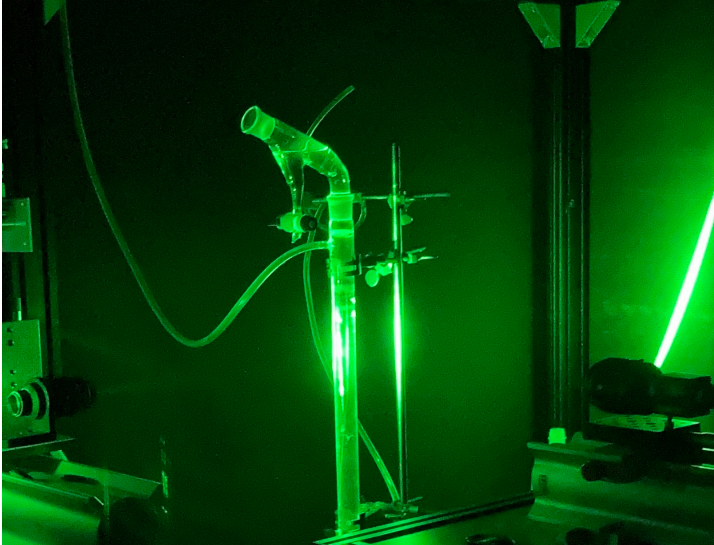


Figure 4.10.: Observation setup equipped with the Hallimond tube under laser illumination.

Different measurements were realized, with different sizes of nanoparticles and flow rates, as well as different conditions of concentration and illumination as well as simulant fluids. After full homogenization of the solution, no clear reduction of the concentration was observed during the bubbling for the nanoparticle solutions (250 nm, 530 nm and 870 nm). As seen for example in the case of the 250 nm nanoparticles in Figure 4.11, no clear reduction of the concentration can be observed. From the initial (-5 min) to the final (35 min) points, in both solutions

(regardless the viscosity), the concentration remained stable and did not show variations during the bubbling (from 0 min to 30 min).

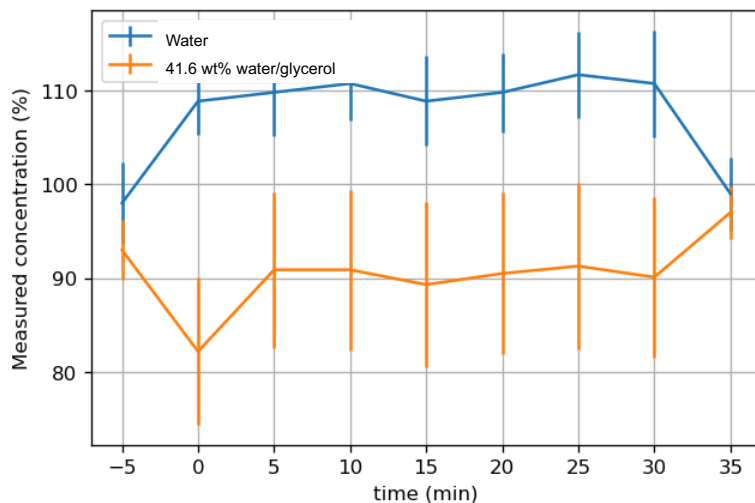


Figure 4.11.: Corrected relative concentration evolution over time of the 530 nm polystyrene nanoparticles in water and 41.6 wt% glycerol in the bubbly column (flow rate: 20 sccm) measured by LIF.

Despite the modifications and multiples experiments, the Hallimond system did not prove its effectiveness in the present experimental conditions, and did not allow to confirm the preliminary results obtained by Capelli with the nanoparticles of molybdenum. In fact, this device that uses gravity to concentrate the removed particles in the conical outlet, is probably less efficient in general for nanoparticles of low density, and especially for the polystyrene particles used in this work. Surface dyeing of metallic particles of gold, silver and molybdenum were tested to compare with higher density nanoparticles. But these experiments did not meet the fluorescence properties to perform Laser Induced Fluorescence measurements. Since the Hallimond tube did not perform as required for the removal of nanoparticles with the actual experimental setup, others methods of separation were investigated.

4.3.2. RESEARCH ON ALTERNATIVE SYSTEMS

Alternative systems of particles removal were investigated to solve the open issue of the extraction of nanoparticles from the column.

NO FILTRATION

The objective of the first set of experiments, where no specific filtration system was put in place, was to observe local displacement of particles from the bottom to the top of the column, by determining the proportion of particles delocalized

during the bubbling. The aim was to confirm that the removal of particles from the column can take place without extraction device. Measurements were performed quasi-simultaneously at the lowest observation window of the column and at the highest observation window. Images were taken at different stages of the experiments: before, during and after the bubbling.

The relative concentrations was based on the initial setting of the concentration and are strongly dependent on the position of the laser and observation window, which are affected by the position changing on the horizontal axis on 30 cm (from the bottom to the top of the column). Considering the homogeneous distribution of the particles in the column, the concentration was found equal all along the column. So, at $t = 0$ min, initial conditions, the concentration is the same at the bottom or the top of the column even if the measured concentration (125% and 93%) is different because of the different light conditions.

It was observed that the concentration is stable throughout the column, even during the bubbling. Considering the empirical observation that particles attached to some bubbles, it can be concluded that the particles reaching the top are transported back into the solution without removal at the top due to the back flow of particles.

SOLID FILTRATION

The next investigated method was the use of filter paper on top of the bubble column. The particles should be either trapped in its pores, or the particles should pass through and not return back towards the bottom of the column. The gas could be trapped underneath the filter, however, which would significantly block the flow. To determine how the filter influenced the gas buildup under the filter, it was checked whether there was bubbling above the filter at the used gas flow rates (from 6 to 10 sccm). Concentration measurements were conducted, in 41.6 wt% glycerol without particles, demonstrated its efficiency, while in water a continuously declining trend was observed but was not found to be reproducible. It was concluded that this method with this type of filter was also not effective to remove particles from the column. In the case of glycerol, possible explanations of the ineffectiveness could be found in the composition of the filter paper, which is cellulose and lignin, that may react with the glycerol (which might occupy the chemical site limiting the particle adsorption). Alternatively, the paper saturation with water, and the repellent surface tension forces between the now hydrophilic paper and the hydrophobic polystyrene particles might inhibit the particles adhesion to the paper. If considering the theory that the particles pass through the filter and do not return, the fluid might also have occupied the voids in the filter, which would trap the particles below the filter.

4.3.3. LIQUID FILTRATION

One challenge in this work was to define a clear boundary at the top of the system that could be used in numerical modeling. An alternative concept was designed and developed in this work and is described below. This concept enforces that particles that leave the column will not return, i.e., being an advective boundary condition for particles.

CONCEPT

The principle is to fill the column with two completely immiscible liquid solutions: an aqueous solution at the bottom of the column and an organic solution (such as oil) in the superior part, that is deposited on the surface of the first solution. The particles are in suspension in the aqueous solution and the bubbling is introduced as described above. Obviously, the organic solution is selected with a lower density than the aqueous solution. During the bubbling, the particles attach to the bubbles and go up the column and through the second liquid to the interface with air. The main aim of this method is to provide an advective boundary condition for the particles and to influence the flow dynamics in the aqueous phase as little as possible. The concept is described in the sketch figure below.

4

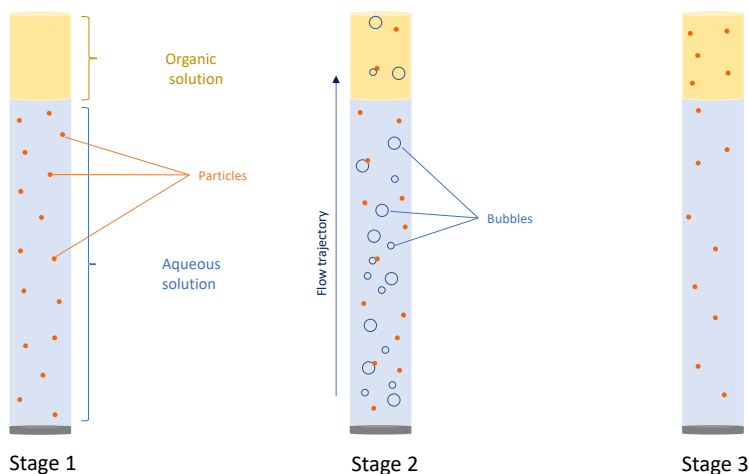


Figure 4.12.: Sketch of the 3 steps of the Liquid filtration concept.

PARTICLE RETENTION IN THE ORGANIC PHASE

The organic solution has to be selected to minimize the resistance at the interface. Basically, the bubble should not be stopped by the oil layer by surface effects, hence cross it without motion interruption. The selection of an oil with low viscosity is therefore necessary. Under a continuous bubbling flow, coalescence of the bubbles was observed at the interface with a flow rate above 20 sccm. Below (between 5 and 20 sccm), no accumulation of bubbles was seen, even after 4 hours of bubbling.

The question that arises was the effectiveness of the retention of particles is by the organic solution. In the case of hydrophobic particles, this retention was ensured by

the nature of the solution itself, naturally hydrophobic too. An empirical observation was realized in this work. A volume of polystyrene fluorescent particles was diluted in a solution of oil until a uniform colloidal solution was obtained. The solution of oil/particles was superposed to the aqueous one in the bubbling column. Then the flow rate was varied (from 5 to 200 sccm) and the LIF system was used to control the interface variations. Even with the highest intensity of bubbling, no transport of the particles was observed into the aqueous solution, confirming the stability of the simulant particles in the organic solution and the efficiency of the liquid system for the retention of particles.

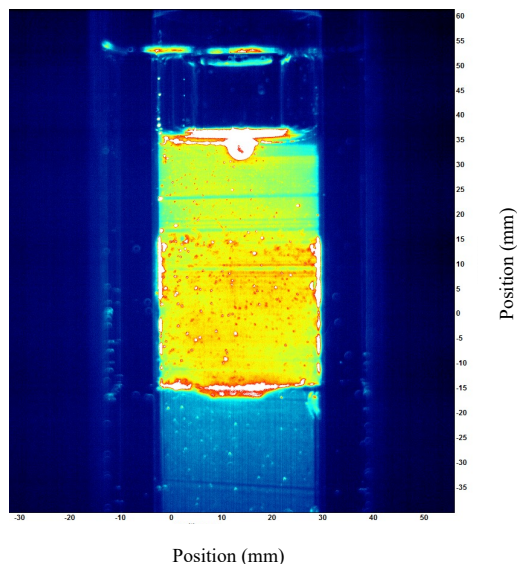


Figure 4.13.: Image of the interface of the two phases after the bubbling collected by LIF (a color treatment was applied). The nanoparticles can be distinguished in both phases. The particles in the organic phase (top) are immobile whereas the particles are in motion in the aqueous phase (bottom).

Secondly, it was verified that without any bubbling, particles in the aqueous solution do not reach the organic phase. Different biphasic solutions were tested, for different stirring and for different periods (from hours to week). No particle exchange was observed between the phases. Hence, it may be concluded that in the experiments, particles are merely transported from the aqueous phase to the organic phase by bubbles.

INTRINSIC LUMINOSITY OF THE OIL

The oils used in this work, being mainly natural alimentary oils, are yellow colored. These oils induce fluorescence under the laser exposition as shown in Figure 4.13.

The intrinsic luminosity can be considered as constant in each experimental setup and did not affect the evolution of the light intensity during the bubbling in the observation window.

4.3.4. LIQUID FILTRATION EXPERIMENTS

EXPERIMENTAL PARAMETERS

In this work, sun flower oil showed the best properties regarding particle retention and low disturbance of the bubbles while passing the interface. The particles (250 nm, 530 nm and 870 nm) used in these experiments are the same as presented above. Considering the linearity of the number of bubbles as function of the flow rate and stability of the bubbles size, the water was chosen as aqueous simulant fluid.

The objective was then to measure the removal efficiency of particles as function of the nanoparticle size and the gas flow rate. In this work, three different flow rates were used: 5, 10 and 15 sccm, more representative of the process conditions and limiting the formation of a foamy layer at the interface oil/water, which could occur after a few hours of observation. Considering that the maximal removal efficiency is expected during the first 30 minutes of the process, the measurements were performed for 2 hours.

The measurements started with a first 100 images collection of the initial aqueous solution before introducing bubbles, and after the colloid solution was homogeneous. During the bubbling, 100 images were collected every 5 minutes for the first 30 min and every 30 min for the last 1h 30. When the bubbling stopped, a last series of 100 images was collected after complete stabilization of the solution (no remaining bubbles and homogeneity of the particles).

The height of the aqueous phase was fixed at 35 cm above the bubbling sparger and the organic solution height at 5 cm. All the measurements were realized in the same setup, with the same light calibration (pulsed, exposition time 10,000 μ s). The initial concentration of particles in the aqueous solution in each solution was fixed to 100 ± 10 ppm, or 0.5 mL of the commercial solutions. These are higher concentrations than investigated in the MSFR safety study, but present the most accurate observations in the present setup.

DATA TREATMENT

For each series of 100 collected images at each measurement, an increase of the measured light intensity was observed in the first 40 images due to the warming up of the laser. The measured intensity light was stable on the last 60 images; thus, the results were extracted from these images. For the initial and final stage of the experimental observation (without bubbles), measurements of the light intensity were very stable with a very low variability. The concentrations could be extracted directly from the calibration curve (as presented in Figure 4.4). For each measurement, an average light intensity was determined from those 60 images, but it was observed that some peaks of high intensity were observed in the results (see Figure 4.14). By analysis of the images measured, it was observed that these

peaks were caused by bubbles reflecting the light in the observation window thereby increasing the intensity measured on the particular point. These measurements were removed from the average, reducing the standard deviation and uncertainty as shown in Figure 4.15.

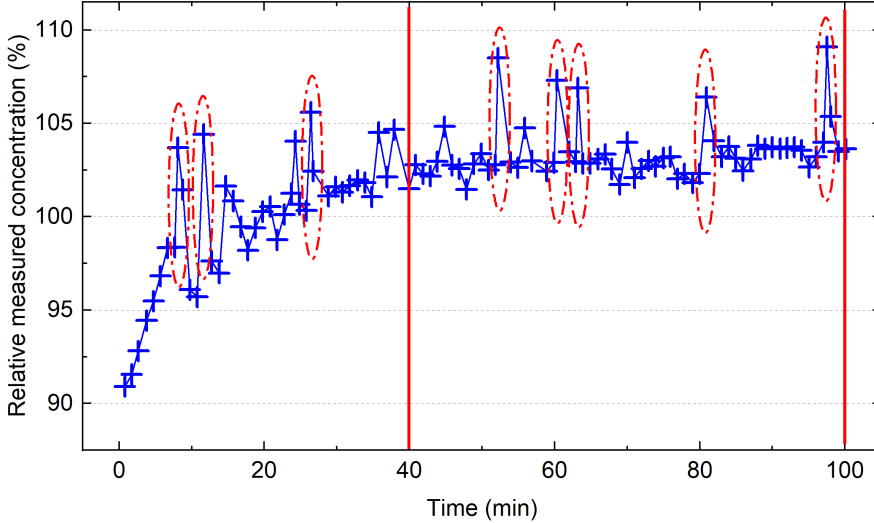


Figure 4.14.: Concentration measurements for 100 successive collected images with the aberrant intensities (circled peaks), for the 870 nm particles with a 10 sccm flow rate (after $t = 15$ min). The average concentration for the entire measurement was measured at 96.0%, on the images range of stability of the light intensity (40 to 100, between red lines) measured at 99.5%. The standard deviation was calculated at 1.4%.

Two types of measurements were considered: the initial/final measurements and the intermediate measurements. The initial and final measurements were performed at $t = 0$ (before any bubbling) and $t = 120$ min (after the end of the bubbly flow) respectively, so with mostly no bubbles in the observation window. The intermediate measurements were performed during the active bubbling. These measurements were therefore impacted more by the bubble's disturbances on the measured light intensity (shadow or reflection on the bubbles). For this reason, the initial and final measurements could not be compared directly with the intermediates. The concentration calculated for the initial measurement is compared to the concentration calculated in the final measurement to get the extraction rate after 120 min, according to the following equation:

$$\text{Extraction rate}_{120}(\%) = \frac{C_{Initial} - C_{Final}}{C_{Initial}} \quad (4.1)$$

As the bubbly flow was homogeneous, the intermediate measured relative

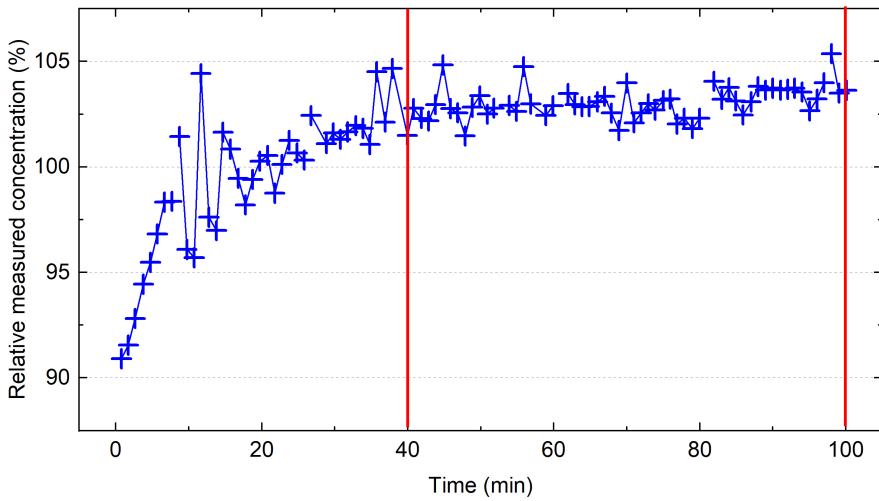


Figure 4.15.: Concentration measurements for 100 successive collected images after the removal of the aberrant intensities (circled peaks), for the 870 nm particles with a 10 sccm flow rate (after $t = 15$ min). The average concentration for the entire measurement was measured at 95.4%, on the images range of stability of the light intensity (40 to 100, between red lines) measured at 99.4%. The standard deviation was calculated at 0.58%.

concentrations were calculated to describe the direct evolution of nanoparticles concentration over time, during the bubbling, and the fitted equation transposed to a final extraction rate results curve, after correction of the impact of bubbles on the intensity value. The final result is a good representation of the removal of particles after two hours with the extraction rate as a function of time as shown in Figure 4.16, where the initial and final concentrations were determined at 0 and 120 min, respectively, and the intermediate points were issued from the transposition of the intermediate measured concentrations. An indicative fitted curve could be derived to describe extraction rate as a function of time (Figure 4.16), nanoparticle size and bubbly flow rate. As described in Capelli's work [7], the removal of particles as a function of time can be described as a logarithmic function. The results presented here tend to confirm this behavior and the fitting were derived with the fitting tool of the software OriginPro®.

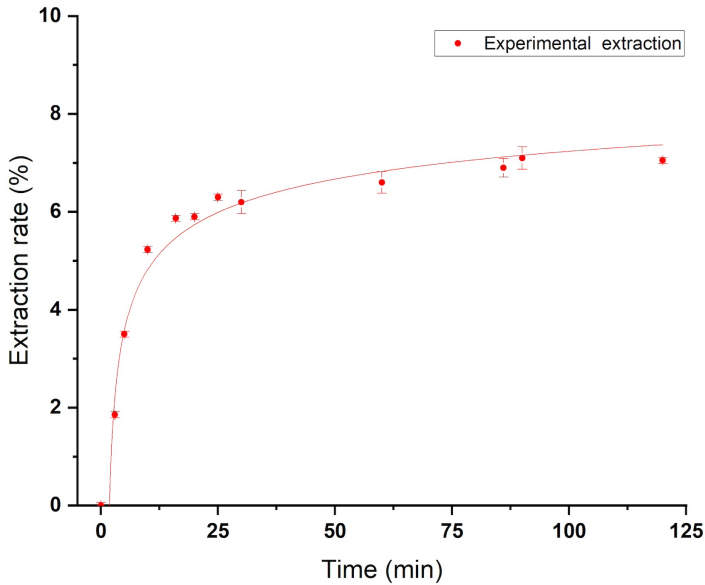


Figure 4.16.: Experimental extraction rate vs time (red points) with the superposed fitting curve (red line) for the 530 nm nanoparticles with a 15 sccm flow rate by OriginPro®.

EFFECTIVENESS OF THE TECHNIQUE

To confirm the efficiency of the setup for the removal of particles, a first test was realized with micrometer size fluorescent particles ($2.11 \mu\text{m}$), in order to compare with the precedent assessment on the extraction realized by Capelli with metallic

micro-sized particles into the Hallimond tube device [19]. The average removal efficiency of 14% (considering the initial concentration as 100% even if the relative concentration is measured at 73%) after 30 min of a 10 sccm flow rate bubbling is very comparable with the results of 15% obtained in the precedent work of Capelli. The method of the liquid filtration therefore provides comparable results with the classic overflow method (Figure 4.17).

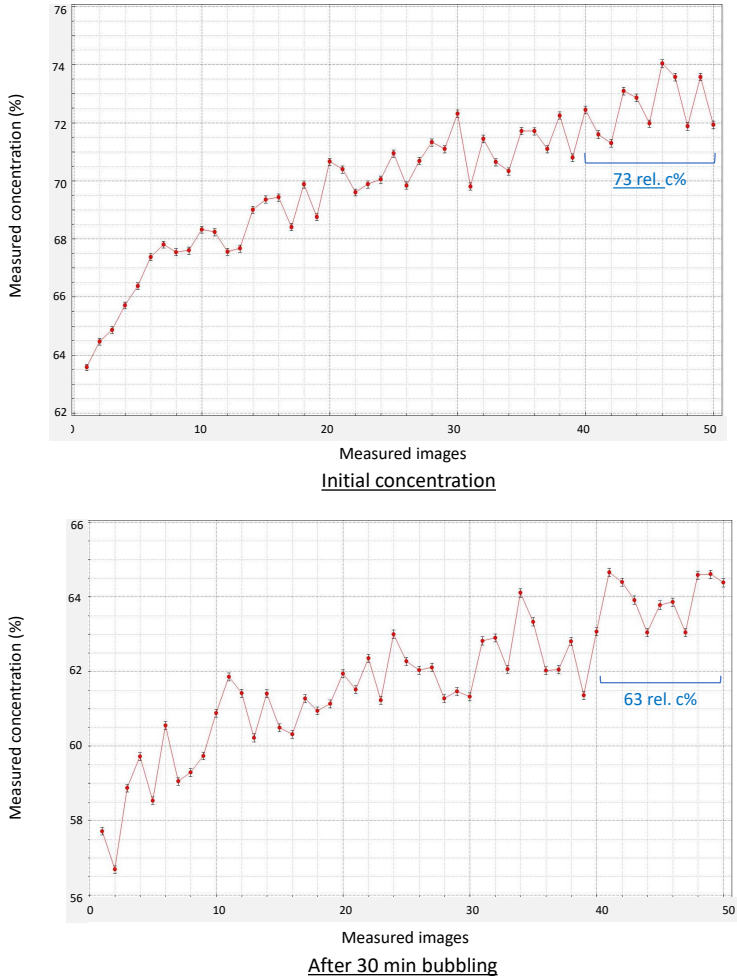


Figure 4.17.: Measured intensity of the aqueous solution with $2.11 \mu\text{m}$ particles at the initial concentration and after 30 min bubbling (10 sccm flow rate), the relative concentration is based on the calibration.

Finally, after an observation period of some days, the measured concentration in the organic phase was exactly the same as at the end of the experiment, confirming the stability of the interface. This confirmed that the bubbles were the only transport

mean for the particles to access to the organic phase (Figure 4.18).

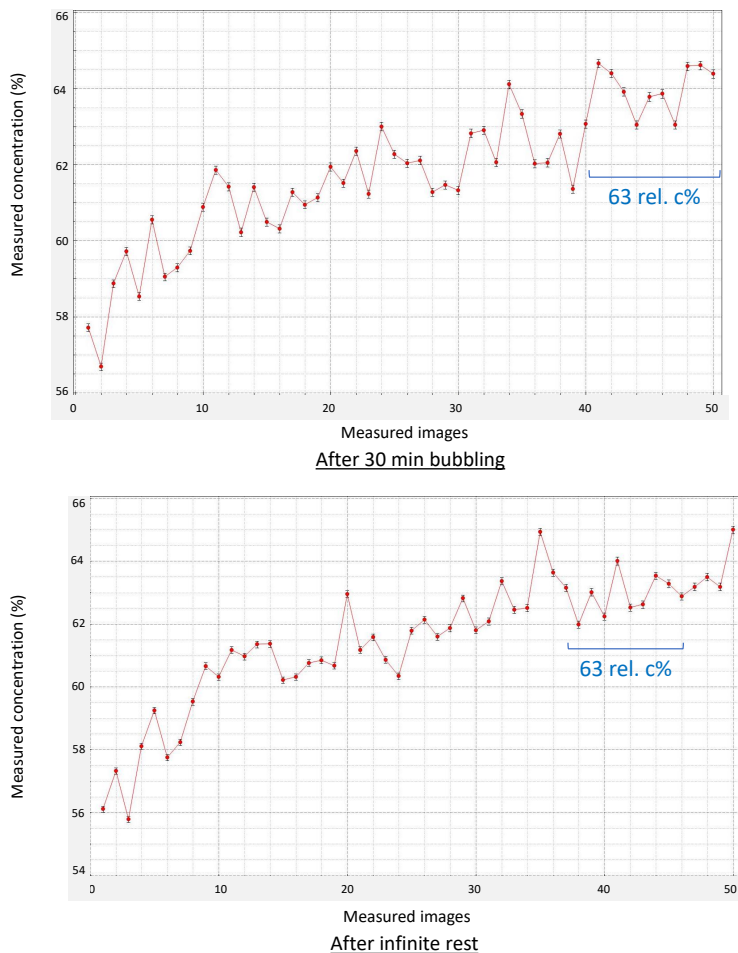


Figure 4.18.: Comparison between the measured intensity in the aqueous solution of 2.11 μm after the 30 min bubbling (10 sccm flow rate) and after a 3 days' rest.

4.4. RESULTS

4.4.1. EXTRACTION OF NANOPARTICLES

Successful results were obtained for the extraction of 250 nm particles for flow rates of 10 and 15 sccm, in the whole range of flow rates for 530 nm particles, and with flow rates of 5 and 10 sccm for 870 nm particles. The final results are presented in

Table 4.1 below.

Table 4.1.: Extraction of nanoparticles after 120 min of bubbly flow as a function of particle size and the gas flow rate

NP sizes	250 nm			530 nm			870 nm		
Gas flow rates (sccm)	5	10	15	5	10	15	5	10	15
Extraction rate ₁₂₀ (%)	19.17*	4.71	5.22	1.67	3.95	7.05	8.29	10.2	-**

*Aberrant result because of an unexpected variation of the laser setting. **Data not usable

Due to an unexpected change in the setting of the initially calibrated laser during the experimental measurement of the 250 nm nanoparticles with the 5 sccm bubbly flow rate, the light intensity was decreased in the observation window and the final result could not be considered as reliable. In the case of the 870 nm nanoparticles with the 15 sccm bubbly flow rate, the formation of bubble agglomerates in the column during the measurement induced a light pollution in the observation window making the images not usable. From the successful measurements, it is shown that the extraction efficiency is enhanced by the intensity of bubbling. A direct comparison between the different sizes of particles at a same flow rate seems to show a maximum removal efficiency for the biggest particles (870 nm). The results for the 250 nm and 530 nm particles do not allow to determine the extraction efficiency for these two sizes. Overall, it can be observed that the extraction becomes better for larger particles.

4.4.2. EVOLUTION OF THE PARTICLE EXTRACTION

Combining the initial and final measurements with the relative direct concentration measured during the bubbling using the method described earlier, indicative equations approximating the evolution of the particle extraction over time were determined with OriginPro[®] software for each measurement.

In each case, the extraction rate over time could be described with a logarithmic evolution (Table 4.2). This is in agreement with the literature on the removal of different sizes of particles by a bubbly flow [20, 21], and the results of Capelli [7]; where most of the particles were collected during the first 10 min of bubbling. The latter observations were not mathematically fitted in the references, and the functions presented hereafter are a tool to describe the evolution.

The comparison of the fitted extraction rates for the 530 nm nanoparticles were the most representative examples, where a clear increase of the extraction as function of the flow rate was observed, with a clear logarithmic evolution (Figure 4.19).

Considering the lack of experimental data to compare to in the case of the 250 nm and 870 nm particles, more mitigated results were obtained for the latter sizes. For the 250 nm nanoparticles, the final measured removal was slightly higher for the 10 sccm flow rate, but the extraction during the first 60 minutes was also observed slightly higher in the case of the 10 sccm flow rate. The difference in extraction as function of the flow rate was not clearly determined for the 250 nm nanoparticles. In the case of the 870 nm ones, the same trend was observed (Figure 4.19).

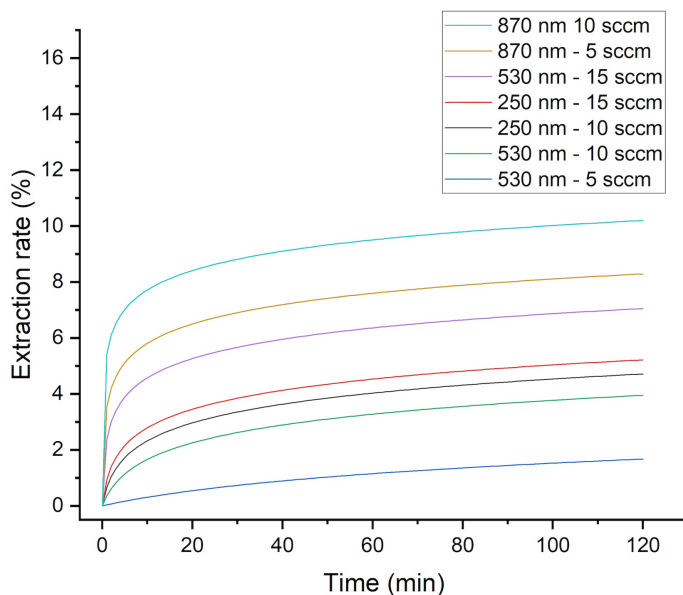


Figure 4.19.: Graphical representation of the extraction rates for 250 nm, 530 nm and 870 nm nanoparticles as a function of the time for different flow rates.

NP sizes	Gas flow rates	Fitted extraction rate
250 nm	10 sccm	$\ln(1 + 0.92T)$
	15 sccm	$\ln(1 + 1.53T)$
530 nm	5 sccm	$\ln(1 + 0.036T)$
	10 sccm	$\ln(1 + 0.425T)$
	15 sccm	$\ln(1 + 9.6T)$
870 nm	5 sccm	$\ln(1 + 33.2T)$
	10 sccm	$\ln(1 + 224T)$

Table 4.2.: Indicative fitting equation of the extraction rates (in %) of different sizes of nanoparticles and gas flow rates as a function of the time (T) in minutes

4.4.3. CONCLUSION

It can be concluded that the liquid filtration technique provides a possible option to remove sub-micron (from 250 to 870 nm) solid fission products from the salt and moreover allows to get well-defined boundary conditions at the surface of the column. These conditions allowed the determination of a first database for the removal efficiency of nano-sized particles with a bubbly flow. Further conclusions are:

- An innovative method using Laser Induced Luminescence was developed to observe and measure the concentration of nanoparticles in a bubbly flow.
- The modified Hallimond tube, which has demonstrated its effectiveness in the removal of micro-sized metallic particles, did not show its effectiveness in the case of the sub-micron particles.
- An alternative technique, using a supernatant solution as filtrating system, was designed. Promising results were obtained in terms of retention of solid particles.
- The removal of nanoparticles by a bubbly flow was measured experimentally for the first time with the Laser Induced Fluorescence technique.
- Overall, the extraction efficiency of the nanoparticles by helium bubbling was measured as relatively low. These results are in agreement with the simulations results predicting the collection efficiency of nanoparticles [22, 23].

REFERENCES

- [1] R. J. Kedl. *Fluid Dynamic studies of the Molten-Salt Reactor Experiment (MSRE) Core*. ORNL-TM-3229. 1970. DOI: 10.2172/4080377.
- [2] C. H. Gabbard. *Development of a Venturi Type Bubble Generator for Use in the Molten-Salt Reactor Xenon Removal System*. ORNL-TM-4122. Dec. 1972. DOI: 10.2172/12784156.
- [3] R. J. Kedl. *Migration of a class of fission products (noble metals) in the Molten-Salt Reactor Experiment*. ORNL-TM-3884. 1972. DOI: 10.2172/4471292.
- [4] C. Tripodo, A. D. Ronco, S. Lorenzi, and A. Cammi. "Development of a control-oriented power plant simulator for the molten salt fast reactor". In: *EPJ Nuclear Sciences & Technologies* 5 (2019). Ed. by J. L. Kloosterman, E. Merle, and J. Ragusa, p. 13. DOI: 10.1051/epjn/2019029.
- [5] M. Allibert, M. Aufiero, M. Brovchenko, S. Delpech, V. Ghetta, D. Heuer, A. Laureau, and E. Merle-Lucotte. "7 - Molten salt fast reactors". In: ed. by I. L. Pioro. Woodhead Publishing Series in Energy. Woodhead Publishing, Jan. 2016, pp. 157–188. DOI: 10.1016/B978-0-08-100149-3.00007-0.
- [6] E. Capelli, E. M. A. Frederix, A. Mathur, R. P. Hania, J.-L. Kloosterman, and R. J. M. Konings. "Noble metal behaviour and extraction in molten salt reactor". In: *Thorium energy conference*. Brussels, 2018.
- [7] E. Capelli. *Molten Salt Chemistry - Final project Report*. Tech. rep. TU Delft, 2019.
- [8] E. Frederix. "Estimates of noble metal particle growth in a molten salt reactor". In: *Colloids and Surfaces A: Physicochemical and Engineering Aspects* 655 (Dec. 2022), p. 130167. DOI: 10.1016/j.colsurfa.2022.130167.
- [9] F. Lemoine, M. Wolff, and M. Lebouche. "Simultaneous concentration and velocity measurements using combined laser-induced fluorescence and laser Doppler velocimetry: Application to turbulent transport". In: 20 (1996), pp. 319–327. ISSN: 0723-4864. DOI: 10.1007/bf00191013.
- [10] M. J. Sathe, I. H. Thaker, T. E. Strand, and J. B. Joshi. "Advanced PIV/LIF and shadowgraphy system to visualize flow structure in two-phase bubbly flows". In: 65 (2010), pp. 2431–2442. ISSN: 0009-2509. DOI: 10.1016/j.ces.2009.11.014.
- [11] M. W. Hlawitschka, P. Kováts, K. Zehringer, and H.-J. Bart. "Simulation and experimental validation of reactive bubble column reactors". In: 170 (2017), pp. 306–319. ISSN: 0009-2509. DOI: 10.1016/j.ces.2016.12.053.

- [12] J. Zhao, L. Jensen, J. Sung, S. Zou, G. C. Schatz, and R. P. Van Duyne. “Interaction of Plasmon and Molecular Resonances for Rhodamine 6G Adsorbed on Silver Nanoparticles”. In: *Journal of the American Chemical Society* 129.24 (2007). PMID: 17521187, pp. 7647–7656. DOI: 10.1021/ja0707106. URL: <https://doi.org/10.1021/ja0707106>.
- [13] A. G. Asil, A. N. Pour, and S. Mirzaei. “Intrinsic Hydrodynamic Investigation of Three-Phase Bubble Column: Comparative Experimental Study on Gas Holdup”. In: 54 (2020), pp. 331–341. ISSN: 0040-5795. DOI: 10.1134/s0040579520020050.
- [14] I. Lakerveld. “Helium Bubbling in the Molten Salt Fast Reactor”. MA thesis. Delft University of Technology, 2021.
- [15] A. Grooten. “Helium Bubbling in the Molten Salt Fast Reactor”. B.S. thesis. Delft University of Technology, 2021.
- [16] E. Cervi, S. Lorenzi, L. Luzzi, and A. Cammi. “Multiphysics analysis of the MSFR helium bubbling system: A comparison between neutron diffusion, SP3 neutron transport and Monte Carlo approaches”. In: *Annals of Nuclear Energy* 132 (2019), pp. 227–235. DOI: <https://doi.org/10.1016/j.anucene.2019.04.029>.
- [17] D. Lucas and T. Ziegenhein. “Influence of the bubble size distribution on the bubble column flow regime”. In: *International Journal of Multiphase Flow* 120 (Nov. 2019), p. 103092. DOI: 10.1016/j.ijmultiphaseflow.2019.103092.
- [18] D. Journee. “Helium bubbling in a molten salt fast reactor”. MSc thesis. TU Delft, 2016.
- [19] E. Capelli. *Notes on flotation*. Tech. rep. TU Delft, 2016.
- [20] J. Drzymala, T. Chmielewski, K. Wolters, D. Birlingmair, and T. Wheelock. “Microflotation measurement based on modified Hallimond tube”. In: *Translations of the Institution of Mining and Metallurgy: Section C, Mineral processing and Extractive metallurgy* 101.C (1992), pp. 17–24.
- [21] J. Drzymala. “Technical Note Entrainment of Particles with Density between 1.01 and 1.10 g/cm³ in a monobubble Hallimond flotation tube”. In: *Minerals Engineering* 12.3 (1999), pp. 329–331.
- [22] A. V. Nguyen, P. George, and G. J. Jameson. “Demonstration of a minimum in the recovery of nanoparticles by flotation: Theory and experiment”. In: 61 (2006), pp. 2494–2509. ISSN: 0009-2509. DOI: 10.1016/j.ces.2005.11.025.
- [23] N. Mishchuk, J. Ralston, and D. Fornasiero. “The analytical model of nanoparticle recovery by microflotation”. In: 179-182 (2012), pp. 114–122. ISSN: 0001-8686. DOI: 10.1016/j.cis.2012.06.008.

5

THERMODYNAMIC ASSESSMENT OF THE AF-CrF₃ (A = Li, Na, K) AND CrF₂-CrF₃ SYSTEMS

The understanding of the corrosion mechanisms and the effect of the corrosion products on the basic properties of the salt (e.g. melting point, heat capacity etc.) is fundamental for the safety assessment and durability of the Molten Salt Reactor technology. This work focuses on the thermodynamic assessment of the CrF₂-CrF₃ system and the binary systems of chromium trifluoride CrF₃ with alkali fluorides (LiF, NaF, KF) using the CALPHAD (Computer Coupling of Phase Diagrams and Thermochemistry) method. In this work, the modified quasichemical model in the quadruplet approximation has been used to develop new thermodynamic modeling assessments of the binary solutions, which are highly relevant to assess the corrosion process in Molten Salt Reactors. The agreement between these assessments and the phase equilibrium data available in the literature is generally good. The excess properties (mixing enthalpies, entropies and Gibbs energies) calculated in this work are consistent with the expected behavior of decreasing enthalpy and Gibbs energy of mixing with increasing ionic radius of the alkali-cations.

THE Molten Salt Reactor (MSR) was selected as one of the six reactor designs retained by the Generation IV International Forum (GIF) for the next generation of nuclear reactors [2], which aims to replace the current fleet of Light Water Reactors in the next decades. Fluoride salts containing alkali fluorides are considered a promising heat transfer medium and coolant in the primary and secondary loops of the MSR systems. A major concern for the operation of these reactors is the degradation of structural materials caused by the corrosive properties of the fluoride salt at high temperatures. The understanding of corrosion phenomena is fundamental for the safety of the MSR and commercial exploitation in a near

Parts of this chapter have been published in Thermo special issue 1, 205-219 (2021) [1].

future. An example of a typical fuel salt composition is ${}^7\text{LiF}-\text{ThF}_4-\text{UF}_4-(\text{UF}_3)$, proposed for the European Molten Salt Fast Reactor (MSFR) design [3], or ${}^7\text{LiF}-\text{NaF}-(\text{KF})-\text{AnF}_4-\text{AnF}_3$ (An=actinide) considered for the MSR-burner [4]. The so-called FLiNaK salt (LiF-NaF-KF mixture) is moreover a potential choice for secondary coolant systems of the MSFR designs [4].

Ni-based alloys, which have shown the best resistance to fluoride salts, with alloying elements such as Fe, Cr, and Mo, are currently the reference. Chromium is the least stable element in this alloy, leading to the dissolution of Cr_xF_y fluorides inside the fluoride salt matrix, and to the formation of discrete voids in the Ni-based alloy which could affect the general integrity of the structure of the reactor. Depending on fluorine potential and temperature, the formed chromium fluoride species will be stable as divalent or trivalent species. The current reference structural alloy for MSRs fueled with a fluoride fuel salt is Hastelloy-N, which has the following composition: Ni(70.6 wt%), Mo(16.8 wt%), Cr(7.01 wt%), Fe(4.16 wt%), Mn(0.52 wt%), Al(0.15 wt%), Ti(0.002 wt%), Si(0.36 wt%) and C(0.055 wt%) [5]. This material has demonstrated promising performance during the Molten Salt Reactor Experiment (MSRE) of the Oak Ridge National Laboratory (ORNL) in the 1950s [6]. The presence of a 7 wt% fraction of chromium appears as a good proportion to provide the required mechanical strength for the core components, while not being overly exposed to salt corrosion. The redox potential of the fuel salt, controlled by the UF_4/UF_3 ratio, determines the rate of corrosion of the structural material. During the fission process, free fluorine is formed, which reacts with UF_3 hence, increasing the UF_4/UF_3 ratio and redox potential of the salt results in an increase in the corrosion rate of the structural material. This leads to oxidation reactions such as $\text{Cr}(\text{alloy}) + 2\text{UF}_4(\text{salt}) = \text{CrF}_2(\text{salt}) + 2\text{UF}_3(\text{salt})$ [7]. Olson *et al.* conducted a comparative study with different Ni-based alloys including Hastelloy with different contents of chromium [8, 9]. The authors studied the corrosion rate at high temperature (1123 K) of FLiNaK salt (LiF-NaF-KF: 46.50-11.5-42 mol%) with an immersion device and confirmed the correlation between Cr content and corrosion resistance of the Ni-based alloy. Except for the quasi pure nickel metal, Hastelloy-N proved superior resistance to corrosion. A high proportion of Cr (≈ 20 wt%) lead to high Cr depletion of the structural material, and the degradation was particularly enhanced in the presence of Cr^{3+} cations in solution [10].

The understanding of the effect of the corrosion products on the basic properties of the salt (e.g. melting point, heat capacity etc.) is fundamental for the safety assessment and durability of the MSR technology. This work thus focuses on a thermodynamic modeling assessment of the CrF_2 - CrF_3 system and the binary systems of chromium trifluoride CrF_3 with alkali fluorides (LiF, NaF, KF), based on data previously reported in the literature on these systems.

5.1. LITERATURE REVIEW

5.1.1. STRUCTURAL DATA

The binary and ternary compounds stable in the systems under investigation in this work are CrF_2 , CrF_3 , Cr_2F_5 , Li_3CrF_6 , NaCrF_4 , Na_3CrF_6 , $\text{Na}_5\text{Cr}_3\text{F}_{14}$, KCrF_4 , K_2CrF_5 ,

$K_2Cr_5F_{17}$ and K_3CrF_6 . The most relevant reported structural properties on the latter phases are listed in Table 5.1.

Table 5.1.: Lattice parameters of the intermediate compounds of the $AF-CrF_3$ (A = Li, Na,K) systems.

Compound	Symmetry	Space group	a(Å)	b(Å)	c(Å)	β (°)	Ref.
$\alpha-Li_3CrF_6$	Monoclinic	C2/c	14.4058(10)	8.6006(4)	10.0122(6)	94.714(5)	[11, 12]
$\beta-Li_3CrF_6$	Orthorhombic	Pna2 ₁	9.5796(1)	8.4071(1)	4.9793(7)	90	[11, 12]
$\alpha-NaCrF_4$	Monoclinic	P2 ₁ /c	7.862(2)	5.328(2)	7.406(2)	101.65(4)	[13]
$\beta-NaCrF_4$	Tetragonal	P4/mmm*	15.330(5)	5.330(5)	6.279(3)	90	[14]
Na_3CrF_6	Monoclinic	P2 ₁ /c	5.46(1)	5.68(1)	7.88(1)	90	[15]
$\alpha-Na_5Cr_3F_{14}$	Monoclinic	P2 ₁ /c	10.5096(3)	7.2253(2)	7.2713(2)	90.6753(7)	[16]
$\beta-Na_5Cr_3F_{14}$	Orthorhombic	C222 ₁	10.49(1)	10.19(1)	10.21(1)	90	[17]
$\gamma-Na_5Cr_3F_{14}$	Tetragonal	P4 ₁ 2 ₁ 2	7.32(2)	7.32(2)	10.24(2)	90	[17]
$KCrF_4$	Orthorhombic	Pnma	15.761(10)	7.448(5)	18.361(11)	90	[18, 19]
K_2CrF_5	Orthorhombic	Pbcn	7.334(2)	12.804(4)	20.151(5)	90	[20]
$K_2Cr_5F_{17}$	Orthorhombic	Pmmm*	12.56(1)	7.25(1)	7.36(1)	90	[21, 22]
$\gamma-K_3CrF_6$	Cubic	Fm $\bar{3}$ m	8.66(1)	8.66(1)	8.66(1)	90	[21]

* These structural data have not been confirmed experimentally and were based on theoretical calculations

Most of the chromium fluoride solid compounds have been reported as green crystal powder [17, 23, 24] or sometimes as a black powder [25]. Most of the intermediate compounds in the $LiF-CrF_3$, $NaF-CrF_3$ and $KF-CrF_3$ systems, first described as early as 1969 by de Kozak [17, 23], have been confirmed by more recent structural studies (reference in Table 5.1). Some doubts remain regarding the structural determinations of $Na_5Cr_3F_{14}$, $K_2Cr_5F_{17}$ and K_3CrF_6 , however. $Na_5Cr_3F_{14}$ is known to have three crystalline forms: α -monoclinic, β -tetragonal and γ -orthorhombic [17], but the reported differential calorimetry experiments have not allowed to identify clearly the phase transition temperatures between the different crystalline forms [26]. De Kozak found by X-ray diffraction that $K_2Cr_5F_{17}$ has an orthorhombic structure (space group Pmmm) in 1971 [21]. But this study does not report the atomic positions, so the data for this compound are incomplete. De Kozak [17] postulated different crystalline phases for K_3CrF_6 with transitions: $\alpha \xrightleftharpoons[446K]{} \beta \xrightleftharpoons[495K]{} \gamma$. Only the γ -cubic phase has been formally identified by X-ray diffraction at 523 K [21].

5.1.2. THERMODYNAMIC DATA

The thermodynamic data available on the aforementioned binary and ternary compounds are rather limited in the literature. Hansen [27] performed adiabatic calorimetry measurements between 15 and 300 K on CrF_3 and derived the standard entropy at 298.15 K as $(93.88 \pm 0.15) \text{ J}\cdot\text{K}^{-1}\cdot\text{mol}^{-1}$ and the heat capacity at 298.15 K as $(78.75 \pm 0.01) \text{ J}\cdot\text{K}^{-1}\cdot\text{mol}^{-1}$. In this work, data provided by the IVTAN tables [28] and SGPS - SGTE pure substances database [29] have been used for the thermodynamic functions for CrF_3 . The fusion temperature has been measured experimentally at $(1698 \pm 20) \text{ K}$ for CrF_3 and $(1167 \pm 2) \text{ K}$ for CrF_2 by Sturm [25] in 1962 and are

still considered as an appropriate reference. No other data has been found for the thermodynamic properties for CrF₂. In this work, the IVTAN/SGPS - SGTE databases have also been used for the thermodynamic functions (Table 5.2).

Thermodynamic data have been barely explored for the intermediate compounds in the AF-CrF₃ systems. De Kozak [17] reported the temperature of fusion of Li₃CrF₆ to be $T_{fus} = 1125$ K. For NaCrF₄, Yin derived based on first principles calculations the enthalpy of formation from the binary species NaF and CrF₃ at 0 K as -39.990 kJ·mol⁻¹. The mixing enthalpy has been calculated to be -36.498 kJ/mol for the liquid phase at the (NaF:CrF₃) = (1:1) composition at 1500 K [30]. The same method was applied to estimate the formation enthalpies of NaF and CrF₃ at 0 K of Na₃CrF₆ and Na₅Cr₃F₁₄ as -96 kJ·mol⁻¹ and -197 kJ·mol⁻¹, respectively [31]. Yin reported a formation enthalpy from KF and CrF₃ at 0 K of -64.912 kJ·mol⁻¹ for the KCrF₄ intermediate compound and a mixing enthalpy of -51.633 kJ·mol⁻¹ at 1500 K for the liquid of this composition [31]. For K₂CrF₅, K₂Cr₅F₁₇ and K₃CrF₆, no thermodynamic data are available to this date in the open literature.

5.1.3. PHASE DIAGRAM DATA

CrF₂-CrF₃ SYSTEM

Only one study has been reported in 1962 on the phase equilibria of the CrF₂-CrF₃ system by Sturm [25] based on quenching experiments. Two invariant equilibria were observed in the system: an eutectic point at $X(\text{CrF}_3) = 0.14$ with a temperature of (1104 ± 5) K and a peritectic equilibrium at $X(\text{CrF}_3) = 0.29$ and $T = (1270 \pm 5)$ K. A single intermediate compound has been identified in the region between $X(\text{CrF}_3) = 0.40$ and $X(\text{CrF}_3) = 0.45$, corresponding to the mixed valence state compound Cr₂F₅ with extended region of stability [18, 32]. Sturm [25] suggested the composition of the solution phase "Cr(II,III) fluoride" between 0.42 and 0.46, so slightly below the ideal 0.50 composition, but did not explore the temperature below 1023 K. Tressaud *et al.* [32] and Lacorre *et al.* [18] reported crystallographic data for the Cr₂F₅ compound. Its melting point has been determined as (1270 ± 5) K [25]. Two solid solutions have been finally identified, from $X(\text{CrF}_3) = 0$ to $X(\text{CrF}_3) = 0.01$ and from $X(\text{CrF}_3) = 0.90$ to $X(\text{CrF}_3) = 1$, respectively. No thermodynamic model has been developed for this system to this date. A sketch of the phase diagram was drawn by Sturm in accordance with the experimental data collected in his work [25].

AF-CrF₃ (A=Li, Na, K) BINARY SYSTEMS

The first study of the phase equilibria in the LiF-CrF₃, NaF-CrF₃ and KF-CrF₃ binary systems was performed by de Kozak in 1969 [17, 23]. Based on the rather complete experimental data set obtained by Differential Thermal Analysis (DTA) measurements, sketches of the phase diagrams were established [17]. Thermodynamic modeling assessments of these systems have been performed based on these data by Yin *et al.* [30, 31], using an associate model to describe the liquid phase. In this work, a re-assessment using the modified quasichemical formalism is proposed, compatible with the thermodynamic database developed for nuclear salt systems by the JRC [4].

5.2. THERMODYNAMIC MODELING

In this study, thermodynamic models are built using the CALPHAD (CALCulation of PHase Diagrams) method [33, 34] and the FactSage software [35].

5.2.1. GIBBS ENERGIES OF PURE COMPOUNDS

The Gibbs energies of pure compounds is expressed by:

$$G(T) = \Delta_f H_m^o(298.15) - S_m^o(298.15) \times T + \int_{298.15}^T C_{p,m}(T) dT - T \int_{298.15}^T \frac{C_{p,m}}{T} dT \quad (5.1)$$

where $\Delta_f H_m^o(298.15)$ is the standard enthalpy of formation and $S_m^o(298.15)$ is the standard entropy of the pure compound at standard pressure and reference temperature 298.15 K. $C_{p,m}$ is the heat capacity expressed by:

$$C_{p,m}(T) = a + bT + cT^2 + dT^{-2} + eT^3 \quad (5.2)$$

In this work, in the absence of thermodynamic data in the literature for intermediate chromium salt compounds, the Neumann-Kopp estimation technique has been used [36] based on the heat capacities of the end-member compounds AF (A=Li, Na, K) and CrF_3 . The thermodynamic functions for solid alkali fluorides (LiF, NaF, KF) were taken from the JRC database [4] and for the chromium fluorides from the IVTAN tables/SGTE database [28, 29] as CrF_2 , CrF_3 and Cr_2F_5 are not yet included in the JRC databank of relevant molten salt materials for nuclear applications (Table 5.2).

5.2.2. SOLID SOLUTIONS

Three solid solutions are presented in this work for the CrF_2 - CrF_3 system and have been modelled based on the data collected by Sturm [25]. A regular solution model using a polynomial description of the Kohler-Toop interpolation was used to describe the solid solution around the Cr_2F_5 composition, with CrF_2 and Cr_2F_5 as the end-member compositions. A two-sublattice polynomial model was used to describe the two solid solutions around the end-member compositions quasi- CrF_2 and quasi- CrF_3 , respectively. In this case, the considered cationic species on the first sublattice are Cr^{2+} and Cr^{3+} , and the anionic species on the second sublattice is F^- , meaning the end-member compositions correspond to the CrF_2 and CrF_3 stoichiometry, respectively. The Gibbs energy function $G(T)$ of the solid solution is described by the equation:

$$G(T) = X_A \cdot G_A^o + X_B \cdot G_B^o + X_A RT \ln X_A + X_B RT \ln X_B + \Delta G_m^{xs} \quad (5.3)$$

where G_A^o and G_B^o are the molar Gibbs energies of the pure end-members, X_A and X_B their site molar fraction, R the universal gas constant and ΔG^{xs} is the excess Gibbs energy. The excess Gibbs energy can be expressed by:

$$\Delta G_m^{xs} = \sum_{i,j} y_A^i \cdot y_B^j \cdot L_{i,j} \quad (5.4)$$

Table 5.2: Thermodynamic data for end-members and intermediate compounds used in this work for the thermodynamic assessment. Standard enthalpy of formation $\Delta_f H_m^0$ (298.15 K), standard entropy S_m^0 (298.15 K) and heat capacity coefficient of pure compounds $C_{p,m}$ (T/K)/(J·K⁻¹·mol⁻¹) = a + b·T + c·T² + d·T⁻² + e·T³. Optimized data are presented in **bold**.

Compound	$\Delta_f H_m^0$ (298.15 K) (KJ·mol ⁻¹)	S_m^0 (298.15 K) (J·K ⁻¹ ·mol ⁻¹)	a	b	c	d	e	T(K)	Ref.
LiF ^(cr)	-616.931	35.66	43.30898	0.016312168	5.0470398·10 ⁻⁷	-569123.6	-	298.15-2500	[37]
LiF ^(l)	-598.654	42.96	64.183	-	-	-	-	298.15-6000	[37]
NaF ^(cr)	-576.650	51.21	47.630	0.01479	-	-464300	-	298.15-2500	[37]
NaF ^(l)	-557.730	52.75	72.989	-	-	-	-	298.15-6000	[37]
KF ^(cr)	-568.606	66.55	68.757414	-0.057756882	7.5404856·10 ⁻⁵	-766718.34	-2.3885627·10 ⁻⁸	298.15-2000	[37]
KF ^(l)	-554.374	67.77	71.965	-	-	-	-	298.15-6000	[37]
CrF ₂ ^(cr)	-781.8	86.87	76.68345	0.0105410	-1.386756·10 ⁻⁹	-1338373	-	298.15-1167	[28, 29]
CrF ₂ ^(l)	-764.692	86.308	100	-	-	-	-	1167-4000	[27-29]
CrF ₃ ^(cr)	-1160.0	93.88	75.86301	0.0404446	-4.20805·10 ⁻⁶	-782870	-	298.15-1100	[27-29]
CrF ₃ ^(l)	-	-	226.552	-0.0870137	2.020701·10 ⁻⁵	-49199760	-	1100-1698	[28, 29]
CrF ₃ ^(cr)	-	-	130	-	-	-	-	1698-2500	[28, 29]
CrF ₃ ^(l)	-1125.281	83.0567	152.54646	0.05098565	-4.20944·10 ⁻⁶	-2121243	-	298.15-6000	[28], This work
Li ₃ CrF ₆ ^(cr)	-1950.8	181.0	205.78995	0.089381104	-2.6933806·10 ⁻⁶	-2490240.8	-	298.15-1100	[28], This work
Li ₃ CrF ₆ ^(l)	-3070.0	210.6	356.47894	-0.038077196	2.172112194·10 ⁻⁵	-50907130.8	-	1100-3000	[28], This work
Li ₃ CrF ₆ ^(cr)	-	-	123.49301	0.0552346	-4.20805·10 ⁻⁶	-1247170	-	298.15-3000	[28], This work
α-Na ₃ CrF ₆ ^(cr)	-1777.5	156.2	218.75301	0.0848146	-4.20805·10 ⁻⁶	-2175770	-	298.15-913	[28], This work
β-Na ₃ CrF ₆ ^(cr)	-2935.9	314.5	218.75301	0.0848146	-4.20805·10 ⁻⁶	-2175770	-	913-3000	[28], This work
Na ₃ CrF ₆ ^(cr)	-2925.4	326.3	218.75301	0.0848146	-4.20805·10 ⁻⁶	-2175770	-	298.15-3000	[28], This work
α-Na ₃ CrF ₆ ^(l)	-6545.65	584.2	465.739030	0.1952838	-1.262415·10 ⁻⁵	-4670110	-	298.15-3000	[28], This work
β-Na ₃ CrF ₆ ^(l)	-1772.8	181.9	144.620424	-0.017312282	7.1196806·10 ⁻⁵	-1549588.34	-2.3885627·10 ⁻⁸	298.15-1066	[28], This work
α-K ₂ CrF ₄ ^(cr)	-1768.8	185.9	144.620424	-0.017312282	7.1196806·10 ⁻⁵	-1549588.34	-2.3885627·10 ⁻⁸	1066-3000	[28], This work
β-K ₂ CrF ₄ ^(cr)	-2378.6	251.0	213.377838	-0.075069164	1.4660166·10 ⁻⁴	-2316306.68	-4.7771254·10 ⁻⁸	298.15-3000	[28], This work
K ₂ CrF ₄ ^(l)	-7067.5	632.8	516.828878	0.086709236	1.2976946·10 ⁻⁴	-544786.68	-4.7771254·10 ⁻⁸	298.15-3000	[28], This work
α-K ₃ CrF ₆ ^(cr)	-2941.2	338.5	282.135252	-0.132826046	2.2200652·10 ⁻⁴	-3083025.02	-7.1656881·10 ⁻⁸	298.15-499	[28], This work
β-K ₃ CrF ₆ ^(cr)	-2925.0	371.3	282.135252	-0.132826046	2.2200652·10 ⁻⁴	-3083025.02	-7.1656881·10 ⁻⁸	499-3000	[28], This work

where $L_{i,j}$ is an interaction coefficient which can depend on temperature T described by the equation:

$$L_{i,j} = A + BT \quad (5.5)$$

and where y_A and y_B are the equivalent site fractions of the end-member species for the regular solution, defined by:

$$y_A = \frac{Z_A X_A}{Z_A X_A + Z_B X_B} \quad (5.6)$$

Z_A is the coordination number of the A (resp. B) species in the end-member. Here Z_A is set equal to 1 (default value), meaning that the equivalent site fractions are equal to the molar site fractions.

For the two-sublattice polynomial model, the equivalent site fractions $y_{Cr(II)}$ and $y_{Cr(III)}$ are described as a charge equivalent site fractions:

$$y_{Cr(II)} = \frac{2X_{Cr(II)}}{2X_{Cr(II)} + 3X_{Cr(III)}} \quad (5.7)$$

$$y_{Cr(III)} = \frac{3X_{Cr(III)}}{2X_{Cr(II)} + 3X_{Cr(III)}} \quad (5.8)$$

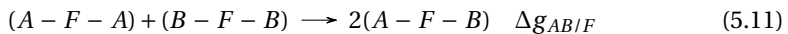
The optimized excess energy parameters, obtained by manual iteration, are given by the following equations:

$$G_{(Cr(II),Cr(III))F}^{xs} = y_{CrF_2}^2 y_{CrF_3} \cdot 4920 + y_{CrF_2} y_{CrF_3}^2 \cdot 7600 \quad \text{J mol}^{-1} \quad (5.9)$$

$$G_{Cr_{1+x}F_{2+3x}}^{xs} = y_{CrF_2} y_{Cr_2F_5} \cdot 23850 + y_{CrF_2}^2 y_{Cr_2F_5} \cdot (-19500) + y_{CrF_2}^2 y_{Cr_2F_5} \cdot 3500 \quad \text{J mol}^{-1} \quad (5.10)$$

5.2.3. LIQUID SOLUTION

To describe the liquid solution, the modified quasichemical model in the quadruplet approximation has been used [38, 39]. This quadruplet is defined by two anions and two cations symmetrically dispatched around an axis. Two interactions are considered, the First Nearest Neighbour (FNN) interaction which describes the interaction cation - anion and the Second Nearest Neighbour (SNN) interaction which describes the interactions between the two closest ions in the same sublattice. This model is particularly well adapted for the description of ionic liquids as it allows one to choose the composition of maximum short-range ordering in a binary system by varying the ratio between the cation-cation coordination numbers $Z_{AB/FF}^A$ and $Z_{AB/FF}^B$. Short-range ordering is defined by the quadruplet approximation and includes the SNN interactions between each cation and each anion. In a simple representation where A and B are two cations and F, the anion (fluorine anion F^- in this work), the following reaction is obtained:



where $\Delta g_{AB/F}$ is the parameter of the Gibbs energy change associated with the SNN exchange reaction described as:

$$\Delta g_{AB/F} = \Delta g_{AB/F}^0 + \sum_{i \geq 1} g_{AB/F}^{i0} \chi_{AB/F}^i + \sum_{j \geq 1} g_{AB/F}^{0j} \chi_{BA/F}^j \quad (5.12)$$

where $\Delta g_{AB/F}^0$ and $g_{AB/F}^{ij}$ are possibly affected by temperature, but independent of composition, and optimized to fit as best as possible the experimental data of a given system. The dependence on composition is given by the term $\chi_{AB/F}$ defined as:

$$\chi_{AB/F} = \frac{X_{AA}}{X_{AA} + X_{AB} + X_{BB}} \quad (5.13)$$

where X_{AA} , X_{AB} and X_{BB} represent the different cation-cation pair fractions. To maintain electro-neutrality in the system, the anion-anion coordination should be determined. The following equation is applied after the selection of cation-cation coordination numbers:

$$\frac{q_A}{Z_{AB/FF}^A} + \frac{q_B}{Z_{AB/FF}^B} = 2 \times \frac{q_F}{Z_{AB/FF}^F} \quad (5.14)$$

with q_i representing the charges of the different ions and $Z_{AB/FF}^F$ is the anion-anion coordination number, directly dependent of the choice of the cation-cation coordination numbers $Z_{AB/FF}^A$ and $Z_{AB/FF}^B$. These choices are based on the optimization of the systems in order to get the maximum short range ordering and highest excess Gibbs energy at a composition usually close to the lowest eutectic in the phase diagram. The coordination numbers selected in this work are listed in Table 5.3. The optimized excess Gibbs energy of the liquid solutions for the

Table 5.3.: Cation-cation coordination numbers of the liquid solution

A	B	$Z_{AB/FF}^A$	$Z_{AB/FF}^B$	$Z_{AB/FF}^F$
Li ⁺	Li ⁺	6	6	6
Na ⁺	Na ⁺	6	6	6
K ⁺	K ⁺	6	6	6
Cr ²⁺	Cr ³⁺	6	6	2.4
Li ⁺	Cr ³⁺	2	6	2
Na ⁺	Cr ³⁺	4	6	2.7
K ⁺	Cr ³⁺	6	6	3

LiF–CrF₃, NaF–CrF₃ and KF–CrF₃ systems are given by the following equations:

$$\begin{aligned} \Delta g_{LiCr/FF} = & -25000 - 5 \cdot T + (4000 - 5 \cdot T) \chi_{LiCr/FF} \\ & + (-2000 - 5 \cdot T) \chi_{CrLi/FF} + (-2000 - 2 \cdot T) \chi_{CrLi/FF}^2 \quad \text{J mol}^{-1} \end{aligned} \quad (5.15)$$

$$\begin{aligned} \Delta g_{NaCr/FF} = & -29870 - 5.5 \cdot T + (4700 - 16 \cdot T)\chi_{NaCr/FF} \\ & + (4100 + 3.3 \cdot T)\chi_{CrNa/FF} + 1000\chi_{NaCr/FF}^2 \quad \text{J mol}^{-1} \quad (5.16) \end{aligned}$$

$$\begin{aligned} \Delta g_{KCr/FF} = & -29600 - 5 \cdot T + (-6800 - 6 \cdot T)\chi_{KCr/FF} \\ & + (15600 + 3.25 \cdot T)\chi_{CrK/FF} + (-9800 - 4 \cdot T)\chi_{CrK/FF}^2 \quad \text{J mol}^{-1} \quad (5.17) \end{aligned}$$

$$\begin{aligned} \Delta g_{Cr(II)Cr(III)/FF} = & -2900 + 5 \cdot T + (-5875 - 8 \cdot T)\chi_{Cr(II)Cr(III)/FF} \\ & + (-9800 - 5.5 \cdot T)\chi_{Cr(III)Cr(II)/FF} + (6450 - 5.35 \cdot T)\chi_{Cr(II)Cr(III)/FF}^2 \quad \text{J mol}^{-1} \quad (5.18) \end{aligned}$$

5.3. RESULTS AND DISCUSSION

5.3.1. CrF₂-CrF₃

The calculated phase diagram for the CrF₂-CrF₃ system is shown in Figure 5.1 where it is compared to the experimental data of Sturm [25]. The general agreement between calculated and experimental data is good. The CrF₂-rich solid solution extends up to X(CrF₃)= 0.054. The range of stability of the Cr₂F₅ solid solution extends from X(CrF₃)= 0.382 to X(CrF₃)= 0.5. Finally, the CrF₃-rich solid solution is stable down to X(CrF₃)= 0.88. The calculated invariant equilibria are listed in Table 5.4 and compared to the data by Sturm [25].

Table 5.4.: Invariant equilibria in the CrF₂-CrF₃ system.

Equilibrium	Invariant reaction	This study(calc.)		Sturm <i>et al.</i> [25]	
		X(CrF ₃)	T/K	X(CrF ₃)	T/K
Eutectic	CrF ₂ (cr) + Cr ₂ F ₅ (cr)=L	0.115	1104	0.14*	1103 ± 5
Peritectic	Cr ₂ F ₅ (ss)=CrF ₃ (cr) + L	0.28	1271	0.29	1272 ± 5

*The composition data was extracted from the sketch of the phase diagram provided by Sturm [25]

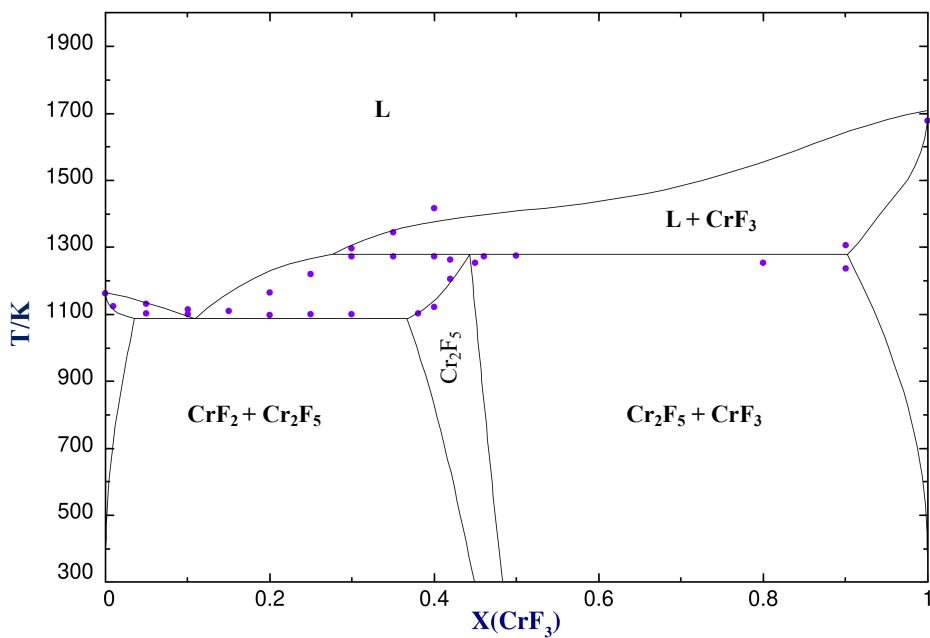


Figure 5.1.: Phase diagram of the CrF₂-CrF₃ system optimized in this work and comparison with experimental data provided by Sturm [25].

5.3.2. AF-CrF₃ (A = Li, Na, K)

The calculated phase diagrams for the LiF–CrF₃, NaF–CrF₃ and KF–CrF₃ systems are shown in Figures 5.2, 5.3 and 5.4, respectively.

LiF–CrF₃

The LiF–CrF₃ system shows, according to the data of de Kozak, two eutectic equilibria: the first at a composition of $X(\text{CrF}_3) = 0.15$ and a temperature of 1003 K, and the second at a composition of $X(\text{CrF}_3) = 0.35$ and temperature of 1059 K [17]. The calculated phase diagram (Figure 5.2) shows good agreement, with a first eutectic point calculated at $X(\text{CrF}_3) = 0.136$ and at a temperature of 1008 K, and a second at $X(\text{CrF}_3) = 0.363$ with a temperature of 1062 K. The last invariant equilibrium represents congruent melting, at a temperature of 1129 K at the stoichiometric composition (Li_6CrF_6) or $X(\text{CrF}_3) = 0.25$. The calculated equilibrium is lower in temperature (1111 K), which is still considered a reasonable deviation considering the agreement with the other liquidus points around this composition.

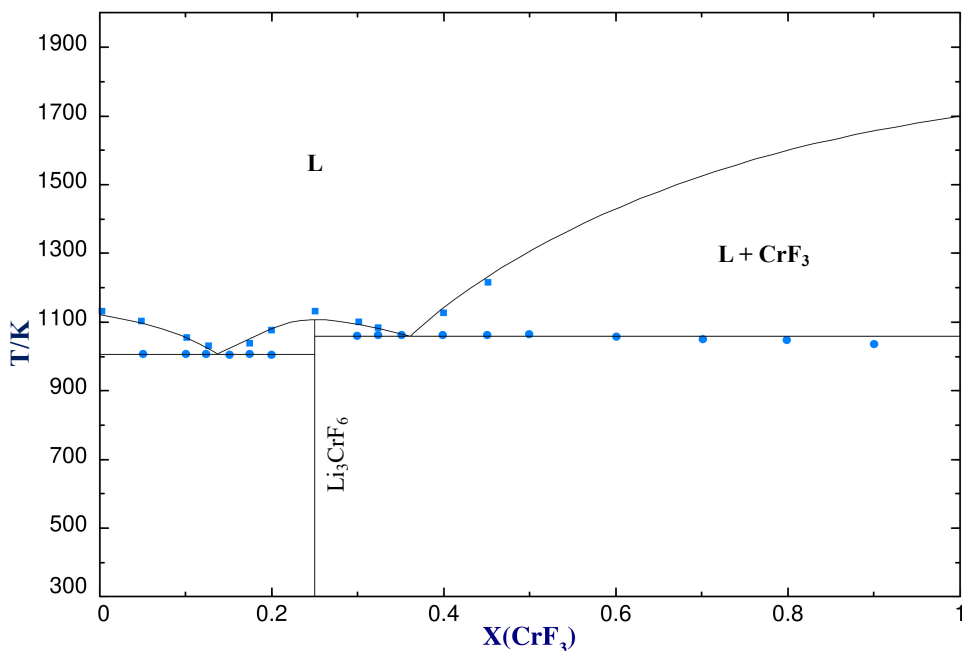


Figure 5.2.: Phase diagram of the LiF–CrF₃ system optimized in this work and comparison with experimental data provided by de Kozak [17]. Blue squares represent liquidus points and blue circles represent solidus points.

Table 5.5.: Invariant equilibria in the LiF–CrF₃ system.

Equilibrium	Invariant reaction	This study(calc.)		De Kozak [17]		Yin <i>et al.</i> (calc.) [31]	
		X(CrF ₃)	T/K	X(CrF ₃)	T/K	X(CrF ₃)	T/K
Eutectic	LiF(cr) + Li ₃ CrF ₆ (cr)=L	0.136	1008	0.15	1003	0.148	1003
Congruent melting	Li ₃ CrF ₆ (cr)=L	0.25	1111	0.25	1129	0.25	1125
Eutectic	Li ₃ CrF ₆ (cr) + CrF ₃ (cr)=L	0.363	1062	0.35	1059	0.354	1058

NaF-CrF₃

Experimentally, an eutectic equilibrium has been identified at a composition of $X(\text{CrF}_3) = 0.125$ and a temperature of 1166 K [17]. The calculated phase diagram shows an eutectic point at $X(\text{CrF}_3) = 0.106$ and a temperature of 1175 K. A gap is observed for the composition of this eutectic and the temperature in this model. This difference is within the uncertainties of the experimental work as is evident from the different values for the melting temperature of pure NaF (1278 K according to de Kozak and 1266 K in this work based on most recent data). Congruent melting has been measured at a temperature of 1413 K for the Na₃CrF₆ stoichiometric compound [17]. In this study, the optimized temperature is lower (1385 K), which is resulting from the fact that the model was designed in order to get the best balance between the different invariant points presented next. An eutectic equilibrium is computed at $X(\text{CrF}_3) = 0.371$ and a temperature of 1145 K, in good agreement with de Kozak's value at $X(\text{CrF}_3) = 0.375$ and 1145 K. An experimental validation needs to be performed for a better understanding of this area, however. In fact, de Kozak proposed a peritectic equilibrium at $X(\text{CrF}_3) = 0.375$ and a close eutectic point at $X(\text{CrF}_3) = 0.384$. In the assessment proposed by Yin *et al.* [31], two eutectic points are calculated at $X(\text{CrF}_3) = 0.367$ (1142 K) and $X(\text{CrF}_3) = 0.383$ (1141 K), respectively. In this model, comparable equilibria have been calculated, the compositions and temperatures are described in the Table 5.3 and show a good agreement with the values by Yin [31]. A peritectic point was identified at the stoichiometric composition NaCrF₄ and a temperature of 1232 K [17].

Table 5.6.: Invariant equilibria in the NaF–CrF₃ system. *The reactions in italic have been calculated and have not been experimentally confirmed.*

Equilibrium	Invariant reaction	This study(calc.)		De Kozak [17]		Yin <i>et al.</i> (calc.) [31]	
		X(CrF ₃)	T/K	X(CrF ₃)	T/K	X(CrF ₃)	T/K
Eutectic	NaF(cr) + Na ₃ CrF ₆ (cr)=L	0.106	1175	0.123	1166	0.114	1162
Congruent melting	Na ₃ CrF ₆ (cr)=L	0.25	1385	0.25	1413	0.25	1416
<i>Eutectic</i>	<i>Na₅Cr₃F₁₄(cr) + Na₃CrF₆=L</i>	<i>0.371</i>	<i>1145</i>	-	-	<i>0.367</i>	<i>1142</i>
<i>Congruent melting</i>	<i>Na₅Cr₃F₁₄(cr)=L</i>	<i>0.375</i>	<i>1145</i>	-	-	<i>0.375</i>	<i>1142</i>
<i>Eutectic</i>	<i>Na₅Cr₃F₁₄(cr) + NaCrF₄=L</i>	<i>0.381</i>	<i>1144</i>	-	-	<i>0.383</i>	<i>1141</i>
Peritectic	NaCrF ₄ (cr)=L + CrF ₃ (cr)	0.5	1232	0.5	1234	0.5	1239

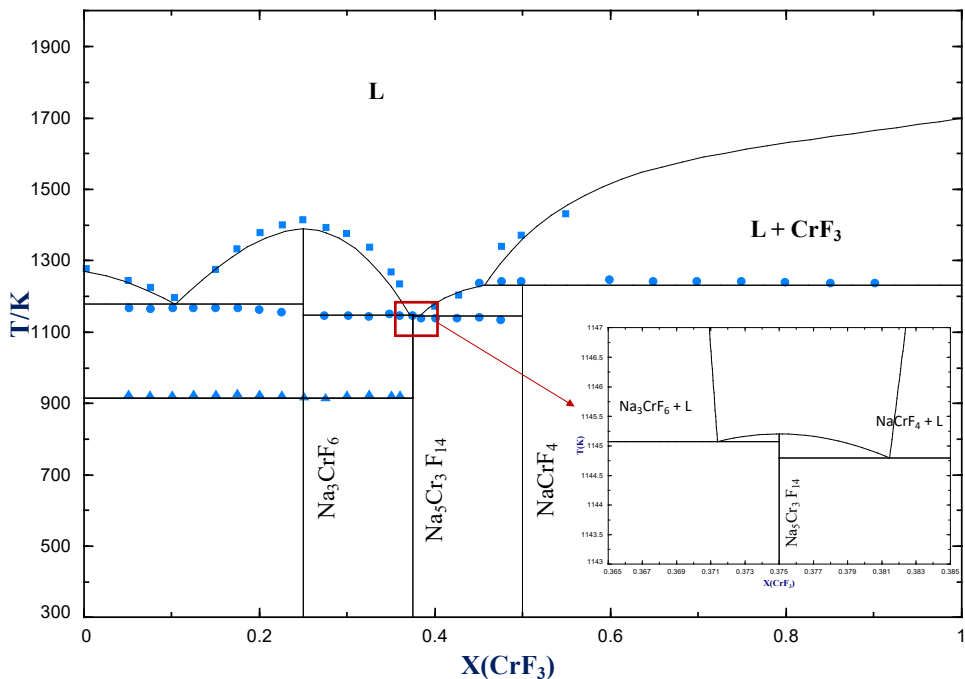


Figure 5.3.: Phase diagram of the NaF–CrF₃ system optimized in this work and comparison with the data provided by de Kozak [17]. Blue squares represent liquidus points, blue circles represent solidus points and blue triangles phase transition points. The area $0.365 < X(\text{CrF}_3) < 0.385$ is zoomed in the right window.

KF-CrF₃

For the KF–CrF₃ system, the situation is similar to the two previous cases. A first eutectic equilibrium is computed at a composition of $X(\text{CrF}_3) = 0.041$ and a temperature of 1108 K, which is in good agreement with the experimental value of $X(\text{CrF}_3) = 0.048$ (1115 K) [17]. A congruent melting point is calculated at 1553 K for the K₃CrF₆ intermediate compound, which is in very good agreement with the data of de Kozak (1553 K). A peritectic transition is identified at $X(\text{CrF}_3) = 0.333$ and a temperature of 1130 K, with a good agreement with the experimental data, i.e. $X(\text{CrF}_3) = 0.333$ (1133 K). The second eutectic is modeled at a composition of $X(\text{CrF}_3) = 0.432$ and a temperature of 1112 K, with a relatively close agreement with the experimental data ($X(\text{CrF}_3) = 0.45$ (1112 K)). Then a peritectic equilibrium is calculated at $X(\text{CrF}_3) = 0.50$ (1191 K) and another peritectic transition at $X(\text{CrF}_3) = 0.714$ (1390 K), with a good agreement with the data by de Kozak, $X(\text{CrF}_3) = 0.50$ (1200 K) and $X(\text{CrF}_3) = 0.714$ (1390 K), respectively.

Table 5.7.: Invariant equilibria in the KF–CrF₃ system.

Equilibrium	Invariant reaction	This study(calc.)		De Kozak [17]		Yin <i>et al.</i> (calc.) [31]	
		X(CrF ₃)	T/K	X(CrF ₃)	T/K	X(CrF ₃)	T/K
Eutectic	KF(cr) + K ₃ CrF ₆ (cr)=L	0.041	1108	0.048	1115	0.045	1113
Congruent melting	K ₃ CrF ₆ (cr)=L	0.25	1553	0.25	1553	0.25	1548
Peritectic	K ₂ CrF ₅ (cr)=K ₃ CrF ₆ (cr) + L	0.333	1130	0.333	1133	0.333	1135
Eutectic	K ₂ CrF ₅ (cr) + KCrF ₄ (cr)=L	0.432	1112	0.45	1112	0.426	1107
Peritectic	KCrF ₄ (cr)=K ₂ Cr ₅ F ₁₇ (cr) + L	0.50	1191	0.50	1200	0.50	1195
Peritectic	K ₂ Cr ₅ F ₁₇ (cr)=L + CrF ₃ (cr)	0.714	1390	0.714	1390	0.714	1388

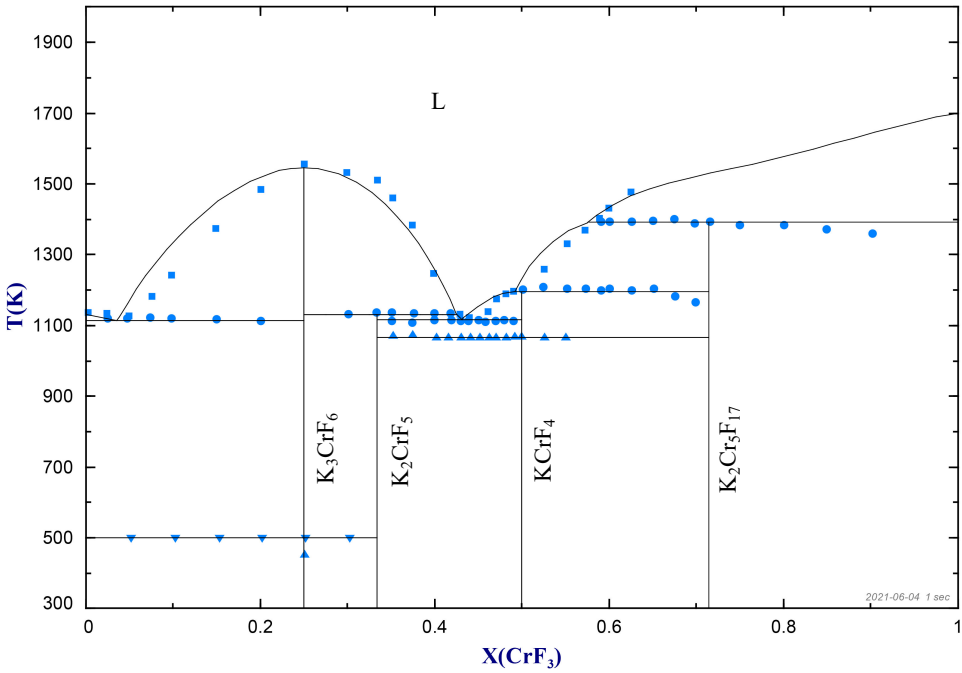


Figure 5.4.: Phase diagram of the KF–CrF₃ system optimized in this work and comparison with the data provided by de Kozak [17]. Blue squares represent liquidus points, blue circles represent solidus points and blue triangles phase transition points.

5.3.3. EXCESS PROPERTIES

The mixing enthalpy of the liquid solution is a very useful quantity to assess the reliability and consistency of the models developed for complex systems such as AF-CrF₃. The expectation is that the mixing enthalpy becomes more negative when the ionic radius of the alkali fluoride increases along the series LiF, NaF and KF [40]. Unfortunately, no experimental data have been reported for this system to compare with the calculated results obtained in this work. The only comparison available for these systems is that optimized by Yin *et al.* [30, 31] using their associate model. Their calculated data for the mixing enthalpy are slightly higher at 1500 K than the results provided in this work but confirm the same trend along the series of alkali-ions.

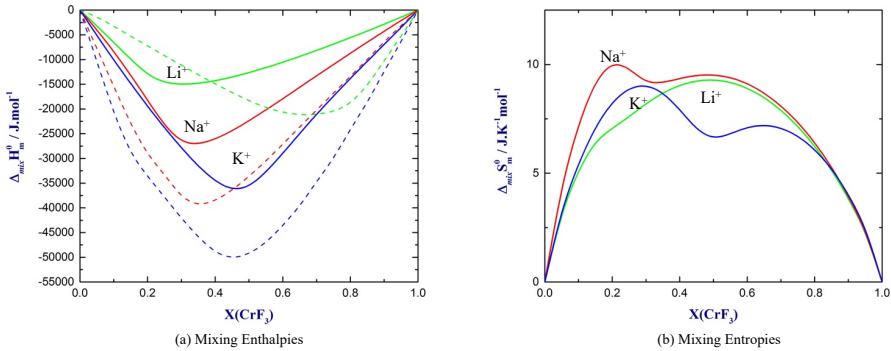


Figure 5.5.: (a) Mixing enthalpies and (b) mixing entropies of the LiF-CrF₃, NaF-CrF₃ and KF-CrF₃ systems calculated from the present models at T=1500 K. Mixing enthalpies represented with dashed lines (a) are the values presented by Yin at T=1500 K [31]

Mixing enthalpies calculated in this work show minima around the compositions $X(\text{CrF}_3) = 0.25$ for LiF-CrF₃ and $X(\text{CrF}_3) = 0.40$ for NaF-CrF₃ at respective energy values $\Delta_{mix}H_m^0(\text{LiF-CrF}_3) = -14.9 \text{ kJ}\cdot\text{mol}^{-1}$ and $\Delta_{mix}H_m^0(\text{NaF-CrF}_3) = -27.5 \text{ kJ}\cdot\text{mol}^{-1}$. The minimum is reached around the stoichiometric composition $X(\text{CrF}_3) = 0.50$ for the KF-CrF₃ system and a energy value of $\Delta_{mix}H_m^0(\text{KF-CrF}_3) = -35.4 \text{ kJ}\cdot\text{mol}^{-1}$. The location of the extrema (corresponding to maximum short-range ordering in the liquid solution) are directly related to the choice of the cation-cation coordination numbers. The mixing entropy of the LiF-CrF₃ system shows a regular profile, while that calculated in the NaF and KF-based systems both show an inflection around the $X(\text{CrF}_3) = 0.30-0.35$ and $0.50-0.55$ compositions, respectively. This evolution indicates a stronger short range ordering that is favored in certain concentration regions. The same observation was made for the LiF-ThF₄ system by Capelli *et al.* [41] and related to the local structure properties of the melt.

Following a similar interpretation, a high concentration of free F⁻ ions is expected in the NaF (resp. KF) rich regions, and a high concentration of bridged F⁻ ions in

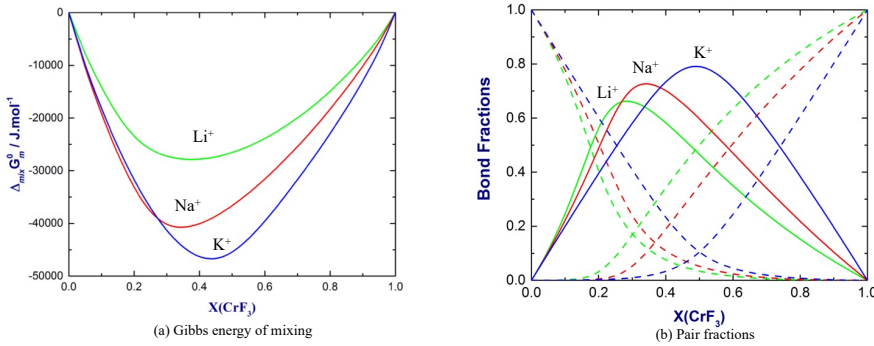


Figure 5.6.: (a) Gibbs energies and (b) bond fractions of the $\text{Li}-\text{CrF}_3$, $\text{Na}-\text{CrF}_3$ and $\text{K}-\text{CrF}_3$ systems calculated from the present thermodynamic models at $T=1500$ K. Dashed lines starting at the left y-axis: A-A-F-E, solid lines A-Cr-F-E, dashed lines starting at the right y-axis: Cr-Cr-F-F pair fractions.

the CrF_3 rich region. The bridging of F^- ions and formation of clusters/chains of Cr cations leads to ordering of the system, and thus to a decrease in entropy. Such network formation has been observed in several fluoride systems such as $\text{AF}-\text{ThF}_4$ and $\text{AF}-\text{UF}_4$ [41, 42]. Considering the three-dimensional polyhedral form of the CrF_3 compound, comparable to ThF_4 and UF_4 , it is likely to occur in these liquids as well.

Finally, Figure 5.6b shows the calculated pair fractions using the optimized models. The respective locations of the A-Cr-F-F pair fractions maxima ($X(\text{CrF}_3) = 0.25, 0.40$ and 0.5 for the LiF , NaF and KF systems), are again directly correlated to the choice of the coordination numbers. The maxima moreover show a round shape with corresponding fractions varying between 0.6 and 0.8, indicating a moderately basic system, as was also the case for the $\text{AF}-\text{NiF}_2$ systems [43]. A strongly basic system with quasi perfect second-nearest neighbor ordering leads to a SNN fraction close to one at the composition of maximum SRO, and to a sharp minimum in the calculated Gibbs energy of mixing [43].

5.4. CONCLUSION

In this work, new thermodynamic assessments of the $\text{AF}-\text{CrF}_3$ ($A = \text{Li}, \text{Na}, \text{K}$) phase diagrams have been presented using the CALPHAD method in combination with the modified quasichemical model in the quadruplet approximation. The models are based on the only experimental data reported in literature by de Kozak [17], and show a good agreement. Based on the same method, the $\text{CrF}_2-\text{CrF}_3$ binary system has been modeled based on the experimental data of Sturm [25]. Knowledge of the phase diagrams of all four systems helps improving the understanding of the role of products ($\text{CrF}_2, \text{CrF}_3$), which can be formed as a result of the corrosion of Hastelloy used as structural material in Molten Salt Reactors, on the properties of the liquid

fuel salt. The AF-CrF₃ systems are characterized by strongly negative Gibbs energies of mixing, decreasing from Li to K, and the calculated bond fractions suggest a moderately basic behavior.

ACKNOWLEDGMENTS

T. Dumaire acknowledges gratefully financial support from the Nuclear Research and Consultancy Group (NRG, Petten, Netherlands) and would like to thank Jaén Ocádiz-Flores for helpful discussions on the modeling methods.

REFERENCES

- [1] T. Dumaire, R. J. M. Konings, and A. L. Smith. “Thermodynamic Assessment of the AF–CrF₃ (A = Li, Na, K) and CrF₂–CrF₃ Systems”. In: *Thermo* 1 (2021), pp. 205–219. DOI: 10.3390/thermo1020014.
- [2] J. E. Kelly. “Generation IV International Forum: A decade of progress through international cooperation”. In: *Progress in Nuclear Energy* 77 (2014), pp. 240–246. DOI: 10.1016/j.pnucene.2014.02.010.
- [3] A. Tosolin, P. Souček, O. Beneš, J.-F. Vigier, L. Luzzi, and R. J. M. Konings. “Synthesis of plutonium trifluoride by hydro-fluorination and novel thermodynamic data for the PuF₃-LiF system”. In: *Journal of Nuclear Materials* 503 (2018), pp. 171–177. DOI: 10.1016/j.jnucmat.2018.02.037.
- [4] O. Beneš and R. J. M. Konings. “Molten Salt Reactor Fuel and Coolant”. In: (2012), pp. 359–389. DOI: 10.1016/b978-0-08-056033-5.00062-8.
- [5] Y. Liu, Y. Song, H. Ai, M. Shen, H. Liu, S. Zhao, Y. Liu, Z. Fei, X. Fu, and J. Cheng. “Corrosion of Cr in molten salts with different fluoroacidity in the presence of CrF₃”. In: *Corrosion Science* 169 (2020), p. 108636. DOI: 10.1016/j.corsci.2020.108636.
- [6] E. S. Bettis, W. B. Cottrell, E. R. Mann, J. L. Meem, and G. D. Whitman. “The Aircraft Reactor Experiment—Operation”. In: *Nuclear Science and Engineering* 2.6 (1957), pp. 841–853. DOI: 10.13182/nse57-a35497.
- [7] S. Delpech, C. Cabet, C. Slim, and G. S. Picard. “Molten fluorides for nuclear applications”. In: *Materials Today* 13.12 (2010), pp. 34–41. DOI: 10.1016/s1369-7021(10)70222-4.
- [8] L. C. Olson, J. W. Ambrosek, K. Sridharan, M. H. Anderson, and T. R. Allen. “Materials corrosion in molten LiF–NaF–KF salt”. In: *Journal of Fluorine Chemistry* 130.1 (2009), pp. 67–73. DOI: 10.1016/j.jfluchem.2008.05.008.
- [9] P. Sabharwall, M. Ebner, M. Sohal, P. Sharpe, A. Mark H., and A. Todd R. “Molten Salts for High Temperature Reactors: University of Wisconsin Molten Salt Corrosion and Flow Loop Experiments Issues Identified and Path Forward”. In: *Journal of Fluorine Chemistry* 130 (2010), pp. 67–73.
- [10] J. Liu, H. Huang, R. Liu, Z. Zhu, Q. Lei, A. Liu, and Y. Li. “In situ TEM observation of the evolution of helium bubbles in Hastelloy N alloy during annealing”. In: *Journal of Nuclear Materials* 537 (2020), p. 152184. DOI: 10.1016/j.jnucmat.2020.152184.

- [11] A. K. Tyagi and J. Köhler. "Preparation, magnetic properties and structure of β - Li_3CrF_6 ". In: *Materials research bulletin* 35.1 (Jan. 2000), pp. 135–141. DOI: 10.1016/s0025-5408(00)00177-x.
- [12] W. Massa and W. Rüdorff. "Über α - und β - Li_3MeF_6 -Verbindungen On α - and β - Li_3MeF_6 Compounds". In: *Zeitschrift für Naturforschung B* 26.12 (1971), pp. 1216–1218. DOI: 10.1515/znb-1971-1203.
- [13] G. Knoke. "Kristallstrukturbestimmungen an den Verbindungen NaCrF_4 , CsCrF_4 und $\text{Cs}_4\text{Cr}_5\text{F}_{19}$ sowie weitere Untersuchungen an ternären Chrom(III)fluoriden". PhD thesis. 1977. 192 pp.
- [14] P. García-Fernández, M. Moreno, and J. A. Aramburu. "Electrostatic Control of Orbital Ordering in Noncubic Crystals". In: *The Journal of Physical Chemistry C* 118.14 (2014), pp. 7554–7561. DOI: 10.1021/jp412329x.
- [15] G. Brunton. "The crystal structure of Na_3CrF_6 ". In: *Materials Research Bulletin* 4.9 (1969), pp. 621–626. DOI: 10.1016/0025-5408(69)90071-3.
- [16] A. L. Bail and A.-M. Mercier. "Distorted chiolite crystal structures of α - $\text{Na}_5\text{M}_3\text{F}_{14}$ (M= Cr, Fe, Ga) studied by X-ray powder diffraction". In: *Powder Diffraction* 18.2 (June 2003), pp. 128–134. DOI: 10.1154/1.1556990.
- [17] A. de Kozak. *Comptes rendus hebdomadaires des séances de l'Académie des sciences*. Série C. Research rep. 268. Académie des sciences de Paris, 1969, pp. 416–418.
- [18] P. Lacorre, M. Leblanc, J. Pannetier, and G. Ferey. "Ordered magnetic frustration: XV. Re-examination of the magnetic structure of α - KCrF_4 ". In: *Journal of magnetism and magnetic materials* 94.3 (1991), pp. 337–341.
- [19] H. Manaka, T. Etoh, Y. Honda, N. Iwashita, K. Ogata, N. Terada, T. Hisamatsu, M. Ito, Y. Narumi, A. Kondo, *et al.* "Effects of geometrical spin frustration on triangular spin tubes formed in CsCrF_4 and α - KCrF_4 ". In: *Journal of the Physical Society of Japan* 80.8 (2011), p. 084714. DOI: 10.1143/JPSJ.80.084714.
- [20] C. Sassoie and A. de Kozak. "Crystal Structure and Thermal Behaviour of $\text{K}_2[\text{CrF}_5 \cdot \text{H}_2\text{O}]$ ". In: *Zeitschrift für anorganische und allgemeine Chemie* 632.3 (2006), pp. 445–448.
- [21] A. de Kozak. "Etude de quelques composés fluores du chrome". In: *Revue de Chimie Minerale* 8 (1971), pp. 301–337.
- [22] M. Baran, H. Szymczak, W. Wardzyński, and B. M. Wanklyn. "EPR and optical absorption spectra of $\text{K}_2\text{Cr}_5\text{F}_{17}$ monocrystals". In: *physica status solidi (b)* 90.1 (Nov. 1978), K59–K61. DOI: 10.1002/pssb.2220900163.
- [23] A. de Kozak and M. Samouël. "Le système ternaire NaF , ZnF_2 , CrF_3 . I. étude radiocristallographique. Triangulation". In: *Journal of the Less Common Metals* 40.2 (1975), pp. 185–193.
- [24] W. O. J. Boo and J. W. Stout. "Heat capacity and entropy of CuF_2 and CrF_2 from 10 to 300 K. Anomalies associated with magnetic ordering and evaluation of magnetic contributions to the heat capacity". In: *The Journal of Chemical Physics* 71.1 (1979), pp. 9–16.

- [25] B. J. Sturm. "Phase equilibria in the system chromium (II) fluoride-chromium (III) fluoride". In: *Inorganic Chemistry* 1.3 (1962), pp. 665–672.
- [26] J.-P. Miranday, G. Ferey, C. Jacoboni, J.-M. Dance, A. Tressaud, and R. De Pape. "Croissance cristalline, polymorphisme et propriétés magnétiques de $\text{Na}_5\text{Cr}_3\text{F}_{14}$ ". In: *Revue de Chimie Minerale* 12 (1975), pp. 187–192.
- [27] W. N. Hansen and M. Griffel. "Heat Capacities of CrF_3 and CrCl_3 from 15 to 300 K". In: *The Journal of Chemical Physics* 28.5 (1958), pp. 902–907. DOI: 10.1063/1.1744294.
- [28] V. S. Iorish, N. M. Aristova, G. Bergman, L. Gorohov, A. Gusarov, Y. Yezhov, A. Kulikov, E. Osina, E. Shenyavskaya, N. Handamirova, and V. Jungmann. "Thermodynamic properties of substances (1978-2004)". In: Publishing House Nauka: Moscow, Russia, 2004.
- [29] I. Ansara, B. Sundman, and The Scientific Group ThermoData Europe (SGTE). *Computer Handling Determination of data*. Publishing house: Elsevier Science Pub. Co. Amsterdam, 1987, pp. 154–158.
- [30] H. Yin, K. Wang, L. Xie, H. Han, and W. Wang. "Thermodynamic modeling of KF-CrF_3 binary system". In: *Chemical Research in Chinese Universities* 31 (2015), pp. 461–465. DOI: 10.1007/s40242-015-4319-8.
- [31] H. Yin, P. Zhang, X. An, J. Cheng, X. Li, S. Wu, X. Wu, W. Liu, and L. Xie. "Thermodynamic modeling of LiF-NaF-KF-CrF_3 system". In: *Journal of Fluorine Chemistry* 209 (2018), pp. 6–13.
- [32] A. Tressaud, J. M. Dance, J. Ravez, J. Portier, P. Hagenmuller, and J. B. Goodenough. "Crystal chemistry and magnetic properties of CrIIIBIIIIF_5 compounds". In: *Materials Research Bulletin* 8.12 (Dec. 1973), pp. 1467–1477. DOI: 10.1016/0025-5408(73)90032-9.
- [33] U. R. Kattner, H. J. Seifert, and H. L. Lukas. "Editorial: Integrated computational materials engineering, CALPHAD". In: *CALPHAD: Computer Coupling of Phase Diagrams and Thermochemistry* 34 (2010), pp. 385–386. ISSN: 0364-5916. DOI: 10.1016/j.calphad.2010.10.005.
- [34] Y. A. Chang, S. Chen, F. Zhang, X. Yan, F. Xie, R. Schmid-Fetzer, and W. A. Oates. "Phase diagram calculation: past, present and future". In: *Progress in Materials Science* 49.3-4 (2004), pp. 313–345. DOI: 10.1016/s0079-6425(03)00025-2.
- [35] C. W. Bale, P. Chartrand, S. Degterov, G. Eriksson, K. Hack, R. B. Mahfoud, J. Melançon, A. Pelton, and S. Petersen. "FactSage thermochemical software and databases". In: *Calphad* 26.2 (2002), pp. 189–228.
- [36] J. Leitner, P. Voňka, D. Sedmidubský, and P. Svoboda. "Application of Neumann–Kopp rule for the estimation of heat capacity of mixed oxides". In: *Thermochimica Acta* 497.1–2 (2010), pp. 7–13. ISSN: 0040-6031. DOI: 10.1016/j.tca.2009.08.002.
- [37] M. W. Chase Jr. and National Information Standards Organization (US). "NIST-JANAF Thermochemical Tables". In: *Journal of Physical and Chemical Reference Data*. Vol. 9. Washington DC: American Chemical Society, 1998.

- [38] A. D. Pelton, S. Degterov, G. Eriksson, C. Robelin, and Y. Dessureault. “The modified quasichemical model I—binary solutions”. In: *Metallurgical and Materials Transactions B* 31.4 (Aug. 2000), pp. 651–659. ISSN: 1543-1916. DOI: 10.1007/s11663-000-0103-2.
- [39] O. Beneš, M. Beilmann, and R. J. M. Konings. “Thermodynamic assessment of the LiF–NaF–ThF₄–UF₄ system”. In: *Journal of Nuclear Materials* 405.2 (2010), pp. 186–198. DOI: 10.1016/j.jnucmat.2010.08.017.
- [40] K. C. Hong and O. J. Kleppa. “Enthalpies of mixing in some binary liquid alkali fluoride mixtures”. In: *The Journal of Chemical Thermodynamics* 8 (1976), pp. 31–36. ISSN: 0021-9614. DOI: 10.1016/0021-9614(76)90147-6.
- [41] E. Capelli, O. Beneš, M. Beilmann, and R. J. M. Konings. “Thermodynamic investigation of the LiF–ThF₄ system”. en. In: *The Journal of Chemical Thermodynamics* 58 (2013), pp. 110–116. ISSN: 0021-9614. DOI: 10.1016/j.jct.2012.10.013.
- [42] J. A. Ocadiz-Flores, A. E. Gheribi, J. Vlieland, D. de Haas, K. Dardenne, J. Rothe, R. J. M. Konings, and A. L. Smith. “Examination of the short-range structure of molten salts: ThF₄, UF₄, and related alkali actinide fluoride systems”. In: *Physical Chemistry Chemical Physics* 23.18 (2021), pp. 11091–11103. DOI: 10.1039/d1cp00566a.
- [43] J. A. Ocadiz-Flores, E. Capelli, P. E. Raison, R. J. M. Konings, and A. L. Smith. “Thermodynamic assessment of the LiF–NiF₂, NaF–NiF₂ and KF–NiF₂ systems”. In: *The Journal of Chemical Thermodynamics* 121 (June 2018), pp. 17–26. DOI: 10.1016/j.jct.2018.01.023.

6

THERMODYNAMIC BEHAVIOR OF CrF₂ CORROSION PRODUCT IN THE MOLTEN LiF-ThF₄ SALT SYSTEM

This work examines the thermochemistry of the chromium difluoride CrF₂ corrosion product in the molten LiF-ThF₄ fuel salt system. Through a combination of experimental investigations and thermodynamic modeling assessment, the study elucidates the thermodynamic properties, phase diagram equilibria, and overall thermodynamic behavior of CrF₂ corrosion product, following dissolution from a structural material to the molten salt fuel environment. In this work, two different synthesis methods were developed for pure CrF₂, further allowing to experimentally measure the phase equilibria in the LiF-CrF₂, CrF₂-ThF₄, and LiF-CrF₂-ThF₄ systems. Then, thermodynamic models were developed using the CALPHAD method based on the quasichemical model in the quadruplet approximation.

6.1. INTRODUCTION

THE recommendations of the Intergovernmental Panel on Climate Change require a profound adaptation of the energy production mix [1]. A wider use of nuclear power is suggested as one of the solutions to replace fossil fuels with high expectations for advanced reactor technologies.

The Molten Salt Reactor (MSR) is an advanced reactor design of the 4th generation, that uses liquid fluoride or chloride salts as both the fuel and coolant [2–5]. MSRs offer several advantages compared to traditional solid fueled and water-cooled nuclear reactors, such as inherent safety, with built-in passive safety mechanisms. MSRs can also accommodate a wide variety of fertile and fissile materials, including thorium, natural or depleted uranium, or re-processed plutonium, which are abundant naturally or from the nuclear fuel cycle of traditional Light Water Reactors [6].

The LiF-ThF₄-UF₄ salt mixture is one of the reference fuel salt selected for the

Molten Salt Fast Reactor (MSFR) concept [5]. Lithium fluoride (LiF) serves as the solvent, or matrix, for the other components in the fuel mixture. It has good heat transfer properties, is chemically stable at high temperatures [7], and is compatible with a fast neutron spectrum as long as it is enriched in lithium-7 (⁷Li) [8]. Thorium tetrafluoride (ThF₄), with the isotope ²³²Th, is a fertile material, meaning it can capture neutrons and be converted into fissile uranium-233 (²³³U) [9, 10]. Uranium tetrafluoride (UF₄) is a fissile material, which can sustain a nuclear chain reaction under its enriched forms in isotopes ²³³U and ²³⁵U.

Fluoride salts are corrosive in their molten state at high temperatures, which implies high requirements on the materials composing the reactor vessel [11]. Ni-based alloys with a high concentration of chromium, such as Hastelloy-N (7 wt% chromium content), were recommended in the preliminary studies realized by the Oak Ridge National Laboratory (ORNL) in the 1960s and 1970s during the Molten Salt Reactor Experiment (MSRE) and Molten Salt Breeder Reactor (MSBR) program [12]. Experimental investigations were realized in thermal convection loops, with the aim to simulate the material degradation of key components of the reactor (e.g. hot and cold parts, welded connections, angles). Hastelloy-N specimens were exposed, during nine years, to a LiF–BeF₂–ZrF₄–UF₄–ThF₄ (approximately 70-23-5-1-1 mol%) fuel salt, circulating between 833 K (560°C) and 973 K (700 °C) [13]. The different cross section observations, by macro and microstructural analyses, showed the formation of interstitial voids due to chromium depletion (and to some extent iron depletion). The post-analysis of the salt composition after nine years showed a significant increase in the concentration of Cr in the fuel salt (from 100 ppm to 1800 ppm) [13, 14]. These observations were confirmed by several subsequent studies [15–18]. According to the different investigations mentioned, the presence of oxidized chromium in the salt solution is mainly driven by the redox equilibrium:



To some extent, ionic impurities Ni²⁺ and Fe²⁺ dissolved into the salt after corrosion can also contribute to the further depletion of chromium from the structural material [13, 14], according to the following equilibria:



It was also found that oxidized chromium, in the cationic form of Cr²⁺ or Cr³⁺, could enhance the kinetics of redox reactions involved in the degradation of structural materials in contact with Li-based molten fluoride salts [19]. Based on their first results, ORNL researchers initially considered CrF₃ to be more stable, but the studies were focused on dissolution in FLiNaK salt. A study by Qiu *et al.* showed that the main corrosion product of chromium was in trivalent form (in a complex K₂NaCrF₆) and showed the stability of Cr(III) because of the strong basic solvent properties of the FLiNaK salt, leading to the disproportionation of Cr(II) [20]. In the case of pure LiF salt, CrF₃ was found to be unstable [21]. CrF₂ shows higher stability in the latter salt, but the phase equilibria and solubility of CrF₂ in LiF salt were never investigated to this date.

In this work, different synthesis methods of chromium difluoride were explored. The phase equilibria in the binary systems LiF–CrF₂, CrF₂–ThF₄, and the ternary LiF–CrF₂–ThF₄ system, were then assessed experimentally. Based on these results, thermodynamic CALPHAD models based on the quasichemical model in the quadruplet approximation for the liquid solution were developed for the first time.

6.2. EXPERIMENTAL

6.2.1. SAMPLE PREPARATION

STARTING MATERIALS

LiF (99.99%), CrF₃ (99.98%), and chromium powder (99.8%, 1250 mesh) (see, Table 6.1) were provided by Alfa Aesar, and dried in a furnace under argon at 573 K for 8 h. ThF₄ was synthesized at the Joint Research Center in Karlsruhe, using the process developed in-house by Souček *et al.* [22], consisting of the fluorination of ThO₂ with HF gas at 873 K.

Table 6.1.: Supplier and purity of the chemicals used in this work

Compound	Supplier	Purity	Concentration
LiF powder	Alfa Aesar	99.99%	
CrF ₃ powder	Alfa Aesar	99.98% (metal basis)	
Chromium powder (1250 mesh)	Alfa Aesar	99.8% (metal basis)	
Acetic acid	Alfa Aesar	99.7%	
Acetic anhydride	Alfa Aesar	99+%	
Hydrobromic acid	Alfa Aesar		47%
Ammonium hydroxide	Alfa Aesar		25%
Hydrofluoric acid	Bernd Kraft		47 to 51%

The purity was controlled by X-ray Diffraction (XRD) analysis and by Differential Scanning Calorimetry (DSC) measurement (these techniques are described in further details in Sections 6.2.2 and 6.2.3, respectively). The XRD spectrum of ThF₄ confirmed the monoclinic structure (C2/c) of the product, while the DSC data indicated a melting temperature of (1387 ± 5) K, in good agreement with the data of Souček *et al.*, (1384.6 ± 5) K. Pure LiF was found to melt at (1124 ± 5) K, in close agreement with the melting temperature measured by Capelli *et al.* [23], i.e. 1119 K, and its diffractogram showed a cubic structure (Fm $\bar{3}$ m), corroborating the purity of the chemical. The XRD and DSC analyses of CrF₂ are detailed in Section 6.4.1.

CrF₂ SYNTHESIS: CrF₃ REDUCTION ON CHROMIUM METAL

It is challenging to prepare CrF₂ at high purity by the reaction of gaseous HF on metallic chromium [24, 25], as handling HF gas is hazardous, and the process is not very effective. Two methods were used to synthesize pure CrF₂ in this work. The first one consisted in a reduction of pure CrF₃ powder on an excess of pure chromium

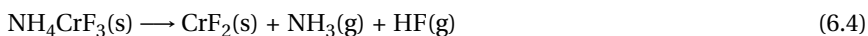
powder, i.e. (Cr:CrF₃)=(1.25:2), according to the reaction below:



Limited to small batches, i.e. 100 to 150 mg, the powders were thoroughly mixed and placed in a boron nitride liner, itself contained in a closed stainless steel crucible. The mixture was heated under argon atmosphere at 1053 K for 60 hours with a heating and cooling rates of 5 K min⁻¹ in a ceramic tubular furnace. The product was manually re-grinded in a mortar and heated using the same procedure twice more to a final mass yield of around 74%. The mass loss is due to the dispersion of the material during the grinding phases, to adhesion to the surface of the boron nitride liner, and formation of chromium gaseous phases (such as CrF₅). The final product was a dark green powder.

CrF₂ SYNTHESIS: SOLUTION ROUTE

A second method was developed in order to get better repeatability. Inspired by the method reported by de Kozak [26], but simplified, the synthesis route consists in 3 steps given by the following reactions:



Firstly, reproducing the chromium tetraacetate synthesis route developed by Levy *et al.* [27], 8 grams of chromium metal powder were placed in a 200 mL solution of acetic anhydride and acetic acid (ratio 1:4) in a round flask equipped with a stirring bar and a hot plate under an argon atmosphere. Immediately, 4.5 ml of hydrobromic acid (HBr) were added to the solution. The mixture was then heated up to 598 K (225 °C) for 45 minutes at reflux. A brown precipitate was formed after the solution was cooled down to room temperature. This precipitate was cleaned twice with deoxygenated acetone, and was recovered by filtration under inert atmosphere (Figure 6.1 (a)).

In the second step, the anhydrous dichromium(II) tetraacetate (Cr₂(O₂CCCH₃)₂) obtained was dissolved into 50 mL of deoxygenated distilled water in a polycarbonate vial under argon atmosphere. 35 mL of ammonia and then 26 mL of hydrofluoric acid were progressively diluted in 50 mL degassed distilled water in another polycarbonate vial. This solution was heated up to 323 K (50 °C) and quickly injected in the dichromium(II) tetraacetate solution under intensive stirring. A light blue precipitate was formed after a few seconds. After two successive decanting steps with 50 mL of a 1:1 deoxygenated water/methanol solution and then 50 mL of pure methanol, the product was filtered under vacuum. The final product was a pale blue powder (Figure 6.1 (b)). It should be stressed that this product is not air sensitive, but was still maintained under argon atmosphere during storage and further handling.

The final step was based on de Kozak's recommendation [26]: a thin layer (2 to 4 mm high) of NH₄CrF₃ powder was placed inside an alumina boat in batches

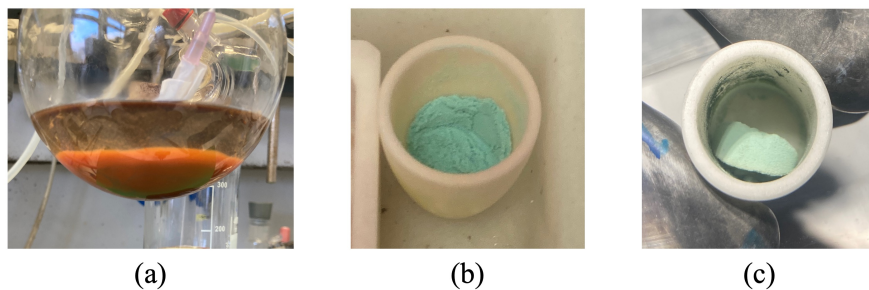


Figure 6.1.: The products obtained at every step of the synthesis, (a) $\text{Cr}_2(\text{COOCH}_3)_4$ precipitate in acetone cleaning solution, (b) NH_4CrF_3 dry powder, and (c) CrF_2 powder.

of about 200 mg and placed in a ceramic furnace under argon atmosphere. The thermolysis was carried out at a temperature of 873 K (600°C) for 1 hour, with a heating rate of 5 K min^{-1} . A pale green powder was obtained thereafter (Figure 6.1 (c)). It should be noted that larger batches can be used for this step, as long as the powder layer remains thin in the crucible. When using a thicker layer, formation of impurities such as Cr_2F_5 was observed.

6.2.2. X-RAY DIFFRACTION

The purity of the pure compounds used in this work as starting material for the measurements and synthesis, were checked using X-ray Diffraction (XRD) at room temperature ($T = 293 \pm 2$ K). For the inactive samples, a PANalytical X'Pert PRO X-Ray diffractometer with a Cu anode (0.4 x 12 mm line focus, 45 kV, 40 mA) was used. Samples were homogeneously placed on a sample holder closed by a Kapton[®] film under argon atmosphere. X-ray data were collected by step scanning in the range $10^\circ < 2\theta < 120^\circ$ in a Bragg-Brentano configuration. The X-ray scattered intensities were measured with a real time multi strip (RTMS) detector (X'Celerator). For the active samples containing thorium, the X-ray measurements were performed using a Bruker D8 X-ray diffractometer mounted in a Bragg-Brentano configuration with a curved Ge monochromator (1, 1, 1) and a ceramic copper tube (40 kV, 40 mA), equipped with a LinxEye position-sensitive detector. The device was installed in a glovebox under inert nitrogen atmosphere. The purities of each powder was analyzed by Rietveld refinement method using the FullProf suite software [28, 29].

6.2.3. CALORIMETRY MEASUREMENTS

Thermogravimetric measurements were conducted using a Netzsch STA 449C apparatus to assess the decomposition of NH_4CrF_3 . The temperature was controlled by a Pt-Rh (10%) thermocouple. The measurements were made on powder samples (10–20 mg) up to 873 K in alumina crucibles, and the applied heating and cooling

rates were 5 K min⁻¹.

3D heat flux Differential Scanning Calorimetry (DSC) measurements were conducted on a Setaram Multi Detector HTC module of the 96 line calorimeter. Every measurement consisted of at least four consecutive heating cycles with 5 or 10 K min⁻¹ heating rates, and cooling rates of 5 to 10 K min⁻¹. The solidus and eutectic transition temperatures were extracted on heating, from the onset of the linear integration of the corresponding endothermic heat flow peak, while the liquidus transition temperatures were taken from the maximum of the corresponding peak according the NIST recommendations [30]. A correction was applied on the measured temperatures using a calibration equation determined with pure metals (Sn, Pb, Al, Ag, Au), as function of the heating rate. The uncertainties on the measurements are estimated at 5 K for the solidus and eutectic transitions, and 10 K for the liquidus transitions (because of the broader nature of the heat flow profile). The data retained for the phase equilibria determination were the ones collected on heating. The data collected on cooling were used as a more sensitive quality check for the amount of equilibria. The samples were prepared from the LiF, CrF₂ and ThF₄ end-member powders, closely mixed at the desired molar composition and inserted in a pure nickel liner. The liners were hermetically closed in stainless steel crucibles designed according to the concept developed at the Joint Research Centre in Karlsruhe [31], ensuring the stability of the samples' compositions and limiting the vapor releases during heating. The data collected in this work for the LiF-CrF₂, CrF₂-ThF₄, and LiF-CrF₂-ThF₄ systems are listed in Tables 6.5, 6.6 and 6.8, respectively.

6.2.4. LOW-TEMPERATURE HEAT CAPACITY OF CrF₂

Low-temperature heat capacity measurements were performed on the synthesized CrF₂ material, using a thermal-relaxation method [32] on $m = (1.83 \pm 0.05)$ mg and (6.35 ± 0.05) mg pellets in the temperature range $T = (1.9-389)$ K, with a PPMS (Physical Property Measurement System, Quantum Design) instrument. Measurements were done both with no applied magnetic field ($B = 0$ T), and under magnetic field ($B = 1, 4, 6, 8, 10, 12, 14$ T), so as to get more insight into the origin of the anomaly observed around 49 K. The contributions of the sample platform, wires, and grease were obtained by a separate measurement of an addenda curve. Based on previous works with this instrument with standard materials, metallic, and oxide compounds, the uncertainty was estimated to be around 1-2% in the middle range of acquisition (from 10 to 70 K), and around 3-4% near room temperature and towards the lowest temperatures.

6.2.5. MAGNETIZATION MEASUREMENTS ON CrF₂

Magnetization measurements were carried out in the temperature range $T = (2-300)$ K and in magnetic fields up to 70 kOe using a SQUID-VSM instrument (MPMS3, Quantum Design). Due to the sensitivity of the material to air and moisture, encapsulation of the sample ($m = 32.4 \pm 0.2$ mg) was performed in a dry air plexiglas container. The latter was calibrated beforehand, and its magnetic contribution

was fitted with high precision (better than 5 %). Measurements obtained by the VSM technique, i.e. DC magnetization (M), allowed us to derive DC magnetic susceptibility M/H (with H the applied magnetic field). AC magnetic measurements were moreover performed around the magnetic transition in 0 DC field, with an AC excitation field of 10 Oe at 35.798 Hz. The reader is referred to the Appendix A for further details on the measurement results.

6.3. THERMODYNAMIC MODELING

For pure compounds, the Gibbs energy is expressed by:

$$G(T) = \Delta_f H_m^o(298.15) - S_m^o(298.15) \cdot T + \int_{298.15}^T C_{p,m}(T) dT - T \int_{298.15}^T \frac{C_{p,m}}{T} dT \quad (6.5)$$

where $\Delta_f H_m^o(298.15)$ is the standard enthalpy of formation, and $S_m^o(298.15)$ is the standard entropy of the pure compound at standard pressure and reference temperature 298.15 K. $C_{p,m}$ is the heat capacity defined as:

$$C_{p,m}(T) = a + bT + cT^2 + dT^{-2} \quad (6.6)$$

The thermodynamic data for LiF were taken from the JRCMSD database [33], and from the re-evaluation of Tosolin *et al.* for ThF₄ [34, 35]. For CrF₂, the thermodynamic functions were taken from the IVTAN database [36]. All the thermodynamic data used in this work are summarized in Table 6.2.

6.3.1. LIQUID SOLUTION

The modified quasichemical model in the quadruplet approximation was used to describe the liquid solutions [40, 41]. This model describes well ionic liquids with strong short-range ordering. The basic unit of the liquid solution in this model is a quadruplet composed of two anions (F⁻ twice in this case) and two cations (Aⁿ⁺ and B^{m+}). The composition of maximum short-range ordering in this model is selected by varying the ratio between the cation-cation coordination numbers $Z_{AB/FF}^A$ and $Z_{AB/FF}^B$. Two interactions are considered: the First Nearest Neighbor (FNN) interaction (cation - anion interaction) and the Second Nearest Neighbor (SNN) interaction (interactions between the two nearest ions in the same sublattice). Short-range ordering is defined by the quadruplet approximation and includes the SNN interactions between each cation and each anion. Here, $\Delta g_{AB/F}$ is defined as the parameter of the Gibbs energy change associated with the SNN exchange reaction described as:

$$\Delta g_{AB/F} = \Delta g_{AB/F}^0 + \sum_{i \geq 1} g_{AB/F}^{i0} \chi_{AB/F}^i + \sum_{j \geq 1} g_{AB/F}^{0j} \chi_{BA/F}^j \quad (6.7)$$

where $\Delta g_{AB/F}^0$ and $g_{AB/F}^{ij}$ can be dependent on temperature, but independent of composition. These parameters are optimized to match as best as possible the

Table 6.2: Thermodynamic and structural data for end-members and intermediate compounds used in this work for the thermodynamic assessment. Standard enthalpy of formation $\Delta_f H_m^\circ$ (298.15 K), standard entropy S_m° (298.15 K) and heat capacity coefficient of pure compounds $C_{p,m}(T/K)/(JK^{-1} \text{mol}^{-1}) = a + b \cdot T + c \cdot T^2 + d \cdot T^{-2}$.

Compound	Space group	$\Delta_f H_m^\circ$ (298.15 K) (kJ mol ⁻¹)	S_m° (298.15 K) (JK ⁻¹ mol ⁻¹)	$C_{p,m}(T/K)/(JK^{-1} \text{mol}^{-1}) = a + b \cdot T + c \cdot T^2 + d \cdot T^{-2} + e \cdot T^3$				T(K)	Ref.
				a	b	c	d		
LiF ^(cr)	Fm-3m(225)	-616.931	35.66	43.30898	1.6312168·10 ⁻²	5.0470398·10 ⁻⁷	-5.691236·10 ⁵	298.15-2500	[37]
LiF ^(l)		-598.654	42.96	64.183	-	-	-	298.15-6000	[37]
CrF ₂ ^(cr)	P2 ₁ /c(14)	-781.800	86.87	76.68345	1.054105·10 ⁻²	-1.386756·10 ⁻⁹	-1.338373·10 ⁶	298.15-1167	[36]
CrF ₂ ^(l)		-764.692	86.31	100	-	-	-	298.15-4000	[36]
ThF ₄ ^(cr)	C2/c(15)	-2097.900	142.05	111.46	2.69·10 ⁻²	-	-7.8·10 ⁵	298.15-2500	[35, 38, 39]
ThF ₄ ^(l)		-2100.360	106.61	168.0	-	-	-	298.15-2500	[35, 38, 39]
Li ₃ ThF ₇ ^(cr)	Ccca(68)	-3960.000	248.9	241.387	7.5836·10 ⁻²	1.5141·10 ⁻⁶	-2.4873·10 ⁶	298.15-2500	[23, 35]
LiThF ₅ ^(cr)	I4 ₁ /a(88)	-2720.300	179.1	167.8	2.7·10 ⁻²	-	-1.513510·10 ⁶	298.15-2500	[23, 35]
LiTh ₂ F ₉ ^(cr)	P4 ₁ /mmm(129)	-4820.200	324.29	291.3	3.86·10 ⁻²	-	-3.076934·10 ⁶	298.15-2500	[23, 35]
LiTh ₄ F ₁₇ ^(cr)	I4 ₁ /m(87)	-9016.100	609.0	536.2	6.22·10 ⁻²	-	-5.051854·10 ⁶	298.15-2500	[23, 35]

experimental data available for each system. The dependence on composition is given by the term $\chi_{AB/F}$ defined as:

$$\chi_{AB/F} = \frac{X_{AA}}{X_{AA} + X_{AB} + X_{BB}} \quad (6.8)$$

where X_{AA} , X_{AB} and X_{BB} represent the different cation-cation pair fractions. The anion-anion coordination is then calculated such that electro-neutrality in the system is maintained. The selection of anion-anion coordination is made according to the following equation:

$$\frac{q_A}{Z_{AB/FF}^A} + \frac{q_B}{Z_{AB/FF}^B} = 2 \cdot \frac{q_F}{Z_{AB/FF}^F} \quad (6.9)$$

where q_i represent the charges of the different ions, and $Z_{AB/FF}^F$ represents the anion-anion coordination number. The ratio of cation-cation coordination numbers $Z_{AB/FF}^A$ and $Z_{AB/FF}^B$ is selected to match the composition of maximum short-range ordering, usually found close to the lowest eutectic in the phase diagrams, where the Gibbs energy is expected to reach its minimum. The coordination numbers selected in this work are listed in Table 6.3.

Table 6.3.: Cation-cation and anion-anion coordination numbers of the liquid solution used in this work for the thermodynamic modeling.

A	B	$Z_{AB/FF}^A$	$Z_{AB/FF}^B$	$Z_{AB/FF}^F$
Li ⁺	Li ⁺	6	6	6
Cr ²⁺	Cr ²⁺	6	6	3
Th ⁴⁺	Th ⁴⁺	6	6	1.5
Li ⁺	Cr ²⁺	6	6	4
Li ⁺	Th ⁴⁺	2	6	1.71
Cr ²⁺	Th ⁴⁺	2	6	1.2

The optimized excess Gibbs energies for the LiF–CrF₂ and CrF₂–ThF₄ binary systems of the liquid solutions are given by the following equations:

$$\Delta g_{LiCr/FF} = -4993 + (-600 + 2.75 \cdot T)\chi_{LiCr/FF} + (279 + 3.2 \cdot T)\chi_{CrLi/FF} \quad \text{J mol}^{-1} \quad (6.10)$$

$$\Delta g_{CrTh/FF} = -669 + (-5045 + 5 \cdot T)\chi_{CrTh/FF} + (-3531 + 7 \cdot T)\chi_{ThCr/FF} \quad \text{J mol}^{-1} \quad (6.11)$$

These equations were optimized by manual iteration with support from the FactSage Calphad Optimizer version 1.3. For the LiF–ThF₄ system, the equation and intermediate compounds data were taken from Ocadiz *et al.* [35]. The optimized excess Gibbs energy parameters are reproduced here for completeness.

$$\Delta g_{LiTh/FF} = -10878 + (-6694 + 2.929 \cdot T)\chi_{LiTh/FF} + (-20920 + 19.25 \cdot T)\chi_{ThLi/FF} \quad \text{J mol}^{-1} \quad (6.12)$$

LIQUID SOLUTION FOR THE TERNARY SYSTEM

The ternary phase diagram of the LiF-CrF₂-ThF₄ system was calculated from the three binary sub-systems described above, using the Kohler/Toop interpolation [42]. This is an asymmetric interpolation model for which two symmetry groups are considered: LiF belongs to the first group of symmetry, i.e. the monovalent group, which tends to remain a dissociated ionic liquid; CrF₂ (divalent) and ThF₄ (tetravalent) belong to the second group of symmetry, which is more apt to form molecular species in the melt. No ternary excess parameter was needed to describe the phase equilibria in the ternary system. Based on the binary models optimized here, the experimental ternary data were found in sufficient agreement without any excess term (see section 6.4.4).

6.4. RESULTS & DISCUSSIONS

6.4.1. CrF₂ SYNTHESIS AND PRODUCT CHARACTERIZATION

Using the first synthesis route, i.e. reduction of CrF₃ mixed with Cr metal, the product purity after 3 cycles was determined at $(99 \pm 1)\%$ based on Rietveld refinement of the XRD data, and the melting temperature measured at (1164 ± 5) K by DSC, in good agreement with literature data from Sturm [43]: (1167 ± 6) K. Impurities of CrF₃ and Cr₂F₅ were still detected in the XRD measurement. We hypothesize that the excess of Cr⁰ mainly diffused into the porosity of the boron nitride liner.

Using the second synthesis route, i.e. in solution, the final product purity was determined to be $(99.5 \pm 0.5)\%$, based on the combined XRD and DSC data. No secondary phases were detected, and the melting temperature of the compound was measured at (1167 ± 5) K, in excellent agreement with the measurement of Sturm [43]. In the intermediate steps, the formation of NH₄CrF₃ dry powder was also confirmed by XRD. A Thermal Gravimetric Analysis (TGA) showed that total vaporization of NH₃(g) and HF(g) occurs during the thermolysis at a temperature of 633 K (360°C) (see Figure 6.2). The temperature selected in the synthesis was 873 K (600 °C) so as to ensure a high crystallinity of the final product.

On the basis of the success of the second method, the mass yields and purities of the final products, the synthesis route in solution was considered more robust overall. CrF₂ crystallizes with monoclinic symmetry, in space group $P2_1/c$. The refined lattice parameters and atomic positions obtained in this work are listed in Table 6.4.

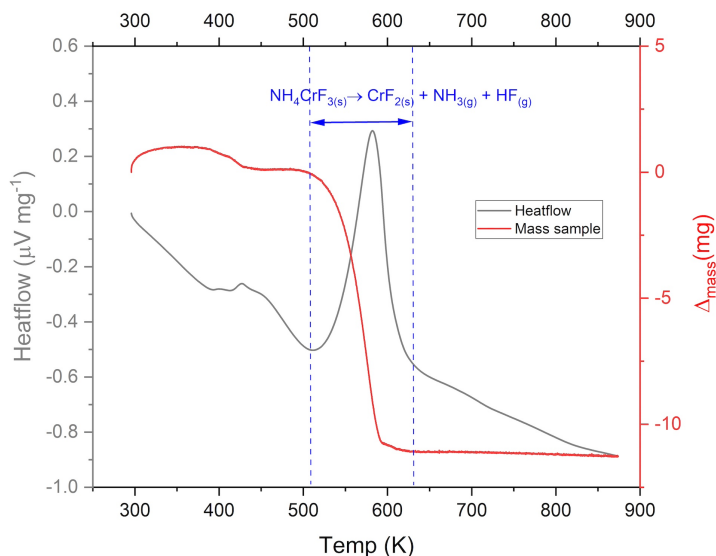


Figure 6.2.: TGA profile of the decomposition of NH_4CrF_3 under a 5 K min^{-1} heating from 293 to 873 K under argon flow.

6

Table 6.4.: Refined lattice parameters and atomic positions for CrF_2 , obtained in this work by the solution route. CrF_2 crystallizes with monoclinic symmetry, in space group $P2_1/c$ (space group 14).

Lattice parameters	a(Å)	b(Å)	c(Å)	Angle β (°)
	3.5132(1)	4.7131(2)	5.5650(2)	122.413(1)
Atomic positions	Wyck.	x	y	z
Cr	2a	0	0	0
F	4e	0.259(2)	0.303(1)	0.308(1)

6.4.2. CrF_2 LOW-TEMPERATURE HEAT CAPACITY

Using the high purity material prepared with the solution route, low temperature heat capacity measurements were conducted using thermal relaxation calorimetry in the range (1.9-389) K. The data collected in this work are found in very good agreement with the data reported in 1979 by Boo and Stout [44] in the temperature range (10-300 K) using adiabatic calorimetry (see Figures 6.4). The present data extend the range of temperature from (1.9-10 K) and (300-389 K), respectively. Boo and Stout [44] performed a very thorough analysis of the heat capacity of this compound, including the accounting of Cr^{2+} crystal field electronic ground state

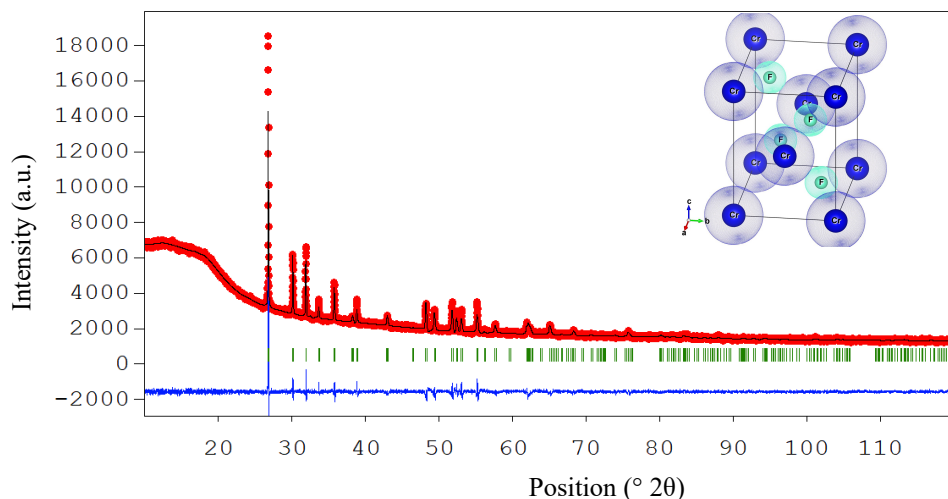


Figure 6.3.: Diffractogram of CrF₂ synthesized by the solution route Y_{obs} (red dots), measured at (293 ± 2) K with a Cu anode, compared to the Rietveld refinement performed on the FullProf suite software. Y_{calc} (black line) is the calculated XRD pattern; $Y_{\text{obs}} - Y_{\text{calc}}$ (blue line) is the differential calculation between observed and calculated data. The Bragg's reflection angular positions of CrF₂ are shown by green marks. The inset shows a schematic representation of the unit cell. Cr atoms are shown in blue, while fluorine atoms are shown in light green.

6

contribution. In accordance with Lim and Stout [45, 46], the authors report a ligand field of D_{4h} symmetry, a ${}^5B_{1g}$ ground orbital level, and a low-lying orbital level ${}^5A_{1g}$ at 116 cm^{-1} . We retain here the standard entropy value recommended by the authors at $86.87 \text{ J}\cdot\text{K}^{-1}\cdot\text{mol}^{-1}$ for the thermodynamic modeling assessment.

It is also worth pointing out that the measured data above 300 K (estimated to have a 3-4% uncertainty) is in good agreement with the heat capacity function recommended in the IVTAN tables [36], as shown in Figure A.2 in the Appendix A, supporting the selection of thermodynamic data.

Moreover, the magnetic anomaly reported by Boo and Stout [44] around (49.26 ± 0.01) K is confirmed with our heat capacity data, although the shape of the λ anomaly is not as sharp. Nevertheless, we can confirm the antiferromagnetic nature of the magnetic transition, as the anomaly shifts to slightly lower temperatures upon application of a magnetic field (see Figure A.1 in Appendix A). Complementary magnetization studies were then performed, as detailed in Appendix A, to get more insight into the magnetic properties of this compound.

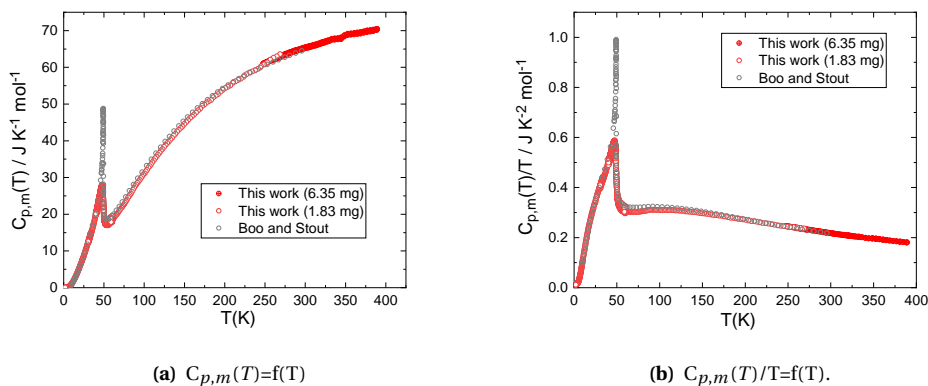


Figure 6.4.: Heat capacity of CrF₂ measured in this work, and compared to the data measured by Boo and Stout [44].

6.4.3. BINARY SYSTEMS

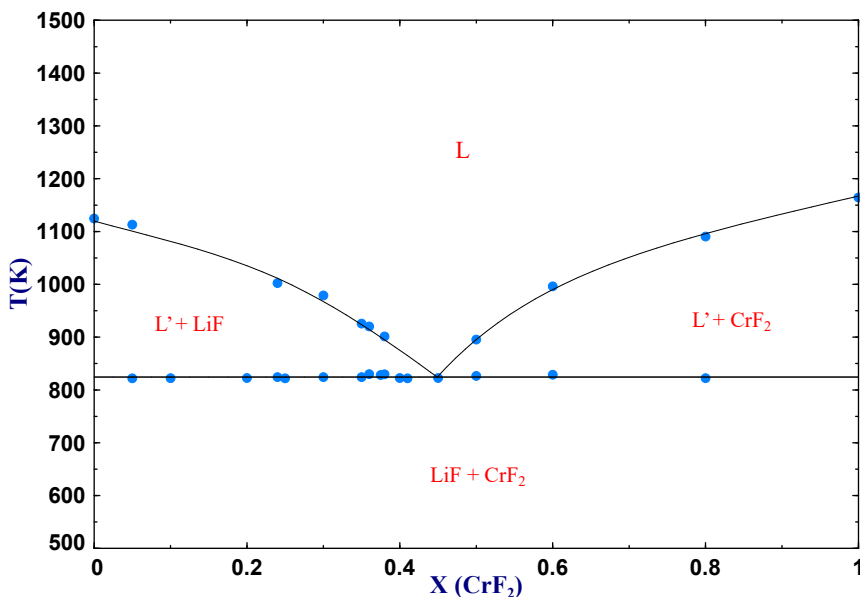
LiF-CrF₂

The phase equilibria measurements on this system do not indicate the presence of any stable intermediate compound. Only thermodynamic equilibria identified as eutectic and liquidus transitions were observed. X-ray Diffraction analyses performed after DSC measurements showed only XRD patterns of LiF and CrF₂ end-members. The consistency of the solidus line temperatures measured along all the range of compositions, and the logical liquidus trend confirmed this hypothesis. A unique eutectic equilibrium was measured at $X_{\text{CrF}_2} = 0.45$ and at a temperature of (822 ± 5) K. The model was optimized based on the measured experimental data (Table 6.5, Figure 6.5).

Table 6.5.: Phase diagram equilibria in the LiF-CrF_2 system collected by DSC in this work.

X_{LiF}	X_{CrF_2}	T (K)	Equilibrium	Reaction	X_{LiF}	X_{CrF_2}	T (K)	Equilibrium	Reaction
1	0	1124.3	Melting	$\text{LiF} = \text{L}$	0.625	0.375	828	Eutectic	$\text{LiF} + \text{CrF}_2 = \text{L}$
0.95	0.05	822	Eutectic	$\text{LiF} + \text{CrF}_2 = \text{L}$	0.625	0.375	877	Liquidus	$\text{LiF} + \text{L}' = \text{L}$
0.95	0.05	1113	Liquidus	$\text{LiF} + \text{L}' = \text{L}$	0.62	0.38	829	Eutectic	$\text{LiF} + \text{CrF}_2 = \text{L}$
0.90	0.10	822	Eutectic	$\text{LiF} + \text{CrF}_2 = \text{L}$	0.62	0.38	901	Liquidus	$\text{LiF} + \text{L}' = \text{L}$
0.80	0.20	822	Eutectic	$\text{LiF} + \text{CrF}_2 = \text{L}$	0.60	0.40	822	Eutectic	$\text{LiF} + \text{CrF}_2 = \text{L}$
0.76	0.24	824	Eutectic	$\text{LiF} + \text{CrF}_2 = \text{L}$	0.59	0.41	822	Eutectic	$\text{LiF} + \text{CrF}_2 = \text{L}$
0.76	0.24	1002	Liquidus	$\text{LiF} + \text{L}' = \text{L}$	0.55	0.45	822	Eutectic	$\text{LiF} + \text{CrF}_2 = \text{L}$
0.75	0.25	822	Eutectic	$\text{LiF} + \text{CrF}_2 = \text{L}$	0.50	0.50	826	Eutectic	$\text{LiF} + \text{CrF}_2 = \text{L}$
0.70	0.30	824	Eutectic	$\text{LiF} + \text{CrF}_2 = \text{L}$	0.50	0.50	895	Liquidus	$\text{CrF}_2 + \text{L}' = \text{L}$
0.70	0.30	979	Liquidus	$\text{LiF} + \text{L}' = \text{L}$	0.40	0.60	829	Eutectic	$\text{LiF} + \text{CrF}_2 = \text{L}$
0.65	0.35	824	Eutectic	$\text{LiF} + \text{CrF}_2 = \text{L}$	0.40	0.60	996	Liquidus	$\text{CrF}_2 + \text{L}' = \text{L}$
0.65	0.35	926	Liquidus	$\text{LiF} + \text{L}' = \text{L}$	0.20	0.80	822	Eutectic	$\text{LiF} + \text{CrF}_2 = \text{L}$
0.64	0.36	830	Eutectic	$\text{LiF} + \text{CrF}_2 = \text{L}$	0.20	0.80	1090	Liquidus	$\text{CrF}_2 + \text{L}' = \text{L}$
0.64	0.36	920	Liquidus	$\text{LiF} + \text{L}' = \text{L}$	0	1	1164.2	Melting	$\text{CrF}_2 = \text{L}$

The uncertainties on the temperature measurement are estimated at ± 5 K for the melting and eutectic transitions, and ± 10 K for the liquidus transitions.

**Figure 6.5.:** Phase diagram of the LiF-CrF_2 system, blue circles (●) represent the experimental data collected in this work (Table 6.5).

CrF₂-ThF₄

As for the system described above, the calorimetry measurements showed a consistent eutectic temperature for all the range of compositions. The liquidus transitions were also in-line with a simple eutectic system. The XRD spectra collected for different representative compositions settled that the mixtures were composed of CrF₂ and ThF₄ only. The eutectic composition was not measured directly. The measurement at the composition $X_{\text{CrF}_2} = 0.324$, showed only one transition at a temperature of (1034 ± 5) K on the heating curve. However, the cooling curve showed clearly the presence of a liquidus/solidification peak at a higher temperature, which was too close to be differentiated on the heating curve. The phase diagram was modeled on the basis of the collected data, with an eutectic composition calculated at $X_{\text{CrF}_2} = 0.31$ (see Table 6.6 and Figure 6.6).

Table 6.6.: Phase diagram equilibria in the CrF₂-ThF₄ system collected by DSC in this work.

X_{CrF_2}	X_{ThF_4}	T (K)	Equilibrium	Reaction	X_{CrF_2}	X_{ThF_4}	T (K)	Equilibrium	Reaction
1	0	1167.5	Melting	CrF ₂ = L	0.468	0.532	1034	Eutectic	CrF ₂ + ThF ₄ = L
0.949	0.051	1027	Eutectic	CrF ₂ + ThF ₄ = L	0.468	0.532	1197	Liquidus	ThF ₄ + L' = L
0.949	0.051	1050	Liquidus	CrF ₂ + L' = L	0.443	0.557	1034	Eutectic	CrF ₂ + ThF ₄ = L
0.733	0.267	1034	Eutectic	CrF ₂ + ThF ₄ = L	0.443	0.557	1205.6	Liquidus	ThF ₄ + L' = L
0.733	0.267	1055	Liquidus	CrF ₂ + L' = L	0.367	0.633	1034	Eutectic	CrF ₂ + ThF ₄ = L
0.676	0.324	1034	Eutectic	CrF ₂ + ThF ₄ = L	0.367	0.633	1238	Liquidus	ThF ₄ + L' = L
0.610	0.390	1034	Eutectic	CrF ₂ + ThF ₄ = L	0.316	0.684	1035	Eutectic	CrF ₂ + ThF ₄ = L
0.610	0.390	1106	Liquidus	ThF ₄ + L' = L	0.316	0.684	1284	Liquidus	ThF ₄ + L' = L
0.601	0.399	1034	Eutectic	CrF ₂ + ThF ₄ = L	0.104	0.896	1029	Eutectic	CrF ₂ + ThF ₄ = L
0.550	0.450	1034	Eutectic	CrF ₂ + ThF ₄ = L	0.104	0.896	1366	Liquidus	ThF ₄ + L' = L
0.550	0.450	1121	Liquidus	ThF ₄ + L' = L	0	1	1386.8	Melting	ThF ₄ = L
0.504	0.496	1031	Eutectic	CrF ₂ + ThF ₄ = L					

The uncertainties on the temperature measurement are estimated at ± 5 K for the melting and eutectic transitions, and ± 10 K for the liquidus transitions.

Table 6.7.: Invariant equilibria in LiF-CrF₂ and CrF₂-ThF₄ systems modeled in this work, compared to the measured data.

System	Invariant reaction	Equilibrium	Composition	Modeled temperature (K)	Measured temperature (K)
LiF-CrF ₂	LiF + CrF ₂ = L	Eutectic	$X_{\text{CrF}_2} = 0.45$	823	(822 ± 5)
LiF-ThF ₄	LiF + Li ₃ ThF ₇ = L	Eutectic	$X_{\text{ThF}_4} = 0.24$	835.8	$(832 \pm 5)^a$
	Li ₃ ThF ₇ = L	Congruent melting	$X_{\text{ThF}_4} = 0.25$	836.9	$(832 \pm 5)^a$
	Li ₃ ThF ₇ + LiThF ₅ = L	Eutectic	$X_{\text{ThF}_4} = 0.28$	834.4	$(826 \pm 5)^a$
	LiThF ₅ = LiTh ₂ F ₉ + L'	Peritectic	$X_{\text{ThF}_4} = 0.50$	872.1	$(870 \pm 5)^a$
	LiTh ₂ F ₉ = LiTh ₄ F ₁₇ + L'	Peritectic	$X_{\text{ThF}_4} = 0.67$	1036.3	$(1038 \pm 5)^a$
	LiTh ₄ F ₁₇ = ThF ₄ + L'	Peritectic	$X_{\text{ThF}_4} = 0.80$	1173.8	$(1176 \pm 5)^a$
CrF ₂ -ThF ₄	CrF ₂ + ThF ₄ = L	Eutectic	$X_{\text{ThF}_4} = 0.31$	1029	(1034 ± 5)

^aThe experimental data presented here were collected by Capelli *et al.* [23].

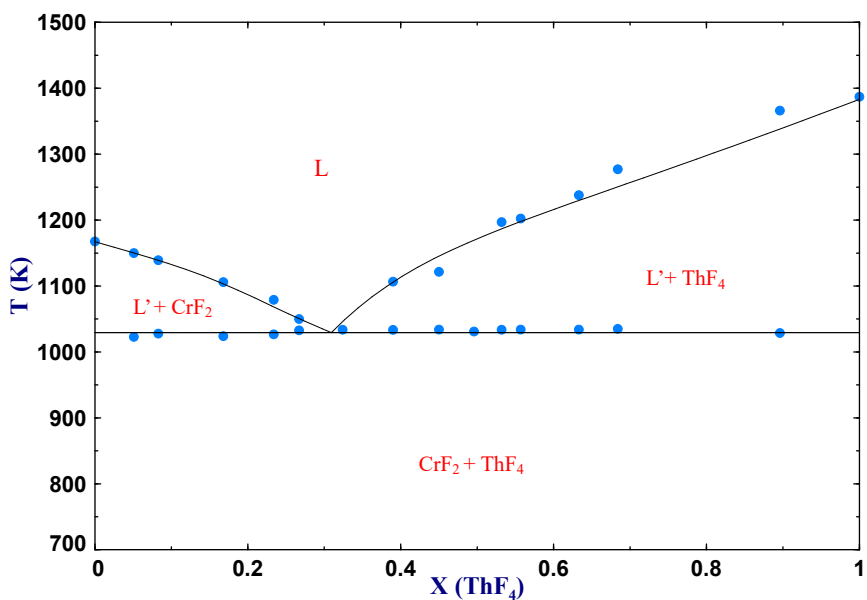


Figure 6.6.: Phase diagram of the CrF_2 - ThF_4 system, blue circles (●) represent the experimental data collected in this work (Table 6.6).

6.4.4. TERNARY SYSTEM LiF-CrF₂-ThF₄

The initial phase diagram calculation of the ternary system was based on the three binary models: LiF-CrF₂, CrF₂-ThF₄, and LiF-ThF₄ (optimized by Ocádiz *et al.* [35]). Based on this model, experimental data were collected at different compositions selected on the isopleth sections with 10% and 20% CrF₂ (see Table 6.8). A last experimental measurement was made at the composition LiF-CrF₂-ThF₄ (0.20-0.60-0.20), so as to get a more detail impression of the ternary phase diagram. The results are listed in Table 6.8.

The collected experimental data, projected on the isopleth section 0.9 (LiF-ThF₄)+0.1 CrF₂, show a very good agreement with the model. The invariant equilibria are well reproduced, with reasonable discrepancies as seen in Figure 6.7.

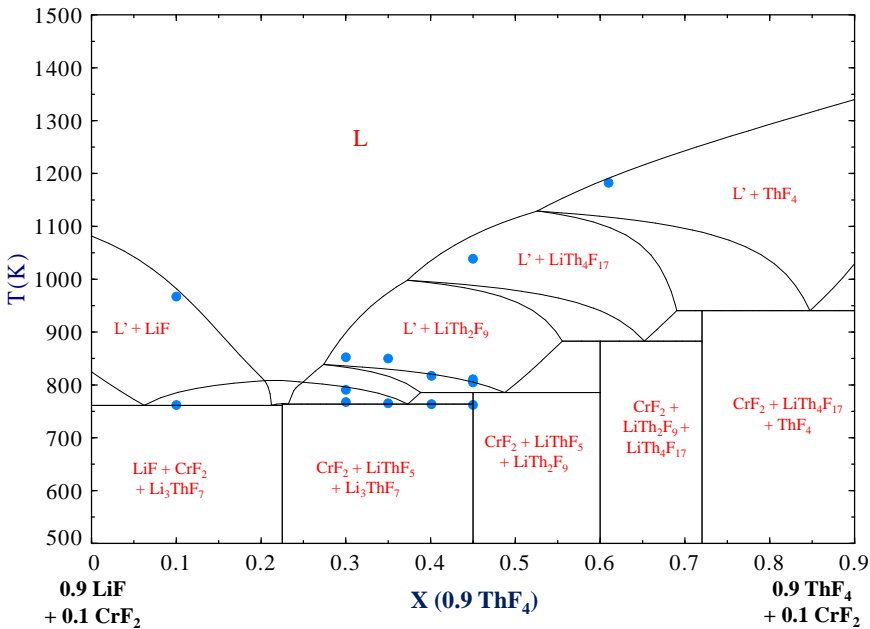


Figure 6.7.: Phase diagram of the isopleth 0.9 (LiF-ThF₄) + 0.1 CrF₂ section, blue circles (●) represent the experimental data collected in this work (Table 6.8). Note that for the composition X(0.9 ThF₄)=0.61, 4 to 5 events were detected on the cooling curves as expected from the phase equilibria, but are not indicated here, as the derived temperatures were shifted due to undercooling effects.

Table 6.8.: Phase diagram equilibria of the LiF-CrF₂-ThF₄ system collected by DSC in this work.

X _{LiF}	X _{CrF₂}	X _{ThF₄}	T(K)	Model T(K)	Equilibrium	Reaction	X _{LiF}	X _{CrF₂}	X _{ThF₄}	T(K)	Model T(K)	Equilibrium	Reaction
0.80	0.10	0.10	761.7	761	eutectic	LiF + CrF ₂ + Li ₃ ThF ₇ = L	0.29	0.10	0.61	1182.1	1191	liquidus	ThF ₄ + L' = L
0.80	0.10	0.10	966.9	981	liquidus	L' + LiF = L	0.60	0.20	0.20	760.5	761	eutectic	LiF + CrF ₂ + Li ₃ ThF ₇ = L
0.60	0.10	0.30	767.3	763	quasi-peritectic	L + LiThF ₅ = CrF ₂ + Li ₃ ThF ₇	0.60	0.20	0.20	766.7	763	liquidus	L' + Li ₃ ThF ₇ = L' LiF
0.60	0.10	0.30	790.4	796	liquidus	L' + Li ₃ ThF ₇ = L' + LiThF ₅	0.60	0.20	0.20	784.9	777	liquidus	LiF + L' = L
0.60	0.10	0.30	851.9	836	liquidus	L' + LiThF ₅ = L' + LiTh ₂ F ₉	0.40	0.20	0.40	754.2	763	quasi-peritectic	L + LiThF ₅ = CrF ₂ + Li ₃ ThF ₇
0.55	0.10	0.35	764.9	763	quasi-peritectic	L + LiThF ₅ = CrF ₂ + Li ₃ ThF ₇	0.40	0.20	0.40	808.1	785	quasi-peritectic	L + LiTh ₂ F ₉ = CrF ₂ + LiThF ₅
0.55	0.10	0.35	849.6	830	liquidus	L' + LiThF ₅ = L' + LiTh ₂ F ₉	0.40	0.20	0.40	877.6	-	-	-
0.50	0.10	0.40	763.4	763	quasi-peritectic	L + LiThF ₅ = CrF ₂ + Li ₃ ThF ₇	0.40	0.20	0.40	992.5	1045	liquidus	LiTh ₂ F ₉ + L' = L
0.50	0.10	0.40	817.1	820	liquidus	L' + LiThF ₅ = L' + LiTh ₂ F ₉	0.21	0.20	0.59	977.3	-	-	-
0.45	0.10	0.45	761.9	763	quasi-peritectic	L + LiThF ₅ = CrF ₂ + Li ₃ ThF ₇	0.21	0.20	0.59	1231.5	1192	liquidus	ThF ₄ + L' = L
0.45	0.10	0.45	804.6	805	liquidus	L' + LiThF ₅ = L' + LiTh ₂ F ₉	0.20	0.60	0.20	796.9	785	peritectic	LiThF ₅ = CrF ₂ + LiTh ₂ F ₉ + L
0.45	0.10	0.45	810.4	805	-	-	0.20	0.60	0.20	914.9	926	liquidus	LiTh ₂ F ₉ + L' = L
0.45	0.10	0.45	1038.5	1080	liquidus	L' + LiTh ₂ F ₉ = L	0.20	0.60	0.20	1026.5	1015	liquidus	CrF ₂ + L' = L

Even if the discrepancies are a bit more pronounced, in the 0.8 (LiF–ThF₄) + 0.2 CrF₂ section, the agreement of the model with the experimental data is reasonably good (Figure 6.8).

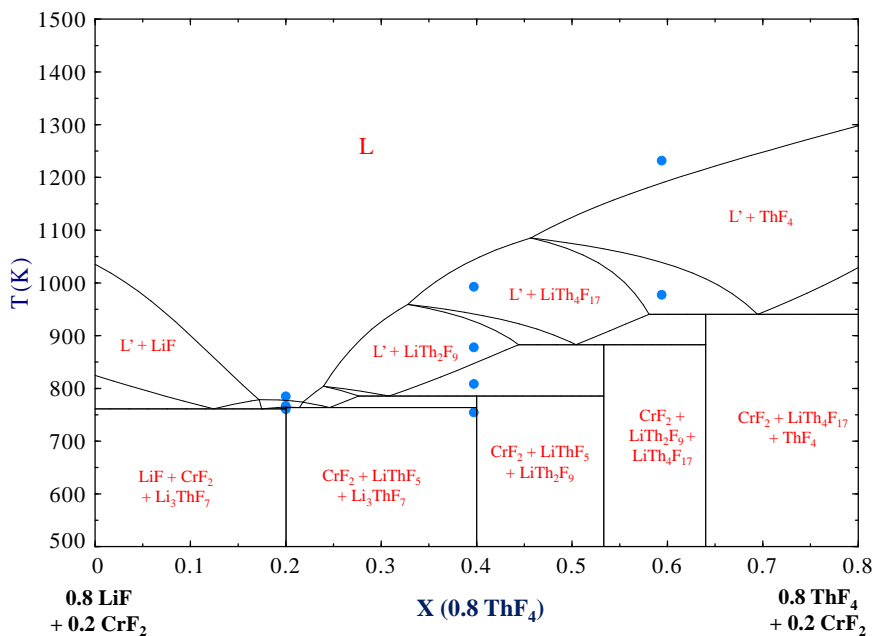


Figure 6.8.: Phase diagram of the isopleth $0.8 \text{ (LiF–ThF}_4\text{)} + 0.2 \text{ CrF}_2$ system, blue circles (●) represent the experimental data collected in this work (Table 6.8).

At LiF–CrF₂–ThF₄ (0.20-0.60-0.20) the three data points obtained fit almost perfectly with the calculated invariant equilibria (Figure 6.9).

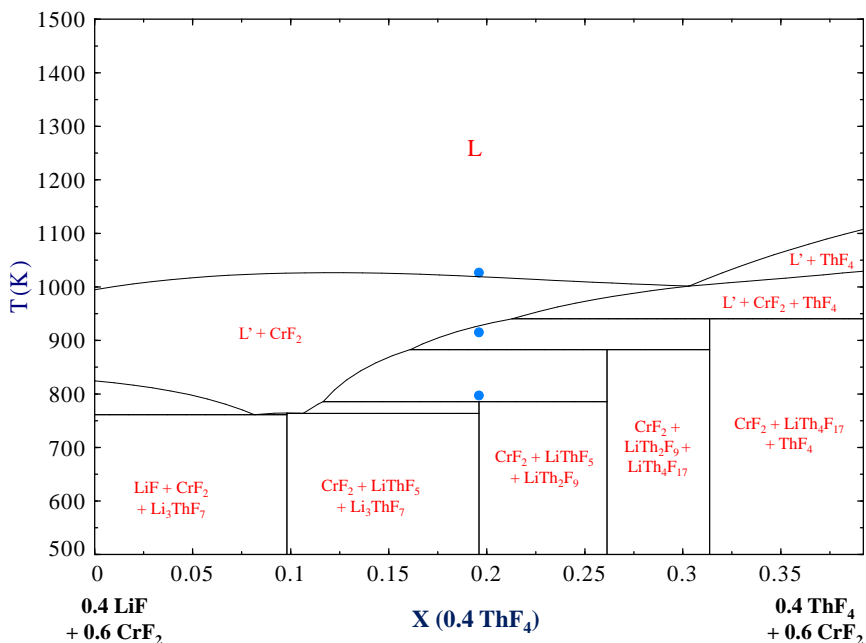


Figure 6.9.: Phase diagram of the isopleth 0.4 (LiF–ThF₄) + 0.6 CrF₂ system, blue circles (●) represent the experimental data collected in this work (Table 6.8).

Post-XRD measurements of the calorimetric samples showed, once again, no evidence for the formation of an intermediate compound. Instead, the intermediates compounds of the LiF–ThF₄ system, in their area of predominance, were detected, or the pure end-members in addition to CrF₂.

Based on the overall good agreement of the modeled ternary phase diagram with the experimental data, it appeared that no ternary excess parameter, i.e. no additional optimization, was needed. The final ternary phase diagram plotted as liquidus projection, is shown in Figure 6.10 and the invariant equilibria are listed in Table 6.9. The systems displays one ternary eutectic, and four quasi-peritectic equilibria. Several isotherms computed at $T = 750, 850, 950,$ and 1050 K are also shown in Figure A.4 of the Appendix A.

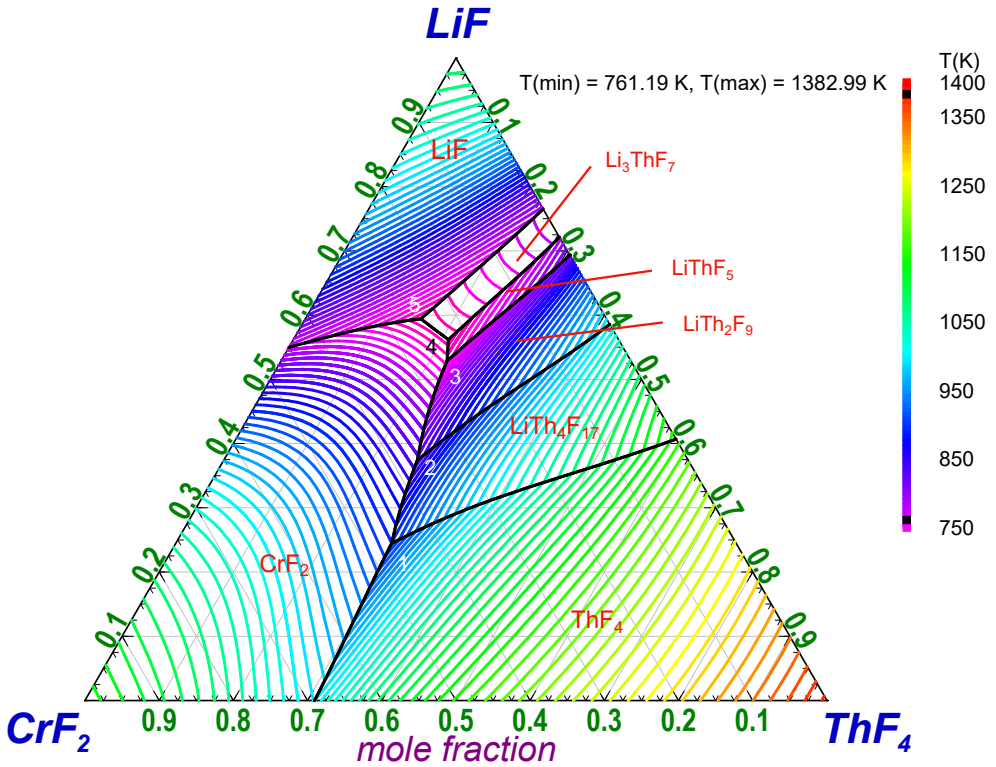


Figure 6.10.: Liquidus projection of the LiF–CrF₂–ThF₄ system calculated in this work from 750 K to 1400 K with an increment of 10 K. Primary crystallization fields are detailed in the figure.

Table 6.9.: Invariant equilibria calculated for the LiF–CrF₂–ThF₄ system.

N°	X_{LiF}	X_{CrF_2}	X_{ThF_4}	T (K)	Invariant equilibrium	Reaction
1	0.245	0.464	0.291	940	Quasi-peritectic	$L + ThF_4 = CrF_2 + LiTh_4F_{17}$
2	0.375	0.365	0.261	883	Quasi-peritectic	$L + LiTh_4F_{17} = CrF_2 + LiTh_2F_9$
3	0.529	0.247	0.224	785	Quasi-peritectic	$L + LiTh_2F_9 = CrF_2 + LiThF_5$
4	0.562	0.229	0.209	764	Quasi-peritectic	$L + LiThF_5 = CrF_2 + Li_3ThF_7$
5	0.594	0.250	0.156	761	Eutectic	$CrF_2 + Li_3ThF_7 + LiF = L$

Unlike CrF_3 , CrF_2 does not form any intermediate compound with lithium fluoride [21]. In this work, it was demonstrated that it also remains soluble in molten LiF-ThF_4 solution. To assess the impact on the phase diagram equilibria of the LiF-ThF_4 molten salt system, computations were performed for several amounts of CrF_2 dissolved in the salt, and are shown in Figure 6.11. As shown in Figure 6.11 (a), a 1% addition of CrF_2 has very little impact on the phase equilibria, and thus on the thermodynamic behavior. In the case of a 15% addition, i.e. a large excess compared to what would be expected under operating conditions, a significant decrease in the liquidus temperature of approximately 70 K would occur. This information is fundamental to support the safety assessment of the Molten Salt Reactor. The stability of CrF_2 limits the risk of oxidation to CrF_3 , and consequently the increase of the fluoroacidity, and further chromium depletion in the structural alloy, as reported by Liu *et al.* [11].

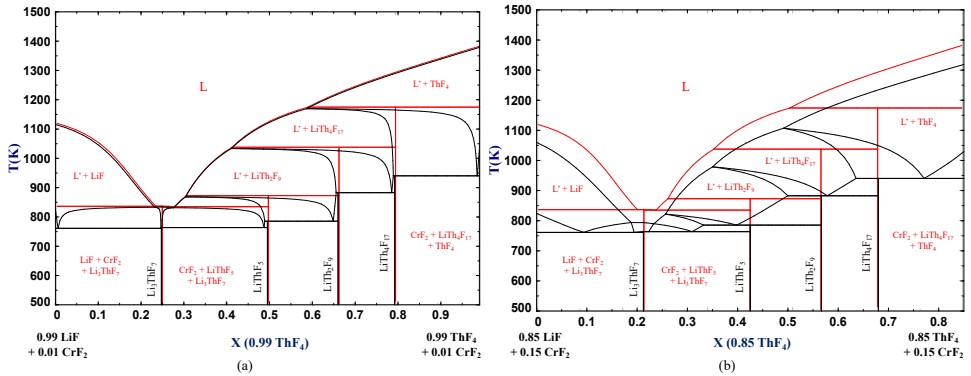


Figure 6.11.: Phase diagram of the pseudo-binary (a) 0.99 (LiF-ThF_4) + 0.01 CrF_2 and (b) 0.85 (LiF-ThF_4) + 0.15 CrF_2 systems, the binary phase diagram of the LiF-ThF_4 system, derived from the model of Ocádiz Flores *et al.* [35], is superimposed in red.

6.5. CONCLUSION

In this work, two methods are reported for the synthesis of pure CrF_2 . Calorimetric measurements were moreover carried out for the first time in the LiF-CrF_2 , $\text{CrF}_2\text{-ThF}_4$, and $\text{LiF-CrF}_2\text{-ThF}_4$ systems. Using the modified quasichemical model in the quadruplet approximation for the liquid solution, thermodynamic models of the aforementioned systems were then developed. CrF_2 does not form any quaternary intermediate compound in the molten LiF-ThF_4 system. This constitutes new knowledge for the safety assessment of the Molten Salt Reactor, especially related to the effect of corrosion products on the fuel salt behavior. The logic extension of this work is the consideration of the effect of UF_4 on the molten salt fuel, and its possible interaction with CrF_2 according to the reaction $\text{UF}_4 + \text{CrF}_2 = \text{UF}_3 + \text{CrF}_3$. Follow-up studies should also consider the influence of the ratio UF_4/UF_3 and redox

equilibria with the $\text{CrF}_2/\text{CrF}_3$ couple.

ACKNOWLEDGMENTS

T. Dumaire acknowledges gratefully financial support from the Nuclear Research and Consultancy Group (NRG, Petten, Netherlands) and the SAMOSAFER project which has received funding from the Euratom research and training program 2014-2018 under grant agreement N°847527. The authors acknowledge P. Souček for his work on the synthesis of ThF_4 , H. Hein for his help with TGA measurements and E. Dahms for X-ray analysis.

REFERENCES

- [1] J. Rogelj, D. Shindell, K. Jiang, S. Fifita, P. Forster, V. Ginzburg, C. Handa, H. Khesghi, S. Kobayashi, E. Kriegler, L. Mundaca, R. Sférian, and M. V. Vilarino. “2018: Mitigation Pathways Compatible with 1.5 °C in the Context of Sustainable Development.” In: *Global Warming of 1.5 °C. An IPCC Special Report on the impacts of global warming of 1.5 °C above pre-industrial levels and related global greenhouse gas emission pathways, in the context of strengthening the global response to the threat of climate change, sustainable development, and efforts to eradicate poverty*. Ed. by V. Masson-Delmotte, P. Zhai, H.-O. Pörtner, D. Roberts, J. Skea, P. Shukla, A. Pirani, W. Moufouma-Okia, C. Péan, R. Pidcock, S. Connors, J. B. R. Matthews, Y. Chen, X. Zhou, M. I. Gomis, E. Lonnoy, T. Maycock, M. Tignor, and T. Waterfield. Intergovernmental Panel on Climate Change, 2018, pp. 93–174.
- [2] D. LeBlanc. “Molten salt reactors: A new beginning for an old idea”. In: *Nuclear Engineering and Design* 240.6 (2010), pp. 1644–1656. DOI: 10.1016/j.nucengdes.2009.12.033.
- [3] J. E. Kelly. “Generation IV International Forum: A decade of progress through international cooperation”. In: *Progress in Nuclear Energy* 77 (2014), pp. 240–246. DOI: 10.1016/j.pnucene.2014.02.010.
- [4] J. Serp, M. Allibert, O. Beneš, S. Delpech, O. Feynberg, V. Ghetta, D. Heuer, D. Holcomb, V. Ignatiev, J.-L. Kloosterman, L. Luzzi, E. Merle-Lucotte, J. Uhlř, R. Yoshioka, and D. Zhimin. “The molten salt reactor (MSR) in generation IV: Overview and perspectives”. In: *Progress in Nuclear Energy* 77 (Nov. 2014), pp. 308–319. ISSN: 0149-1970. DOI: 10.1016/j.pnucene.2014.02.014.
- [5] O. Beneš and R. J. M. Konings. “Molten Salt Reactor Fuel and Coolant”. In: *Comprehensive Nuclear Materials*. Ed. by R. J. M. Konings and R. E. Stoller. Amsterdam: Elsevier, 2020, pp. 609–644. DOI: 10.1016/b978-0-12-803581-8.11790-4.
- [6] M. Allibert, M. Aufiero, M. Brovchenko, S. Delpech, V. Ghetta, D. Heuer, A. Laureau, and E. Merle-Lucotte. “7 - Molten salt fast reactors”. In: ed. by I. L. Piore. Woodhead Publishing Series in Energy. Woodhead Publishing, Jan. 2016, pp. 157–188. DOI: 10.1016/B978-0-08-100149-3.00007-0.
- [7] O. Beneš and P. Souček. “Molten salt reactor fuels”. In: *Advances in Nuclear Fuel Chemistry*. Amsterdam: Elsevier, 2020, pp. 249–271. DOI: 10.1016/b978-0-08-102571-0.00007-0.

- [8] L. Mei, X. Cai, D. Jiang, J. Chen, W. Guo, and W. Xiong. “Investigation of thermal neutron scattering data for BeF₂ and LiF crystals”. In: *Journal of Nuclear Science and Technology* 50.4 (Apr. 2013), pp. 419–424. DOI: 10.1080/00223131.2013.773169.
- [9] M. Übeyli. “Neutronic performance of HYLIFE-II fusion reactor using various thorium molten salts”. In: *Annals of Nuclear Energy* 33.17-18 (Nov. 2006), pp. 1417–1423. DOI: 10.1016/j.anucene.2006.09.006.
- [10] D. Heuer, E. Merle-Lucotte, M. Allibert, M. Brovchenko, V. Ghetta, and P. Rubiolo. “Towards the thorium fuel cycle with molten salt fast reactors”. In: *Annals of Nuclear Energy* 64 (2014), pp. 421–429. DOI: 10.1016/j.anucene.2013.08.002.
- [11] Y. Liu, Y. Song, H. Ai, M. Shen, H. Liu, S. Zhao, Y. Liu, Z. Fei, X. Fu, and J. Cheng. “Corrosion of Cr in molten salts with different fluoroacidity in the presence of CrF₃”. In: *Corrosion Science* 169 (2020), p. 108636. DOI: 10.1016/j.corsci.2020.108636.
- [12] P. N. Haubenreich and J. R. Engel. “Experience with the Molten-Salt Reactor Experiment”. In: *Nuclear Applications and Technology* 8.2 (1970), pp. 118–136. DOI: 10.13182/nt8-2-118.
- [13] J. W. Koger. *Evaluation of Hastelloy N alloys after nine years exposure to both a molten fluoride salt and air at temperatures from 700 to 560°C*. ORNL-TM-4189. Dec. 1972. DOI: 10.2172/4468052.
- [14] W. D. Manly, J. H. Coobs, J. H. DeVan, D. A. Douglas, H. Inouye, P. Patriarca, T. K. Roche, and J. L. Scott. “Metallurgical Problems in Molten Fluoride Systems”. In: *Progress in Nuclear Energy*. IV 2 (1960), pp. 164–179.
- [15] M. Kondo, T. Nagasaka, A. Sagara, N. Noda, T. Muroga, Q. Xu, M. Nagura, A. Suzuki, and T. Terai. “Metallurgical study on corrosion of austenitic steels in molten salt LiF–BeF₂ (FLiBe)”. In: *Journal of Nuclear Materials* 386-388 (2009), pp. 685–688. DOI: 10.1016/j.jnucmat.2008.12.317.
- [16] K. Sridharan and T. R. Allen. “Corrosion in Molten Salts”. In: *Molten Salts Chemistry*. Elsevier, 2013, pp. 241–267. DOI: 10.1016/b978-0-12-398538-5.00012-3.
- [17] M. Liu, J. Zheng, Y. Lu, Z. Li, Y. Zou, X. Yu, and X. Zhou. “Investigation on corrosion behavior of Ni-based alloys in molten fluoride salt using synchrotron radiation techniques”. In: *Journal of Nuclear Materials* 440.1 (Sept. 2013), pp. 124–128. ISSN: 0022-3115. DOI: 10.1016/j.jnucmat.2013.04.056.
- [18] G. Zheng and K. Sridharan. “Corrosion of Structural Alloys in High-Temperature Molten Fluoride Salts for Applications in Molten Salt Reactors”. In: *Journal of The Minerals, Metals & Materials Society* 70.8 (2018), pp. 1535–1541. DOI: 10.1007/s11837-018-2981-2.
- [19] H. Sun, X. Ding, H. Ai, G. Lei, X. Yang, and J.-Q. Wang. “Interaction mechanisms of a Hastelloy N-316L stainless steel couple in molten LiF–NaF–KF salt”. In: *Corrosion Science* 164 (2020), p. 108317. DOI: 10.1016/j.corsci.2019.108317.

- [20] Q. Jie, Z. Yang, Y. Guo-Jun, H. Shang-Ming, L. Wen-Guan, J. Yan-Yan, L. Zhi-Jun, and X. Hong-Jie. "Speciation study of chromium corrosion product in molten LiF-NaF-KF salt". In: *Nuclear Science and Techniques* 26 (2015), pp. 127–130. DOI: 10.13538/j.1001-8042/nst.26.060602.
- [21] T. Dumaire, R. J. M. Konings, and A. L. Smith. "Thermodynamic Assessment of the AF–CrF₃ (A = Li, Na, K) and CrF₂–CrF₃ Systems". In: *Thermo* 1 (2021), pp. 205–219. DOI: 10.3390/thermo1020014.
- [22] P. Souček, O. Beneš, B. Claux, E. Capelli, M. Ougier, V. Tyrpekl, J.-F. Vigier, and R. J. Konings. "Synthesis of UF₄ and ThF₄ by HF gas fluorination and re-determination of the UF₄ melting point". In: *Journal of Fluorine Chemistry* 200 (2017), pp. 33–40. DOI: 10.1016/j.jfluchem.2017.05.011.
- [23] E. Capelli, O. Beneš, M. Beilmann, and R. J. M. Konings. "Thermodynamic investigation of the LiF–ThF₄ system". en. In: *The Journal of Chemical Thermodynamics* 58 (2013), pp. 110–116. ISSN: 0021-9614. DOI: 10.1016/j.jct.2012.10.013.
- [24] C. Poulenc. "Contribution à l'étude des fluorures anhydres et cristallisés". French. In: *Annales de Chimie et de Physique*. Ed. by Berthelot, Pasteur, Friedel, and Mascart. 7 2. Paris: G. Masson, 1894, pp. 5–77.
- [25] A. de Kozak. *Comptes rendus hebdomadaires des séances de l'Académie des sciences*. Série C. Research rep. 268. Académie des sciences de Paris, 1969, pp. 416–418.
- [26] A. de Kozak. "Etude de quelques composés fluores du chrome". In: *Revue de Chimie Minerale* 8 (1971), pp. 301–337.
- [27] O. Levy, B. Bogoslavsky, and A. Bino. "Anhydrous chromous acetate revisited - A very simple synthetic route". In: *Inorganica Chimica Acta* 391 (Aug. 2012), pp. 179–181. DOI: 10.1016/j.ica.2012.04.029.
- [28] L. B. McCusker, R. B. V. Dreele, D. E. Cox, D. Louër, and P. Scardi. "Rietveld refinement guidelines". In: *Journal of Applied Crystallography* 32.1 (1999), pp. 36–50. DOI: 10.1107/s0021889898009856.
- [29] J. Rodriguez-Carvajal. "Recent advances in magnetic structure determination by neutron powder diffraction". In: *Physica B: Condensed Matter* 192.1-2 (1993), pp. 55–69.
- [30] W. J. Boettinger, U. R. Kattner, K.-W. Moon, and J. H. Perepezko. *NIST recommended practice guide: DTA and Heat-flux DSC Measurements of Alloy Melting and Freezing*. Ed. by N. I. of Standards and Technology. U.S. Government Printing Office, 2006. DOI: 10.6028/nbs.sp.960-15.
- [31] O. Beneš, R. J. M. Konings, S. Wurzer, M. Sierig, and A. Dockendorf. "A DSC study of the NaNO₃–KNO₃ system using an innovative encapsulation technique". In: *Thermochimica Acta* 509.1-2 (2010), pp. 62–66. DOI: 10.1016/j.tca.2010.06.003.

- [32] J. Lashley, M. Hundley, A. Migliori, J. Sarrao, P. Pagliuso, T. Darling, M. Jaime, J. Cooley, W. Hults, L. Morales, D. Thoma, J. Smith, J. Boerio-Goates, B. Woodfield, G. Stewart, R. Fisher, and N. Phillips. “Critical examination of heat capacity measurements made on a Quantum Design physical property measurement system”. In: *Cryogenics* 43.6 (2003), pp. 369–378. ISSN: 0011-2275. DOI: 10.1016/s0011-2275(03)00092-4.
- [33] Joint Research Centre - European Commission. *Joint Research Centre Molten Salt Database - JRCMSD*. Ed. by E. S. Hub. https://joint-research-centre.ec.europa.eu/joint-research-centre-molten-salt-database-jrcmsd_en. Accessed: 2024-02-05.
- [34] A. Tosolin, E. Capelli, R. J. M. Konings, L. Luzzi, and O. Beneš. “Isobaric Heat Capacity of Solid and Liquid Thorium Tetrafluoride”. In: *Journal of Chemical & Engineering Data* 64.9 (2019), pp. 3945–3950. ISSN: 0021-9568. DOI: 10.1021/acs.jced.9b00348.
- [35] J. A. Ocadiz-Flores, R. Konings, and A. L. Smith. “Using the Quasi-chemical formalism beyond the phase Diagram: Density and viscosity models for molten salt fuel systems”. In: *Journal of Nuclear Materials* 561 (Apr. 2022), p. 153536. DOI: 10.1016/j.jnucmat.2022.153536.
- [36] V. S. Iorish, N. M. Aristova, G. Bergman, L. Gorohov, A. Gusarov, Y. Yezhov, A. Kulikov, E. Osina, E. Shenyavskaya, N. Handamirova, and V. Jungmann. “Thermodynamic properties of substances (1978-2004)”. In: Publishing House Nauka: Moscow, Russia, 2004.
- [37] M. W. Chase Jr. and National Information Standards Organization (US). “NIST-JANAF Thermochemical Tables”. In: *Journal of Physical and Chemical Reference Data*. Vol. 9. Washington DC: American Chemical Society, 1998.
- [38] J. P. M. van der Meer and R. J. M. Konings. “Thermal and physical properties of molten fluorides for nuclear applications”. In: *Journal of Nuclear Materials* 360.1 (2007), pp. 16–24. ISSN: 0022-3115. DOI: 10.1016/j.jnucmat.2006.08.010.
- [39] E. Capelli and R. J. M. Konings. “Halides of the Actinides and Fission Products Relevant for Molten Salt Reactors”. In: *Konings, Rudy JM and Stoller Roger E (eds.) Comprehensive Nuclear Materials 2nd edition*. Vol. 7. Elsevier, 2020, pp. 256–283. DOI: 10.1016/b978-0-12-803581-8.11794-1.
- [40] A. D. Pelton, S. Degterov, G. Eriksson, C. Robelin, and Y. Dessureault. “The modified quasichemical model I—binary solutions”. In: *Metallurgical and Materials Transactions B* 31.4 (Aug. 2000), pp. 651–659. ISSN: 1543-1916. DOI: 10.1007/s11663-000-0103-2.
- [41] O. Beneš, M. Beilmann, and R. J. M. Konings. “Thermodynamic assessment of the LiF–NaF–ThF₄–UF₄ system”. In: *Journal of Nuclear Materials* 405.2 (2010), pp. 186–198. DOI: 10.1016/j.jnucmat.2010.08.017.
- [42] A. D. Pelton. “A general “geometric” thermodynamic model for multicomponent solutions”. In: *Calphad* 25.2 (2001), pp. 319–328. DOI: 10.1016/s0364-5916(01)00052-9.

- [43] B. J. Sturm. "Phase equilibria in the system chromium (II) fluoride-chromium (III) fluoride". In: *Inorganic Chemistry* 1.3 (1962), pp. 665–672.
- [44] W. O. J. Boo and J. W. Stout. "Heat capacity and entropy of CuF_2 and CrF_2 from 10 to 300 K. Anomalies associated with magnetic ordering and evaluation of magnetic contributions to the heat capacity". In: *The Journal of Chemical Physics* 71.1 (1979), pp. 9–16.
- [45] P. E. Lim and J. W. Stout. "Polarized crystal spectra of CrF_2 from 6000 to 38000 cm^{-1} ". In: *The Journal of Chemical Physics* 63.11 (1975), pp. 4886–4902. ISSN: 1089-7690. DOI: 10.1063/1.431232.
- [46] P. E. Lim and J. W. Stout. "Erratum:" in: *The Journal of Chemical Physics* 68.9 (1978), pp. 4331–4331. ISSN: 1089-7690. DOI: 10.1063/1.436336.

7

A PROMISING FUEL FOR FAST NEUTRON SPECTRUM MOLTEN SALT REACTOR: NaCl-ThCl₄-PuCl₃.

Chloride salts are considered a good alternative to fluoride salts as fuel carrier in the Molten Salt Fast Reactor concepts. The NaCl-ThCl₄-PuCl₃ fuel salt solution seems very promising, with low melting temperature eutectic compositions, and the potential to be used in a breeder and burner type of reactor design. This work focuses on the first thermodynamic modeling assessment of the ThCl₄-PuCl₃ binary system and the NaCl-ThCl₄-PuCl₃ ternary system, using the CALPHAD (Computer Coupling of Phase Diagrams and Thermochemistry) method and the quasichemical formalism in the quadruplet approximation. The investigated system shows potential for a high flexibility with respect to composition at operating temperatures, which can be beneficial to accommodate the requirements on other essential fuel properties (e.g. neutronic and thermo-hydraulic).

7.1. INTRODUCTION

FAST neutron spectrum Molten Salt Reactors (MSRs) are considered very promising for the production of energy in the future. MSRs give the access to a more compact and safer source of nuclear energy thanks to the use of a molten salt as nuclear fuel and coolant, that shows a number of advantageous physico-chemical properties. Fast MSR designs are well adapted to operate with a thorium bearing fuel (i.e. with fertile material), and offer a potential solution to recycle and transmute some of the large stock of plutonium and minor actinides (e.g. Np, Am, Cm) accumulated over the years in the spent fuel of the current generation of Light Water Reactors or in high-enriched military stockpiles [2]. To this date, fluoride salts are considered for most of MSR designs including for instance the LiF-ThF₄-²³³UF₄ salt

Parts of this chapter have been published in Calphad **79**, 102496 (2022) [1].

mixture of the European Molten Salt Fast Reactor (MSFR) [3]. This is largely due to the experience gained during the Molten Salt Reactor Experiment (MSRE) carried out between 1965 and 1969 at the Oak Ridge National Laboratory [4], which was the first thorough demonstration of a civilian Molten Salt test Reactor. Recently, the interest in the use of chloride salts is also rising as an appealing alternative for fast neutron spectra reactors [5]. The latter allow in particular operation with fuel at lower temperatures compared to reactors operated on a fluoride fuel salt mixture [6].

Examples of chloride salt mixtures under consideration are NaCl-PuCl_3 [7], or $\text{NaCl-PuCl}_3\text{-MgCl}_2$ [8]. The chloride fuel salt mixture $\text{NaCl-ThCl}_4\text{-PuCl}_3$ is a still relatively unexplored, but an appealing option. Previous experimental characterization by Vorobei *et al.* has demonstrated relatively low melting temperatures (598 K and 603 K, respectively) for the eutectic $46.5 \text{ NaCl} - 35 \text{ ThCl}_4 - 18.5 \text{ PuCl}_3$ and $58.5 \text{ NaCl} - 23 \text{ ThCl}_4 - 18.5 \text{ PuCl}_3$ compositions [9]. Furthermore, this solution shows multiple advantages, related to a rich neutron economy [10] and the intrinsic value of its three end-member compounds.

The sodium chloride (NaCl) based salt is a quasi unlimited resource, commonly called rock salt; it is available in multiple geological deposits and in the ocean, and represents an interesting alternative to lithium, a scarce resource already in high demand [11]. As a fertile isotope, thorium-232 is considered for the fuel cycle of the next generation of nuclear reactors (the Generation IV systems). The use of thorium is particularly interesting for countries with limited access to uranium resources and/or which have abundant sources of thorium such as India [11]. Moreover, the associated fuel cycle produces less long-lived actinide waste compared to the traditional **U/Pu** fuel cycle. Plutonium used as fissile material is considered in multiple Generation IV designs as experience has already been gained in current Light Water Reactors operating with MOX (Mixed-OXide) fuel and in prototype and demonstration Sodium-cooled Fast Reactors such as the Russian BOR-60, Japanese Monju Reactor or French Superphenix [12–14]. It has intrinsic fissile quality, particularly ^{239}Pu , which shows a better neutron economy than the uranium isotopes [15]. The global stockpile of separated plutonium (weapons grade and civilian) was estimated at (505 ± 10) metric tons worldwide in 2014 by the International Panel on Fissile Materials [2]. Integration and re-use of plutonium in Molten Salt Reactor concepts is thus an appealing option, including for the recycling of future plutonium waste streams generated by the current Light Water Reactors.

A thermodynamic model the $\text{NaCl-ThCl}_4\text{-PuCl}_3$ ternary system has not yet been reported in the literature. Thermodynamic assessments of the three binary constituting sub-systems (NaCl-PuCl_3 , NaCl-ThCl_4 and $\text{ThCl}_4\text{-PuCl}_3$) are reported in this work followed by an extrapolation and optimization of the ternary system based on available phase diagram information. The excess Gibbs energy of the liquid solution has been expressed using the modified quasichemical formalism in the quadruplet approximation.

7.2. THERMODYNAMIC MODELING

The thermodynamic models reported herein were developed using the FactSage software version 8.2 and the OptiSage Optimizer [16], and are based on the CALPHAD (CALculation of PHase Diagrams) method [17, 18]. The optimization of the different parameters of the Gibbs energy functions for all phases present in the systems was based on available phase diagram and mixing enthalpy data [9, 19–24].

7.2.1. GIBBS ENERGIES OF PURE COMPOUNDS

The Gibbs energy of pure compounds is expressed by:

$$G(T) = \Delta_f H_m^o(298.15) - S_m^o(298.15) \cdot T + \int_{298.15}^T C_{p,m}(T) dT - T \int_{298.15}^T \frac{C_{p,m}(T)}{T} dT \quad (7.1)$$

where $\Delta_f H_m^o(298.15)$ is the standard enthalpy of formation and $S_m^o(298.15)$ is the standard entropy of the pure compound at standard pressure and reference temperature 298.15 K. $C_{p,m}$ is the heat capacity expressed as:

$$C_{p,m}(T) = a + bT + cT^2 + dT^{-2} \quad (7.2)$$

In this work, the thermodynamic data for NaCl(cr,l) were taken from the IVTAN database [25] with an exception for the heat capacity of the liquid phase, which was recently revised by van Oudenaren *et al.* [26]. The ThCl₄(cr,l) functions were taken from the recommendations by Rand *et al.* [27] and by Capelli and Konings [28]. The occurrence of a polymorphic transition between an α -ThCl₄, low-temperature metastable tetragonal phase (space group I4₁/a), and a high temperature form β -ThCl₄ (tetragonal, space group I4₁/amd) was observed by Chiotti *et al.* at 679 K [28, 29]. This transition was included by Ocádiz *et al.* in their thermodynamic assessment of the NaCl–ThCl₄ system [30]. However, the α metastable phase is not apparent in the experimental phase diagram investigations of the latter system, nor that of ThCl₄–PuCl₃ [9]. Only Mason *et al.* reported its observation when using a very slow cooling rate [31]. The inclusion of this phase in the modeling of ThCl₄–PuCl₃ appeared rather challenging in relation with the existence of a (Th,Pu)Cl₄ solid solution at low PuCl₃ content. Since the extent of such a solid solution is also unknown for the α modification, it was decided not to include the α form in the assessment of the ternary system (Table 7.1).

As for the only intermediate compound described in this work, Na₂ThCl₆, the Neumann-Kopp approximation was used [32] based on the heat capacities of the end-member compounds, while the other thermodynamic functions were taken from the optimization by Ocádiz *et al.* of the NaCl–ThCl₄ binary system [30]. PuCl₃(cr,l) functions were selected from the review by Capelli and Konings [28]. The enthalpy of formation and melting point are the very few experimental data available for this compound [33, 34]. The standard entropy and heat capacity are based on estimations by comparison with the uranium and lanthanides trichlorides [35–37]. All the thermodynamic data used in this work are summarized in Table 7.1.

Table 7.1.: Thermodynamic data for end-members and intermediate compound used in this work for the thermodynamic assessment. Standard enthalpy of formation $\Delta_f H_m^0$ (298.15 K), standard entropy S_m^0 (298.15 K) and heat capacity coefficient of pure compounds $C_{p,m}(T/K)/(J K^{-1} mol^{-1}) = a + b \cdot T + c \cdot T^2 + d \cdot T^{-2}$. Optimized data are shown in **bold**.

Compound	$\Delta_f H_m^0$ (298.15 K) (kJ mol ⁻¹)	S_m^0 (298.15 K) (J K ⁻¹ mol ⁻¹)	$C_{p,m}(T/K)/(J K^{-1} mol^{-1}) = a + b \cdot T + c \cdot T^2 + d \cdot T^{-2}$				T(K)	Ref.
			a	b	c	d		
NaCl _(cr)	-411.260	72.15	47.72158	0.0057	1.21466·10 ⁻⁵	-882.996	298.15-1074	[26, 38]
NaCl _(l)	-390.853	83.30249	68	-	-	-	298.15-2500	[26]
PuCl _{3(cr)}	-959.600	161.4	91.412	0.03716	-	27400	298.15-6000	[28]
PuCl _{3(l)}	-931.116	170.46	144	-	-	-	298.15-6000	[28]
ThCl _{4(cr)}	-1186.300	183.499	120.293	0.0232672	-	-615050	298.15-6000	[27, 28]
ThCl _{4(l)}	-1149.716	197.71	167.4	-	-	-	298.15-2500	[27, 28]
Na ₂ ThCl _{6(cr)}	-2051.540	328.0	215.73616	0.0346672	2.42932·10 ⁻⁵	-616815.992	298.15-1074	[30]

7.2.2. SOLID SOLUTION

One solid solution was included in the ThCl₄-PuCl₃ system on the ThCl₄-rich side of the phase diagram (Figure 7.3), based on the data of Vorobei *et al.* [9]. A two-sublattice polynomial model was used to describe the solution, to be consistent with the formalism used for other solid solutions in the JRC molten salt database [39, 40]. In this case, the considered cationic species on the first sublattice are Th⁴⁺ and Pu³⁺, and the anionic species on the second sublattice is Cl⁻, meaning the end-member compositions correspond to the ThCl₄ and PuCl₃ stoichiometries, respectively. The Gibbs energy function $G(T)$ of the solid solution is described by the equation:

$$G(T) = X_{Th(IV)} \cdot G_{m,Th(IV)}^0 + X_{Pu(III)} \cdot G_{m,Pu(III)}^0 + X_{Th(IV)} RT \ln X_{Th(IV)} + X_{Pu(III)} RT \ln X_{Pu(III)} + \Delta G_m^{xs} \quad (7.3)$$

where $G_{m,Th(IV)}^0$ and $G_{m,Pu(III)}^0$ are the molar Gibbs energies of the pure end-members, $X_{Th(IV)}$ and $X_{Pu(III)}$ their site molar fraction, R the universal gas constant and ΔG_m^{xs} is the excess Gibbs energy. The excess Gibbs energy can be expressed by:

$$\Delta G_m^{xs} = \sum_{i,j} y_{Th(IV)}^i \cdot y_{Pu(III)}^j \cdot L_{i,j} \quad (7.4)$$

where $L_{i,j}$ is an interaction coefficient which can depend on temperature T described by the equation:

$$L_{i,j} = A + BT \quad (7.5)$$

and where $y_{Th(IV)}$ and $y_{Pu(III)}$ are the equivalent site fractions of the end-member species, described as charge equivalent site fractions. In this case, the equivalent site fractions $y_{Th(IV)}$ and $y_{Pu(III)}$ are defined by:

$$y_{Th(IV)} = \frac{4X_{Th(IV)}}{4X_{Th(IV)} + 3X_{Pu(III)}} \quad (7.6)$$

$$y_{Pu(III)} = \frac{3X_{Pu(III)}}{4X_{Th(IV)} + 3X_{Pu(III)}} \quad (7.7)$$

The optimized excess energy parameters, obtained via optimization in the OptiSage - Calphad Optimizer (version 1.0.0) of FactSage and subsequent manual iteration, are given by the following equation:

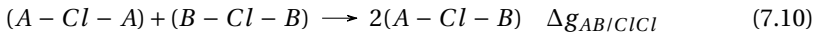
$$\Delta G_{(Th(IV),Pu(III)Cl}^{xs} = y_{Th(IV)}^2 y_{PuCl(III)} \cdot (43699.7 - 43.1384 \cdot T) \quad \text{J mol}^{-1} \quad (7.8)$$

In addition, to avoid the formation of a solid solution on the PuCl_3 rich side of the phase diagram, the Gibbs energy of the PuCl_3 end-member of the solid solution had to be destabilized according to:

$$G_{\text{PuCl}_3(ss)} = G_{\text{PuCl}_3} + 5000 \quad \text{J mol}^{-1} \quad (7.9)$$

7.2.3. LIQUID SOLUTIONS

To describe the liquid solution, the modified quasichemical model in the quadruplet approximation was used [41, 42]. A quadruplet is defined by two anions and two cations symmetrically dispatched around an axis. Two interactions are considered, the First Nearest Neighbor (FNN) interaction which describes the interaction cation - anion and the Second Nearest Neighbor (SNN) interaction which describes the interactions between the two closest ions in the same sublattice. This model is particularly well adapted for the description of ionic liquids as it allows to choose the composition of maximum short-range ordering in a binary system by varying the ratio between the cation-cation coordination numbers $Z_{AB/ClCl}^A$ and $Z_{AB/ClCl}^B$. Short-range ordering is defined by the quadruplet approximation and includes the SNN interactions between each cation and each anion. In a simple representation where A and B are two cations and Cl, the anion, the following reaction is obtained:



where $\Delta g_{AB/ClCl}$ is the parameter of the Gibbs energy change associated with the SNN exchange reaction described as:

$$\Delta g_{AB/ClCl} = \Delta g_{AB/ClCl}^0 + \sum_{i \geq 1} g_{AB/ClCl}^{i0} \chi_{AB/ClCl}^i + \sum_{j \geq 1} g_{AB/ClCl}^{0j} \chi_{BA/ClCl}^j \quad (7.11)$$

where $\Delta g_{AB/ClCl}^0$ and $g_{AB/ClCl}^{ij}$ are possibly dependent on temperature, but independent of composition, and optimized to fit as best as possible the experimental data available on a given system. The dependence on composition is given by the term $\chi_{AB/ClCl}$ defined as:

$$\chi_{AB/ClCl} = \frac{X_{AA}}{X_{AA} + X_{AB} + X_{BB}} \quad (7.12)$$

where X_{AA} , X_{AB} and X_{BB} represent the different cation-cation pair fractions. To maintain electro-neutrality in the system, the anion-anion coordination should be determined. The following equation is applied after the selection of cation-cation coordination numbers:

$$\frac{q_A}{Z_{AB/ClCl}^A} + \frac{q_B}{Z_{AB/ClCl}^B} = 2 \cdot \frac{q_{Cl}}{Z_{AB/ClCl}^{Cl}} \quad (7.13)$$

with q_i representing the charges of the different ions and $Z_{AB/ClCl}^{Cl}$ is the anion-anion coordination number. These choices are based on the optimization of the systems in order to get the maximum short range ordering and highest excess Gibbs energy at a composition usually close to the lowest eutectic in the phase diagram. The coordination numbers selected in this work are listed in Table 7.2.

Table 7.2.: Cation-cation and anion-anion coordination numbers of the liquid solution

A	B	$Z_{AB/ClCl}^A$	$Z_{AB/ClCl}^B$	$Z_{AB/ClCl}^{Cl}$
Na ⁺	Na ⁺	6	6	6
Th ⁴⁺	Th ⁴⁺	6	6	1.5
Pu ³⁺	Pu ³⁺	6	6	2
Na ⁺	Th ⁴⁺	3	6	2
Na ⁺	Pu ³⁺	3	6	2.4
Th ⁴⁺	Pu ³⁺	3	6	1.09

The optimized excess Gibbs energy of the liquid solutions of respectively the NaCl–PuCl₃ and ThCl₄–PuCl₃ binary systems are given by the following equations:

$$\Delta g_{NaPu/ClCl} = -8450 - 3220\chi_{NaPu/ClCl} - 5658\chi_{PuNa/ClCl} \quad \text{J mol}^{-1} \quad (7.14)$$

$$\Delta g_{PuTh/ClCl} = -5360 - 5050\chi_{ThPu/ClCl} + 8.7 \cdot T\chi_{PuTh/ClCl} \quad \text{J mol}^{-1} \quad (7.15)$$

as optimized in this work, whereas the equation for the NaCl–ThCl₄ is taken from Ocadiz *et al.* [30]:

$$\Delta g_{NaTh/ClCl} = -27700 - 7500\chi_{NaTh/ClCl} - 14000\chi_{ThNa/ClCl} \quad \text{J mol}^{-1} \quad (7.16)$$

7.2.4. LIQUID SOLUTION FOR THE TERNARY SYSTEM

The ternary diagram of the NaCl–ThCl₄–PuCl₃ system was established from the three binary sub-systems described above, using the Kohler/Toop interpolation [43]. The latter is an asymmetric extrapolation model for which two groups of symmetry are considered: monovalent NaCl with a tendency to remain as dissociated ionic liquid, and tetravalent ThCl₄ and trivalent PuCl₃ which are more susceptible to form molecular species in the melt. The optimized ternary excess parameters of the system are presented below:

$$\Delta g_{NaTh(Pu)/ClCl}^{001} = -21700 \quad \text{J mol}^{-1} \quad (7.17)$$

$$\Delta g_{ThPu(Na)/ClCl}^{001} = 10500 \quad \text{J mol}^{-1} \quad (7.18)$$

$$\Delta g_{PuNa(Th)/ClCl}^{001} = 39500 \quad \text{J mol}^{-1} \quad (7.19)$$

7.3. RESULTS

7.3.1. NaCl-PuCl₃ SYSTEM

This model is an update of the model developed by Beneš and Konings [8], necessary because of a different choice of the thermodynamic data for solid and liquid NaCl as discussed in section 2.1. The adjustment was only minimal. The system calculated in this work shows a very good agreement with the experimental thermodynamic data measured with a combination of thermal and experimental thermal analysis techniques by Bjorklund *et al.* [19], as shown in Figure 7.1. The eutectic equilibrium is calculated at a composition of $X_{\text{PuCl}_3} = 0.385$ and at a temperature $T = 725$ K. The eutectic equilibrium proposed by Bjorklund *et al.* is slightly lower in composition ($X_{\text{PuCl}_3} = 0.360$), and was based on the extrapolation of the liquidus curve. The present value is considered accurate considering the good fit with the rest of the experimental data. The comparison between invariant equilibria calculated in the model and the literature dataset is presented in Table 7.3.

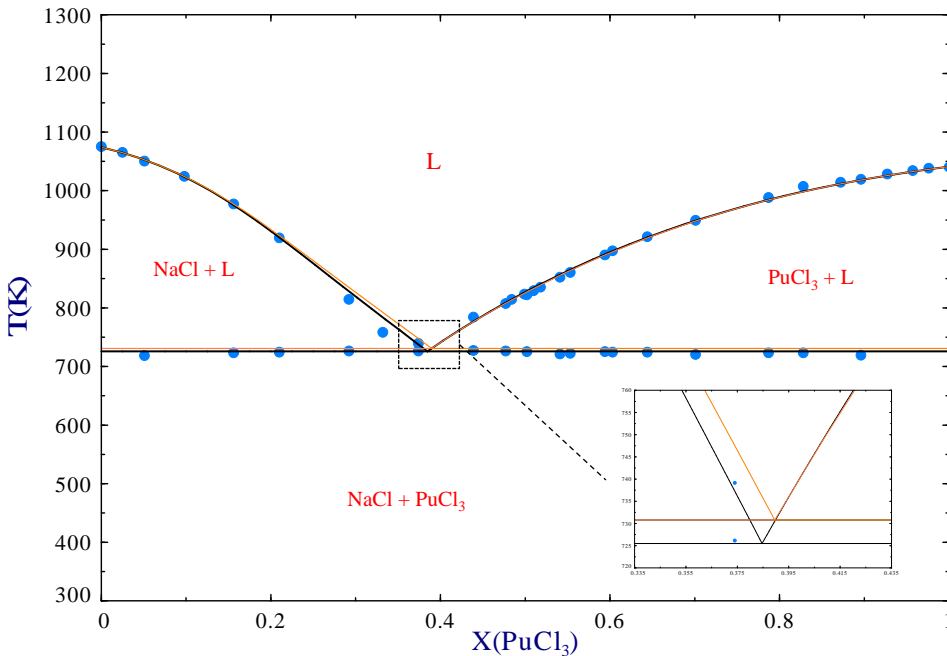


Figure 7.1.: NaCl–PuCl₃ phase diagram calculated in this work (—) and ● data from Bjorklund *et al.* [19]. The phase diagram (—) shown in orange is calculated from the previous model of Beneš and Konings [8].

Mixing enthalpy data have not been reported in the literature for the NaCl–PuCl₃ system, but have been predicted by Yin *et al.* [44] using an empirical method

proposed by Davis [45], based on the linear extrapolation of the ionic parameters of cations with same charge as Pu^{3+} . The estimated mixing enthalpy value at a composition of $X_{\text{PuCl}_3} = 0.5$ and a temperature of 1123 K is shown in Figure 7.2 together with the computed values in the present CALPHAD model and that of Beneš and Konings. The mixing enthalpy calculated in this work is generally slightly lower than the two previous works but the minimum energy is found around the same composition of maximum short-range ordering ($X_{\text{PuCl}_3} = \mathbf{0.423}$ with a corresponding mixing enthalpy value of $\mathbf{-6969 \text{ J}\cdot\text{mol}^{-1}}$). A more recent work by Schorne-Pinto *et al.* [20] used a semi-empirical method, building on the method of Davis, and based on the previous estimation of the composition of maximum short range ordering and value of mixing enthalpy at that particular composition by comparison with data on known systems. With this method, the minimum in the mixing enthalpy has been calculated at $-7193 \text{ J}\cdot\text{mol}^{-1}$ for a composition of $X_{\text{PuCl}_3} = 0.436$, in close agreement with the values optimized in the present work. Furthermore, a comparison is made with the experimental mixing enthalpies data of three analogous systems: NaCl-NdCl_3 [46], NaCl-UCl_3 [47], and NaCl-LaCl_3 [48]. With a similar ionic radius and the same oxidation state, those systems are expected to yield mixing enthalpy values very close to each other. According to the theory of Hong and Kleppa [49], the magnitude of the mixing enthalpy value is related to the so-called relative ionic potential of the cations Na^+ and $\text{Pu}^{3+}/\text{U}^{3+}/\text{Nd}^{3+}/\text{La}^{3+}$ given by the formula:

$$\Delta_{IP} = Z_1/r_1 - Z_2/r_2 \quad (7.20)$$

where Z_1 and Z_2 are the oxidation states, and r_1 and r_2 the ionic radii of the cations. The corresponding mixing enthalpy values are thus expected in the same range, more specifically in the order $\text{La} < \text{U} < \text{Pu} < \text{Nd}$ given the Shannon ionic radii of La^{3+} (1.032 Å), U^{3+} (1.025 Å), Pu^{3+} (1 Å) and Nd^{3+} (0.98 Å) in six-fold coordination. The good agreement with this trend for the mixing properties of the NaCl-PuCl_3 system lends support to the predictive capability of the model developed in this work (Figure 7.2).

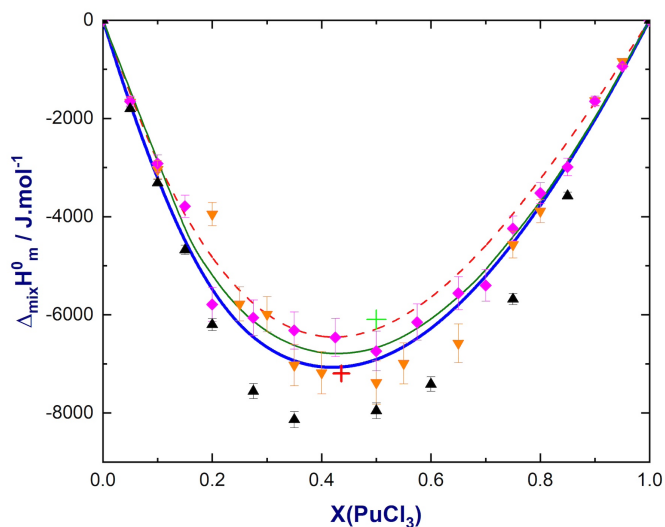


Figure 7.2.: Mixing enthalpy of the NaCl–PuCl₃ system calculated at 1123 K in this work (—), compared with values calculated from the model by Beneš and Konings [8] (—). Empirical evaluated values from model (---) and for the mixing enthalpy at $X_{\text{PuCl}_3} = 0.5$ (+) by Yin *et al.* [44]. The mixing enthalpy estimated at the composition of maximum short range ordering at 1123 K (+) by Schorne-Pinto *et al.* [20]. The data are moreover compared to the experimental data of the mixing enthalpy of NaCl–NdCl₃ at 1124 K (♦) by Gaune-Escard *et al.* [46], NaCl–UCl₃ at 1113 K (▼) by Matsuura *et al.* [47] and NaCl–LaCl₃ at 1173 K (▲) by Papatheodorou and Ostvold [48].

7.3.2. ThCl_4 - PuCl_3 SYSTEM

The model proposed in this work (Figure 7.3) is based on the only experimental data set available in the literature, by Vorobei *et al.* from 1971 [9], who used differential thermal analysis [50]. It shows a good agreement with the liquidus transition data and the eutectic equilibrium, calculated at a composition of $X_{\text{PuCl}_3} = 0.323$ and temperature $T = 895$ K, in the interval of composition defined in the reference data at $X_{\text{PuCl}_3} = 0.32$ - 0.33 .

The extent of the $(\text{Th,Pu})\text{Cl}_{4/3}$ solid solution as calculated in this work is slightly less than reported experimentally. The present model provides the best compromise we could reach between the fitting of the solid solubility limit, the solidus and liquidus curves in the ThCl_4 rich region, and the composition of the eutectic equilibrium. We recommend performing complementary measurements to confirm and/or better define the phase equilibria on the ThCl_4 rich side. The maximum extent of the solid solution is calculated at $X_{\text{PuCl}_3} = 0.154$ at a temperature of 895 K in good agreement with the experimental data of Vorobei *et al.* [9]. The calculated and the literature data are compared in Table 7.3.

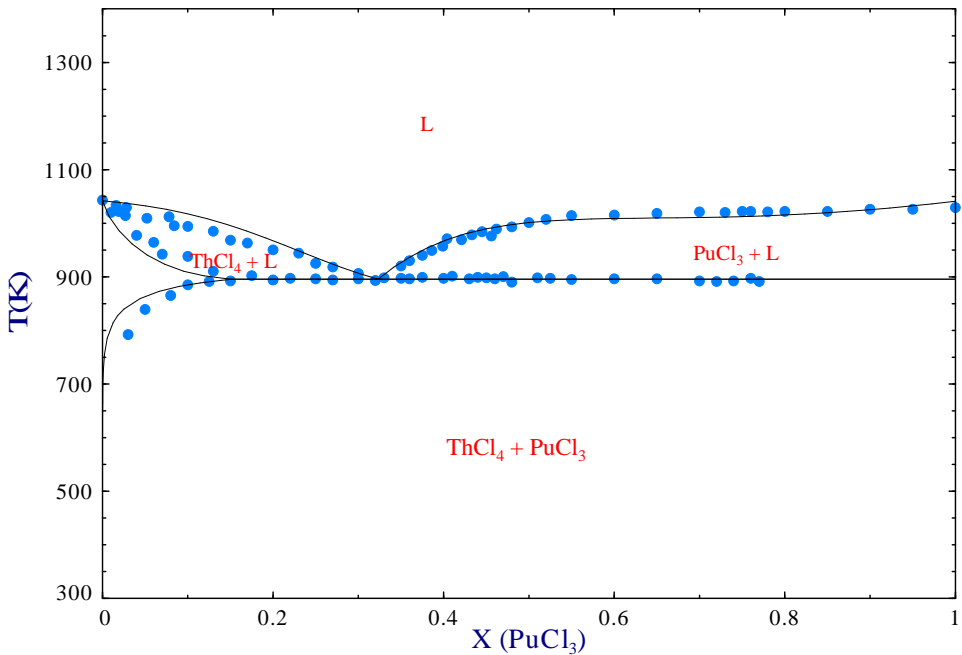


Figure 7.3.: Phase diagram of the ThCl_4 - PuCl_3 system modeled in this work. (●) Data from Vorobei *et al.* [9].

7.3.3. NaCl-ThCl₄ SYSTEM

This model (Figure 7.4) has been developed by Ocádiz Flores *et al.* in their work on the ACl-ThCl₄ (A = Li, Na, K) systems [30]. Three different works have been used as reference data [21–23]. The choice was made not to include the stoichiometric compound, NaThCl₅, considering that only one study reports it [51], and by analogy with NaCl-UCl₄ for which no such intermediate compound is reported. The choice to include only the β phase for ThCl₄ does not affect the agreement with the phase diagram data obtained with the different datasets, as summarized in Table 7.3.

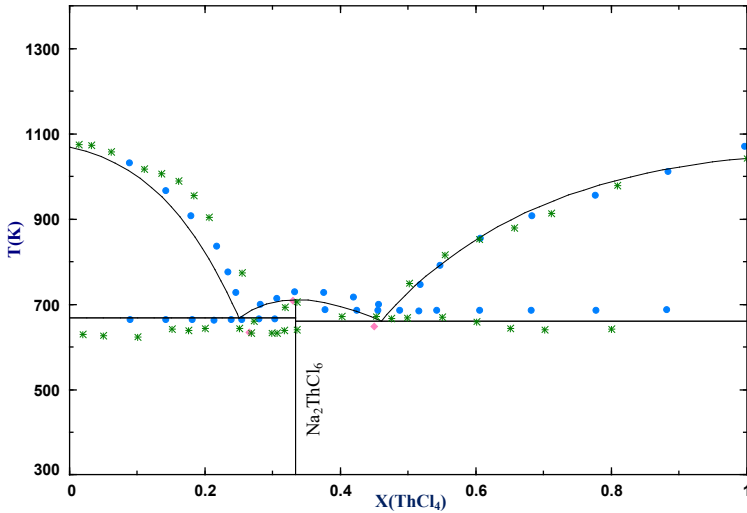


Figure 7.4.: NaCl-ThCl₄ calculated phase diagram by Ocádiz-Flores *et al.* [30], but excluding the low temperature metastable α phase. (*) Data from Tanii *et al.* [21], (●) data from Oyamada [22] and (◆) data from Vokhmyakov *et al.* [23]

Table 7.3: Invariant equilibria calculated in this work in the NaCl–PuCl₃, ThCl₄–PuCl₃ and NaCl–ThCl₄ systems compared to the reference data provided in the literature.

System	Invariant Reaction	Equilibrium	Phase diagram calculated and literature data					
			This study		Bjorklund <i>et al.</i> [19]		Beneš and Konings [8]	
NaCl–PuCl ₃	NaCl + PuCl ₃ =L	Eutectic	X(PuCl ₃)	T (K)	X(PuCl ₃)	T (K)	X(PuCl ₃)	T (K)
			0.385	724	0.360	726	0.383	725
			This study					
ThCl ₄ –PuCl ₃	ThCl ₄ + PuCl ₃ =L	Eutectic	X(PuCl ₃)	T (K)	X(PuCl ₃)	T (K)		
			0.323	895	0.32-0.33	893		
			Ocaáiz Flores <i>et al.</i> [30]		Tanii <i>et al.</i> [21]		Oyamada [22]	
NaCl–ThCl ₄	NaCl=L NaCl + Na ₂ ThCl ₆ =L Na ₂ ThCl ₆ =L Na ₂ ThCl ₆ + ThCl ₄ =L	Congruent melting Eutectic Congruent melting Eutectic	X(ThCl ₄)	T (K)	X(ThCl ₄)	T (K)	X(ThCl ₄)	T (K)
			0	1074	0	1074	-	-
			0.251	667	-	639	0.255	633
			0.333	710	0.333	708	0.333	708
			0.461	660	-	637	0.45	648
						X(ThCl ₄)	T (K)	
						0	1097	
						0.26	667	
						0.333	729	
						0.49	686	

7.3.4. TERNARY ASSESSMENT

Based on the three models of the binary systems as detailed above and the addition of ternary excess parameters, the ternary phase diagram was optimized for the first time (Figure 7.5). The system is characterized by two ternary eutectics, which is in agreement with the only experimental study of this system realized by Desyatnik *et al.* [24]. The experimental details on the measurement conditions of the melting temperatures are not shared by the authors except for a standard uncertainty of ± 2 K. A comparison between the calculated and the experimentally observed invariant equilibria is made in Table 7.4. The model presented in this work shows a good agreement in terms of composition and temperature for the eutectic 1. Small discrepancies are observed in the composition of the eutectic 2: its position on the cotectic line between the primary crystallization fields of NaCl and Na_2ThCl_6 was selected as the best compromise that could be reach with the experimental data. Furthermore, the calculated eutectic in the pseudo-binary section $(2\text{NaCl} + \text{ThCl}_4) - \text{PuCl}_3$ shows a good match with the temperature and composition measured by Desyatnik *et al.* [24], confirming the accuracy of the model presented here (Figure 7.6).

Table 7.4.: Invariant equilibria calculated in this work and comparison with the experimental data of Desyatnik *et al.* [24].

Compound	T(K)	X(NaCl)	X(ThCl_4)	X(PuCl_3)	Ref.
Ternary eutectic 1	597	0.470	0.354	0.176	This work [24]
	598	0.465	0.350	0.185	
Ternary eutectic 2	598	0.574	0.223	0.203	This work [24]
	603	0.585	0.230	0.185	
Eutectic on the $\text{Na}_2\text{ThCl}_6 - \text{PuCl}_3$ pseudo-binary section	628	0.521	0.261	0.218	This work [24]
	643	0.520	0.260	0.220	

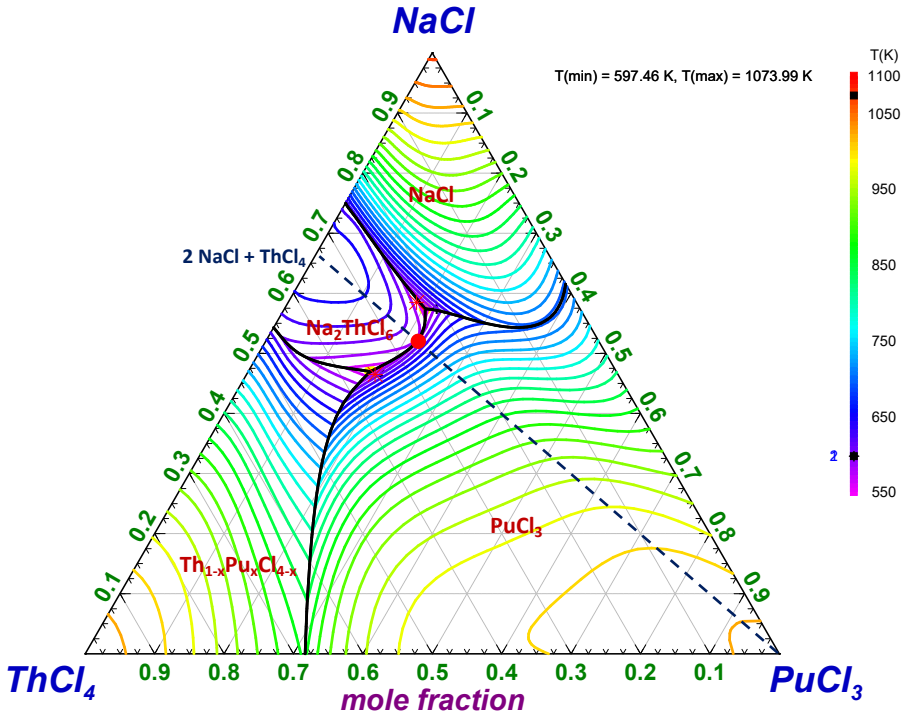


Figure 7.5.: Liquidus projection of the NaCl–ThCl₄–PuCl₃ system assessed in this work from 550 K to 1100 K with an increment of 20 K. Primary crystallization fields are indicated in the figure: NaCl; Na₂ThCl₆; Th_{1-x}Pu_xCl_{4-x}; PuCl₃. (*) Positions of the ternary eutectics and (●) the eutectic on the (2 NaCl + ThCl₄)–PuCl₃ pseudo-binary section measured by Desyatnik *et al.* [24].

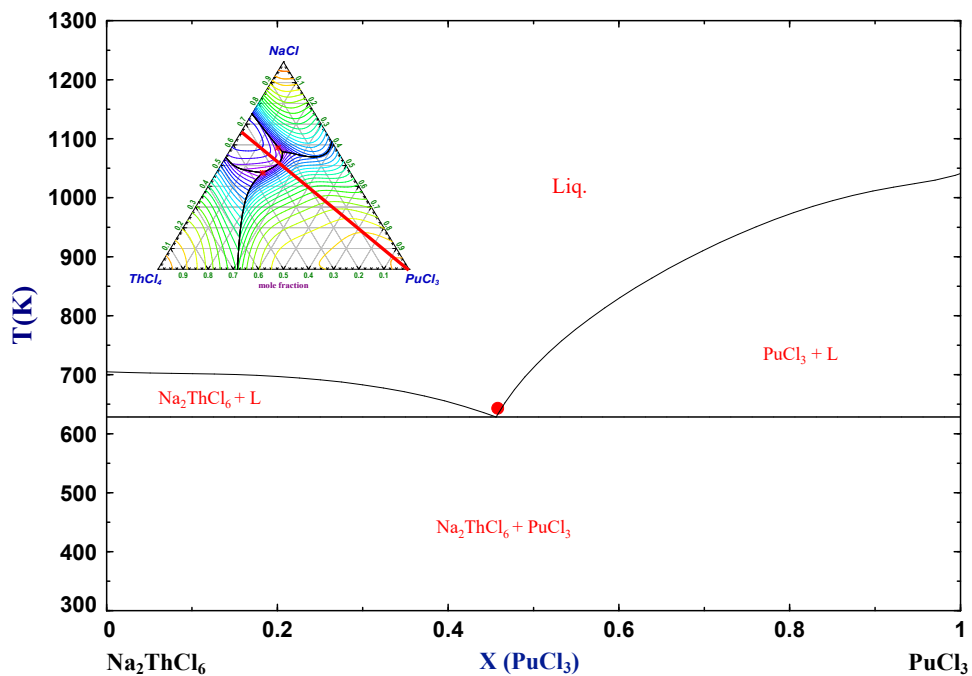


Figure 7.6.: Calculated pseudo-binary phase diagram of the Na_2ThCl_6 - PuCl_3 system. (●) The position of the eutectic on the pseudo-binary section from Desyatnik *et al.* [24].

7.4. DISCUSSION

The relatively low temperatures around the ternary eutectics calculated here make the NaCl–ThCl₄–PuCl₃ system a promising choice for technological applications. In other chloride fuel salt mixtures in which plutonium was included, such as NaCl–UCl₃–PuCl₃, even an addition of MgCl₂ did not allow to reach a comparable range [8], with a quaternary eutectic at $T = 696.5 \text{ K}$ (62.9 NaCl - 16.5 MgCl₂ - 1.1 UCl₃ - 19.5 PuCl₃), nor the introduction of KCl that does not show quaternary eutectic melting temperatures lower than $T = 774.3 \text{ K}$ (22 NaCl - 33 KCl - 38 UCl₃ - 7 PuCl₃) [44]. The substitution of uranium by thorium as fertile compound avoids the introduction of another chloride salt which could to some extent act as a neutron poison.

In terms of safety concerns, this system exhibits an interesting margin with respect to the operating minimal inlet temperature investigated for the MSFR, i.e. 923 K [6]. Supposing a required margin of at least 50 K (873 K), the composition range of stability of the liquid is large, as illustrated below. This allows to consider a large panel of compositions for the fuel and to tailor its composition based on other requirements such as for instance neutronic or thermo-hydraulic properties.

The different fast spectrum chloride MSR concepts are designed to accommodate a high content of plutonium. For example, TerraPower's Molten Chloride Fast Experiment project based its fuel on the binary system NaCl–PuCl₃ at the eutectic composition 64 NaCl – 36 PuCl₃ [7], and the equilibria defined by Bjorklund *et al.* [19]. The safe area of operation as defined above is shown in Figure 7.7 (left) on the NaCl–PuCl₃ phase diagram optimized in this work, with an eutectic transition at a composition 61.5 NaCl – 38.5 PuCl₃. On this figure, we see that the interval of "safe" plutonium chloride concentrations extends between $X_{\text{PuCl}_3} = 0.245$ and 0.565. A calculation is then performed in the ternary melt of the maximum concentration of ThCl₄ (as a substitute for NaCl) allowed if one wants to remain below the safety temperature for different fixed concentrations in PuCl₃ in the interval defined previously (i.e. between $X_{\text{PuCl}_3} = 0.245$ and 0.565, as shown in Figure 7.7 (right)). It is observed that with high concentration of PuCl₃, the corresponding concentration of ThCl₄ becomes very limited. Figure 7.8, showing the range of PuCl₃ concentration allowed to remain below the safe temperature as function of the concentration in ThCl₄, confirms this evolution. A "safe" area can be observed at the composition 40 (NaCl–PuCl₃) + 60 ThCl₄ between $X_{\text{PuCl}_3} = 0$ and $X_{\text{PuCl}_3} = 0.28$, which offers only a very limited margin with the safety temperature, thus could not be recommended.

A pseudo-binary phase diagram passing through the ternary eutectic (57.4 NaCl – 22.3 ThCl₄ – 20.3 PuCl₃) at fixed PuCl₃ content is moreover shown in Figure 7.9. It demonstrates a large interval of "safe" composition ranging from $X_{\text{ThCl}_4} = 0.0956$ (0.12 multiply by 0.797 ThCl₄) to $X_{\text{ThCl}_4} = 0.638$ (0.80 times 0.797 ThCl₄).

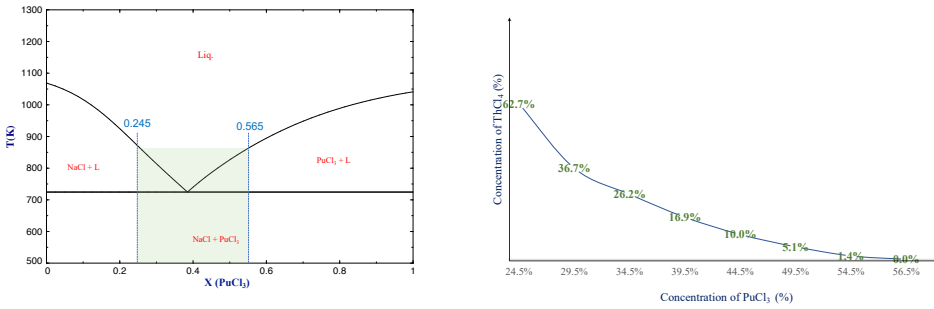


Figure 7.7.: Phase diagram of the NaCl–PuCl₃ system with the composition area of safety with the minimum temperature minus 50 K (873 K) superposed in green (left), and curve of the maximal safe molar concentration* of ThCl₄ in the ternary solution NaCl–ThCl₄–PuCl₃ as a function of the concentration of PuCl₃. *Maximum concentration ensuring melting temperature of the ternary solution below 873 K.

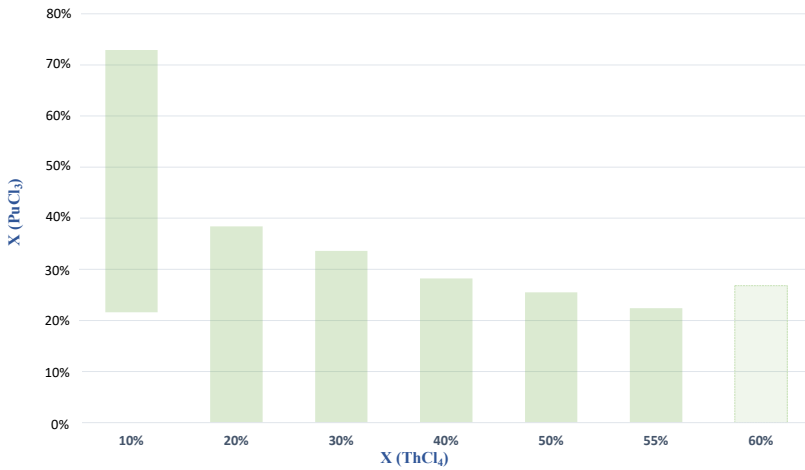


Figure 7.8.: Chart of the maximal safe molar concentration* of PuCl₃ in the ternary solution NaCl–ThCl₄–PuCl₃ as function of the concentration of ThCl₄ according to the ternary model. *Maximum concentration ensuring melting temperature of the ternary solution below 873 K.

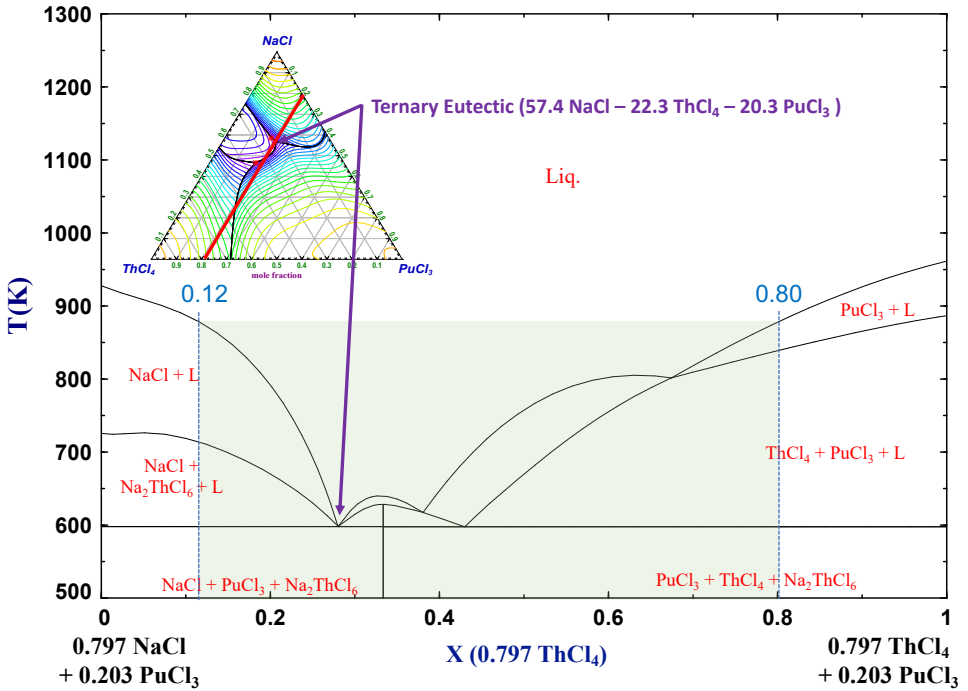


Figure 7.9.: Calculated pseudo-binary phase diagram of the 79.7 (NaCl–ThCl₄) + 20.3 PuCl₃ system, intercepting the ternary eutectic determined in Section 3.4. The green area represents the range of compositions with a liquidus transition below the minimum safety temperature of operation (T = 873K).

The potential of this fuel is finally illustrated by the computation of the pseudo-binary systems at the constant concentration of 70 % (Figure 7.10) and 60 % NaCl (Figure 7.11). With fixed concentrations of heavy metal chloride ($\text{ThCl}_4 + \text{PuCl}_3$) of respectively 30 % and 40 %, all possible combinations between these two compounds in the ternary solution are meeting the safety requirements. The flexibility proposed by these systems is a major advantage that allows to optimize other necessary properties in order to get the most adapted fuel for a MSR.

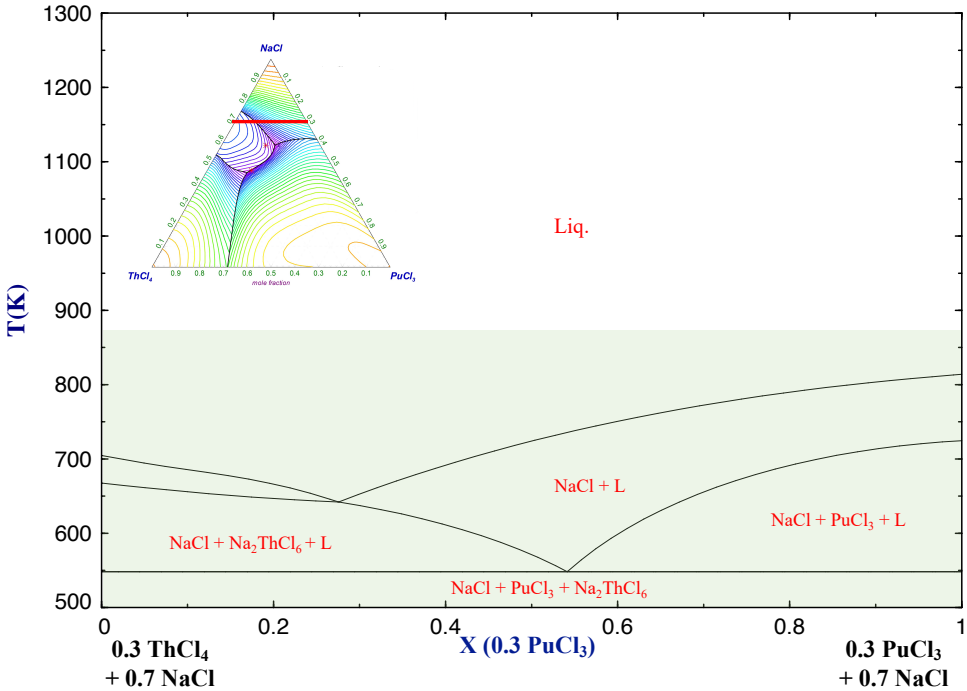


Figure 7.10.: Phase diagram of the pseudo-binary 30 (ThCl_4 – PuCl_3) + 70 NaCl system with the composition area of safety with the minimum inlet temperature minus 50 K (873 K) superposed in green.

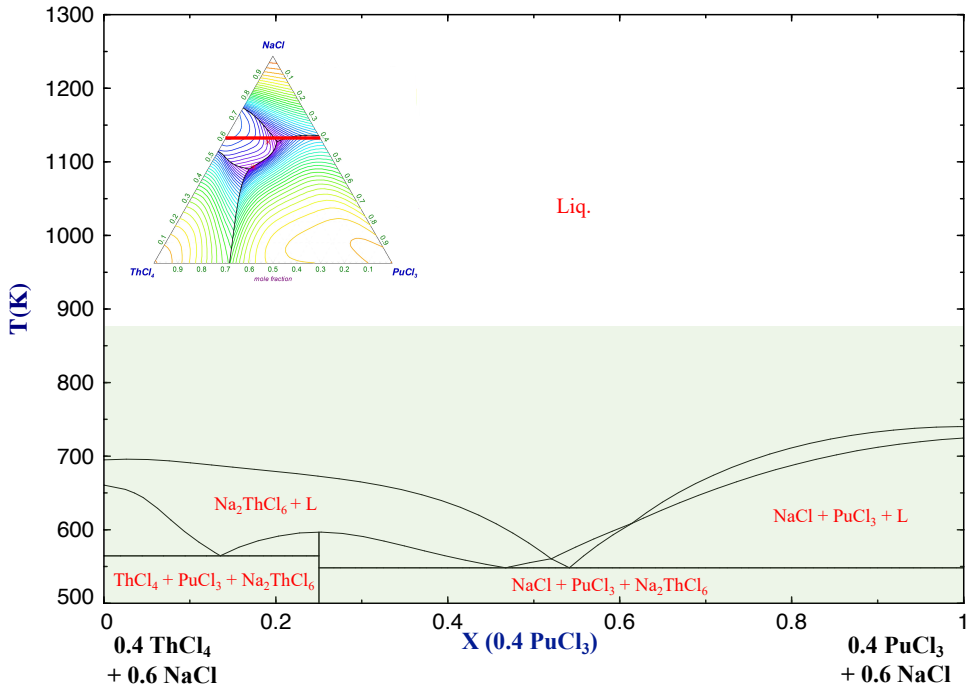


Figure 7.11.: Phase diagram of the pseudo-binary 40 (ThCl_4 - PuCl_3) + 60 NaCl system with the composition area of safety with the minimum inlet temperature minus 50 K (873 K) superposed in green.

An experimental study of the thermodynamic phase transition data of the mentioned key compositions appears essential, however, to validate the present model and for the development of this potential fuel in the framework of the fast neutron spectrum MSR. The evolution of the chemical composition of the fuel upon fission of plutonium (and uranium-233 generated from the fertile thorium), should also be monitored carefully as well as its impact on the thermo-physical properties. A more comprehensive picture of the fuel salt chemistry should then include the melts $\text{NaCl-ThCl}_4\text{-UCl}_3$ and $\text{NaCl-ThCl}_4\text{-UCl}_4$ as well as the extrapolation to the higher order system $\text{NaCl-ThCl}_4\text{-PuCl}_3\text{-UCl}_3\text{-UCl}_4$.

7.5. CONCLUSION

A thermodynamic assessment of the $\text{NaCl-ThCl}_4\text{-PuCl}_3$ system is reported for the first time based on the modified quasichemical formalism in the quadruplet approximation, including the modeling of the different binary constituting sub-systems. Two ternary eutectic transitions have been calculated at the compositions 47.0 NaCl – 35.4 ThCl₄ – 17.6 PuCl₃ and 57.4 NaCl – 22.3 ThCl₄ – 20.3 PuCl₃ at temperatures of 597 K and 598 K, respectively. This melt could be an interesting option as fuel for the fast neutron spectrum MSR concept as it offers a low melting temperature over a very wide range of composition, allowing flexibility in the choice of the final composition to accommodate neutronics, thermohydraulic and other requirements.

ACKNOWLEDGMENTS

T. Dumaire acknowledges gratefully financial support from the Nuclear Research and Consultancy Group (NRG, Petten, Netherlands).

REFERENCES

- [1] T. Dumaire, J. A. Ocádiz-Flores, R. J. M. Konings, and A. L. Smith. “A promising fuel for fast neutron spectrum Molten Salt Reactor: NaCl-ThCl₄-PuCl₃”. en. In: *Calphad* 79 (2022), p. 102496. DOI: 10.1016/j.calphad.2022.102496.
- [2] International Panel on Fissile Materials (IPFM). *Global Fissile Material Report 2015: Nuclear Weapon and Fissile Material Stockpiles and Production*. 8. International Panel on Fissile Materials (IPFM), 2015.
- [3] D. Heuer, E. Merle-Lucotte, M. Allibert, M. Brovchenko, V. Ghetta, and P. Rubiolo. “Towards the thorium fuel cycle with molten salt fast reactors”. In: *Annals of Nuclear Energy* 64 (2014), pp. 421–429. DOI: 10.1016/j.anucene.2013.08.002.
- [4] P. N. Haubenreich and J. R. Engel. “Experience with the Molten-Salt Reactor Experiment”. In: *Nuclear Applications and Technology* 8.2 (1970), pp. 118–136. DOI: 10.13182/nt8-2-118.
- [5] O. Beneš and R. J. M. Konings. “Molten Salt Reactor Fuel and Coolant”. In: *Comprehensive Nuclear Materials*. Ed. by R. J. M. Konings and R. E. Stoller. Amsterdam: Elsevier, 2020, pp. 609–644. DOI: 10.1016/b978-0-12-803581-8.11790-4.
- [6] A. Mourogov and P. Bokov. “Potentialities of the fast spectrum molten salt reactor concept: REBUS-3700”. In: *Energy Conversion and Management* 47.17 (2006), pp. 2761–2771. DOI: 10.1016/j.enconman.2006.02.013.
- [7] J. Latkowski. *TerraPower’s Molten Chloride Fast Reactor (MCFR)*. 2021. URL: <https://www.nationalacademies.org/event/02-22-2021/docs/DB0D308269688B2BD7B1AF60BAA143D48890C2DE80BB>.
- [8] O. Beneš and R. J. M. Konings. “Thermodynamic evaluation of the NaCl–MgCl₂–UCl₃–PuCl₃ system”. In: *Journal of Nuclear Materials* 375.2 (2008), pp. 202–208. DOI: 10.1016/j.jnucmat.2008.01.007.
- [9] M. Vorobei, A. Chernakov, O. Skiba, and V. Desyatnik. “A Thermographic Study of the Lead Dichloride Plutonium Trichloride and Thorium Tetrachloride—Plutonium Trichloride Binary Salt systems”. In: *Russian Journal of Inorganic Chemistry* 16.12 (1971), pp. 1793–1794.
- [10] H. Katsuta. *Liquid target/fuel and associated fuel cycle technologies*. Japan Atomic Energy Research Institute, 1997.
- [11] U.S. Geological Survey. *Minerals Yearbook, volume I, Metals and Minerals*. U.S. Geological Survey, 2021. DOI: 10.3133/mybvI.

- [12] A. . Bychkov, S. Vavilov, O. Skiba, P. Porodnov, A. Pravdin, G. P. Popkov, K. Suzuki, Y. Shoji, and T. Kobayashi. *Pyroelectrochemical reprocessing of irradiated FBR MOX fuel. 3. Experiment on high burn-up fuel of the BOR-60 reactor*. 1997.
- [13] M. Akebi. “Overview of the MONJU project.” In: *Proceeding of Fast Reactor and Related Fuel Cycles (FR’91)*. Kyoto, Japan: Atomic Energy Society of Japan., 1991, pp. 8.1/1–8.1/15.
- [14] J. Guidez and G. Prêle. “Superphenix: Technical and Scientific Achievements”. In: Paris: Atlantis Press, 2017. DOI: 10.2991/978-94-6239-246-5.
- [15] J. Krepel, B. Hombourger, and E. Losa. “Fuel cycle sustainability of Molten Salt Reator concepts in comparison with other selected reactors”. In: PHYTRA4. Marrakech, Marocco, 2018.
- [16] C. W. Bale, P. Chartrand, S. Degterov, G. Eriksson, K. Hack, R. B. Mahfoud, J. Melançon, A. Pelton, and S. Petersen. “FactSage thermochemical software and databases”. In: *Calphad* 26.2 (2002), pp. 189–228.
- [17] U. R. Kattner, H. J. Seifert, and H. L. Lukas. “Editorial: Integrated computational materials engineering, CALPHAD”. In: *CALPHAD: Computer Coupling of Phase Diagrams and Thermochemistry* 34 (2010), pp. 385–386. ISSN: 0364-5916. DOI: 10.1016/j.calphad.2010.10.005.
- [18] Y. A. Chang, S. Chen, F. Zhang, X. Yan, F. Xie, R. Schmid-Fetzer, and W. A. Oates. “Phase diagram calculation: past, present and future”. In: *Progress in Materials Science* 49.3-4 (2004), pp. 313–345. DOI: 10.1016/s0079-6425(03)00025-2.
- [19] C. W. Bjorklund, J. G. Reavis, J. A. Leary, and K. A. Walsh. “Phase Equilibria in the Binary Systems PuCl₃–NaCl and PuCl₃–LiCl”. In: *Journal of Chemical Chermistry* 63.10 (1959), pp. 1774–1777. DOI: 10.1021/j150580a049.
- [20] J. Schorne-Pinto, J. A. Yingling, M. S. Christian, A. M. Mofrad, M. A. A. Aslani, and T. M. Besmann. “Correlational Approach to Predict the Enthalpy of Mixing for Chloride Melt Systems”. In: *ACS Omega* 7.1 (2021), pp. 362–371. DOI: 10.1021/acsomega.1c04755.
- [21] S. Tanii. “Phase diagrams of the system thorium chloride- alkali chlorides and thorium chloride- eutectic chlorides(Phase diagrams of thorium chloride-alkali chlorides, and thorium chloride-eutectic chlorides systems- thorium chloride electrolysis)”. In: *Denki Kagaku Oyobi Kogyo Butsuri Kagaku* 32 (1964), pp. 167–170.
- [22] R. Oyamada. “Phase Diagrams of ThCl₄ Systems Containing NaCl, KCl and LiCl and the Limitation of the Congruently Melting Compounds Formation”. In: *Denki Kagaku oyobi Kogyo Butsuri Kagaku* 39.1 (1971), pp. 2–5. DOI: 10.5796/kogyobutsurikagaku.39.2.
- [23] A. Vokhmyakov, V. Desyatnik, and N. Kurbatov. “Interaction of thorium tetrachloride with chlorides of the alkali metals”. In: *Sov. At. Energy (Engl. Transl.)* 35 (6 1973), pp. 1122–1123.

- [24] V. Desyatnik, M. Vorobei, N. Kurbatov, I. Kalashnikov, and O. Siiba. “Melting diagrams of ternary systems containing sodium and potassium chlorides, thorium tetrachloride, and plutonium trichloride”. In: *Soviet Atomic Energy* 38.3 (1975), pp. 219–221. DOI: 10.1007/bf01666673.
- [25] V. S. Iorish, N. M. Aristova, G. Bergman, L. Gorohov, A. Gusarov, Y. Yezhov, A. Kulikov, E. Osina, E. Shenyavskaya, N. Handamirova, and V. Jungmann. “Thermodynamic properties of substances (1978-2004)”. In: Publishing House Nauka: Moscow, Russia, 2004.
- [26] G. I. van Oudenaren, J. A. Ocadiz-Flores, and A. L. Smith. “Coupled structural-thermodynamic modelling of the molten salt system NaCl-UCl₃”. In: *Journal of Molecular Liquids* 342 (2021), p. 117470. DOI: 10.1016/j.molliq.2021.117470.
- [27] M. Rand, J. Fuger, I. Grenthe, V. Neck, and D. Rai. “Chemical Thermodynamics of Thorium (Chemical Thermodynamics)”. In: *Paris: OCDE-NEA* (2008).
- [28] E. Capelli and R. J. M. Konings. “Halides of the Actinides and Fission Products Relevant for Molten Salt Reactors”. In: *Konings, Rudy JM and Stoller Roger E (eds.) Comprehensive Nuclear Materials 2nd edition*. Vol. 7. Elsevier, 2020, pp. 256–283. DOI: 10.1016/b978-0-12-803581-8.11794-1.
- [29] P. Chiotti, G. Gartner, E. Stevens, and Y. Saito. “Heats of Fusion and Transformation for Some Metals and Compounds.” In: *Journal of Chemical and Engineering Data* 11.4 (1966), pp. 571–574.
- [30] J. A. Ocadiz Flores, B. A. S. Rooijackers, R. J. M. Konings, and A. L. Smith. “Thermodynamic Description of the ACl-ThCl₄ (A = Li, Na, K) Systems”. In: *Thermo* 1.2 (2021), pp. 122–133. ISSN: 2673-7264. DOI: 10.3390/thermo1020009.
- [31] J. T. Mason, M. C. Jha, and P. Chiotti. “Crystal structures of ThCl₄ polymorphs”. In: *Journal of the Less-Common Metals* 34 (1974), pp. 143–151. ISSN: 0022-5088. DOI: 10.1016/0022-5088(74)90224-0.
- [32] J. Leitner, P. Voňka, D. Sedmidubský, and P. Svoboda. “Application of Neumann-Kopp rule for the estimation of heat capacity of mixed oxides”. In: *Thermochimica Acta* 497.1–2 (2010), pp. 7–13. ISSN: 0040-6031. DOI: 10.1016/j.tca.2009.08.002.
- [33] J. Fuger and B. B. Cunningham. “Heats of formation of Pu³⁺(aq), PuCl₃(c), PuOCl(c), Am³⁺(aq), AmCl₃(c) and AmOCl(c)”. In: *Journal of Inorganic and Nuclear Chemistry* 25.11 (1963), pp. 1423–1429. DOI: 10.1016/0022-1902(63)80414-5.
- [34] R. J. Lemire *et al.* “Chemical Thermodynamics of Neptunium and Plutonium”. In: *Chemical Thermodynamics*. Ed. by D. B. OECD Nuclear Energy Agency. Vol. 4. Amsterdam: Elsevier, 2001.
- [35] I. Grenthe, J. Fuger, R. J. M. Konings, R. J. Lemire, A. B. Muller, C. Nguyen-Trung, and H. Wanner. “Chemical thermodynamics of uranium”. In: ed. by D. B. OECD Nuclear Energy Agency. Vol. 1. Amsterdam: Elsevier, 1992.

- [36] R. Guillaumont, F. J. Mompean, *et al.* “Update on the chemical thermodynamics of uranium, neptunium, plutonium, americium and technetium”. In: ed. by D. B. OECD Nuclear Energy Agency. Vol. 5. Amsterdam: Elsevier, 2003.
- [37] R. J. M. Konings and A. Kovács. “Thermodynamic properties of the lanthanide(III) halides”. In: *Handbook on the Physics and Chemistry of Rare Earths*. Vol. 33. Elsevier, 2003. Chap. 213, pp. 147–247. DOI: 10.1016/s0168-1273(02)33003-4.
- [38] M. W. Chase Jr. and National Information Standards Organization (US). “NIST-JANAF Thermochemical Tables”. In: *Journal of Physical and Chemical Reference Data*. Vol. 9. Washington DC: American Chemical Society, 1998.
- [39] O. Beneš and R. J. M. Konings. “Thermodynamic Calculations of Molten-Salt Reactor Fuel Systems”. In: *Molten Salts Chemistry - From Lab to Applications*. Ed. by H. G. Frederic Lantelme. Elsevier, 2013, pp. 49–78. DOI: 10.1016/b978-0-12-398538-5.00004-4.
- [40] Joint Research Centre - European Commission. *Joint Research Centre Molten Salt Database - JRCMSD*. Ed. by E. S. Hub. https://joint-research-centre.ec.europa.eu/joint-research-centre-molten-salt-database-jrcmsd_en. Accessed: 2024-02-05.
- [41] A. D. Pelton, S. Degterov, G. Eriksson, C. Robelin, and Y. Dessureault. “The modified quasichemical model I—binary solutions”. In: *Metallurgical and Materials Transactions B* 31.4 (Aug. 2000), pp. 651–659. ISSN: 1543-1916. DOI: 10.1007/s11663-000-0103-2.
- [42] O. Beneš, M. Beilmann, and R. J. M. Konings. “Thermodynamic assessment of the LiF–NaF–ThF₄–UF₄ system”. In: *Journal of Nuclear Materials* 405.2 (2010), pp. 186–198. DOI: 10.1016/j.jnucmat.2010.08.017.
- [43] A. D. Pelton. “A general “geometric” thermodynamic model for multicomponent solutions”. In: *Calphad* 25.2 (2001), pp. 319–328. DOI: 10.1016/s0364-5916(01)00052-9.
- [44] H. Yin, J. Lin, B. Hu, W. Liu, X. Guo, Q. Liu, and Z. Tang. “Thermodynamic description of the constitutive binaries of the NaCl–KCl–UCl₃–PuCl₃ system”. In: *Calphad* 70 (2020), p. 101783. DOI: 10.1016/j.calphad.2020.101783.
- [45] H. T. Davis. “Theory of Heats of Mixing of Certain Charge-Unsymmetrical Fused Salts”. In: *The Journal of Chemical Physics* 41.9 (1964), pp. 2761–2766. DOI: 10.1063/1.1726349.
- [46] M. Gaune-Escard, A. Bogacz, L. Rycerz, and W. Szczepaniak. “Calorimetric investigation of NdCl₃–MCl liquid mixtures (where M is Na, K, Rb, Cs)”. In: *Thermochimica Acta* 236 (1994), pp. 67–80. DOI: 10.1016/0040-6031(94)80256-4.
- [47] H. Matsuura, R. Takagi, L. Rycerz, and M. Gaune-Escard. “Enthalpies of mixing in molten UCl₃–NaCl system”. In: *Journal of Nuclear Science and Technology* 39.3 (2002), pp. 632–634. DOI: 10.1080/00223131.2002.10875547.

- [48] G. N. Papatheodorou and T. Ostvold. "Thermodynamic studies of binary charge unsymmetrical fused salt systems. Calorimetric and electromotive force measurements of liquid lanthanum(III) chloride-alkali chloride mixtures". In: *The Journal of Physical Chemistry* 78.2 (1974), pp. 181–185. DOI: 10.1021/j100595a019.
- [49] K. C. Hong and O. J. Kleppa. "Enthalpies of mixing in some binary liquid alkali fluoride mixtures". In: *The Journal of Chemical Thermodynamics* 8 (1976), pp. 31–36. ISSN: 0021-9614. DOI: 10.1016/0021-9614(76)90147-6.
- [50] F. Paulik, J. Paulik, and L. Erdey. "Derivatography: A complex method in thermal analysis". In: *Talanta* 13.10 (1966), pp. 1405–1430. DOI: 10.1016/0039-9140(66)80083-8.
- [51] V. Vdovenko, A. Gershanovich, and I. Suglobova. "Thermal and X-ray diffraction studies of thorium chloride-lithium chloride and thorium chloride-sodium chloride binary systems". In: *Radiokhimiya* 166 (1974), pp. 886–889.

8

CONCLUSION

THIS thesis aimed to provide essential insights contributing to the safety assessment of Molten Salt Reactors (MSRs). By exploring critical aspects and key factors, the research aimed to enhance our understanding of the safety implications associated with MSR technology. In this concluding chapter, the results are summarized in the next section (8.1), the main outcome is given (section 8.2) and finally, some outlook and suggestions for future work are offered (section 8.3).

8.1. SUMMARY OF THE RESULTS

The empirical observation of the fission product behavior in the molten fuel LiF-ThF_4 and $\text{LiF-ThF}_4\text{-UF}_4$ showed key outcomes result for the Molten Salt Reactor concept. Firstly, the mass spectrometry measurements proved the high retention of Sr, lanthanides (Nb,Ce), Rb and Y in molten fluoride salts. Cesium, as already observed by Beneš *et al.* [1], has showed moderate retention as CsF and low retention as CsI resulting in early vapor release and potential recombination of iodine in LiI form. Zr also shows moderate retention, with a release at a lower temperature than the fuel matrix under Knudsen conditions. Secondly, an essential criteria from an engineering point of view, is the melting temperature of the fuels, which was found to decrease by 21 K upon addition of a large amount of fission products at the eutectic compositions. This must be taken into consideration for the safety margin of operation. Furthermore, the vapor pressure of the elements of the fuel calculated by KEMS on the same mixture, was found almost unchanged compared to the pure fuels measured in the literature. These first results proved the limited impact of the accumulation of the fission products on the vapor pressure of the fuel itself. However the scope of this work remains limited, because the gaseous fission product were not included and the chemical speciation of vapor species could not be determined in this work. Complementary studies of the dissociation patterns would give valuable insights on the speciation.

To prolong the fission product analysis, a dedicated study was performed for two important fission product: zirconium and barium. For the first time, thermodynamic models were established for the binary systems LiF-BaF_2 , LiF-ZrF_4 , and $\text{BaF}_2\text{-ZrF}_4$, as well as the ternary system $\text{LiF - BaF}_2\text{ - ZrF}_4$, by integrating experimentally obtained phase diagram data and information from literature sources on phase diagrams and mixing

enthalpy. These models were developed using the modified quasichemical model in the quadruplet approximation specifically for the liquid solution. A significant portion of the intermediates identified in the $\text{LiF}-\text{BaF}_2-\text{ZrF}_4$ system seem to exhibit stability at the minimum operating temperature of a MSR (873 K). Above 1173 K, solid phases of Ba_2ZrF_8 and $\text{Ba}_3\text{ZrF}_{10}$ are stable. Considering the potential precipitation of solid phases involving LiF , BaF_2 , and ZrF_4 within the operational reactor is essential for conducting a thorough risk assessment of the MSR.

The development of a new method using laser-induced luminescence moreover made it possible to directly measure changes in the concentration, i.e. recovery, of nanoparticles in a bubbly flow. During the evaluation of the different recovery systems, the modified Hallimond tube, which has demonstrated its effectiveness in the removal of micro-sized metallic particles, did not confirm it in the case of the nano-sized particles. An alternative technique was designed, using a supernatant immiscible fluid as collecting support. The first approximation of the recovery of nanoparticles by a bubbly flow was measured as relatively low and strongly dependent on the size of the particles and flow rate. These results are in agreement with the literature observation during comparable studies [2, 3]. Helium bubbling represents probably a good option for the removal of gaseous fission product species, but for the noble and semi noble non-dissolved particles the effectiveness is limited.

Concerning the corrosion products, the focus was made on the most problematic one, namely chromium. In this thesis, phase diagram equilibria of the $\text{AF}-\text{CrF}_3$ ($\text{A} = \text{Li}, \text{Na}, \text{K}$) systems have been optimized using the CALPHAD method combined with the modified quasichemical model in the quadruplet approximation. On the basis of the only experimental data in literature by de Kozak [4], the models of $\text{LiF}-\text{CrF}_3$, $\text{NaF}-\text{CrF}_3$ and $\text{KF}-\text{CrF}_3$ have been modeled with a good agreement. With the same method, the $\text{CrF}_2-\text{CrF}_3$ binary system has been modeled based on the experimental data of Sturm [5]. Understanding the phase diagrams of all four systems contributes to an enhanced comprehension of the impact of corrosion products (CrF_2 , CrF_3) formed due to the corrosion of Hastelloy, employed as the structural material in Molten Salt Reactors, on the characteristics of the liquid fuel salt. To completely assess the impact of chromium in solution in molten $\text{LiF}-\text{ThF}_4$ salt reference fuel, the phase equilibria in the $\text{LiF}-\text{CrF}_2-\text{ThF}_4$ system were also investigated. Firstly, the synthesis of pure CrF_2 has been reported by two different routes. For the first time, phase diagram data in the $\text{LiF}-\text{CrF}_2$, $\text{CrF}_2-\text{ThF}_4$ and $\text{LiF}-\text{CrF}_2-\text{ThF}_4$ systems have been collected. Using the modified quasichemical model in the quadruplet approximation, to describe the liquid solution, thermodynamic models have been made. The essential information in this work has been the experimental observation that the CrF_2 does not form any quaternary intermediate compound in the molten $\text{LiF}-\text{ThF}_4$ system. The entire description of the corrosion product of chromium behavior in the reference fuel, constitutes new knowledge for the safety assessment of the Molten Salt Reactor.

The final chapter opened the door to a promising molten mixture as a compelling option for the fast neutron spectrum molten salt reactor (MSR) concept: $\text{NaCl}-\text{ThCl}_4-\text{PuCl}_3$. Thermodynamic evaluation of the $\text{NaCl}-\text{ThCl}_4-\text{PuCl}_3$ system has been presented for the first time, employing also the modified quasichemical formalism in the quadruplet approximation, encompassing the modeling of the constituting binary sub-systems.

Two ternary eutectic transitions have been computed at compositions 47.0 NaCl – 35.4 ThCl₄ – 17.6 PuCl₃ and 57.4 NaCl – 22.3 ThCl₄ – 20.3 PuCl₃ with corresponding temperatures of 597 K and 598 K, respectively. Its advantage lies in its low melting temperature over a wide range of compositions, which means that the final composition can be chosen according to neutronic requirements, thermal-hydraulic considerations and other factors.

8.2. MAIN OUTCOMES

The main outcomes issued in this work are summarized as follow:

- The addition of 7 mol% fission products to a LiF–ThF₄–UF₄ eutectic mixture has a limited effect on the vapor pressure of the fuel matrix.
- The retention of the fission products under Knudsen conditions is low for CsI, moderate for CsF and ZrF₄, high for the RbF and very high for SrF₂, YF₃ and lanthanides fluorides (CeF₃ and NdF₃).
- The helium bubbling did not prove its effectiveness for the recovery of the solid nanoparticles.
- In the reference fuel, LiF–ThF₄–UF₄, the main corrosion product expected to form has been identified as CrF₂ and does not form complex intermediate compounds in the molten LiF–ThF₄ salt system.
- Thermodynamic calculations allowed to define a fuel well adapted to the fast neutron reactors spectrum, NaCl – ThCl₄ – PuCl₃, which showed good potential in terms of safety and flexibility.

8.3. OUTLOOKS AND SUGGESTIONS

This thesis answered some of the key interrogations concerning the feasibility of the MSR concept. However, to fulfill in more detail the safety assessment, some suggestions of future research development are given hereafter.

If the fission product showed variable degrees of retention in the molten LiF – ThF₄ – UF₄ salt and limited impact on the thermodynamic and vapor pressure properties, in general, however their poisonous impact need to be explored in further detail. Indeed, even if the fission product did not interact with the fuel components, they could affect the fission reaction by interfering with the neutron diffusion. The consequences would be a decrease of the reactivity during the reactor operation.

For the two fission products studied in further detail, zirconium and barium, the current systems developed in this work only provide equilibria with LiF, which is present in large concentrations in the salt mixture. This establishes a foundation for exploring more intricate equilibria within the entire fuel system, such as LiF–ThF₄–UF₄/UF₃, which must be taken into account for a more precise analysis.

A general overview of the literature on molten salts shows a certain optimism and generally focuses on pure "fuel-interacting materials" systems. The impact of potential oxygen contamination is probably underestimated in most of the projects related to the development of MSR technology. From an engineering point of view, it appears unrealistic to prevent the reactor core from all the potential sources of external contamination, for instance during maintenance operations. A thorough safety assessment would include interaction of oxygen and water with the fuel salt.

Concerning the helium bubbling, first of all, performing new series of measurements under the same conditions would allow to reduce the uncertainties. The liquid filtration system could be improved, and different organic phase options could be studied, for instance the use of a completely uncolored solution to reduce parasitic light during the measurements. A dual-camera system could be designed, featuring one observation window for the aqueous solution and another for the organic phase. This setup would enable simultaneous monitoring of concentrations in each phase, enhancing the assessment of direct removal through individual particle tracking.

For the extraction of solid nanoparticles, alternative ways should be explored, with a particular focus on a thermochemical route. For instance, the implementation of a cathodic protection could provide a system of collection of the semi-noble and noble metal particles and even prevent the corrosion of the structural materials of the reactor.

In this work, the thermodynamic behavior of chromium in molten $\text{LiF}-\text{ThF}_4$ has been described in detail. However, a full assessment should include the chemistry of chromium in the complete reference fuel, $\text{LiF}-\text{ThF}_4-\text{UF}_4$. Given the high probability of reduction of UF_4 in UF_3 along the operating period and the importance of controlling the UF_4/UF_3 ratio observed by ORNL [6], both interactions with CrF_2 should be investigated. Thermodynamic properties would include the assessment of phase diagrams for binary systems CrF_2-UF_4 and CrF_2-UF_3 , as well as ternary systems $\text{LiF}-\text{CrF}_2-\text{UF}_4$ and $\text{LiF}-\text{CrF}_2-\text{UF}_3$. Finally, the quaternary systems $\text{LiF}-\text{CrF}_2-\text{UF}_3-\text{UF}_4$, $\text{LiF}-\text{CrF}_2-\text{ThF}_4-\text{UF}_4$ and $\text{LiF}-\text{CrF}_2-\text{ThF}_4-\text{UF}_3$ and possibly higher-order systems need to be investigated. These studies should also explore the impact of chromium ions on the UF_4/UF_3 ratio under equilibrium conditions, in particular whether it has an impact on the fluoroacidity of the salt mixture, i.e. on the corrosion rate.

A further suggestion for corrosion studies of structural materials would be to study in depth the impact of radiation damage on corrosion. Much work has focused on exposing materials to "simple" molten-salt fuels, but an operating reactor would involve radiation damage from neutrons, recoil of fission products, etc. The combined effects of radiation damage and corrosion should also be considered and understood.

REFERENCES

- [1] O. Beneš, E. Capelli, N. Morelová, J.-Y. Colle, A. Tosolin, T. Wiss, B. Cremer, and R. J. M. Konings. “Cesium and iodine release from fluoride-based molten salt reactor fuel”. In: *Physical Chemistry Chemical Physics* 23.15 (2021), pp. 9512–9523. DOI: 10.1039/d0cp05794k.
- [2] A. V. Nguyen, P. George, and G. J. Jameson. “Demonstration of a minimum in the recovery of nanoparticles by flotation: Theory and experiment”. In: 61 (2006), pp. 2494–2509. ISSN: 0009-2509. DOI: 10.1016/j.ces.2005.11.025.
- [3] N. Mishchuk, J. Ralston, and D. Fornasiero. “The analytical model of nanoparticle recovery by microflotation”. In: 179-182 (2012), pp. 114–122. ISSN: 0001-8686. DOI: 10.1016/j.cis.2012.06.008.
- [4] A. de Kozak. *Comptes rendus hebdomadaires des séances de l'Académie des sciences*. Série C. Research rep. 268. Académie des sciences de Paris, 1969, pp. 416–418.
- [5] B. J. Sturm. “Phase equilibria in the system chromium (II) fluoride-chromium (III) fluoride”. In: *Inorganic Chemistry* 1.3 (1962), pp. 665–672.
- [6] J. H. Shaffer. *PREPARATION AND HANDLING OF SALT MIXTURES FOR THE MOLTEN SALT REACTOR EXPERIMENT*. Tech. rep. Oak Ridge National Laboratory, Jan. 1971. DOI: 10.2172/4074869.

A

APPENDICES: THERMODYNAMIC BEHAVIOR OF CrF_2 CORROSION PRODUCT IN THE MOLTEN LiF-ThF_4 SALT SYSTEM

A.1. LOW TEMPERATURE HEAT CAPACITY OF CrF_2

The existence of an antiferromagnetic transition in CrF_2 is confirmed by the low-temperature heat capacity data collected under varying magnetic fields (Figure A.1). The anomaly shifts to slightly lower temperatures upon application of a magnetic field.

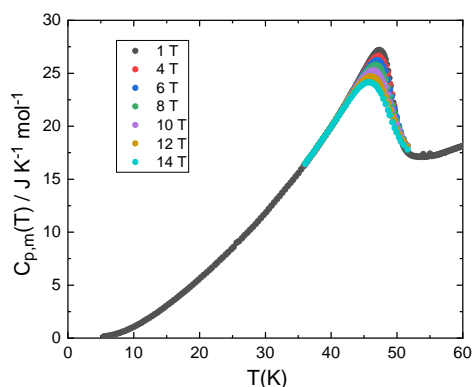


Figure A.1.: Evolution of the heat capacity of CrF_2 upon application of a magnetic field $B=(1, 4, 6, 8, 10, 12, 14)$ Tesla.

Figure A.2 shows the measured low-temperature heat capacity together with the function at higher temperatures recommended in the IVTAN tables [1], showing the good accordance between the two temperature regimes.

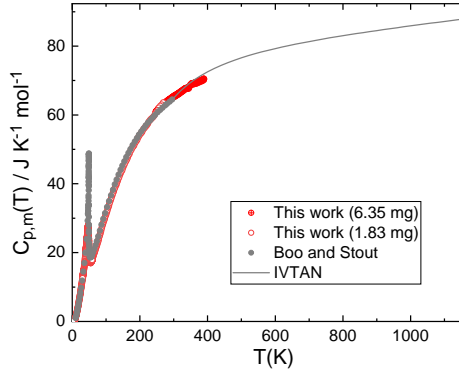


Figure A.2.: Evolution of the heat capacity of CrF_2 up to melting (1167 K).

A.2. MAGNETIZATION MEASUREMENTS OF CrF_2

Magnetization measurements of CrF_2 show a clear anti-ferromagnetic order at $T_N = 49.6$ K, as reported by Stout et al. [2] and Boo et al. [3]. Measurements in DC and AC techniques confirmed this value (Figures A.3). Interestingly, below the anti-ferromagnetic transition temperature T_N , we observe a strong anisotropic behavior in the ordered state, that is of ferromagnetic type, similarly to anisotropic features reported below 308 K for antiferromagnetic Cr_2O_3 [4], or for some other reported Cr based materials [5]. Zero-Field Cooling (ZFC) measurements show negative response versus the applied magnetic field, while Field-Cooling (FC) curves at low magnetic fields are characteristics of a ferromagnetic-like ordered state. This ZFC diamagnetic response disappears at 10 kOe. The estimated coercive field at 45 K is still 2500 Oe. ZFC and FC curves are joining at T_N , but difference between ZFC-FC magnetization curves is still present up to the maximum magnetic field applied (70 kOe). Neutron diffraction measurements [6] have shown CrF_2 to be a two-sublattice antiferromagnet with a distorted rutile structure of monoclinic symmetry, containing two Cr^{2+} ions per unit cell. This supports the intrinsic anisotropy features in the low temperature ordered state with a ferromagnetic canted moment responding strongly to applied magnetic fields. In the paramagnetic temperature range ($T < T_N$), we observe a very good reproducibility of DC magnetic susceptibility for all magnetic fields applied. Fitting this paramagnetic field from 100 to 300 K by a modified Curie Weiss law, we obtain an effective moment μ_{eff} close to $5.7(3) \mu_B$, and a paramagnetic temperature θ_P close to -70 K. Cr^{2+} effective moment in the free ion model is $4.9 \mu_B$.

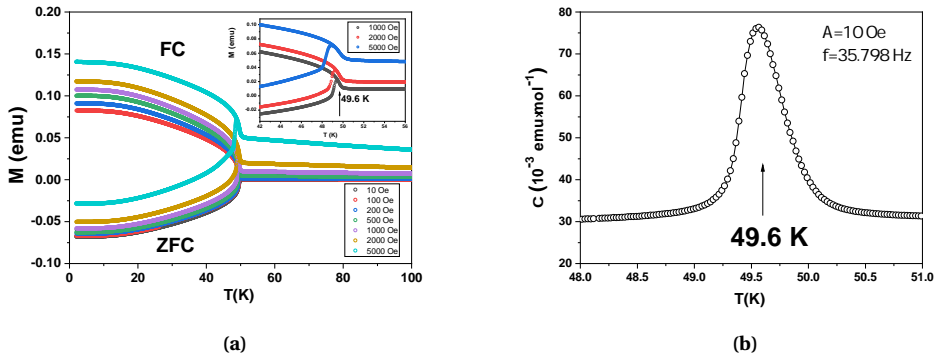


Figure A.3.: (a) Evolution of the DC magnetization M of CrF_2 below T 100 K in ZFC and FC. (b) AC magnetic measurements showing the evolution of the AC magnetic susceptibility χ .

A.3. TERNARY EQUILIBRIA

In the Figure A.4, the isothermal sections calculated for different temperatures (750 K, 850 K, 950 K and 1050 K) in the ternary system $\text{LiF}-\text{CrF}_2-\text{ThF}_4$, showing the stability of the solid phases.

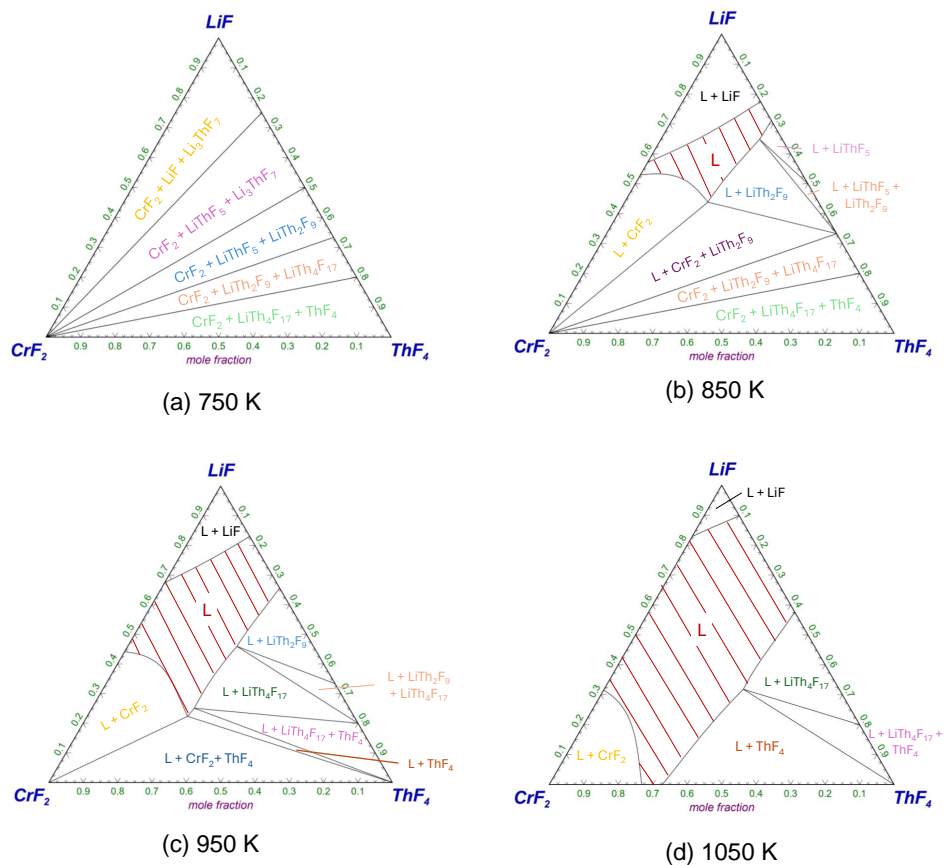


Figure A.4.: Isothermal sections of the ternary system LiF - CrF_2 - ThF_4 at (a) 750 K, (b) 850 K, (c) 950 K and (d) 1050 K. The different stable solids and the liquid phases are indicated in the figures.

ACKNOWLEDGMENTS

Throughout this PhD, I could count on many wonderful people who made this work possible. From Delft to Karlsruhe, despite the obstacles we have encountered over the last few years.

First of all, I can't express how grateful I am to Anna for having supervised me during this thesis. Her high standards combined with her unfailing support have enabled me to produce a thesis of which I am proud.

I would also like to thank Rudy for his attentiveness and his ability to clarify in a few words all the questions I might have had. And also Martin, who kindly supported me as a chemist in the midst of a physicist. Thank you for all these impromptu meetings, at the end of which I had more and more experimental paths to explore.

I would like to express my deep gratitude to my first chemistry teacher, Antonin Barriaux, who taught me the guidelines for the scientist I am today. Special thanks to my friend Élise, without whom I probably would not be standing here today.

I acknowledge the SAMOSAFAER project and the Nuclear Research and Consultancy Group (NRG) for funding this thesis project. Special thanks go to Ralph Hania and Geert-Jan de Haas for the kind look they have taken at my work over the years, and to Edo Frederix for helpful discussions on helium bubbling.

I would like to thank my colleagues at the Reactor Institute, Aldo, Daniel, Bouke, Andries, Fahad, Matt, Tibi, Danny, Zolt'an for all the fun lunches and drinks at the 't Koe-peltje we have had over the years. And our boss Jan-Leen, for his availability and kindness. A big thank you to Dick and John for their invaluable help in solving all the technical problems, Trudy and Karin who were essential to surviving in the Dutch administration. Special thanks to my group of "Padeleros": Paloma, Marc, the "actinide wizard" Jaén and my office-closing mate, Oscar, for all the good times we shared in Delft together!

At the Joint Research Centre of Karlsruhe, I would like to express my gratitude to Ondrej, who gave me a warm welcome (and some beer), support my research and allow me to work freely in this great institution. I am grateful to Petra and Vladka for their invaluable help with the German administrative challenge. I would like to thank Jean-Yves, Mark, Pavel, Jean-Christophe and the legendary Olaf, for their invaluable help with my research. A big thank you Elisa, I do not think anyone has read your work as much as I have and it was a great lead to follow, I discovered your kindness and your availability and I hope we will meet again. My time in Germany has also been brightened up, both at work and outside it, thanks to Maxime, Jérémie, Tristan, Viktoria, Angela, Megan and Sirella, with whom we will be in touch in the future.

I would like to thank all my friends in France, who have not forgotten me, far from home, rarely available and barely answering messages. Thanks for the vacations, the celebrations and the reminder that sport needs practice. I have a big thought for my strong squad, Nico, Roro and Alex, who helped me clear my mind during our trips to

Verdansk.

Eternal thanks to Ronan and Sebastian, who opened their home to me in Delft and gave me so much support during my first few months of the thesis and especially during the curfew period.

A big thank you to my most beautiful encounter in this thesis: Morgane. Her kind look at my stupid jokes and her patience during the writing process were incredibly supportive.

Je ne pourrais jamais assez remercier mes parents et frères pour avoir accompagné l'étudiant au long cours que j'ai été, et de votre soutien malgré la distance. Ce fut un long voyage et je n'y serais jamais arrivé sans vous.

LIST OF PUBLICATIONS

JOURNAL PUBLICATIONS

6. **T. Dumaire**, O. Walter, O. Beneš, J.-C. Griveau, E. Colineau, R.J.M. Konings & A.L. Smith (2024) Thermodynamic behavior of CrF_2 corrosion product in the molten LiF-ThF_4 salt system. *CALPHAD: Computer Coupling of Phase Diagrams and Thermochemistry*, 86, 102722.
5. **T. Dumaire**, L. Groot, N.M. Schakenraad, O. Beneš, R.J.M. Konings & A.L. Smith (2024) Thermodynamic assessment of the $\text{LiF-BaF}_2\text{-ZrF}_4$ system. *Fluid Phase Equilibria*, 585, 114147.
4. N.L. Scuro, B.W.N. Fitzpatrick, E. Geiger, M. Poschmann **T. Dumaire**, O. Beneš & M.H.A. Piro (2024) Thermodynamic investigations of the NaI-CsI , KI-CsI , and NaF-CsI pseudo-binary systems. *The Journal of Chemical Thermodynamics*, 193, 107272.
3. **T. Dumaire**, J.A. Ocadiz-Flores, R.J.M. Konings & A.L. Smith (2023) A promising fuel for fast neutron spectrum Molten Salt Reactor: $\text{NaCl-ThCl}_4\text{-PuCl}_3$. *Calphad*, 79, 102496.
2. **T. Dumaire**, R.J.M. Konings & A.L. Smith (2021) Thermodynamic Assessment of the AF-CrF_3 (A= Li, Na, K) and $\text{CrF}_2\text{-CrF}_3$ Systems. *Thermo*, 1(2), 205-219.
1. M. Dudek, A. Bertheussen, **T. Dumaire** & G. Øye (2018) Microfluidic tools for studying coalescence of crude oil droplets in produced water. *Chemical Engineering Science*, 191, 448-458.

CONFERENCE PRESENTATIONS

5. **T. Dumaire**, M. Fache, O. Beneš, R.J.M. Konings & A.L. Smith (2023, November 7-9) *Chromium speciation in Molten Salt Reactor fuels* NuFuel conference 2023, Marseille, France.
4. **T. Dumaire**, O. Beneš, P. Souček, R.J.M. Konings & A.L. Smith (2023, June 25-30) *Thermodynamic determination of the $\text{LiF-ThF}_4\text{-CrF}_2$ system*. CALPHAD meeting 2023, MIT-Cambridge, MA, USA.
3. **T. Dumaire**, L. Groot, J.A. Ocadiz-Flores, R.J.M. Konings & A.L. Smith (2022, June 6-8) *Thermodynamic assessments of the $\text{LiF-ZrF}_4\text{-BaF}_2$, $\text{NaF-ZrF}_4\text{-BaF}_2$ and $\text{KF-ZrF}_4\text{-BaF}_2$ systems*. Young Molten Salt Reactor Conference, Lecco, Italy.
2. **T. Dumaire**, J.A. Ocadiz-Flores, R.J.M. Konings & A.L. Smith (2021, September 13-17) *Thermodynamic assessment of the $\text{NaCl-ThCl}_4\text{-PuCl}_3$ system*. NuFuel 2021 Conference, Bangor, Wales.
1. **T. Dumaire**, R. Hania, R.J.M. Konings & A.L. Smith (2020, October 26-30) *Thermodynamic assessments of the LiF-NaF-KF-CrF_3 systems*. 6th Nuclear Materials Conference (NuMat), Gent, Belgium.